ABSTRACT

Title of Document:	COMPUTATIONAL STUDY OF THE STRUCTURE AND MECHANICAL PROPERTIES OF THE MOLECULAR CRYSTAL RDX
	Lynn Munday, Doctor of Philosophy, 2011
Directed By:	Assistant Professor Santiago D. Solares, Department of Mechanical Engineering

Molecular crystals constitute a class of materials commonly used as active pharmaceutical ingredients, energetic and high explosive materials. Like simpler crystalline materials, they possess a repeating lattice structure. However, the complexity of the structure – due to having several entire molecules instead of atoms at each lattice site – significantly complicates the relationship between the crystal structure and mechanical properties. Of particular interest to molecular crystals are the mechanically activated processes initiated by large deformations. These include polymorph transitions, slip deformation, cleavage fracture, or the transition to disordered states. Activation of slip systems is generally the preferred mode of deformation in molecular crystals because the long range order of the crystal and its associated properties are maintained. These processes change the crystal structure and affect the physiological absorption of advanced pharmaceutical ingredients and the decomposition of high explosives.

This work used molecular dynamics to study the energetic molecule RDX, $C_3H_6N_6O_6$, as a model molecular crystal that is a commonly used military high explosive. Molecular dynamics is used to determine the crystal response to deformation by determination of elastic constants, polymorph transitions, cleavage properties, and energy barriers to slip. The cleavage and the free surface energy are determined through interface decohesion simulations and the attachment energy method. The energy barriers to slip are determined through the generalized stacking fault (GSF) procedure. To account for the steric contributions and elastic shearing due to the presence of flexible molecules, a modified calculation procedure for the GSF energy is proposed that enables the distinction of elastic shear energy from the energy associated with the interfacial displacement discontinuity at the slip plane. The unstable stacking fault energy from the GSF simulations is compared to the free surface energy to differentiate cleavage and slip planes. The results are found to be largely in agreement with available experimental data.

COMPUTATIONAL STUDY OF THE STRUCTURE AND MECHANICAL

PROPERTIES OF THE MOLECULAR CRYSTAL RDX

By

Lynn Munday

Dissertation submitted to the Faculty of the Graduate School of the
University of Maryland, College Park, in partial fulfillment
of the requirements for the degree of
Doctor of Philoscophy
2011

Advisory Committee:
Assistant Professor Santiago Solares, Chair/Advisor
Professor Abhijit Dasgupta
Professor Gregory Jackson
Assistant Professor Teng Li
Dr. Peter Chung
Associate Professor Peter Sunderland, Dean's Representative

Acknowledgements

God has blessed me with such a great family and so many opportunities that I am so grateful for. My family has supported and encouraged me through this whole process of finishing up my degree. My parents, brother, sister and their families have always given me the support and love needed to finish up my schooling. My wife Katie and now our new baby May are the perfect loving family and I'm so happy to come home to them every night.

I have had the best advisors, Professors Santiago Solares and Abhijit Dasgupta at the University of Maryland and Dr. Peter Chung at the Army Research Laboratory (ARL), who have given me so much of their valuable time to guide me in my research and give me friendly advice. They have all created great research groups that I am thankful to have been a part of.

Table of Contents

List of Tables

List of Figures

1. Introduction

Molecular crystals constitute a class of materials commonly found and used in the aerospace, defense, agricultural, and pharmaceutical industries. Like simpler crystalline materials, they possess a repeating lattice structure. However, the complexity of the structure – due to having several entire molecules instead of atoms at each lattice site – significantly complicates deformation mechanisms relative to those found in, for instance, materials with a close-packed crystal structure like copper (1). Molecular crystals subjected to large deformations can be mechanically activated to undergo phase transitions, slip deformation, cleavage fracture, or transition to disordered states. Molecular crystals used as active pharmaceutical ingredients (API) are milled to decrease crystal size and increase surface area. Milling reduces the crystal size through fracture but also induces the other common modes of deformation into the smaller crystal. The disordered states are prone to recrystallization and affect the long term stability of the API (2). In energetic and high explosive molecular crystals, the available modes of crystalline deformation affect the initiation sensitivity of the entire munition to accidental shock loading. Deformation mechanisms travel energetic pathways that may intersect and overcome chemical reaction barriers, leading to initiation and detonation. Thus understanding the relationship between the molecular crystal structure and deformation mechanisms is fundamentally important to this exceptionally large and commonplace class of material.

The focus of this dissertation is on atomistic simulations of the nonreactive deformation mechanisms of RDX, $C_3H_6N_6O_6$, the nitramine molecule shown in Figure 1.1a used in its crystalline α-polymorph (Figure 1.1b) as a high explosive (HE). The

molecules in crystalline αRDX form a corrugated layered structure shown by the black lines in Figure 1.1c. This layered structure is common in molecular crystals where layers are produced from strong in-plane bonding between molecules and are held together by weaker interlayer attraction (3) (4) (5). The weakly bonded layers, indicated by the black lines in Figure 1.1c, easily slip under shear loading or cleave in tension (4). Cleavage and slip are both observed modes of deformation in indentation testing of αRDX. These deformation processes produce physically observable features that are used to deduce the slip and cleavage planes of αRDX (6) (7).
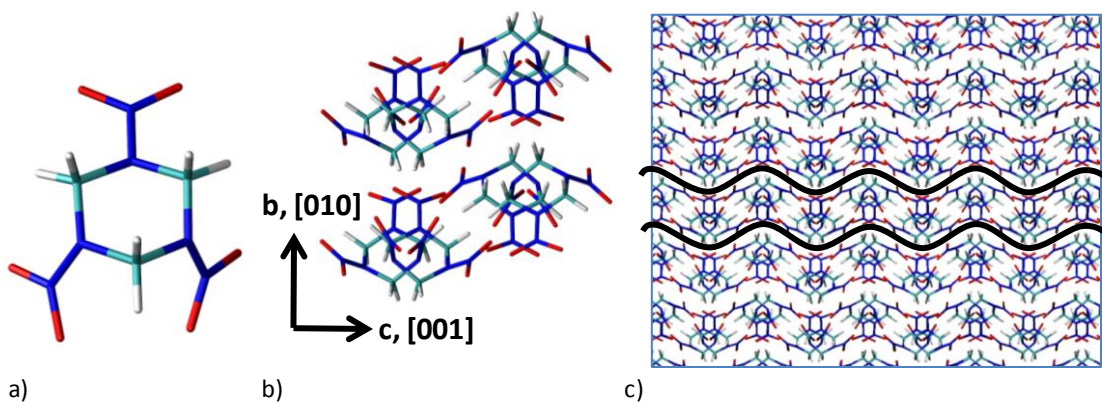
Figure 1.1: (a) Single RDX molecule, (b) αRDX unit cell projected onto the (100) plane and (c) αRDX supercell with (010) slip or cleavage plane shown by the black line between corrugated layers of RDX molecules.

Activation of slip systems is generally the preferred deformation mechanism in molecular crystals because the long range order of the crystal and its associated properties are maintained. The availability of several slip systems allows the molecular crystal to accommodate a general state of strain without fracturing. Slip, as opposed to cleavage or the formation of an amorphous phase, increases the tabletability of pharmaceutical molecular crystals (4) (8). Crystal engineering methods such as

cocrystallization have been developed to exploit this mechanism by increasing the amount of slip in pharmaceutical crystals such as caffeine and paracetamol (8) (9).

In energetic crystals such as αRDX (10) and PETN (11), initiation mechanisms are believed to be sensitive to shock loads that lead to shear deformations that cannot be easily accommodated by slip. A possible mechanism is blockage of certain slip systems by the large molecules on slip planes causing plane-on-plane slip motion to be hindered by steric interactions (11). The steric hindrance initiation model, in particular, presumes that when a large shear stress is directed along a sterically hindered plane, the crystal is unable to accommodate the strain through slip and therefore results in severe intramolecular deformations and bond rupture leading to initiation (11) (12). Other proposed initiation-related events involving slip mechanisms include blocked dislocation motion leading to the pile-up and avalanche of dislocations accompanying a localized increase in temperature (13). The induction time to decomposition in αRDX has also been correlated to the alignment of known slip planes to the direction of shock load (10).

Investigations through nanoindentation have indicated slip traces that suggest inelastic deformation mechanisms that are more complicated but build upon the ideas of dislocation motion on a single slip system (14). Thus, a more thorough understanding of slip systems and deformation mechanisms in molecular crystals is needed and molecular simulations may provide an enabling capability. To this end, molecular dynamics will be used to model these nonreactive mechanisms that lead to localized deformation features.

The atomic interactions of the RDX molecule are described by a flexible molecule potential energy function developed by Smith and Bharadwaj (15) that fits classical molecular potential forms involving bond stretching, angle bending, dihedral torsion, and

3

nonbonded electrostatic and van der Waals interactions to quantum level data. This "flexible" molecule potential allows the molecules to change conformation as the crystal lattice is deformed. The simulations will be used to determine parameters for mesoscale models of material deformation including thermoelasticity, dislocations dynamics and fracture mechanics. This work will extend several well developed methodologies for atomic crystals to the more complex structure of molecular crystals.

For instance, the current methodology for determining active planes in a molecular crystal that undergo slip or cleavage involves a ranking of crystallographic planes based on the attachment energy. The attachment energy technique does not provide a method of differentiating slip from cleavage planes or the slip direction. In this work, Rice's dislocation nucleation criterion (16) is used to determine if a plane of interest in the molecular crystal will deform by slip and the emission of a dislocation or by cleavage and the creation of free surfaces. Brittle versus ductile response of several BCC and FCC metallic crystals have been accurately determined through the application of Rice's model (16). The simulations and methodology in this work provides a useful extension of Rice's model as well as other available atomstic to continuum models to study the operable deformation mechanisms in molecular crystals.

1.1 Motivation and Challenges

The application of molecular crystals requires a thorough understanding of their mechanical properties and modes of deformation. Molecular crystals are not used as structural elements but the mechanical properties still play an important role in determining suitable manufacturing methods, packaging, storage and handling. The aim of this work is to provide a relationship between the molecular crystal structure and resulting mechanical properties. The structure of molecular crystals and their quasistatic thermodynamic properties can be determined experimentally. In simpler atomic crystals like copper it is possible to experimentally observe deformation through the emission of dislocations. Then using an atomistic model, the atomic level details of the experimentally observed dislocations are determined (1). In molecular crystals, these deformation processes cannot be directly observed experimentally but must be inferred from the resulting deformation features. These features can then be correlated with known modes of deformation in simpler materials. For this reason, atomistic models of molecular crystals have the potential to make a great impact on interpreting the experimentally observed features. However, there are several challenges in modeling molecular crystals and the direct application of simpler atomistic models is not directly applicable. In particular, the following challenges are summarized as:

(1) Some atomic crystals have an FCC structure with 4 atoms per unit cell. Molecular crystals are often in low symmetry space groups where each symmetry point contains an entire molecule with both orientation and conformational degrees of freedom. αRDX contains 8 molecules per unit cell and 168 atoms. This complicates any correlation that can be made between an FCC material like copper and a molecular crystal.

(2) The low symmetry unit cell's common to molecular crystals causes their structure to respond anisotropically to stress and temperature. There is also coupling between deformation of the lattice and the molecule conformation and orientation. The molecule conformation is able to store elastic energy and can influence the resulting phases and stacking fault structures.

(3) The actual mode of plastic deformation in molecular crystal is not well understood but is believed to be based on slip through dislocation motion. The actual dislocation may move as an extended defect as observed in complex metallic alloys containing 100's to 1000's of atoms per unit cell (15).

(4) Atomistic models of copper are developed from a large amount of quantum level modeling and experimental data. The complexity of molecular crystals makes this same level of parameterization of the atomistic potential impossible. The molecular potentials are developed to reproduce important features such as crystal structure, molecule conformation and mechanical properties over a limited range of thermodynamic states. Outside this range they become unreliable.

(5) The molecules making up molecular crystals often interact electrostatically through hydrogen bonding. This requires the molecular potential to include long range electrostatic interactions, which are solved in atomistic simulations using the Ewald sum. The Ewald sum requires the simulation cells to be 3D periodic limiting the geometries that can be modeled. The Ewald sum is also computationally expensive, taking up nearly 70% of computational time. This coupled with the large unit cell size of αRDX (168 atoms) greatly limits the size of the atomistic model and in turn the processes that can be simulated.

(6) The attachment energy is the most commonly used technique for determining slip or cleavage in a molecular crystal but is shown to be only 50% accurate (5). It also does not differentiate between slip or cleavage planes. It cannot determine the direction of slip or the energetic barriers to slip and their associated molecular features.

(7) Slip systems include a slip plane and slip direction and can be determined from the generalized stacking fault (GSF) procedure (16). The GSF procedure also elucidates the atomic interactions involved during slip. It can also be used to determine the dislocation core structure and existence of partial dislocations. However, the GSF procedure is only well suited to materials with smooth slip planes and atoms with only a few degrees of freedom. The slip planes in molecular crystals are rough due to the molecules on the slip plane. There are also multiple slip planes per crystallographic plane. The molecular potentials are also complex containing multiple degrees of freedom associated with the molecule's conformation and orientation.

The primary motivation of this work is to extend the techniques developed for studying atomic level deformation in metallic crystals to the more complex molecular crystals by addressing each of the above challenges. Of particular interest is the determination of the generalized stacking faults of molecular crystals. These provide a great amount of detail on the slip processes in metallic materials and will be shown to provide valuable insight into the experimentally observed deformation features of αRDX. This will provide important details for analyzing other molecular crystals and greatly extend our current knowledge of molecular crystal deformation.

1.2 Dissertation Objectives

The objective of this dissertation is to develop a procedure for studying deformation of molecular crystals using molecular dynamics. This work will be accomplished by performing the molecular dynamics simulations and analyzing and comparing the results with experimental data available in Literature. The above challenges address the complexities of applying atomistic modeling techniques that have been proven successful in atomic crystals like copper to molecular crystals. The specific objectives of this work can be summarized as:

(1) Evaluate the application of the Smith and Bharadwaj (17) (SB) flexible molecule potential energy function for the RDX crystal polymorphs by reproducing the experimental crystal structure of RDX in the low and high pressure α and γRDX phases. Also determine the thermal and elastic properties and compare them to experiment.

(2) Determine cleavage properties of αRDX and the free surface energy for experimental cleavage and slip planes.

(3) Develop a technique for determining the generalized stacking fault energy surfaces for αRDX cleavage and slip planes.

(4) Use Rice's (18) dislocation nucleation model with parameters from the molecular dynamics simulations to determine the interplay between cleavage fracture and dislocation emission to provide a physical understanding of the brittle nature of RDX and molecular crystals.

2. Literature Review

Energetic materials contain a metastable mixture of compounds in their gas, liquid or solid state that are triggered to decompose into a more stable material, releasing energy in the form of heat and expanding gases. An explosive is a type of energetic material that rapidly releases its energy through decomposition. A detonation occurs when the decomposition reaction moves through the material faster than the speed of sound in the unreacted material. A high explosive decomposes by detonation. Energetic materials can also decompose through deflagradation or rapid burning at a much slower rate. Low explosives like black powder only decompose through deflagradation producing a subsonic pressure wave. High explosives are rated by the speed a detonation wave travels through the material. This determines the rate that energy is released. Several external factors affect detonation velocity such as confinement pressure, energetic particle size, and energetic material diameter. The detonation speed for RDX, a common military high explosive, is 8.6 km/s (19), compared to its acoustic velocity of 3.8 km/s.

The energetic material of interest to this work is the solid state crystal made of the nitramine molecule cyclotrimethylene trinitramine ($C_3H_6N_6O_6$), or RDX. The nonbonded dispersion and electrostatic forces between RDX molecules cause them to arrange into periodic crystal lattices. This energetic molecular crystal contains a high energy density due to the crystal structure giving it a high detonation velocity.

Explosives are classified according to their susceptibility to initiation. Easily triggered explosives are primary explosives and are used to trigger detonation in less sensitive secondary explosives that make up the main explosive fill in military munitions. Decomposition in secondary explosives is more difficult to initiate and they make up a

majority of the explosives stored at military sites. Most nitramines including RDX are secondary explosives. Plastic bonded explosives (PBX) are composed of energetic crystals encased in a polymeric binder material and make up the main fill in munitions. A bimodal distribution of energetic crystals allow the smaller crystals to fill in the space between the larger crystals. The binder material is chosen to provide the munitions with desirable detonation and storage properties. The sensitivity of the energetic material to accidental detonation is important to the use, handling and storage of munitions.

The process of converting mechanical energy into chemical decomposition in energetic crystals is not well understood but is essential to the design of insensitive munitions. Under operational conditions, a detonation in a secondary explosive is triggered by a strong shock wave produced by the primary explosive. This shock wave is of such energy that the detonation and explosion are accurately described by phenomenological continuum level descriptions of the shock wave. At much lower energies, insensitive munitions can be accidently triggered to decompose. Decomposition under these scenarios is less understood and difficult to reproduce experimentally. Low strain rate loads lead to localized features in the crystal that alter the sensitivity.

It is generally agreed upon that detonation or deflagration is the result of the culmination of localized decomposition regions on the order of micrometers called "hot spots". The cause of hot spots in a heterogeneous explosive fill of energetic material and binder is described by shock wave multiplication caused by variations in density, adiabatic heating of collapsing voids, and shock induced impinging jets of material caused by a shock wave's interactions with a void. Detonation under these conditions is

accurately modeled and predicted using hydrodynamic models of shock waves with phenomenological thermodynamic equations of state fit to large amounts of experimental data.

Under low shock pressures and frictional loads that occur during accidental mishandling, the loading rates are much smaller and individual hot spots develop. Full scale decomposition of the material only occurs if the density of hot spots is great enough for them to culminate into large scale features where full scale decomposition can occur. Under these conditions, a microstructural understanding of the energetic material is required to understand the cause of individual "hot spots" and how they culminate. Individual crystals of energetic material like RDX range in diameter from 10-500 μm. An accurate description of the hot spot formation process and the initial stages of decomposition must accurately account for the discrete microstructural features of the energetic crystal. These discrete features may aid in the initial stages of decomposition through the up-pumping mechanism proposed by Dlott and Fayer (20) where intermolecular vibration energy is transferred to the intramolecular bonds causing them to break.

The cause of these discrete deformation features in molecular energetic crystals could be due to their low symmetry structure, anisotropic material properties and the complex molecule shape. Deformation of these crystals leads to localized high energy deformation features. The localized inelastic deformation results as the material plastically deforms on slip planes and fractures from cleavage. Armstrong (13) theorized that the available energy from deformation could be sufficient to cause dislocations pile-ups caused by grain boundaries to avalanche, releasing enough stored energy to cause

localized adiabatic heating sufficient to trigger decomposition. Dick and Ritchie (11) account for hot spot formation through slip systems becoming sterically hindered from large nitramine molecules, which become excessively deformed. The highly deformed molecules may then be easily excited to high vibrational states breaking their bonds and triggering decomposition. Ramos et al. (14) propose that the low symmetry crystal cannot accommodate a general state of strain leading to low fracture strength.

2.1 RDX Experimental Properties

2.1.1 RDX Molecule Structure

RDX (hexahydro-1,3,5-trinitro-1,3,5 triazine or cyclotrimethylene trinitramine) is a common energetic used by the military as a high explosive because of its stability properties and high energy density. RDX, shown in Figure 2.1b is an organic molecule containing the nitroamino functional group, R_2N-NO_2 shown in Figure 2.1a. The nitroamino functional group is also found in HMX, another military secondary explosive, shown in Figure 2.1c. Functional groups are groups of atoms within a molecule that characterize a particular chemical reactivity of that molecule regardless of the overall molecule size. Having the same nitroamino functional group makes RDX and HMX behave in a similar manner to thermomechanical loads like heat, impact, friction and shock. Similar functional groups should also make potential energy functions describing their atomic interactions transferrable.
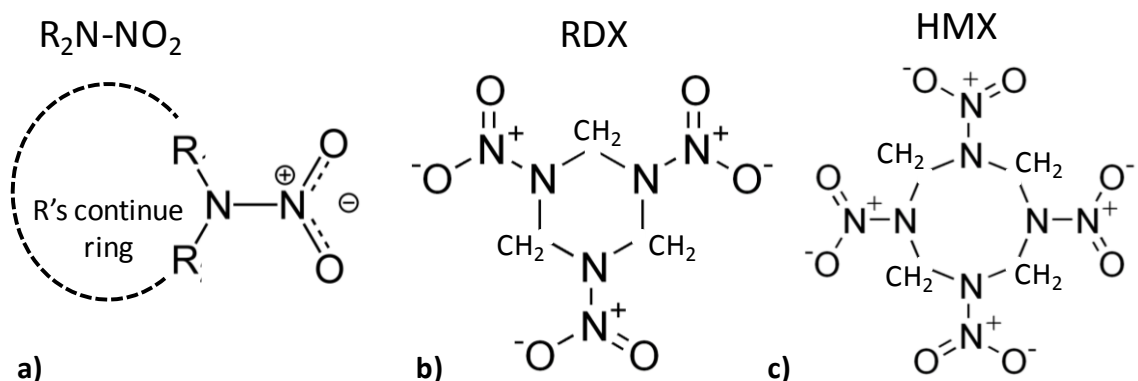
Figure 2.1: a) Nitroamino functional group, $R_2N\text{-}NO_2$ where R's are continuations of the ring. b) RDX molecule containing three $R_2N\text{-}NO_2$ groups where each $R=CH_2$ and c) HMX molecule containing four $R_2N\text{-}NO_2$ groups with $R=CH_2$.

The RDX molecule and atomic numbering is shown in Figure 2.2(a). The conformation of RDX in its crystal form are described by the wag angle, δ, of the N-N bonds with respect to the plane of the C-N-C atoms they are bonded to, shown in Figure 2.2b. In Figure 2.2b, the wag angles of the ambient condition αRDX crystal's molecule are oriented Axial, Axial, Equatorial (*AAE*) with respect to their C-N-C plane. The amine ring of C-N atoms can also take on different conformations and in the αRDX crystal structure takes on a "chair conformation". At higher temperatures, the ring structure can also take on "ship" and "twist" conformations.

RDX contains an oxidizing and a fuel component within a single molecule. The final products of RDX decomposition are HCN, N_2O, H_2CO, H_2O, NO_2, NO, CO_2, and CO. Unimolecular decomposition of RDX is likely to occur through three decomposition pathways (21): (1) Concerted symmetric triple fission of the ring forming three CH_2NNO_2 fragments (22). (2) Cleavage of the NN bond forming an NO_2 group and ring structure, which goes through further decompositions. (3) Successive HONO elimination to form 3HONO fragments and a 1,3,5-triazine (TAZ) molecule which go through

secondary decompositions into the final products. Pathway (1) was determined to be the

main reaction pathway based on mass fragments from laser photolysis of RDX (22).

Pathway (2) is believed to occur because the NN bond attaching the nitro groups to the

ring are the weakest bond in the RDX molecule. NO_2 bond rupture was observed

experimentally (22) but was considered minor compared to pathway (1). Pathway (3)

was determined through quantum level simulations to have the lowest energy barrier to

reaction (21). The final combustion products of RDX and the heat of explosion are

$$C_3H_6N_6O_6 \rightarrow 3CO + 3H_2O + 3N_2 + 5042kJ/kg$$
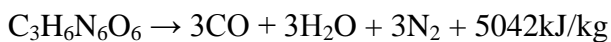
where the heat of explosion is given by the difference of the heats of formation of the

RDX molecule and the reaction products (23).
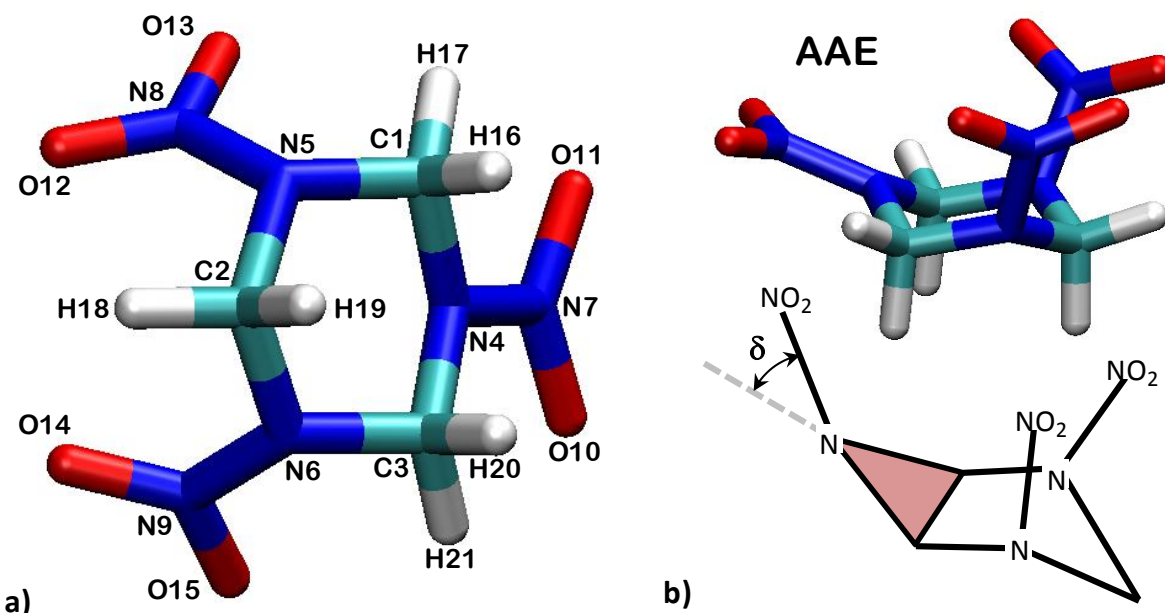
Figure 2.2: a) RDX molecule and atom numbering. b) RDX conformations for αRDX (*AAE*) with schematic defining wag angle, δ.

2.1.2 RDX Crystal Structures

At room temperature and pressure, intermolecular dispersion and electrostatic forces between RDX molecules cause them to pack together into a repeating crystal lattice. The dispersion forces are isotropic as all atoms are mutually attracted to one another and create a close packed crystal structure. On the other hand, electrostatic interactions are both attractive and repulsive. The external atoms on the RDX molecule are the oxygen atoms of the nitro groups and the hydrogen atoms connected to the ring. These two atom types produce strong hydrogen bonds between neighboring molecules. Hydrogen bonding is common in molecular crystals. Strong in-plane hydrogen bonds produce strongly bonded layers of molecules that are only weakly bonded to adjacent layers through dispersion interactions (4). The strength of the in-plane bonds is used to predict slip and cleavage planes (24) (5).

The nonbonded interactions in RDX cause it to be found in two polymorphic forms at ambient conditions, the stable αRDX phase given by Choi and Prince (25) and the unstable βRDX phase given by Millar et al. (26). Choi and Prince used x-ray diffraction to determine the crystal structure of αRDX. They found it to contain eight molecules and belong to the orthorhombic Pbca space group with lattice constants $(a,b,c)=(13.182,11.574, 10.709)$ Å.

The Pbca space group symmetry operators and the resulting αRDX unit cell are shown in Figure 2.3a. The repeating asymmetric unit is a single *AAE* RDX molecule shown in Figure 2.2b. The asymmetric unit is repeated at each symmetry equivalent point and rotated or inverted according the symmetry operators or the Pbca space group, represented by the symbols in Figure 2.3a. The blue molecules in Figure 2.3 maintain the

AAE conformation in the high pressure γRDX structure. The red molecules change conformation to *AAI* in the γRDX structure.

α: P=0.0 GPa

a)

b)

γ: P=5.2GPa

c)

d)
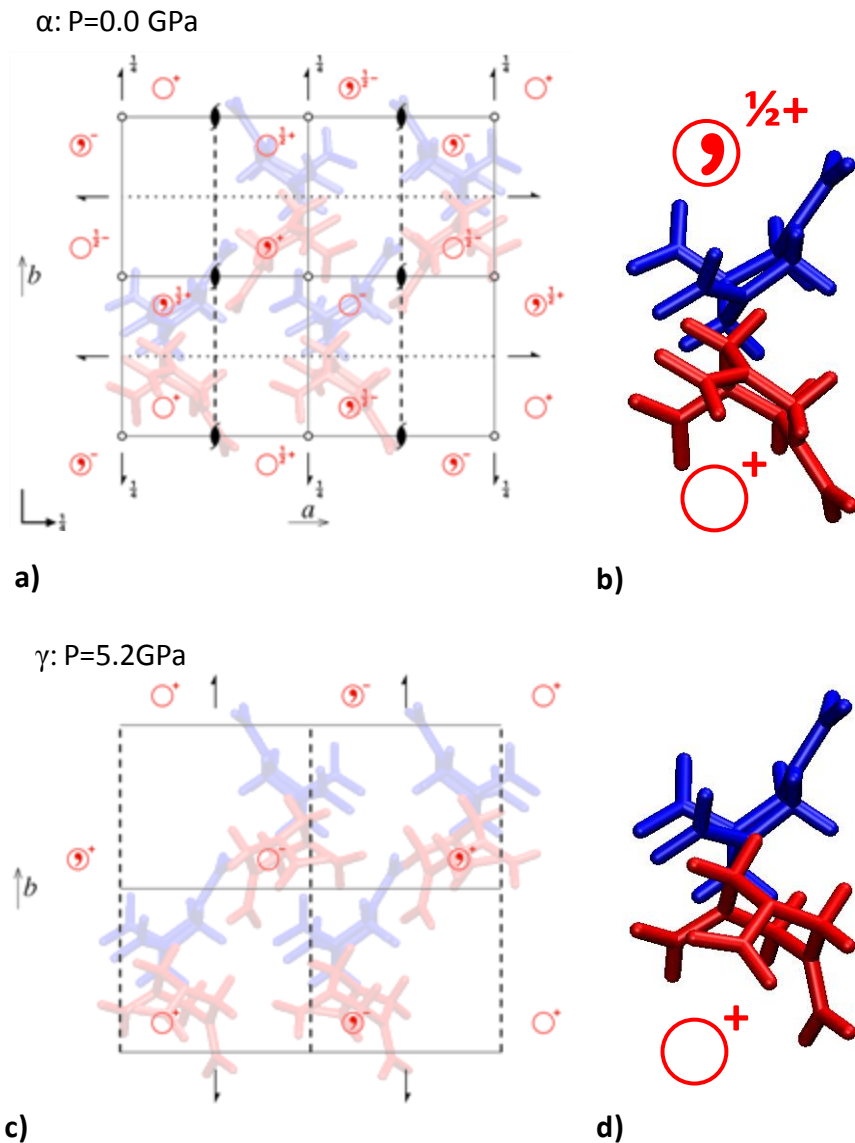
Figure 2.3: (a) Experimental αRDX unit cell (25) at *P*=0GPa, *T*=300K overlaid on the Pbca space group diagram[6]. (b) Two αRDX asymmetric units (single molecule) in the *AAE* conformation. (c) Experimental γRDX unit cell (27) at *P*=5.2GPa, *T*=293K overlaid on the Pb2$_l$a space group diagram (28). (d) γRDX asymmetric unit (2 molecules) in the *AAE* (blue) and *AAI* (red) conformations.

At high pressures, αRDX goes through a second order phase transition from α to γRDX. Davidson et al. (27) determined the structure of the high pressure γRDX phase using neutron powder diffraction. They determined the phase transition to occur at P=3.9GPa. They reported the atomic coordinates for γRDX from single crystal X-ray diffraction data under hydrostatic pressure at P=5.2GPa, shown in Figure 2.3c. They indexed the x-ray reflections to the orthorhombic Pca2$_1$ space group. In this work we use the Pb2$_l$a space group, which switches the b- and c- lattice vectors given by Davidson et al. (28) to coincide with those used by Choi and Prince for αRDX. The γRDX lattice vectors are (a,b,c)=(12.5650, 10.9297, 9.4769)Å implying eight molecules in the unit cell and two independent molecules in the asymmetric unit shown in Figure 2.3d. The type 1 red molecule shown in Figure 2.3d has N-N bond wag angles oriented in the *AAI* positions where *I* is an intermediate orientation between axial and equatorial. The type 2 blue molecule shown in Figure 2.3d is in the *AAE* conformation. The *AAI* molecules are also shown to change their orientation in the crystal by rotating about their amine ring.

A pressure and temperature phase diagram for RDX is given by Ciezak and Jenkins (29). They found a high temperature phase (T>400K) that was found not to be related to the unstable ambient βRDX phase (26). RDX also goes through a second high pressure phase transition from γ to εRDX at P=17.8GPa (30). The β and εRDX phases both belong to the Pca2$_1$ space group and contain molecules in the *AAA* conformation.

2.1.3 RDX Thermoelastic Properties

Elastic constants describing the stress-strain relationship for a single αRDX crystal were determined by Schwarz et al. (31) using ultrasound spectroscopy. The nine elastic coefficients for this orthotropic material were calculated from the mechanical

resonances of the crystal measured at ambient conditions using resonant ultrasound spectroscopy. The crystal was held by piezoelectric transducers where one transducer applied a constant amplitude signal of varying frequency to the crystal and the other transducer detected the resonant frequencies. A weighted error function that compared calculated frequencies from approximated elastic constants to actual measured frequencies was minimized to find the true elastic constants. Elastic constants for RDX given by Haussühl (32) using sound propagation velocities were used as initial guesses for the linear regression. Haycraft et al. (33) report elastic constants using Brillouin scatter of acoustic phonons. Differences between Haycraft's data and that given by Schwarz or Haussühl are believed to be a result of the low symmetry of αRDX and the differences in crystal quality and age. Elastic constants from these experiments are given in Table 3.1 along with the Voigt bulk modulus for uniform strain, B_v, given by $B_v = \frac{1}{9}\sum_{i,j} C_{ij}$ and the Voigt shear modulus for uniform strain, G_v, given by $G_v = \frac{1}{15}(C_{11} + C_{22} + C_{33}) - \frac{1}{15}(C_{12} + C_{13} + C_{23}) + \frac{1}{5}(C_{44} + C_{55} + C_{66})$.

Table 2.1: Experimental Elastic Constants

Elastic Constants (GPa)	Haycraft et al. (33)	Schwarz et al. (31)	Haussühl (32)
C_{11}	36.67	25.60	25.02
C_{22}	25.67	21.30	19.60
C_{33}	21.64	19.00	17.93
C_{12}	1.38	8.67	8.21
C_{13}	1.67	5.72	5.81
C_{23}	9.17	6.40	5.90
C_{44}	11.99	5.38	5.17
C_{55}	2.72	4.27	4.07
C_{66}	7.68	7.27	6.91
B_v	12.05	11.94	11.38
G_v	9.26	6.39	6.07

Isothermal compression experiments (34) (27) (35) provide lattice constants and volume as a function of pressure. Volume versus pressure data was used to determine the bulk modulus and its derivative. These experiments also provided lattice and volume measurements of the γRDX phase versus pressure and their discontinuity through the α to γRDX phase transition.

The coefficients of thermal expansion for αRDX describing the volumetric response to temperature were reported by Cady (36) using a differential transformer to measure the change in vertical height of the αRDX crystal over the temperature range -160<T<150 C° at atmospheric pressure. The coefficients of thermal expansion data as function of temperature is fit to a sixth degree polynomial for each lattice direction. The average linear coefficients of thermal expansion determined from Cady's CTE versus temperature plot for 0<T<50C° are (a,b,c) = (2.7, 8.7, 7.9)x10^{-5} K^{-1}. The linear coefficients of thermal expansion show linear temperature dependence over the temperature range 0<T<50 C°. The LASL explosive property data volume (19) provides a temperature dependent curve fit for the volumetric coefficient of thermal expansion, which computes to 19x10^{-5} K^{-1} for T=50C°.

2.1.4 RDX deformation features

Gallagher et al. (6) used a Knoop indenter on principal habit planes of αRDX to determine the active slip systems. The indentations on the crystal face were made at 5° intervals as the crystal was rotated. The orientation dependence of the Knoop indentation was used to determine the effective resolved shear stress on different assumed slip systems. Acid etching was also made on the indentation samples to determine the slip planes. They determined the slip planes to be (010), (021) and (02$\bar{1}$) and the slip systems

were believed to be (010)[001], (021)[100], and $(02\bar{1})$[100]. They determined the brittle nature of the material to be due to its anisotropic properties and limited high energy slip systems.

Ramos et al. (14) used nanoindentation with a conical tip and atomic force microscopy (AFM) operating in contact mode to characterize the post-indentation plasticity of αRDX prior to cracking. The small size and load control for nanoindentation made it possible for them to separate the brittle failure and plastic deformation mechanisms. The AFM images of the indentation were overlaid with projections of polar plots of the deformation zone axes of the known/suspected deformation mechanisms. They identify {021}(100), {011}(010) and (010)[100] slip systems and (010)[001] for cross-slip. The small loads allowed them to observe the plastic deformation on the slip systems prior to cracking and to identify possible cross slip mechanisms. They offer a mechanistic explanation to the low cracking threshold based on compatibility conditions where a general state of strain cannot be accommodated by the limited number of slip systems in the low symmetry αRDX crystal.

Hooks et al. (37) impacted the (111), (210), and (100) planes of oriented αRDX crystals to access 3, 2 and 0 slip systems, respectively. Impacts on (210) show distinct elastic and plastic waves, (111) impacts resulted in an overdriven elastic wave and (001) impacts resulted in stepped features that are thought to be the result of brittle fracture.

Cawkwell et al. (38) observed an abrupt change in the elastic-plastic response of shocked (111) αRDX crystals with increasing shock velocity. They used molecular dynamics simulations to show that the change in plastic response is a result of plastic hardening caused by homogenously nucleated dislocation loops. The dislocation loops contained the partial Burgers vector, 0.16[010], and were only stable under applied pressure. The simulations also showed the dislocation loops to contain a molecule conformation change that resulted in a structure similar to γRDX.

2.2 Models

This section will present theoretical and numerical models used to describe the observable features and experimental data for energetic materials. The continuum level models are phenomenological and use continuum theories of shock waves and reaction kinetics to extrapolate the known experimental results to a larger range of conditions. At smaller scales, the discrete nature of the material must be explicitly dealt with using mesoscale methods. At the scales of interest to this work, the discrete atomic structure of the material becomes important and is modeled using molecular dynamics where atomic interactions are dealt with explicitly and the atomic motion is assumed to obey Newton's equations of motion. These simulations are able to provide parameters to the continuum models and help develop theories.

2.2.1 Continuum models

Energetic materials are created to undergo rapid decomposition of their constituents to release energy. This usually occurs or results in extremely high pressures, temperatures, and strain rates. These conditions are best dealt with using hydrodynamic models to describe the continuum features of an energetic material because under these conditions the material behaves almost as a fluid. Hydrodynamic codes solve the continuum equations to conserve mass, momentum, and energy. An equation of state is required to couple the conservation equations. Equations of state models are normally phenomenological, meaning they model physical and chemical processes explicitly based on experimental data. The equation of state must accurately model the energetic material before, during, and after detonation to accurately predict the munitions effects.

Numerical implementation of these codes is often done using spatial and temporal finite difference methods. The availability of high performance computing has driven the resolution of these models to levels where the reaction processes and material heterogeneity must be modeled discretely. At these levels the microstructure becomes important and methods of coupling the discrete features of the microstructure to the overall continuum level events become important. Even at the microscale, these features occur over a range of scales. The localization features believed to be important to the initial stages of decomposition and hot spot formation occur at the molecular level. Chemistry occurring at the molecular level results from dissociation of the individual molecules. Localized features aiding in this initial stage of reaction are caused by crystal defects, which alter the energy barriers of individual molecules to react. Models from literature capable of describing the atomic interactions for energetic materials will be

given in the next sections and features from these models will provide new information for the continued development of more physically realistic equations of state for the continuum models.

2.2.2 Nonreactive Rigid RDX Molecule Models

The nonbonded interactions between RDX molecules causes it to exist in crystalline form over a wide range of conditions. Sorescu, Rice, and Thompson (39) developed a rigid molecule model where the each RDX molecule is treated as a single rigid body. In the Sorescu, Rice and Thompson (SRT) model, only nonbonded interactions between atoms calculated are used to parameterize electrostatic interactions and a Buckingham potential for van der Waals type interactions including exponential repulsion and r^{-6}. The intermolecular potential parameters are fit by minimizing a function of weighted molecular forces, torques and lattice energy for atoms arranged in the αRDX crystal structure. The partial charges for each molecule are fit to quantum mechanics calculations and are fixed during the minimization. Published Buckingham parameters for H…H and C…C are used with combination rules for repulsion/dispersion terms to further reduce the number of variables to minimize. The O...O and N…N parameters are then optimized to minimize the fit criterion using symmetry constrained molecular packing calculations.

These parameters were then used in rigid body molecular dynamics to test their ability to reproduce the crystal structure and obtain coefficients of thermal expansion. The lattice dimensions are reported to be within 4% of experimental values. Good agreement is found for fractional coordinates, which are used to compare the molecules' expected centers of mass from the Pbca symmetry operations to those found from

averaged atomic trajectories during the simulation. Euler angles are also in good agreement, meaning the molecules do not show substantial rotation when compared to the experimental configuration. Sewell and Bennett (40) used the SRT potential to find the temperature and pressure dependent elastic tensor. They conducted isothermal-isobaric simulations and used the strain fluctuation formula given by Parinello and Rahman (41) to solve for the elastic constants and bulk modulus that were in close agreement to experiment (31). Sorescu et al. (42) have also shown that the SRT parameters are transferable to other nitramines and molecules containing similar functional groups.

A different rigid molecule potential energy function was developed by Podeszwa, Rice and Szalewicz (43) from density functional theory (DFT) calculations of two interacting RDX molecules. These were done to better understand the RDX molecule interaction found in the condensed phase. The DFT method used here is also shown to be specially suited for accurately modeling materials that contain strong dispersive forces like molecular crystals. For the DFT calculations, the experimental form for the αRDX molecule is used with a slight variation made in atomic positions to obtain mirror symmetry in the molecule point group. The DFT data was used to find parameters for the Buckingham potential with damping terms for each interaction to deal with short range intermolecular interactions. The new potential was then used in rigid molecule molecular dynamics simulations to evaluate several probable crystal structures of RDX using the αRDX molecule conformation (44). The αRDX crystal structure is found to have the lowest energy and the potential predicts the lattice constants to within 0.5%. The

coefficients of thermal expansion and bulk modulus are comparable to the SRT model (39) and experimental data (25).

Molecular potentials have several tunable parameters that require fitting. It is a difficult task to determine the parameters that can be used from literature and those that need to be determined directly for the system of interest. The number of parameters fitted using rigid molecule models is one way of reducing the number of tunable parameters and if only intermolecular motions are of interest this approximation yields accurate results. Rigid molecule models are not appropriate when the molecule conformation is expected to change as is the case with melting and solid-solid phase transitions. The molecule conformation is also important in cases where a molecule is subjected to a crystal environment different to that from the perfect crystals such as those found at defects caused by free surfaces, dislocations, voids and grain boundaries. Other properties that depend on the high-frequency vibrations of the molecule are also not described. Simulations involving rigid molecules also provide very little computational savings over those that model bonds explicitly since nearly 70% of the computational time in atomistic simulations comes from the Ewald summation of the electrostatic potential. Simulations of rigid molecules also require special rigid body integrators that do not fit well into large scale parallelization schemes and are unavailable in some large scale molecular dynamics packages like DL-POLY 3.10 (45).

2.2.3 Smith and Bharadwaj Nonreactive Flexible RDX Molecule Model

Nitramine molecules are large floppy molecules, which has significant influence on the properties of the crystal. Properties that require knowledge of intramolecular flexibility include any process involving molecule conformational changes and high frequency vibrational modes. Phase transitions including the low to high pressure solid-solid phase transition of α to γRDX and first order transitions like melting require molecule conformational changes. Vibrational energy between molecules is also believed to be "up-pumped" into the intra-molecular vibrations leading to dissociation of the molecular bonds and hot-spot formation (20). Molecule conformations also change in the vicinity of crystal defects, stacking faults, and free surfaces; all of which are believed to be important in hot spot formation.

Smith et al. (46) used quantum mechanics calculations to parameterize nitramide and dimethylnitramine (DMNA) shown in Figure 2.4a and b to develop classical intramolecular bond potentials commonly used in molecular dynamics. Nitramide and DMNA are similar in structure to the nitroamino functional group shown in Figure 2.1a that makes up both HMX and RDX. Due to these similarities, a flexible potential developed for DMNA provides a building block to a flexible molecular potential for the more complex RDX and HMX molecules.

27
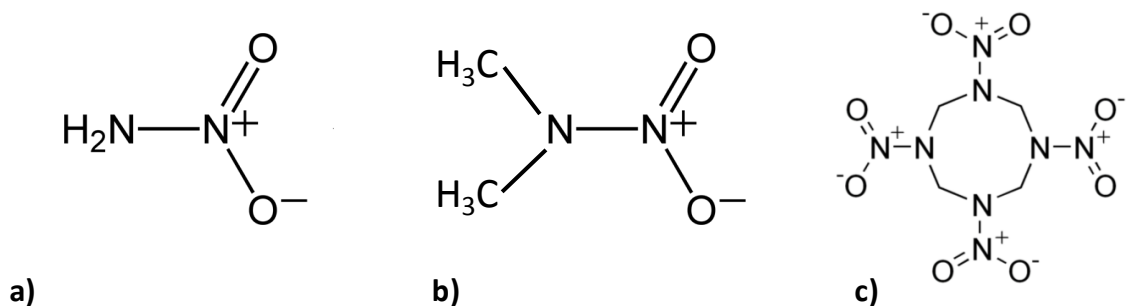
Figure 2.4: Chemical structure representation of (a) Nitramide (b) Dimethylnitramine (c) HMX.

The quantum mechanics data for DMNA was used to fit a bonded potential energy function containing harmonic bond forces, harmonic bending forces, cosine series torsion/dihedral forces, and out-of-plane bending forces of the O-N-O group with the N-N bond modeled as a harmonic improper dihedral. The improper dihedral relates the motion of the two nitrogen's by harmonic torsion about an axis between the two oxygen atoms and works to keep the N-N bond in-plane with the O-N-O group. The nonbonded van der Waals atomic interactions were modeled with an Buckingham exponential-6 repulsion/dispersion model with parameters given in other work (47). The partial charges for Coulombic interactions were found by fitting an electrostatic potential at a grid of point values from the quantum mechanics simulations. Simulations using the DMNA potential are shown to reproduce experimental gas phase peaks on the radial distribution function for atomic pairs and liquid phase vapor pressure, volume, and temperature properties. The liquid phase simulations required the partial charges to be increased by 25% to reproduce experimental results.

Smith and Bharadwaj (17) assumed all valence and dispersion/repulsion terms found for the much simpler DMNA molecule are directly transferable to the potential used for HMX. Additional valence parameters were then determined for HMX bonds

that do not occur in DMNA, namely the N-C-N bend and C-N-C-N dihedral angles of the ring. The potential includes nonbonded coulombic and dispersion/repulsion interactions between all atoms separated by three or more bonds, including those connected by 1-4 dihedrals. Partial charges for the HMX model were refit to reproduce a grid of quantum mechanics data points for HMX with the constraint that "like" atoms have equal charges. The Smith and Bharadwaj (SB) flexible molecule potential was used to find the experimentally unavailable thermal conductivity, shear viscosity and self-diffusion coefficients for the liquid HMX temperature domain $550 < T < 800$ K, which are all important material properties for large length and time scale constitutive models used in continuum hydrodynamic codes (48). The SB potential was then used to model crystalline HMX in the β-, α-, and δ-phases stable at ambient conditions and differ by molecular packing and molecule conformation (49). Bedrov et al. give the full potential, U, used for crystalline HMX as

$$U = \sum_{bonds} \frac{1}{2} K_{ij}^S (r_{ij} - r_{ij}^0)^2 + \sum_{angles} \frac{1}{2} K_{ijk}^B (\theta_{ijk} - \theta_{ijk}^0)^2$$

$$+ \sum_{proper\ dihedrals} \frac{1}{2} K_{ijkl}^T [1 - cos(n\varphi_{ijkl})]$$

$$\tag{2.1}$$

$$+ \sum_{improper\ dihedrals} \frac{1}{2} K_{ijkl}^D \varphi_{ijkl}^2$$

$$+ \sum_{i=1}^{N-1} \sum_{j>i}^{N} \left(+A_{ij} exp(-B_{ij} r_{ij}) - \frac{C_{ij}}{r_{ij}^6} + k_e \frac{q_i q_j}{r_{ij}} \right)$$

with parameters listed below in Table 2.2. This form of the SB potential and the parameter set from Table 2.2 are used to model crystalline RDX in this work and the input files that implement this potential in DLPOLY (50) and LAMMPS (51) are given in

Appendices A and B, respectively. Bedrov et al. (49) accurately predicted lattice constants within 4% and coefficients of thermal expansion within 11% for three polymorphs of HMX (α, β, δ), and lattice angles for the non-orthogonal β and δHMX phases were also accurately determined. Sewell et al. (52) then used the SB potential to find the full elastic tensors at atmospheric pressure and isothermal bulk modulus for the three ambient HMX phases. The bulk modulus was found to be within 11% of experimental acoustic measurements and the volumetric terms of the elastic tensor were within ~20% (31). Jaramillo et al. (53) use the SB potential to determine molecular level deformation features of the HMX crystal under shock loads and interplay between dislocations and amorphous shear bands as the shock strength is increased.

The transferring of the SB potential to RDX was first done by Zheng and Thompson (54) who used the bonded and dispersion/repulsion terms of the SB potential with atomic partial charges from the SRT rigid RDX potential (39) to simulate isothermal compression and melting of a perfect αRDX crystal. They accurately predict the ambient condition density to within 1% of the experimental result and the bulk modulus to within 2% of Olinger et al.'s (34) experimental isotherm data.

Cawkwell et al. (55) showed the SB potential without modification was able to reproduce αRDX elastic parameters, coefficients of thermal expansion, and lattice parameters. Unfortunately, they only published the lattice parameters given by the SB potential. The SB potential has been used to simulate the observed dependence of shock strength and orientation on the nonreactive dynamic processes involved in the elastic plastic response of αRDX (38) (56) (37). Based on their simulations, Ramos et al. (56) and Cawkwell et al. (38) proposed that partial dislocation loops homogenously nucleated

throughout the material as stacking faults cause an anomalous hardening, changing the elastic-plastic response as observed in (111) and (021)-oriented shock experiments. They also determined these stacking faults to be stabilized by stress applied normal to the (001) plane and nucleated by shear stress in the [010] direction (38). However, it was also noted that similar behavior may be observed if the stress was sufficient to induce the transition into the γ-polymorph. Owing to the higher experimentally-known transition pressure and the fairly isotropic dependence on shock orientation (57), the authors concluded this explanation was deemed unlikely (56).

Bedrov et al. (58) performed uniaxial constant stress Hugoniotstat simulations using the SB potential for [100] compression of αRDX that resulted in amorphous shear banding for pressures above 9 GPa. Similar calculations of [001] compression of αRDX produced the α to γRDX transition for pressures above 2.0 GPa (58). Furthermore, Bedrov et al. found differing behavior according to the crystal orientation. Whereas [100] compression yielded amorphization and sudden changes in volume following the initial compression, similar behavior did not occur for [001] compression. Clearly, determining the dependence of this solid-solid phase transition on compression, stress and shear of the material requires further exploration.

Table 2.2: Smith and Bharadwaj potential for HMX/RDX (49)

Bond stretches, $U = 0.5K_{ij}^S\left(r_{ij} - r_{ij}^0\right)^2$		
Bond	K_{ij}^S (kcal/mol/Å^2)	r_{ij}^0 (Å)
O-N	1990.1	1.23
N-N	991.7	1.36
N-C	672.1	1.44
C-H	641.6	1.09

Valence Bends, $U = 0.5K_{ijk}^B\left(\theta_{ijk} - \theta_{ijk}^0\right)^2$		
Angle	K_{ijk}^B (kcal/mol/rad^2)	θ_{ijk}^0 (rad)
O-N-O	125.0	2.1104
O-N-N	125.0	1.8754
N-N-C	130.0	1.6723
C-N-C	70.0	1.843
N-C-H	86.4	1.8676
H-C-H	77.0	1.8938
N-C-N	70.0	1.9289

Torsions, $U = 0.5K_{ijkl}^T\left[1 - \cos\left(n\phi_{ijkl}\right)\right]$		
Dihedral	K_{ijkl}^T (kcal/mol)	n
O-N-N-C	8.45	2
O-N-N-C	0.79	4
O-N-N-C	0.004	8
H-C-N-C	-0.16	3
C-N-C-N	3.30	1
C-N-C-N	-1.61	2
C-N-C-N	0.11	3

Out of plane bends $U = 0.5K_{ijk}^D\phi_{jikl}^2$	
Improper Dihedral	K_{ijk}^D (kcal/mol/rad^2)
C-N-C…*N	8.0
O-N-O…*N	89.3

Where …*N is the atom kept in-plane

van-der-Waals interactions, $U = A_{ij}\exp\left(-B_{ij}r_{ij}\right) - C_{ij}/r_{ij}^6$			
Atoms pair type	A_{ij} (kcal/mol)	B_{ij} (Å^{-1})	C_{ij} (kcal/mol Å^6)
C⋯C	14976.0	3.090	640.8
C⋯H	4320.0	3.415	138.2
C⋯N	30183.57	3.435	566.03
C⋯O	33702.4	3.576	505.6
H⋯H	2649.7	3.740	27.4
H⋯N	12695.88	3.760	116.96
H⋯O	14175.97	3.901	104.46
N⋯N	60833.9	3.780	500.0
N⋯O	67925.95	3.921	446.6
O⋯O	75844.8	4.063	398.9

Atomic partial charges	
Atom type	Q
C	-0.540000
N(amine)	0.056375
N(nitro)	0.860625
O	-0.458500
H	0.270000

2.2.4 Other Nonreactive Flexible RDX Molecule Models

Boyd, Gravelle and Politzer (59) developed a separate flexible molecule potential function for αRDX that reproduces the crystal lattice constants and the molecule conformations as well as the molecule vibrational modes. This potential is similar in form to the SB potential with bonded intramolecular interactions and nonbonded van der Waals and electrostatic interactions. Valence parameter for the harmonic angle bends were chosen to reproduce certain vibrational frequencies of the NO_2 and ring modes. This model was created with special attention paid to inter and intramolecular vibrational modes to study the up-pumping mechanism of hot-spot formation proposed by Dlott and Fayer (20). They are able to leave out the improper dihedral term controlling the wag angle of the N-N bond by including cross coupling terms treating intramolecular nonbonded interactions with an exponential-6 potential. The intermolecular potential uses a separate set of exponential-6 potential terms with an electrostatic potential that includes a cut-off function to increase computational efficiency. Simulations using this potential reproduce the lattice constants and coefficients of thermal expansion to the same order as the SRT rigid molecule potential and SB potential. This model was used by Boyd et al. (60) to perform detailed analyses of void formation energy and molecule conformation changes in the vicinity of small voids created by removing 2-30 molecules. The complexity of including separate intramolecular and intermolecular nonbonded interactions as well as a specialized electrostatic cut-off function makes this potential energy function difficult to apply in most molecular dynamics codes.

Attempts have also been made at modeling αRDX and other nitramines using other commonly available potential energy functions developed for other materials. Agrawal et al. (61) used the generalized AMBER potential to model intramolecular

interactions and the SRT potential was used for intermolecular nonbonded interactions. The generalized AMBER force field (62) is a widely used parameterized force field for organic systems. An additional term was included into the AMBER potential to model the out-of-plane bend of the N-N bond. The model accurately predicted the conformations of the ring structure but the wag angle was not accurately captured. This model was shown to predict the melting point within 5% and the density predicted was 10% lower than the experimental result.

Lu et al. (63) used the COMPASS (64) force field to model βHMX. The COMPASS potential contains a complex set of intramolecular potential energy functions to account for the normal bond, bend, torsion, and out-of-plane terms along with a set of cross coupling terms for each of these intramolecular motions. Valence parameters in COMPASS come from ab initio calculations and empirical data for molecules in isolation. The COMPASS potential predicts the lattice constants and bulk modulus to the same accuracy as the SB potential. The higher order polynomials used to model the intramolecular interactions also seem to aid in accurately predicting a high pressure phase transition at the experimentally reported pressure of 27 GPa.

Ye et al. (65) used published flexible potentials and refit them using the Generalized Utility Lattice Program (GULP) (66) for several nitramine crystals including RDX and HMX. They used published dispersion/repulsion parameters and forms with modification made to the O…H terms to reproduce crystal lattice properties. The experimental crystallographic molecule structure was used in quantum mechanics simulations to fit the partial charges. The intramolecular functions controlling the molecule conformation were then fit to the published functional forms using GULP and the published parameters as starting points for the fitting. The fit was based on matching lattice properties and minimizing potential energy and because this is a lattice dynamics

program, the fit is done at zero Kelvin. The potentials reproduce the crystal lattice of RDX and HMX to within 2% and the bulk modulus and elastic tensor are said to compare well with experimental data and the SB potential.

2.2.5 Reactive Force Field RDX Models

A reactive force field model used in molecular dynamics simulations called ReaxFF developed by Van Duin et al. (67) (68) uses bond order potentials to describe atomic interactions. Describing the atomic interactions using bond orders allows bonds to break and reform resulting in a model suitable to predicting chemical reactions. This is different than the SB potential, which requires explicitly defined atomic bonds and does not allow for chemistry to occur.

Strachan et al. (69) developed a set of ReaxFF parameters for RDX and modeled the initial stages of shock initiation and decomposition. They determined the lattice constants at room temperature to be $(a,b,c)=(13.7781, 12.0300, 10.9609)$Å and the bulk modulus to be 13.9 GPa, all in good agreement with experimental data and within the accuracy of other molecular dynamics methods. The accuracy of these values was recently increased by Liu et al (70) by modifying the ReaxFF potential to include r^{-6} London dispersion. They also accurately reproduce the α to γRDX phase transition. The transition pressure was only slightly overpredicted to occur at ~4.8GPa.

ReaxFF provides one of the best available methods for predicting the conversion of mechanical to chemical energy and the decomposition pathway for detonation. The force field is computationally expensive, on the order 1000 times that of the flexible SB potential. This work focuses on the mechanical processes that lead up to the initiation of chemistry and the computational speed and ease of using the SB potential is determined to be more practical.

3. Smith and Bharadwaj Atomistic Potential Validation

In this section, we study the basic equilibrium properties of and transitions to and from the α and γ polymorphs in crystalline RDX based on the SB potential (17). Atomic-level effects in pre-initiation processes are difficult to discern from measurement but they likely play significant roles in the mechanisms that lead to initiation. Thus, verified atomistic models may offer useful insights to complement experiments. To wit, while it has been shown that the γ-phase is observable using atomistic simulation approaches, to the best of our knowledge, the validation of the computed transition pressure in quasi-statically deformed crystals and properties of the stable γ-structure using the SB potential have not been reported. It would therefore be useful to determine the transition behavior in simple models of RDX (such as that described by the SB potential) and the circumstances that a transition occurs. To this end, we employ molecular dynamics (MD) with the SB potential to model the quasi-static response of the RDX crystal to isotropic and uniaxial compression. We also compute phase transitions under homogenous deformations at room temperature to study the steric mechanisms. In addition, we consider the roles of crystal anisotropy and load orientation on these steric effects through the transition point. Section 3.1 will present the simulations protocol and the equilibrated structures of the α and γRDX crystals. The effect of pressure, strain, and temperature on these structures will be presented in Section 3.2.

3.1 Equilibrated *α* and *γ*RDX Crystal Structure

The molecular dynamics package DL-Poly 2.19 (71) was used to test the application of the Smith-Bharadwaj Flexible Molecular potential (17) given in equation

(2.1) for the ambient crystalline phase of αRDX and high pressure γRDX phase. Simulations were done to check that the potential recreated the proper crystal structure of the two phases by comparing time averaged atomic position data from the simulations to experimental structural data given in Section 2.1.2. The unit cell was replicated to create a 2×3×3 crystal lattice in the (**a**, **b**, **c**) directions, respectively. The α and γRDX unit cells contain 8 molecules and the 2×3×3 RDX crystal contains 18 unit cells, 144 molecules, and 3024 atoms. Parallelepiped periodic boundary conditions are used in the simulations and allow for non-orthogonal lattice vectors of different lengths. Periodic boundary conditions are used to simulate an infinite crystal in all directions in order to get bulk thermodynamic properties free from the effects of surfaces.

The real space cut-off for the non-bonded van der Waals and electrostatic interactions was set to 10Å, which is large enough to allow for interactions between nearest neighbor molecules. The smallest simulation cell dimension must be at least twice as large as the 10Å real space cut off requiring a 2×3×3 unit cell. A long range tail correction to the potential energy is applied to the dispersion portion of the van der Waals interactions to account for the attractive forces between atoms at distances greater than the real space cut-off. The long ranged electrostatic interactions are calculated using the Ewald sum method, which splits the potential up into two parts: atoms separated by a distance less than the cut-off are treated using a direct Coulomb sum and atoms separated at distances larger than the cut-off are treated using a Fourier series sum in reciprocal space. In this work DL POLY (50) is used to automatically set the Ewald parameters by specifying the precision of the relative error in the convergence of the real space sum to

0.3e-6. DL POLY uses the relative error to automatically optimize the reciprocal space **k** vectors and the Ewald convergence parameter.

The simulations were run using the Verlet leapfrog time integrator (50). The highest vibrational frequency in the crystal is the C-H bond stretch with a period of approximately 12fs. In order to conserve the total system energy, approximately 10 integration steps should be taken per period limiting the maximum timestep to approximate 1.0fs.

An isothermal, iso-stress (*NST*) ensemble was used to control the temperature and full stress tensor of the simulation. The temperature is controlled with the Nose-Hoover thermostat. The Nose-Hoover thermostat functions by scaling the velocity using a scalar friction like term that is coupled to an outside heat bath. For these simulations the temperature is set to *T*=300K. The coupling time constant for the thermostat in these simulations is 1.0ps, which is related to the thermostat's "effective" mass.

The pressure of the simulation is controlled with a barostat that is coupled to the thermostat through a modification in the equations of motion. The barostat controls the size and shape of the simulation cell to maintain the prescribed pressure of *P*=0. If the simulation is thought of as occurring in a cylinder with a piston on top, the piston and its mass play a similar role to the barostat. The barostat is applied as a friction like term that scales the velocity and also scales the simulation cell size and shape. In an isobaric simulation, the pressure is controlled by only scaling the cell shape by a scalar friction term. The simulation in this study uses an iso-stress barostat requiring a second order tensor for the barostat friction term allowing the shape and size of the simulation cell to change independently. The iso-stress barostat with the parallelepiped periodic boundary conditions allows for the simulation to proceed under the least geometrically constrained

boundary conditions and to reach an equilibrated structure predicted by the molecular potential at the applied temperature and pressure. The barostat coupling time in these simulations is set to 1.0ps, which is related to the barostat's "effective" mass.

All simulations are started with an initial warm up period where the random velocities used to seed the simulation are scaled every 5 integration steps to maintain the correct temperature. The simulation cell is also scaled to the prescribed pressure. Total system energy is not conserved during this part of the simulation as shown by the initial scatter of the total system energy time histories in Figure 3.1(a) where each history is for a different integration step size. In Figure 3.1(a) the green line corresponds to an integration step of 0.1fs and the warm up period for this occurs over the initial 5ps of the simulation, after which point the temperature scaling is turned off. At this point the system is near its thermalized equilibrium. Data from the warm up period is not used to obtain average values of thermodynamic variables from the simulations. The warm up periods for 0.1, 0.5, 1.0, 2.0, 3.0fs timesteps was 5, 10, 20ps respectively. To save on computational time, smaller warm up periods were used for smaller timesteps.

3.1.1 Integration Timestep and Conserved Energy for αRDX

After the initial warm up, the prescribed temperature and volume scaling are turned off and the equilibration portion of the simulation proceeds by integrating the equations of motion modified by the *NST* ensemble to include the thermostat and barostat, allowing energy to flow between an external heat and pressure source in a thermodynamically consistent manner. The equilibration simulation conserves the total system energy and statistically relevant data is collected from this portion of the run. The conserved energy in an *NST* ensemble is the Gibbs free energy whose time history is plotted in Figure 3.1a for five different integration timesteps, 0.1, 0.5, 1.0, 2.0, and 3.0fs.

For timesteps larger than 3.0fs the energy fluctuations become too large and the integration fails to converge. Conservation of energy ensures that the time integrator is properly stepping the system forward in time according to the equations of motion. Smaller timesteps reduce the integration error but add time to the simulation so it is preferred to use large timesteps that keep the fluctuations in the conserved quantity small. Fluctuations in the total energy become apparent in Figure 3.1a for the larger timesteps of 2.0 and 3.0fs. A measure of these fluctuations is given by the average root mean square of total energy plotted as a function of integration step size in Figure 3.1b. Only the equilibration data is used to determine the averages. The fluctuations increase logarithmically with timestep size. Fluctuations in the Gibbs energy for an *NST* ensemble should be less than 1.0e-5 electron Volts per atom (eV/atom) limiting the integration timestep to less than 1.0fs for this simulation.
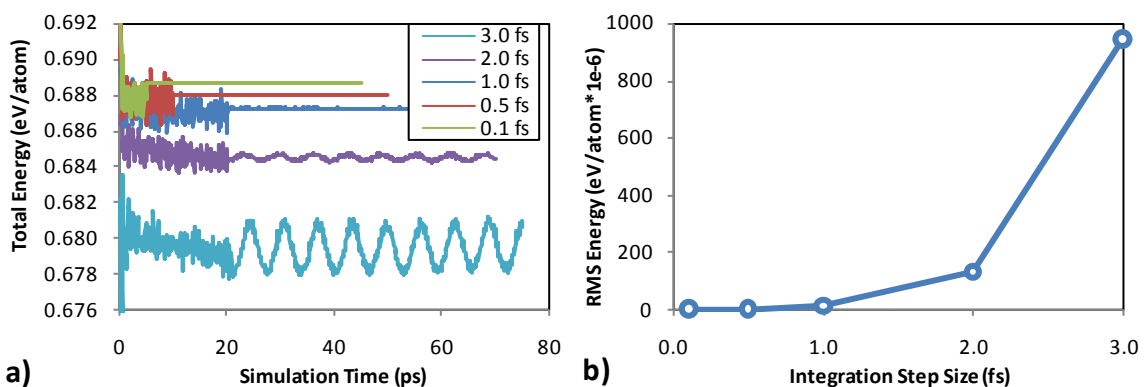
Figure 3.1: (a) Gibbs Energy time history for different integration timesteps. (b) Average total system RMS energy fluctuation per atom versus timestep size.

The total Gibbs energy consists of the kinetic and potential energy resulting from the molecular interactions, as well as some extensive energy components from the thermostat and barostat. Time histories of the kinetic and potential energy are shown in Figure 3.2a and b for different integration step sizes. Regardless of timestep size, the

kinetic energy fluctuates around the thermostat set point of approximately 300K or 0.03877 eV/atom in Figure 3.2b. The fluctuations in the potential energy time history in Figure 3.2a are not centered on an average value but instead have a common minimum value of 0.649 eV/atom. The oscillations observed in the kinetic and potential energies in Figure 3.2b and c are the result of the thermostat and barostat time constants which use the same value. The energy fluctuations in kinetic and potential energy are dependent on one another, the error caused by improperly integrating the atomic trajectory leads to abnormally high reaction forces causing large fluctuations in the velocity reflected by their mutually increasing RMS curves in Figure 3.2c. The lowest energy fluctuation in total energy from Figure 3.1b is for the smallest integration step, 0.1fs, but in Figure 3.2c the minimum in potential and kinetic energy occurs at 0.5 and 1.0fs timesteps. This is a result of the system conserving the Gibbs energy and not the kinetic and potential energy independently.
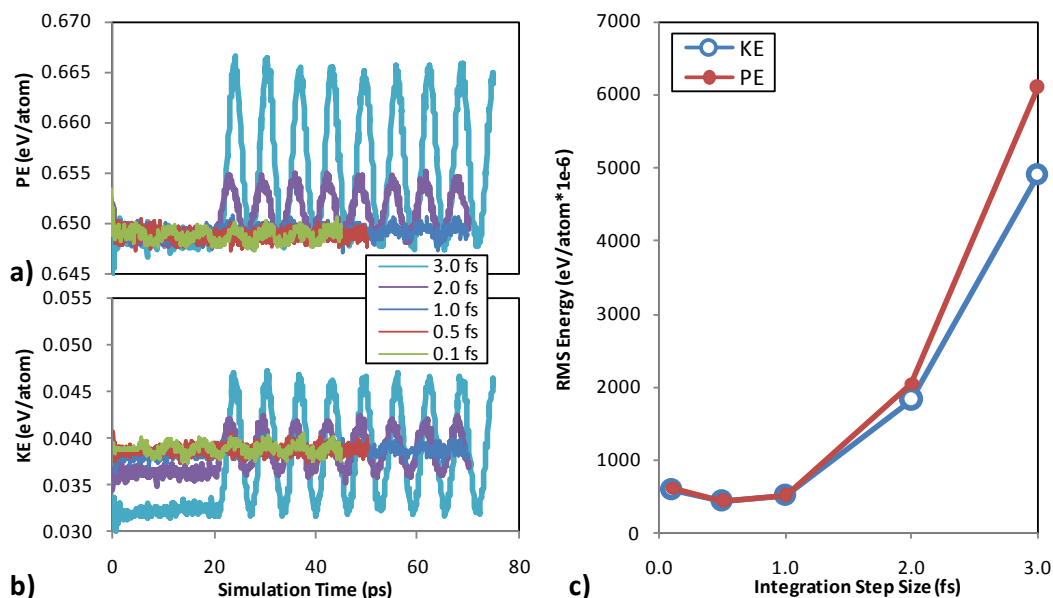
Figure 3.2: (a) Potential and (b) Kinetic energy time history for different integration timesteps drawn with the same x and y scales. (c) Average Kinetic and Potential RMS energy fluctuation per atom versus timestep size.

The SB potential given by equation (2.1) using the parameters in Table 2.2 contains terms parameterized to capture bond stretch, angle bend, proper and improper dihedral torsion, electrostatics, and nonbonded van der Waals interactions. Time histories of each of these terms for the 3.0fs timestep are shown in Figure 3.3. Small fluctuations are observed for the bonded and angle energy time histories in Figure 3.3a. The bond and angle have the stiffest potential parameters in Table 2.2 leading to higher vibrational frequencies needing smaller integration timesteps. Figure 3.3b shows the largest RMS fluctuations for the high frequency bonded and angle terms. Figure 3.3b also shows the change in energy fluctuations is small for the softer potentials such as those for dihedrals and nonbonded interactions. The SRT rigid molecule potential (39) does not include high frequency bonded interactions and larger timesteps can be used while maintaining acceptable energy fluctuations.
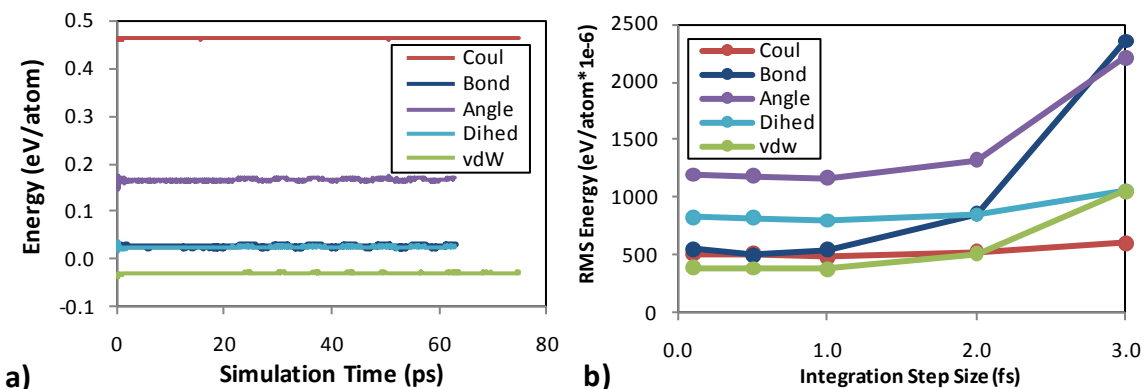
Figure 3.3: (a) Energy history of SB Potential functional terms for 3.0fs timestep. (b) RMS energy fluctuations of SB Potential functional terms as a function of timestep size.

3.1.2 Thermalized α and γRDX Lattice Constants

Figure 3.1 through Figure 3.3 show the effect of the integration step on the energy fluctuations and from these figures and knowledge about the bond frequencies it is determined that a 1.0fs integration timestep is valid for the system and boundary

conditions being simulated. Higher temperatures and pressures may require longer warm up period to reach the equilibrated structrue and shorter timesteps. These can be determined by reevaluating the time history and average RMS of the conserved energy. Figure 3.4 shows the time history of the (a) lattice vectors and (b) volume for an integration step of 1.0fs. The initial 20ps of the simulation is the warm-up period where the lattice constants are scaled to attain the proper pressure. After 20ps the equilibration portion of the simulation starts where lattice constants and particle velocities are controlled by the barostat and thermostat. Large fluctuations occur at the beginning of the equilibration run as the control of the particle velocity and lattice dimensions is handed over to the thermostat and barostat. This portion of the equilibration simulation will skew the averages and is not used.
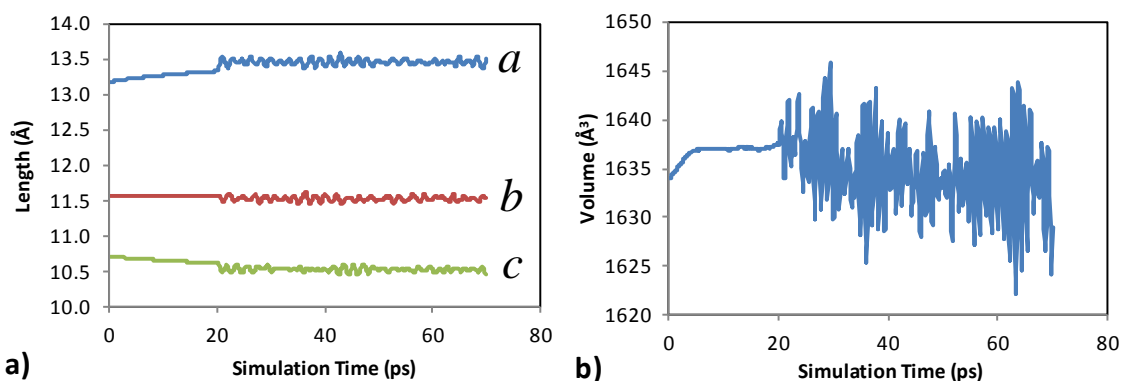
Figure 3.4: Time history of (a) (*a,b,c*) lattice constants and (b) volume for integration timestep of 1.0fs.

The lattice constants in Figure 3.4a flatten out during equilibration ($t > 20$ps) and the RMS fluctuations decrease to about 0.06Å. Averages are take from this portion of the equilibration simulation (*time* > 20ps) for the lattice constants and volume presented in Table 3.1. Experimental data by Choi and Prince (25) and simulations from Sorescu et al. (39) and Podeszwa et al. (44) using the rigid molecule potentials described in Section

2.2.2 are also shown. Percent difference between each potential and experimental data is shown in parentheses. The simulations from this work accurately predict the lattice constants within 2% error. The SAPT simulations were done at $T = 298K$ and they most closely matched the experimental lattice constants. Simulations in the current work most closely match the experimental volume.

Table 3.1: Average lattice constants (a,b,c) and volume for αRDX at P=0GPa and T=300K.

	a (Å)	b (Å)	c (Å)	V (Å^3)
Exptl[a]	13.182	11.574	10.709	1633.8
0.1fs	13.446 (2.00%)	11.531 (-0.37%)	10.534 (-1.63%)	1633.3 (-0.03%)
0.5fs	13.461 (2.12%)	11.531 (-0.37%)	10.533 (-1.64%)	1634.8 (0.06%)
1.0fs	13.463 (2.13%)	11.530 (-0.38%)	10.531 (-1.66%)	1634.7 (0.06%)
2.0fs	13.467 (2.16%)	11.530 (-0.38%)	10.531 (-1.66%)	1635.1 (0.08%)
3.0fs	13.468 (2.17%)	11.524 (-0.43%)	10.532 (-1.65%)	1634.5 (0.04%)
SAPT[b](298)	13.259 (0.58%)	11.634 (0.52%)	10.754 (0.42%)	1658.9 (1.54%)
SRT[c]	13.396 (1.62%)	11.798 (1.94%)	10.732 (0.21%)	1696.2 (3.82%)

[a]Choi, Prince Ref. (25) [c]Podesczwa, Rice, Szalewicz Ref. (44) [b]Sorescu, Rice, Thompson Ref. (39)

The simulation procedure applied to αRDX P=0GPa and T=300K is then applied to the high pressure γRDX phase described in Section 2.1.2. The γRDX simulations use the crystal structure given by Davidson et al. (27) and are simulated at the same temperature and pressure the experimental data was provided at, T=300K, P=5.2GPa. The simulation is thermalized for 75 ps and ensemble averages are collected from this period.

Davidson et al (27) give the γRDX in the Pca2$_1$ space group. In this work we present all material properties in the alternative axes setting Pb2$_1$a, which effectively switches the **b**- and **c**-lattice vectors given by Davidson et al. (27) to match those used by Choi and Prince (25). The γRDX crystal structure maintained an orthorhombic cell during thermalization and the lattice constants and volume are given in Table 3.2. The

lattice constants from these simulations are within 2% error of the experiment. All the

simulations for γRDX over predict the lattice constants leading to a 4% over prediction in

the volume.

Table 3.2: Average lattice constants and volume for γRDX.

	$\langle a \rangle$ (A)	$\langle b \rangle$ (A)	$\langle c \rangle$ (A)	$\langle V \rangle$ (A^3)
Exptl[a]	12.565	10.93	9.477	1301.5
SAPT[b](298)	12.70 (1.1%)	10.92 (0.1%)	9.50 (0.3%)	1317.7 (1.2%)
This Work	12.69 (1.0%)	11.06 (1.2%)	9.64 (1.8%)	1353.3 (4.0%)

[a]Davidson et al Ref. (27)   [b]Podesczwa, Rice, Szalewicz Ref. (44)

3.1.3 Thermalized α and γRDX Radial Distribution Function

It is also important to accurately predict the complex internal structure of the α

and γRDX unit cell. The internal structure includes the space group and its symmetry

operations leading to the position and orientation of molecules relative to one another.

The internal structure of the crystal undergoes changes during first and second order

phase transitions. The radial distribution function is useful in capturing structural

changes that occur during second order or solid-solid phase transitions. The radial

distribution function compares the molecules' relative position to one another and

provides information on the short range order.   The radial distribution function does not

provide information on the orientation or conformation of the molecules.

The position of molecules relative to one another provides information on their

packing. Figure 3.5a shows the total average number of molecule neighbors for an

average molecule in the αRDX crystal, meaning that the total nearest neighbors for every

molecule in the simulation are counted and then normalized by the number of molecules

in the simulation. Choi and Prince's (25) experimental data is represented by the blue

line and increases in steps because the experimental molecule position data is static. The

red line represents the equilibrated simulation data where the average is taken over several timesteps causing thermal vibrations about the molecule equilibrium position to be included in the average. The experimental and simulation results show similar trends. The green line is the number of molecules predicted from the αRDX bulk density, equal to 0.0049 molecules per $Å^3$. The simulation and experimental data converge to the bulk density for large distances.
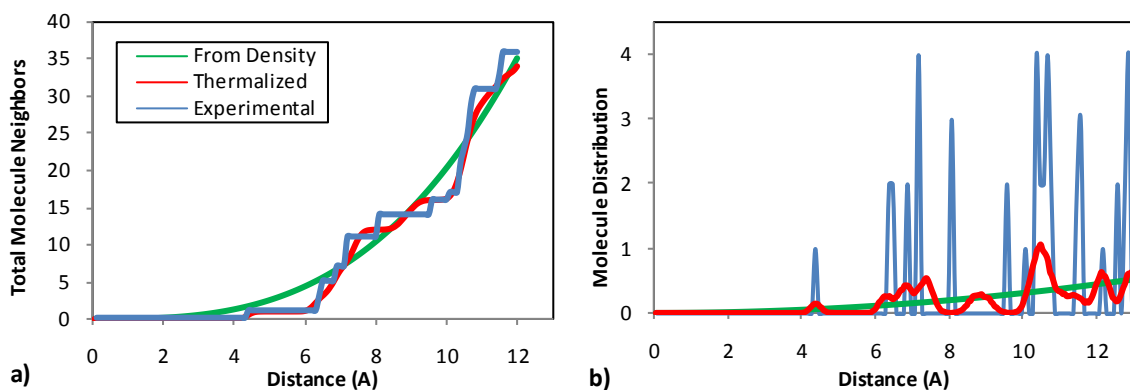
Figure 3.5: (a) Molecule neighbors versus distance and (b) Number of molecules at specified distances of αRDX (25).

Figure 3.5b shows the distribution of molecules about one another found by counting the number of molecules falling into discrete shells of thickness 0.05Å and increasing radius given by the x-axis. Again, these distributions are found for all molecules in the simulation and then normalized by the total number of molecules. The data given in Figure 3.5a is the integral of the data in Figure 3.5b. Plateau regions in Figure 3.5a are regions within the crystal not containing molecules, shown by shells containing zero neighbors in Figure 3.5b. The first set of nearest neighbor molecules are the 14 molecules located within 8Å of the molecule of interest (38). The distance to the nearest neighbor molecules was used to set the nonbonded dispersion/repulsion interaction cut-off to 10Å in the simulations where the non-bonded interactions outside

the cut-off are modeled by the tail correction. The tail correction assumes an isotropic uniform atomic density outside the cut-off. This is well suited to distances where the molecule distribution reaches the average density. Near 10Å the experimental (blue line) and simulation (red line) go to zero meaning this is a region not containing any molecules. The experimental data in Figure 3.5b is used to find the number of molecules at discrete distances, with the closest molecule neighbor located at 4.2Å. Another grouping of 10 molecules occurs between 6.4 to 7.2Å and a separate grouping of three more molecules occurs at 8Å. These 14 molecules located within 0 to 8Å and make up the group of first nearest neighbor molecules (38). In Figure 3.5b, the peaks in the simulation data (red line) are the equilibrium positions of the molecules and thermal oscillations cause them to vibrate about these positions, broadening the peak. The experimental and simulation data in Figure 3.5b show similar peaks or equilibrium positions for the group of 11 molecules at a radius of 7.2Å. The next five molecules with a separation of 7.2 to 10Å from one another begin to show differences in peak location but the total number of molecules are equal in Figure 3.5a at 10Å and this is also a location in Figure 3.5b where neither experiments nor simulations find molecules in the crystal. The green line in Figure 3.5b is the number of molecules per shell with thickness 0.05Å at the specified radius predicted by the bulk molecule density 0.0049 moleculesÅ^{-3}. The nearest neighbors predicted by the density increases at the same rate as the shell volume that is proportional to the distance squared.

The experimental (blue line) and simulation (red line) molecule distribution data for αRDX from Figure 3.5b are normalized by the bulk density (green line) to give the radial distribution function, RDF, shown in Figure 3.6a for αRDX. The radial

distribution function, RDF, is a pair correlation function that describes the time averaged

packing of particles in the system. The RDF in Figure 3.6 is normalized by the density so

that the simulated and experimental RDF converges to unity for large distances. The

largest error between the simulation and experimental RDF occurs between 8-10 Å where

the experimental data shows two distinct peaks and the simulation data shows only a

single peak. Overall, thermal vibrations cause the simulated distributions to become

smoothed out when compared to the experimental data. This combined with the errors

encountered when predicting the lattice constants presented Table 3.1 results in several

peaks experimentally observed peaks being smeared out into a single peak. The single

peak in the simulation data will be shown later to be a result of the simulation results over

predicting the **a**-lattice length.

The RDF for the high pressure γRDX phase is shown in Figure 3.6b at P=5.2GPa

and T=300K. The difference in the location of RDF peaks provides information on the

difference in molecular packing of the α and γRDX phases. The larger compression

isotropically shifts all of the RDF peaks in γRDX toward the origin and is not indicative

of the phase transition. It will be shown later through incremental pressure changes of

the α and γRDX crystal structures that the abrupt shift in the location of the first RDF

peak is caused by the phase transition. Overall, simulations of the γRDX crystal are more

accurate in the location of RDF peaks and lattice constants. However, this could be a

result of the higher pressure γRDX simulations locking the molecules into their initial

experimental structure where their thermal motion is more constrained.
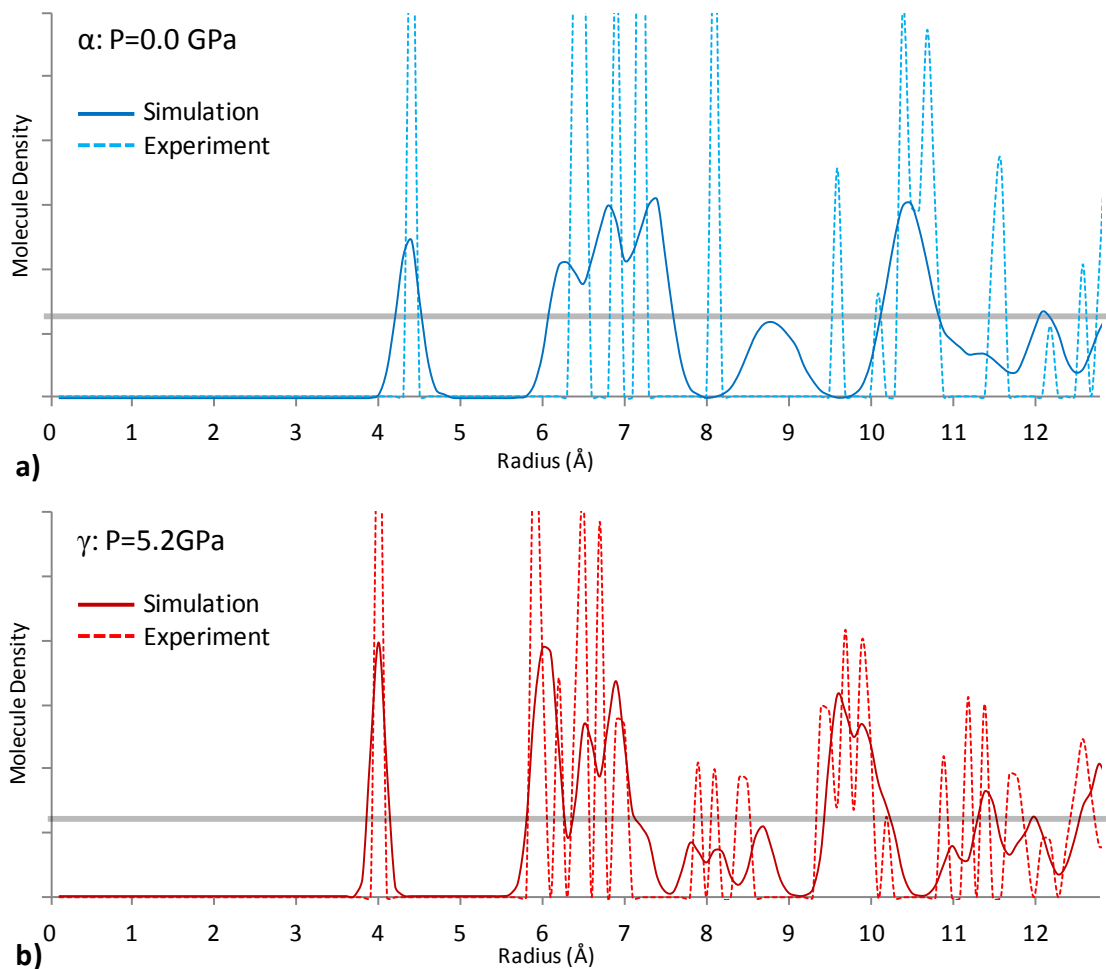
Figure 3.6: Normalized molecule center of mass radial distribution function for experiment (25) (27) (dashed lines) and simulation (solid lines) for (a) αRDX at *P*=0GPa, *T*=300K and (b) γRDX at *P*=5.2GPa, *T*=300K. Gray line is bulk molecular density.

3.1.4 Thermalized α and γRDX Conformation

The conformation of the RDX molecule is mainly controlled by the intramolecular bonds. For a nonreactive potential like the SB potential in equation (2.1), the intramolecular bonds connecting the atoms within a molecule do not change. The atom-atom bonds are harmonic and stiff when compared to the angle and dihedral potentials and do not significantly deviate from their equilibrium position. The angle bonds are also harmonic but have multiple equilibrium positions due to their 180°

49

rotational invariance. The dihedral bonds are made up of a cosine series and contain multiple equilibrium positions with relatively small energy barriers. The SB potential contains dihedral bonds controlling several important molecule conformations for nitramines including the wag angle, δ, of the nitro groups, shown in Figure 3.7a, and the conformations of the amine ring. The two RDX phases, α and γ, to be studied in this work contain noticeably different wag angles. It is common to characterize RDX based on the position of the nitro groups. Nitro groups in the plane of their respective C-N-C bonds are called Equatorial (*E*) and those at ~30° angle are called Axial (*A*). The molecules in the αRDX phase, shown in Figure 3.7b contain their three nitro groups in the Axial (N5-N8), Axial (N6-N9), Equatorial (N4-N7) or *AAE* positions, based on the wag angle, δ, from Figure 3.7b.
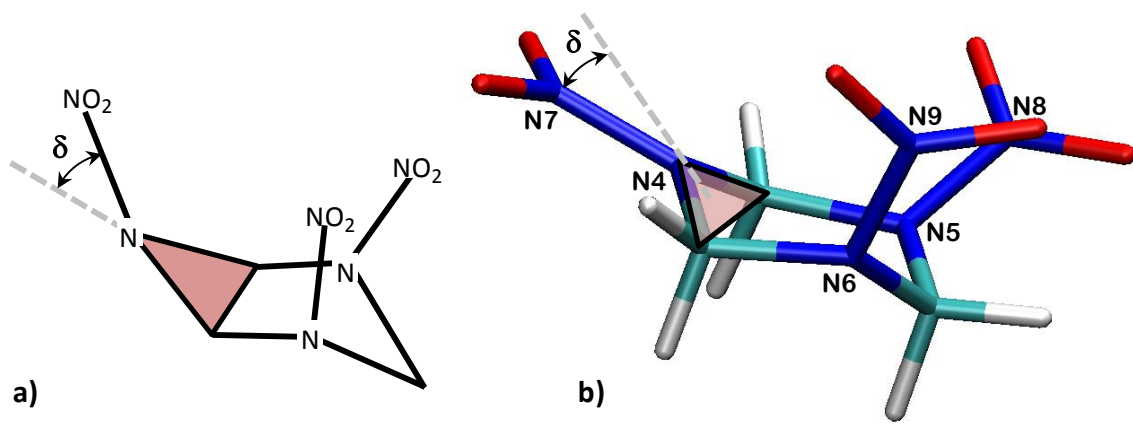
Figure 3.7: a) Wag angle, δ, used to describe nitro group orientation. b) N4-N7 wag angle shown on αRDX *AAE* right handed molecule.

In the SB potential given by equation (2.1), the wag angle is controlled by the N-N-C angle bond, the O-N-N-C dihedral bond and the C-N-C…*N improper dihedral bond. During thermalization, the wag angles will vibrate about their equilibrium position. After the system is equilibrated for 52.5ps, instantaneous atomic position data for the entire

2×3×3 system is recorded and used to compute the three instantaneous wag angles for each of the 144 molecules in the system. The wag angles are computed at 7.5ps intervals up to 75ps for a total of 30 trajectories. The three wag angles at each instant are accumulated separately for each of the eight molecules of the unit cell and then accumulated over all timesteps. This process provides an average of thermalized αRDX configurations used to find the wag angle probability distribution.

The wag angle data is plotted as a probability distribution in Figure 3.8 where the y-axis is the probability in arbitrary units. Each colored line in Figure 3.8a-c represents one of the eight unit cell molecules shown without their hydrogen or oxygen atoms in (d). The color and number for each molecule do not change from plot to plot and the colors and molecule numbering in Figure 3.8d corresponds to the legend in (a). The peak wag angle value is the equilibrium position and the variance is caused by the thermal vibration. The eight molecules show the same distribution for the three wag angles in Figure 3.8 and the SB potential is able to hold the molecules in the *AAE* conformation.
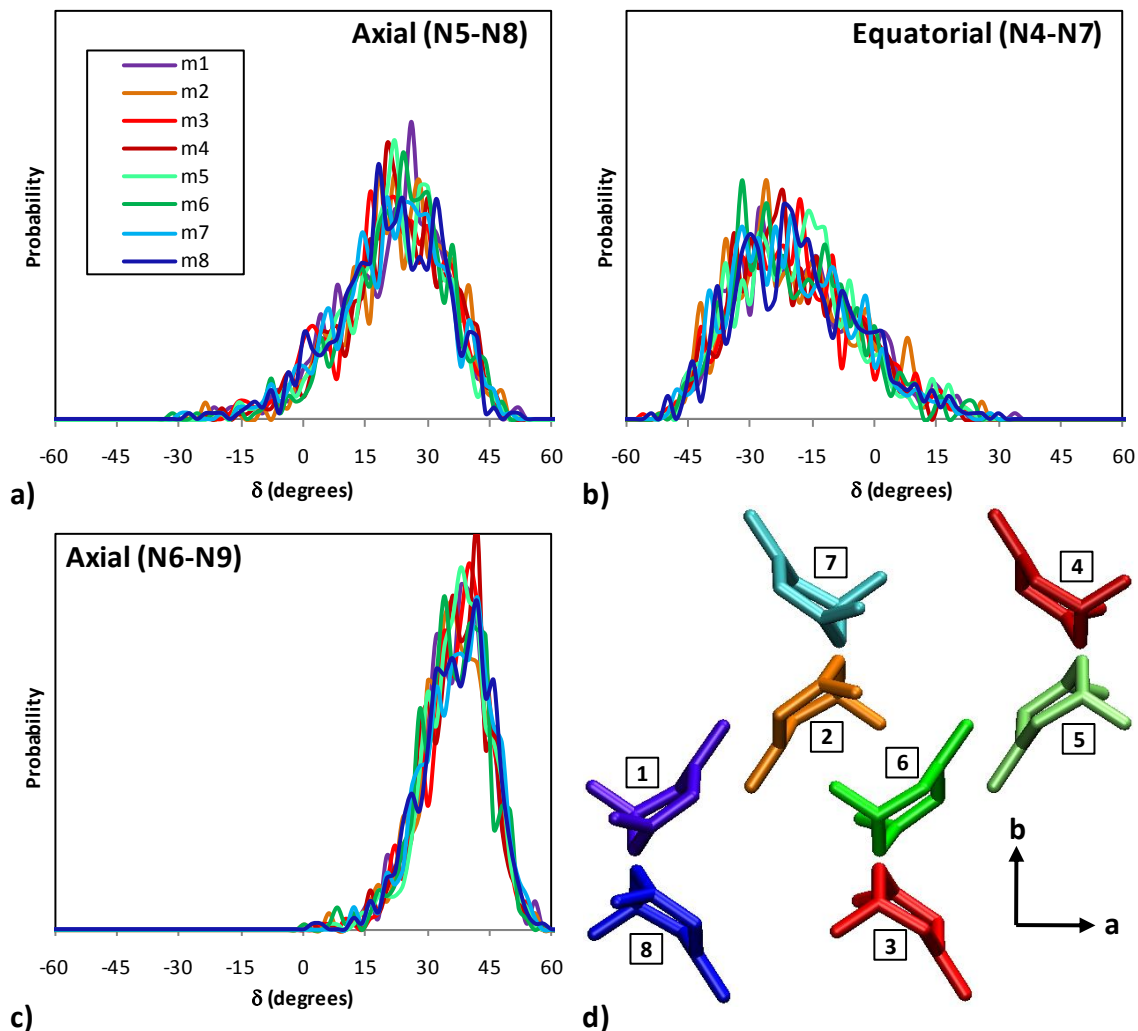
Figure 3.8: Thermalized αRDX wag angle probabilities (y-axis arbitrary units) for each molecule in the unit cell: (a) Axial N5-N8, (b) Equatorial N4-N7 and (c) Axial N6-N9. The molecule numbering legend in (a) applies to (b) and (c) as well. (d) αRDX unit cell with molecules numbered and colored according to legend in (a).

The wag angle distributions for each molecule in Figure 3.8 are accumulated into right (molecules 1 to 4) and left handed (molecules 5 to 8) distributions and plotted in Figure 3.9a for all three wag angles. Figure 3.9b shows molecule 2 (right handed – red amine ring) and molecule 6 (left handed – blue amine ring) from Figure 3.8d with the N-N bond colored to match the wag angle probability plot in Figure 3.9a. The right and left handed molecules have the same wag angle distributions. The peak values from the

simulation data shown in Figure 3.9a are given in Table 3.3 along with the experimental data from Choi and Prince (25). The black circle in the center is the inversion symbol from the Pbca symmetry operators shown in Figure 2.3. An inversion operation causes $(x,y,z) = (-x,-y,-z)$ resulting in the pink and green N-N bonds being equal and is verified by their probability distribution in the plot.

a)   b)
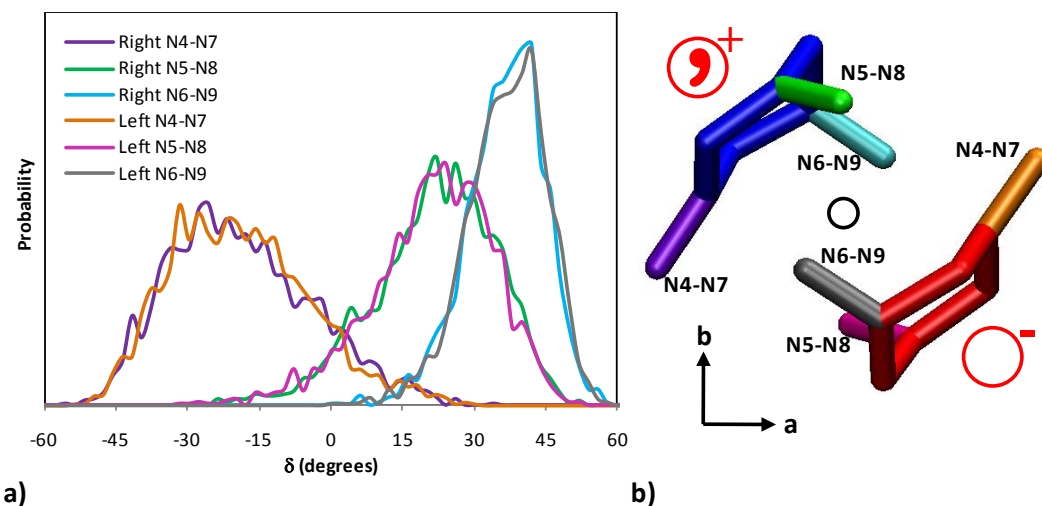
Figure 3.9: (a) Thermalized αRDX wag angle probabilities (y-axis arbitrary units) for right and left handed molecules. (b) Right handed molecule 2 (red) and left handed molecule 6 (blue) from unit cell showing Pbca inversion symmetry operators and colored N-N bonds corresponding to legend in (a).

Table 3.3: Locations of the peaks of the wag angle distributions from this work (shown in Figure 3.9 and Figure 3.11 and from the experimental structure for αRDX *AAE* molecule (25) and γRDX *AAE* and *AAI* molecules (27).

	This Work	Experimental
α-RDX: AAE		
N5-N8 (A)	38°	33°[,a]
N6-N9 (A)	25°	34°[,a]
N4-N7 (E)	-24°	-20°[,a]
γ-RDX: Type 1 AAI		
N5-N8 (A)	34°	35°[,b]
N6-N9 (A)	38°	36°[,b]
N4-N7 (I)	16°	10°[,b]
γ-RDX: Type 2 AAE		
N5-N8 (A)	40°	40°[,b]
N6-N9 (A)	22°	17°[,b]
N4-N7 (E)	-12°	-2°[,b]

[a]Choi and Prince Ref. (25), [b]Davidson et al. Ref. (27)

The RDF and wag angle distributions show the overall structure of αRDX obtained from experiment being maintained using the SB potential under ambient conditions. Other measures should also be accounted for to conduct a full structural analysis. For the molecular degrees of freedom, the torsional orientation of the O-N-O groups about the N-N bond and the conformation of the amine ring should be considered. The Euler angles of each molecule should also be used to determine the changes in their orientation. All of these measures could be combined into an order parameter (54). In this work, the dominant features that result at high pressures and in the vicinity of defects are characterized by the RDF and wag angle distributions.

The RDF's for γ and αRDX are similar because both crystals belong to an orthorhombic space group of similar dimensions containing eight molecules. As mentioned in Section 2.1.2 the main structural difference between the γ and αRDX phases is in the conformation of the molecules with the γRDX asymmetric unit containing two distinct molecule conformations and the αRDX asymmetric unit

containing a single molecule conformation. This conformation difference is highlighted by the wag angle distributions shown for each of the eight molecules in the γRDX unit cell in Figure 3.10a-c with the unit cell shown in (d). Two distinct wag angle distributions are evident in Figure 3.10b and c, with each distribution pertaining to one of the two molecule types in the asymmetric unit of the Pca2$_1$ space group. Type 1 molecules belong to what Davidson et al. (27) refer to as Axial, Axial, Intermediate (*AAI*) because the N4-N7 wag angle takes on a value between axial and equatorial. Type 2 molecules maintain a similar conformation to the *AAE* conformation of αRDX. Type 1 molecules include molecules 1 thru 4 from Figure 3.10d and are shown by red hued colors. Type 2 molecules include molecules 5 thru 8 from Figure 3.10d and are shown by blue and green hued colors.
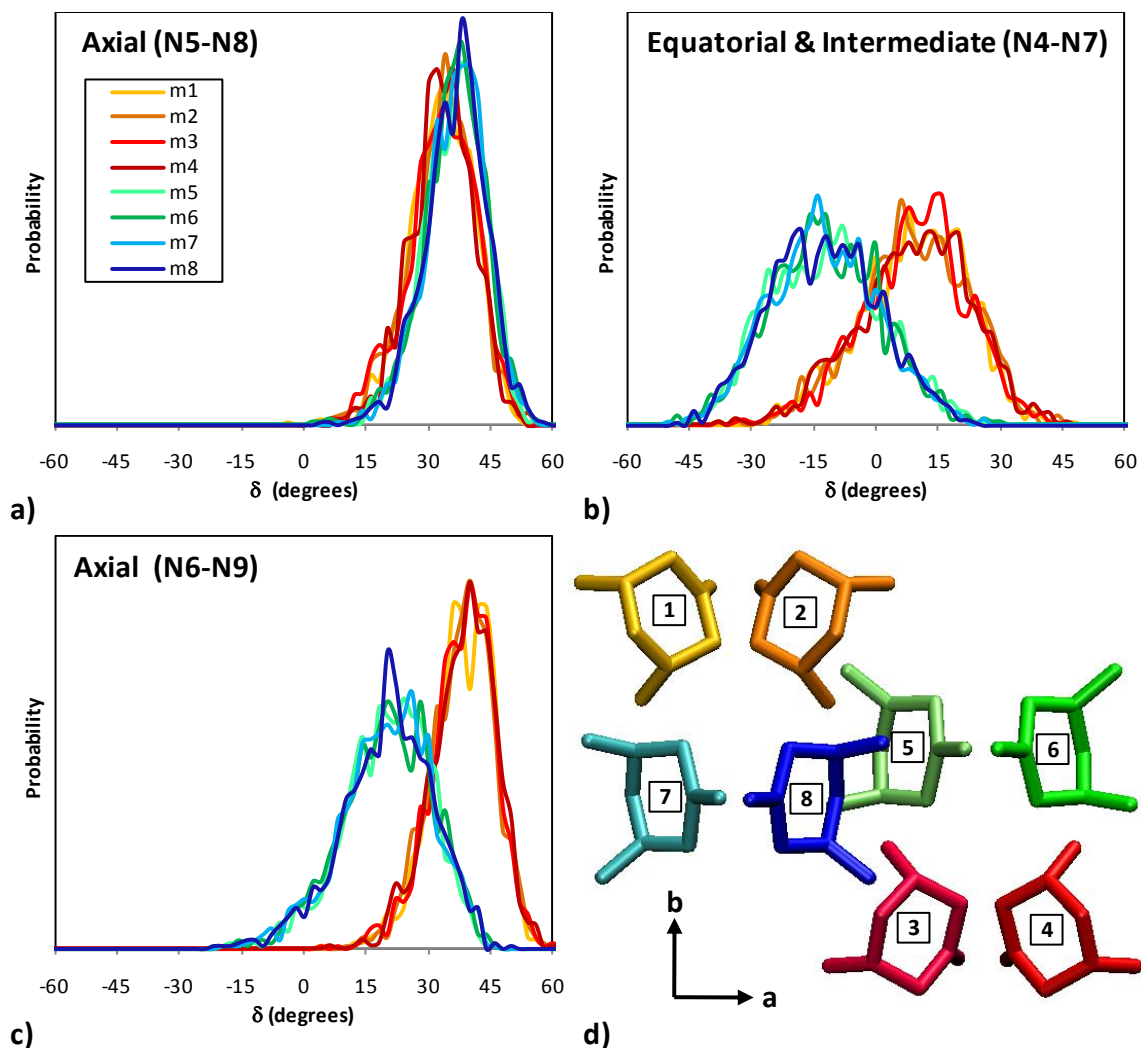
Figure 3.10: Thermalized γRDX wag angle probabilities (y-axis arbitrary units) for each molecule in the unit cell: (a) Axial N5-N8, (b) Equatorial N4-N7 and (c) Axial N6-N9. (d) γRDX unit cell with molecules numbered and colored according to legend in (a).

Each molecule type in Figure 3.10 is accumulated into a single distribution and shown in Figure 3.11a with pictures of the two molecule types shown in (b). The N-N bonds are colored according to the legend in the distribution plots and the amine ring is colored orange for *AAI* molecules and green for *AAE* molecules. The peak values from the distributions in Figure 3.11a for the *AAI* and *AAE* molecules are listed in Table 3.3 along with experimental data given by Davidson et al. [REF: Davidson]. The overall trends in wag angles between simulation and experimental results for the two molecule

conformations are consistent with *AAI* molecules containing two axial N-N groups at ~40° and a slightly positive N-N at ~10°. The *AAE* molecule was also accurately predicted with the largest difference being in the equatorial N4-N7 angle.
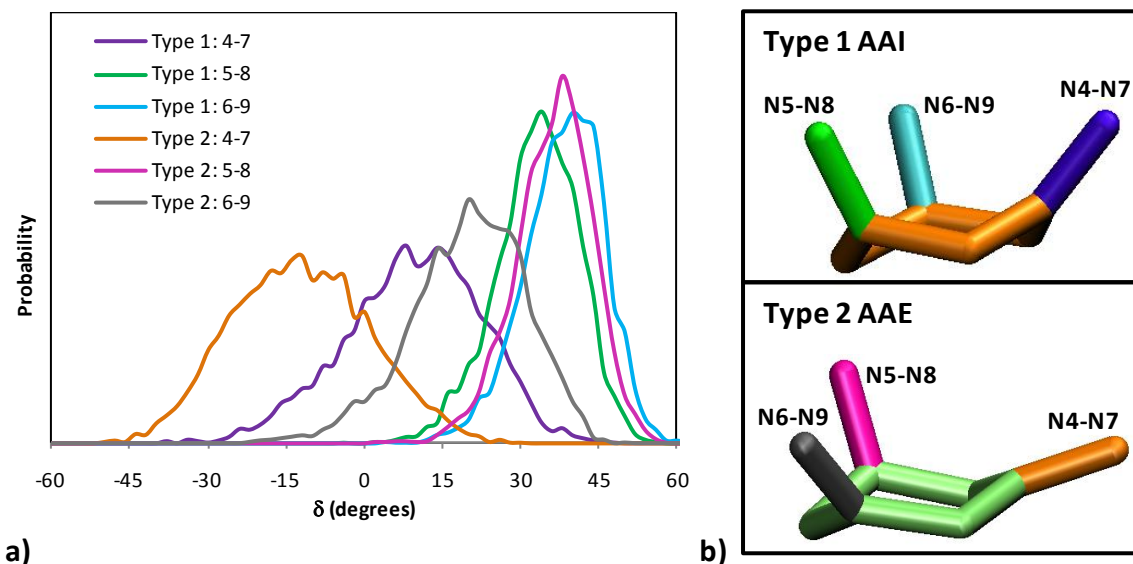
Figure 3.11: a) Thermalized γRDX wag angle probabilities (y-axis arbitrary units) for *AAI* and *AAE* molecules. b) *AAI* molecule and *AAE* molecule with bonds colored according to the distributions in (a).

The peaks on the wag angle distributions are low energy conformations and the wag angles oscillate about these configurations. As the wag angles deviate from the low energy configuration, they increase in energy. The change in energy as a function of the wag angle is determined for a single αRDX *AAE* molecule removed from the crystal, shown in Figure 3.12.

Each nitro group in the isolated RDX molecule is rotated by $\pm 60^{\circ}$ from $\delta=0^{\circ}$ as shown in the Figure 3.12a. The energy is evaluated at each of these new molecule conformations and plotted as a function of the wag angle in Figure 3.12b. The energy plot shown is for rotation of the axial nitro group N5-N8. The total energy from the SB potential in equation (2.1) shown by the solid black line is the sum of the bonded energy

components, U_{intra}, shown by the gray line and nonbonded components, U_{inter}, shown by the dashed line. The nonbonded component, U_{inter}, includes the VDW and electrostatic nonbonded interactions between atoms in the single molecule. The nonbonded energy is symmetric about its minimum value at $\delta=0°$. The wag angle is rotated in a way that does not change the bond distance and U_{intra} only includes angle, dihedral, and improper energy. The dihedral bond controlling the wag angle is a cosine series that reaches a local maximum at $\delta=0°$ and has two global minimums at $\delta\approx\pm45°$. The total energy being a composite of the two energy terms also reaches a local maximum at $\delta=0°$. The total energy also reaches two local minimum values at $\delta\approx\pm30°$ due to the local minima of U_{intra}. At large wag angles the total energy is dominated by U_{inter}.
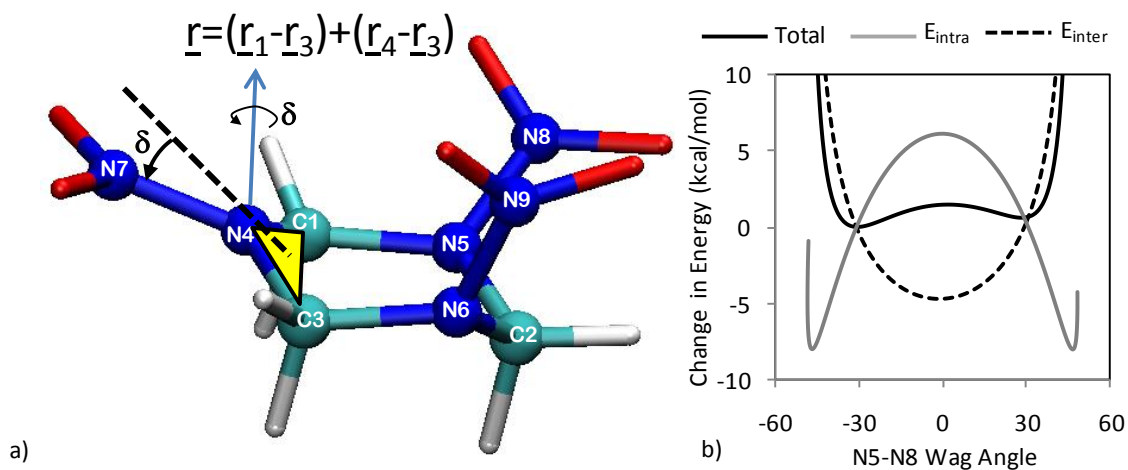
Figure 3.12: Definition of wag angles used to calculate wag angle energy. (b) Change in SB energy for a single molecule as function of the N5-N8 nitro wag angle.

The multiple minima and local maximum at $\delta=0°$ in the total energy profile in Figure 3.12 explains the appearance of the two main wag angles in the distributions, either axial or equatorial. All three of the αRDX nitro group energy profiles are shown by the gray lines in Figure 3.13. The two γRDX conformers are also shown in Figure

3.13 where the black line is *AAE* and the dashed line is *AAI*. The two axial αRDX nitro groups in gray, N5-N8 in (b) and N6-N9 in (c), are nearly identical with two local minima. The equatorial nitro group in Figure 3.13a for all three RDX conformations shows a single minimum near -30°. The γRDX N6-N9 profiles shown by the black and dashed lines also show a global minimum at -30°. This indicates the γRDX molecule conformation is stabilized by the nonbonded molecule-molecule interactions of the crystal. It is also evident that the *AAE* conformation of αRDX is one of several stable molecule conformations outside the crystal. Elastic band calculations by Mathew et al (72) show the energy of these different conformations to be very close. They also show the *AEE* conformation to be the lowest energy single molecule conformation closely followed by the *EEE*.
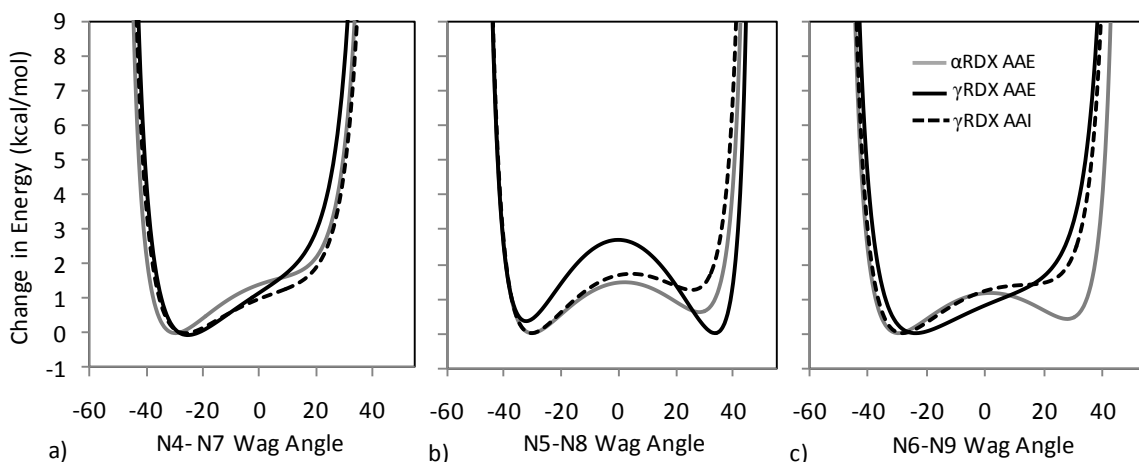
Figure 3.13: Wag angles for all single molecules in αRDX and *AAE* γRDX and *AAI* γRDX

In Figure 3.14, the same procedure was used to find the energy as a function of the wag angle for a single RDX molecule inside the αRDX crystal. In this case, each of the three wag angles of a single molecule were individually rotated inside the crystal and

the energy calculated. In all three sets of energy versus wag angle data, the total energy is almost identical to the nonbonded energy component of the energy. However, the bonded energy plays an important role in determining the overall conformation by controlling to which side of $\delta=0^{o}$ the minimum energy configuration takes. The axial conformation occurs for $\delta>0^{o}$ and equatorial for $\delta<0^{o}$. The nonbonded energy terms control the distribution of wag angles and their asymmetry.
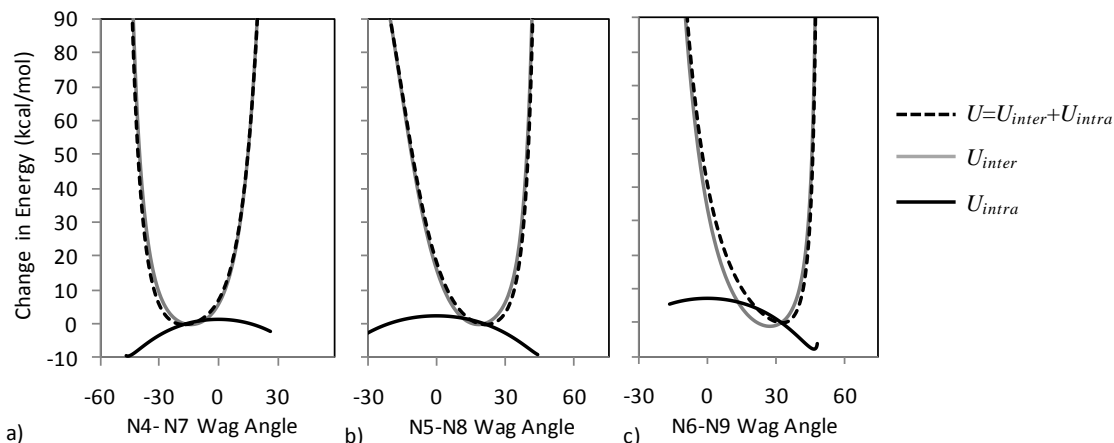
Figure 3.14: SB energy components (U, U_{inter}, and U_{intra}) from equation (2.1) as a function of nitro group wag angle for αRDX crystal.

The αRDX wag angle distributions are plotted versus the wag angle energy in Figure 3.15. The shape of the wag angle distribution is controlled by the shape of the wag angle energy profile. The energy profiles show the same asymmetry as the distributions. N4-N7 energy profile in (a) shows a flat minimum with the energy increasing more rapidly for decreasing δ. This leads to a wag distribution with a sharp drop off for high energy wag angles with $\delta<-30^{o}$. For $\delta>-30^{o}$ the wag distribution trails off more gradually. The shallow minimum results in a wide wag angle distribution. This is opposed to the N6-N9 wag energy with a narrow minimum leading to a more tightly grouped wag distribution. The similarity between the wag distributions and the wag

energy also occurs in the two γRDX conformations in Figure 3.16. The wag energy for the γRDX N4-N7 "intermediate" wag angle shown in Figure 3.16d is shown to move to the δ>0° side of the bonded energy profile.
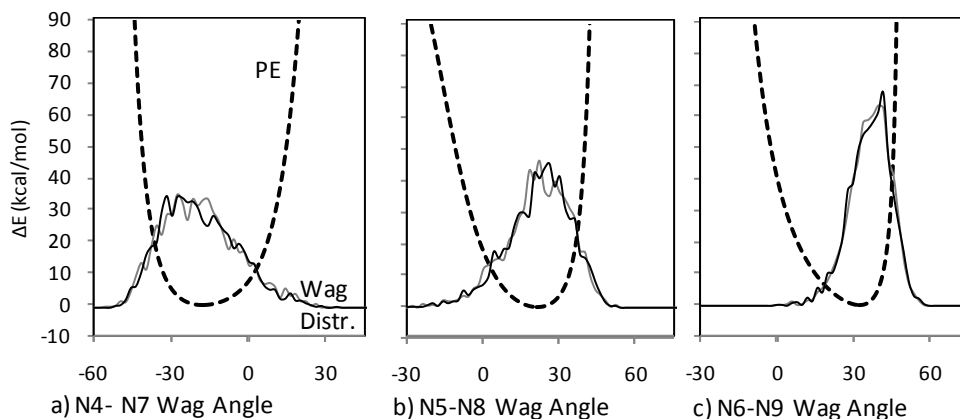
Figure 3.15: αRDX crystal total energy as a function of nitro group wag angle overlaid on the wag angle distributions.
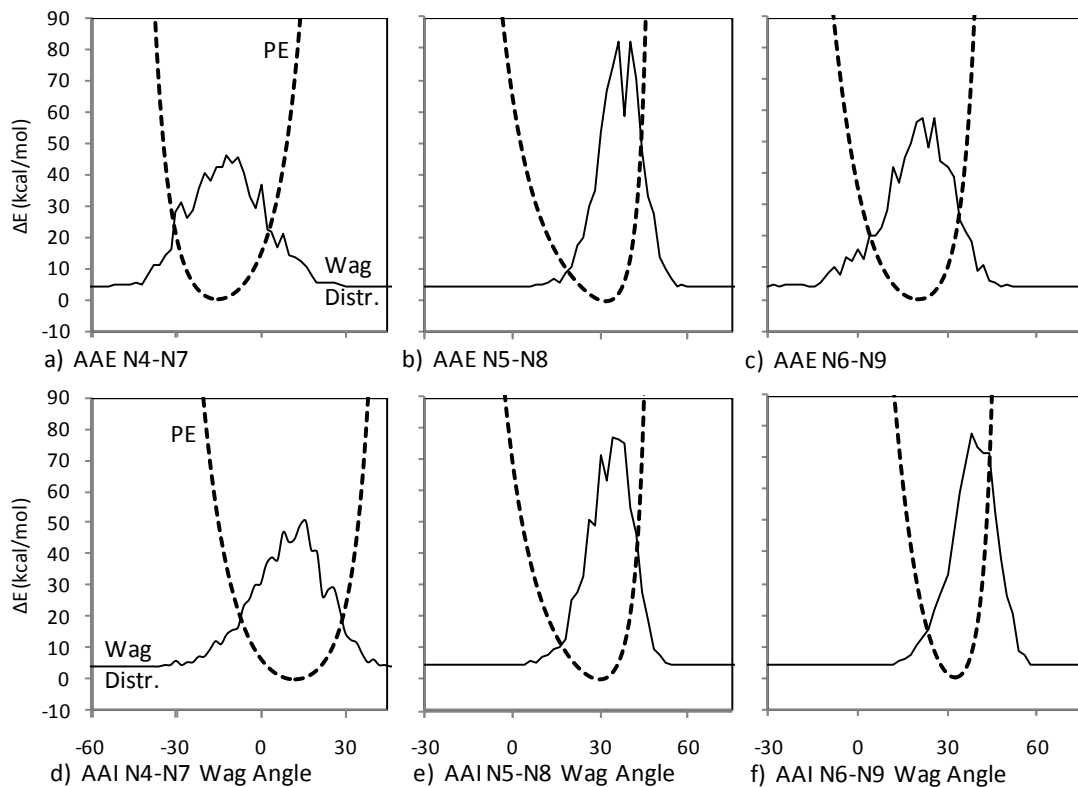
Figure 3.16: γRDX crystal total energy as a function of nitro group wag angle overlaid on the wag angle distributions. The *AAE* molecules are shown in the top row and the *AAI* molecules are shown on the bottom row.

The overall crystal structure is dependent on the conformation of each RDX molecule. The various RDX conformations observed in the α and γRDX crystals differ in the orientation of their wag angles. In this section we showed the wag angles to be accurately predicted by the SB potential. We also showed the effect of the bonded and nonbonded interactions on the resulting wag angle distributions. The bonded energy terms were found to control the conformation while the nonbonded terms controlled the distribution. The molecule neighbors in the crystal structures were also shown to be necessary for stabilizing the γRDX conformations.

3.2 Pressure, Temperature, and Volume Properties

The validity of applying the SB potential (17) to RDX is tested by its ability to predict experimentally measureable thermodynamic properties. Thermodynamic properties relate the thermodynamic states of the system such as the coefficient of thermal expansion relating the temperature and volume. The thermodynamic material properties are related to the second derivative of the thermodynamic potential of the system's state. The thermodynamic material properties are used to develop an equation of state for a constitutive equation that gives mathematical relationships between state variables of a system like pressure, temperature, volume and energy.

The SB potential was shown in Section 3.1 to reproduce the crystal structure and molecule conformations of the α and γRDX crystals. In this section the effect of pressure, volume and temperature on the α and γRDX structure will be presented. The thermodynamic relationships between the various volume, pressure, temperature states will also be given. In Section 3.2.1 the effect of pressure on the α and γRDX crystals and the change between phases is presented. These simulations are used to determine the *PV*

relationship and bulk modulus. Section 3.2.2 presents the effect of volumetric deformation on the αRDX crystals through uniaxial deformation and the resulting phase changes. These simulations are also used to determine the orthotropic stress/strain relationships. In Section 3.3.3 the effect of temperature on the αRDX crystal at constant pressure is used to determine the orthotropic coefficients of thermal expansion. In Section 3.3.4, the temperature and pressure are varied to determine the *PVT* state of a static shock wave by using the Hugoniot equations.

3.2.1 Pressure Dependent Properties

In this section the effect of pressure on the crystal lattice and structure will be studied through a series of simulations at incrementally increasing and decreasing pressures. Two separate sets of simulations are presented. The first set starts in the αRDX crystal structure at T=300K and P=0GPa and the pressure is increased between equilibrations. The second set starts in the γRDX crystal structure at T=300K and P=5.2GPa and the pressure is decreased between equilibrations. The simulation cells contain $2\times3\times3$ unit cells and are equilibrated for 75ps at each pressure increment. The equations of motion are integrated using a Nosé thermostat coupled to a Hoover barostat as implemented in DLPOLY 2.20 (71) and conserve the Gibbs free energy. The thermostat maintains a constant average temperature throughout the simulation and is kept constant between pressure increments. The Hoover barostat keeps the average pressure constant for each simulation and is incremented between simulations. The barostat used in these simulations is a constant stress barostat where the trace of the stress tensor is controlled by the pressure. This allows each lattice vector to be individually varied in response to the stress state and is important for orthorhombic crystals having

63

orthotropic properties. The change in volume is described by the volumetric Lagrange strain (73) as

$$E_V = \frac{1}{2}\left[\left(\frac{V}{V_o}\right)^{2/3} - 1\right] \tag{3.1}$$

where V_o is the reference volume of the αRDX crystal at the reference pressure $P_o{=}0$ and V is volume at the current pressure, P. Figure 3.17 presentes E_v as a function of pressure for the simulations (circle data points) and from experiment (square data points) (34) (27). αRDX data is shown in green and γRDX in red.
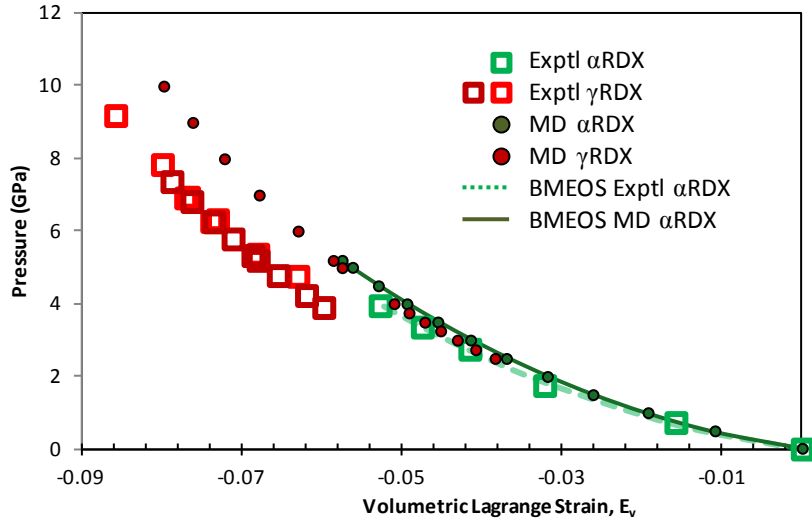
Figure 3.17: Change in volumetric Lagrange strain, E_v, as a function of pressure for the α and γRDX crystal. Data points represent simulation and experimental (34) (27) results. Solid and dashed lines are Birch Murnaghan fits to the αRDX data.

The thermodynamic relationship between pressure and volume at constant temperature, T, is the bulk modulus, B, given by

$$B = -V\left(\frac{\partial P}{\partial V}\right)_T \tag{3.2}$$

where V is volume and P is the pressure. The PV data given in Figure 3.17 is nonlinear at large pressures and the bulk modulus is not constant. The bulk modulus can be determined by numerically differentiating the PV data given in Figure 3.17. Another method is to assume a semi-empirical relationship between PV based on thermodynamics and experimental data. The thermodynamic relationship between pressure, volume and the Helmholtz free energy or strain energy, F, is given by

$$P = dF/dV \tag{3.3}$$

In the Birch Murnaghan equations of state (BMEOS) (74) the strain energy is expanded by a Taylor series in terms of a strain measure. The BMEOS is normally determined by geologists using the Eulerian volumetric strain to model the large compressions in the earth crust. In that work the reference state at $P_o=0$ is not known. In this work the Lagrangian volumetric strain is used because the strain is measured from the known reference state at $P_o=0$ to the compressed state at P. The third order BMEOS is given by expanding the strain energy, F, out to the third order giving

$$F = a + b(-E_v) + c(-E_v)^2 + d(-E_v)^3 + higher\ order\ terms \tag{3.4}$$

where the constants a, b, and c are determined from boundary conditions $F=0$ at $P=0$, $E_v=0$ at $P=0$, and $B=B_o$ and $V=V_o$ at $E_v=0$. Then using the chain rule, the strain energy can be differentiated in terms of Ev by

$$P = \frac{\partial F}{\partial(-E_v)}\frac{\partial(-E_v)}{\partial V} \tag{3.5}$$

Solving equation (3.5) with the boundary conditions for the constants gives the 3rd order BMEOS as

$$P(V) = \frac{3B_o}{2}\left[\left(\frac{V}{V_o}\right)^{-1/3} - \left(\frac{V}{V_o}\right)^{1/3}\right]\left\{1 + \frac{3}{4}B'_o\left[1 - \left(\frac{V}{V_o}\right)^{2/3}\right]\right\} \tag{3.6}$$

where V_o is the volume at zero pressure, B_o and B_o' are the bulk modulus and its derivative at zero pressure (73). The variables B_o and B_o' are found by fitting the data points in Figure 3.17 to equation (3.6). This was done using MATLAB's fminsearch function to minimize the square of the error between the known pressure and volume (data points) and the pressure computed for that volume using equation (3.6). Data for V_o, B_o, and B_o' are given in Table 3.5 for the experimental (34) (27) and simulation data. For γRDX, V_o is also an unknown and must be solved for. For the simulation data the reference volume for γRDX was set to V_o=1600 Å^3 because fminsearch did not provide a physically realistic value for it.

The 3rd order BMEOS is normally determined from the Eulerian volumetric strain and gives a different *PV* function than that given by equation (3.6). This may cause the BMEOS data in Table 3.5 to be slightly different than other reported values. The Lagrange BMEOS was used here because the Lagrangian strain is the main measure of deformation used throughout this work.

Table 3.4: 3rd order BMEOS parameters for α and γRDX for experimental (34) (27) and simulation data fit to equation (3.6).

α-RDX 3rd order BMEOS parameters

	P range (Gpa)	B_o(GPa)	B_o'	V_o(Å³)
This work	0-5.2	10.4	19.8	1634
Olinger[a]	0-3.95	10.0	17.3	1641
Davidson[b]	--	9.8	11.4	1614

γ-RDX 3rd order BMEOS parameters

	P range (Gpa)	B_o(GPa)	B_o'	V_o(Å³)
This work	2.5-9	10.3	26.8	1600*
Olinger[a]	4.76-9.19	8.8	29.9	1570
Davidson[b]	--	17.6	6.8	1557

[a]Computed from Olinger et al. data Ref. (34), [b]Davidson et al. Ref. (27), *Reference volume preset to V_o=1600 Å³

The experimental data in Figure 3.17 shows a large volume change for the α to γRDX phase transition at $P \approx 3.9$GPa. The difference between the two phases in the simulation data is much smaller, shown by the circles. The dark red circles started in the γRDX structure and the pressure was incrementally lowered from 5.2GPa. At ~2.1GPa the γRDX crystal converted to αRDX, shown by the green circles. On the other hand, increasing the pressure of the αRDX crystal from P=0 did not result in the γRDX crystal structure, even up to P=10GPa. Increasing the temperature to T=350K also did not aid in the α to γRDX transition.

The lattice constants as a function of pressure are shown in Figure 3.18 for experimental and simulation data. The simulation data is shown by the circles and black lines and the experimental data by the triangles and purple lines. The data points near the experimental phase transition at $P \approx 3.9$GPa, marked by the vertical gray line, are shown in red. These data points are presented in Table 3.6. Also given in Table 3.6 is the percent change between the α and γRDX lattice lengths at ~4GPa. The simulations result in smaller changes in lattice lengths, with the largest difference for the **c**-lattice.
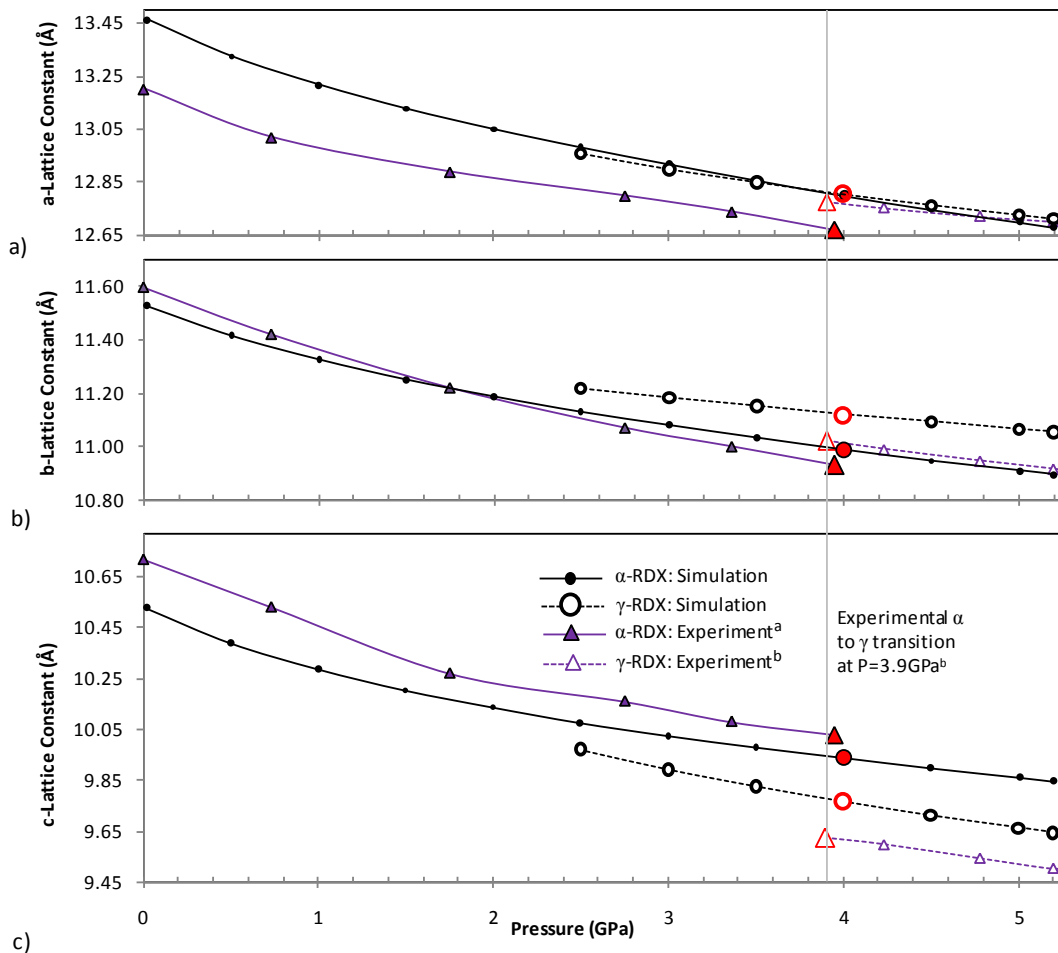
Figure 3.18: Lattice constants versus pressure. Triangles represent experimental values where filled triangles are αRDX (34) and hollow for γRDX (27). Small filled circles and solid lines show αRDX simulations upon pressurization. Large hollow circles and dashed lines show γRDX simulations upon depressurization. The large red data points at the experimental α→γRDX transition pressure are given in Table 3.5.

Table 3.5: Change in lattice constants between α and γRDX phase from this work and experiment near the experimental phase transition pressure (~3.9GPa) shown by gray line in Figure 3.18.

	α-RDX	γ-RDX	α-γ Change	
This Work: P=4GPa				
a_1 (Å)	12.80	12.80	0.00	(0.00%)
b_2 (Å)	10.99	11.12	-0.13	(-1.17%)
c_3 (Å)	9.94	9.77	0.17	(1.74%)
V (Å^3)	1398	1391	7	(0.50%)
Experiment: P=3.9-3.95GPa				
a_1 (Å)	12.67[a]	12.77[b]	-0.10	(-0.78%)
b_2 (Å)	10.93[a]	11.02[b]	-0.09	(-0.82%)
c_3 (Å)	10.03[a]	9.62[b]	0.41	(4.26%)
V (Å^3)	1388[a]	1355[b]	33	(2.44%)

[a]Choi and Prince Ref. (25), [b]Davidson et al. Ref. (27)

The crystal structure and molecule conformation also provide details on the evolution of the crystal structure with pressure. The RDF and wag angle distributions presented in Section 3.1 are shown in Figure 3.19 for the αRDX pressurization. The RDF calculated from the molecule COMs are shown in Figure 3.19a. The blue (αRDX) and red (γRDX) RDFs are the simulation (solid line) and experimental data (dashed line) from Figure 3.6. The black RDFs are from the incrementally increasing pressure simulations. The peak locations slightly shift toward zero as the lattice is compressed and molecules become more tightly packed. This also causes some of the peaks to become more distinguishable as the thermal motion of the molecules becomes more tightly constrained. However, these changes in peak locations do not result in the peak locations shown in red for γRDX.

The αRDX unit cell is shown in Figure 3.19 with the O and H atoms removed for clarity. The red molecules are those that convert to *AAI* in γRDX and the blue molecules remain *AAE* in γRDX. Each wag angle distribution is also shown as a function of pressure in Figure 3.19c-d. The wag angles are grouped and colored by the molecule

colors in the unit cell. Both groups of molecules have an almost identical distribution and only the blue distributions are visible. Increasing pressure has almost no effect on the molecule conformation and the wag angles remain nearly constant. Even the thermal motion of the wag angles described by the width of the distribution is not affected by increasing pressure.
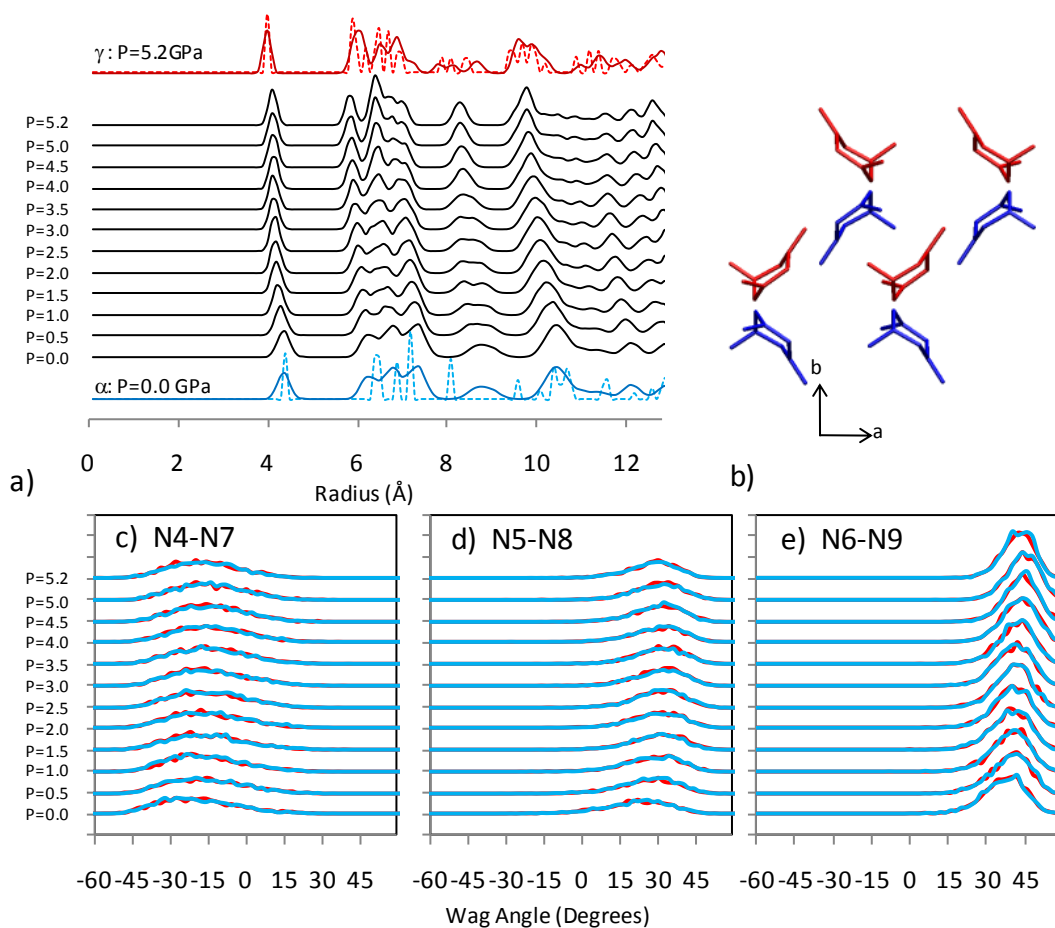
Figure 3.19: (a) Molecular center of mass RDF for compression of αRDX shown by black lines over a range of pressures compared to γRDX (red) and αRDX (blue). (b) Wireframe depiction of the symmetry equivalent molecules in the unit cell of αRDX from simulation at P=0GPa; hydrogen and oxygen atoms are not shown for clarity. (c)-(e) Distribution of nitro wag angles as a function of pressure with line color corresponding to red and blue molecules in (b).

70

The same structural data is shown in Figure 3.20 for the γRDX depressurzation. The simulation data starts at the top where P=5.2GPa and moves down in pressure. In the RDF data in Figure 3.20a there is a shift in the peak locations between P=2.5GPa and 2GPa indicating the phase transition. The first peak represents the molecule pairs closest to one another. In the γRDX structure, Davidson et al. (27) showed the *AAI* and *AAE* molecules form interlocking pairs. In the αRDX structure these pairs no longer have the proper conformation to be interlocked and slightly separate, indicated by the shift in the first peak. The final depressurized RDF matches the RDF of equilibrated αRDX shown in blue.

The unit cell for γRDX is shown in Figure 3.20b where the red molecules are in the *AAI* conformation and the blue in the *AAE*. The blue unit cell is shown overlaid on the αRDX unit cell shown in gray. The red *AAI* molecules are shown to undergo a slight rotation while the blue *AAE* molecules do not move. The wag angle distributions are shown in Figure 3.20c-e and the two distinct conformations of γRDX are apparent at P=5.2GPa. The wag angles distributions remain constant down to P=2GPa where they collapse to a single peak distribution. The single peak distribution is also that of αRDX. The RDF and wag angle data confirm that γRDX transitions into the αRDX crystal structure at decreasing the pressure.
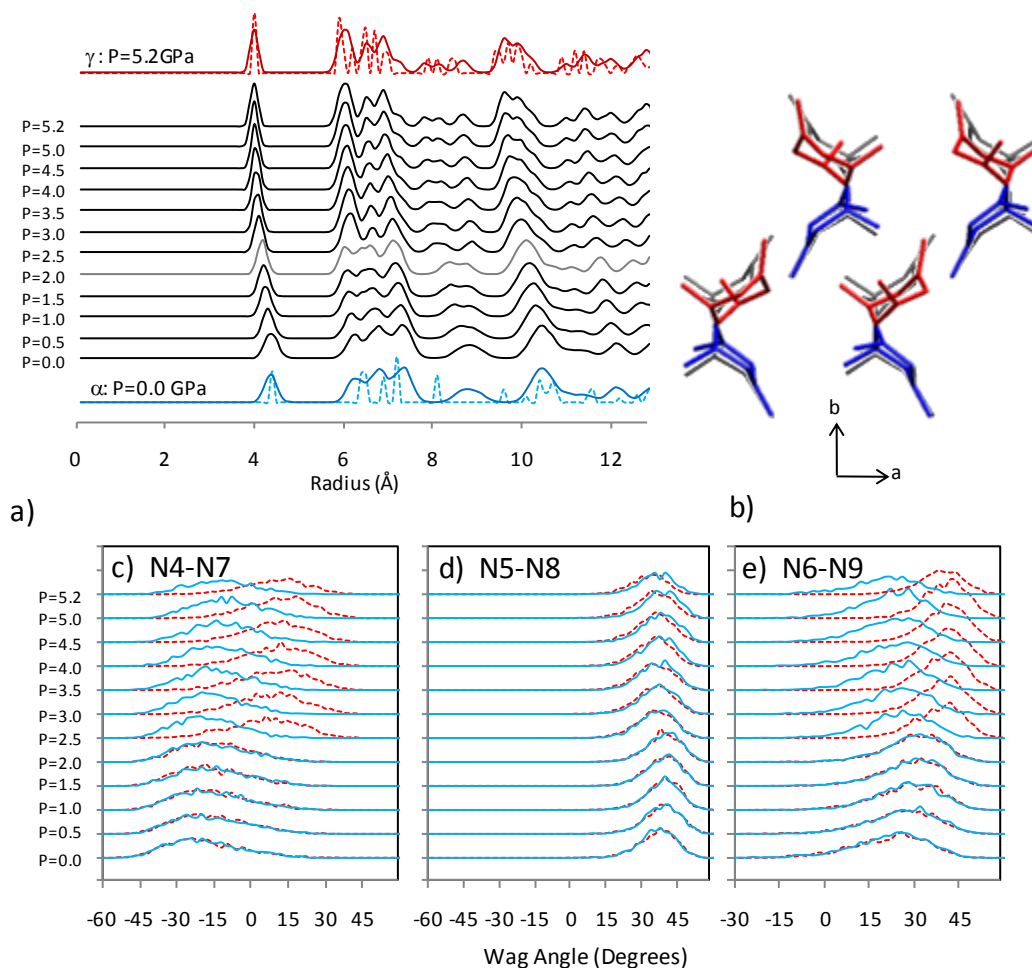
Figure 3.20: (a) Molecular center of mass RDF for decompression of γRDX shown by black lines over a range of pressures compared to γRDX (red) and αRDX (blue). (b) Wireframe depiction of the symmetry equivalent molecules in the unit cell of γRDX from simulation at P=5.2GPa; hydrogen and oxygen atoms are not shown for clarity. This depiction is superimposed on a transparent image of the αRDX unit cell at *P*=0 [see **Figure 3.19**(b)]. (c)-(e) Distribution of nitro wag angles as a function of pressure with line color corresponding to red and blue molecules in (b).

The Gibbs energy was conserved at each pressure increment in these simulations. It will be used to investigate the phase transition. The pressurization simulations of αRDX do not transition to γRDX. This could be due to the high pressure αRDX crystal being the energetically favorable crystal structure and would indicate that the SB potential does not accurately capture the γRDX phase. On the other hand, if γRDX is the

preferred phase at high pressures then the pressure induced α to γRDX phase transition may be impeded by some other mechanism.

The change in Gibbs energy relative to the ambient state, $\Delta U_{Gibbs}=U_{Gibbs}(P)-U_{Gibbs}(P=0)$, is shown versus the volumetric Lagrange strain in Figure 3.21 for the αRDX pressurization (filled circles) and γRDX depressurization (open diamonds). The energy of the αRDX crystal is higher in energy at increasing compression and the γRDX is the lower energy configuration. The inset plot in Figure 3.21 shows the data points near the phase transition labeled by their pressure values. The difference in energy as a function of strain between α and γRDX is ~5kcal/mol. This small difference does not provide a sufficient driving force for αRDX to convert to γRDX at high pressures. At $P \leq 2.1GPa$, the γRDX depressurization data (diamonds) move to the solid line of the αRDX data indicating the phase change.
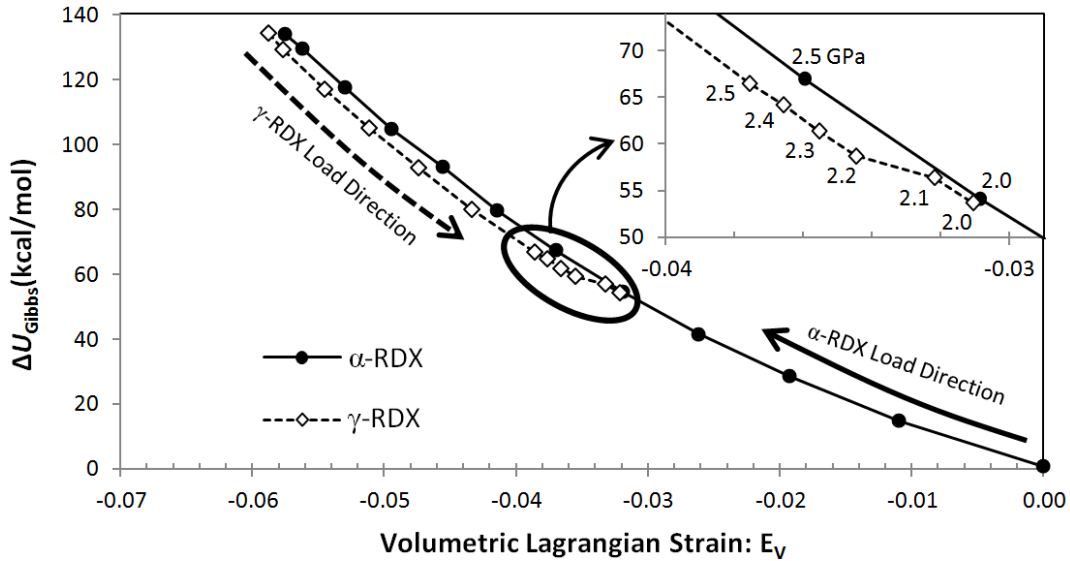
Figure 3.21: Change in Gibbs energy, $\Delta U_{Gibbs}=U_{Gibbs}(P)-U_{Gibbs}(P=0)$ versus mean strain relative to the αRDX configuration at $P=0$. Inset shows the region near the transition with pressure values labeled in GPa units.

The α to γRDX transition involves changes in the molecular conformation as well as abrupt lattice changes. To clarify the impact of these conformational changes, it is helpful to detail the variation in each component of the potential energy described by the SB potential given in equation (2.1) through the transition as shown in Figure 3.22. The data shown in Figure 3.22 is from the decompression of the γRDX crystal, which was shown to transition to αRDX at P=2.1GPa. Compression of αRDX leads to increases in the repulsive component of the van der Waals energy as the molecules are pushed closer together. There is a slight drop in VDW energy at the transition and it continues to increase for compression of γRDX. The coulomb energy contains both attractive and repulsive electrostatic interactions between nearest neighbor atoms and compression does not necessarily result in an increase in this nonbonded energy component. The coulomb energy of αRDX slightly decreases with compression and then near the α to γ transition its slope goes to zero. The transition results in an increase in coulomb energy as it continues to increase with compression of the γRDX crystal.

The conformation of the RDX molecule is mainly controlled by the bonded dihedral and angle energies. These were shown in Section 3.1 to control the wag angle distributions of the α and γRDX crystals. The angle and dihedral energy counteract one another in αRDX where they are almost equal in magnitude but opposite in sign. This indicates the angle and dihedral components are working against one another in the molecule and as the dihedral energy is raised the angle energy is relaxed. At the transition, both energies drop to nearly zero and remain near zero for increasing compression of the γRDX crystal. This indicates that the molecule conformation of

γRDX is not significantly affected by increasing compression. In this case, the RDX molecules respond almost as rigid bodies to increasing pressure.
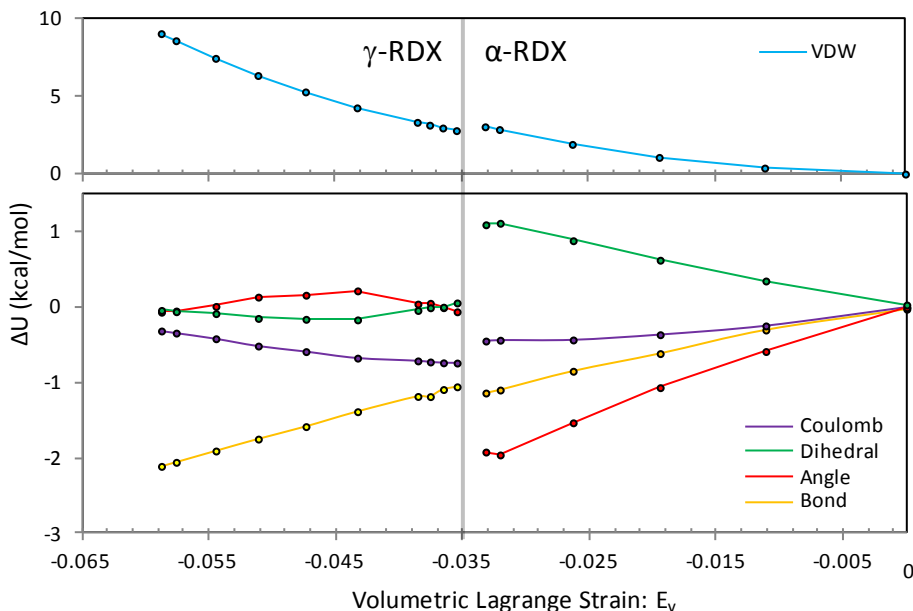
Figure 3.22: Change in energy components of the SB potential energy given in equation (2.1), relative to their respective values of αRDX at $P=0$ verses volumetric strain, E_V. The van der Waals term is shown on a different scale.

These results indicate the following. Firstly, no γRDX structure can be found under equilibration at pressures below a critical value ($P=2.1$ GPa), which indicates that the αRDX phase is indeed the ambient state polymorph using the SB potential. Secondly, the transition is not observable with increasing hydrostatic pressure of pristine αRDX. Such idealized simulations may preclude the transition to the γRDX phase at higher hydrostatic pressures using the SB potential. This is particularly evident in the fact that uniform depressurization of the γ-phase indeed yields the αRDX phase. Finally, the γRDX phase is the energetically favorable phase above $P=2.1$GPa.

Basic equilibrium properties were computed using the *NST* ensemble. The pressure-dependent lattice constants and volume for the α and γRDX crystals were found

to be in agreement with available experimental data (34) (27) as shown in Figure 3.17 and Figure 3.18. The α and γRDX *PV* data for simulation (circles) and experiment (triangles) shown in Figure 3.17 were fit to the 3rd Order Birch-Murnaghan equation of state (BMEOS) (74) (73) by least squares fitting of the bulk modulus and its derivative at zero pressure and were given in Table 3.4.

3.2.2 Uniaxial Strain Properteis

The elastic response of the αRDX crystal is shown to be sensitive to the direction of loading, resulting in orthotropic elastic constants (31). The orthotropic elastic response is related to the orthorhombic αRDX crystal structure. The material response to large deformation leads to molecular and lattice distortions that are also dependent on the crystal axis being loaded (56). These elastic and large deformation responses will be studied in this section through simulations of uniaxially deformed αRDX crystals. By applying varying levels of uniaxial deformation – a non-hydrostatic deformation and state of stress – measurements of the anisotropy and its connection to underlying crystal structure can be determined.

The deformation gradient, **F**, is a second order tensor that provides a mapping of vectors between a reference and deformed configuration as shown in Figure 3.23 (75). All of the vectors in the reference configuration, $\mathbf{a}_o$, $\mathbf{b}_o$, $\mathbf{c}_o$, can be mapped to the final configuration by **F** using the dot product giving

$$\begin{aligned}
\mathbf{a} &= \mathbf{F} \cdot \mathbf{a}_o \\
\mathbf{b} &= \mathbf{F} \cdot \mathbf{b}_o \\
\mathbf{c} &= \mathbf{F} \cdot \mathbf{c}_o
\end{aligned} \qquad (3.7)$$

If the vectors given by **a**, **b**, **c** are not parallel to one another (their cross products are nonzero) they can be used to determine **F** by rearranging equation (3.7) to give

$$\begin{bmatrix} a_1 & a_2 & a_3 \\ b_1 & b_2 & b_3 \\ c_1 & c_2 & c_3 \end{bmatrix} \begin{bmatrix} a_1^o & a_2^o & a_3^o \\ b_1^o & b_2^o & b_3^o \\ c_1^o & c_2^o & c_3^o \end{bmatrix}^{-1} = [\mathbf{h}][\mathbf{h}_o]^{-1} = \mathbf{F} \tag{3.8}$$

where the vectors $\mathbf{a}$, $\mathbf{b}$, and $\mathbf{c}$ form the columns of the 3×3 matrix $[\mathbf{h}]$. Once $\mathbf{F}$ is determined the Lagrange strain, $\mathbf{E}$, is given as

$$\mathbf{E} = \frac{1}{2}(\mathbf{F^T F} - \mathbf{I}) = \frac{1}{2}([\mathbf{h}_o]^{-T}[\mathbf{h}]^T[\mathbf{h}][\mathbf{h}_o]^{-1} - \mathbf{I}) \tag{3.9}$$

where $\mathbf{I}$ is the identity. In this work the vectors $\mathbf{a}$, $\mathbf{b}$, and $\mathbf{c}$ correspond to the lattice vectors with Cartesian coordinates, $\mathbf{e}_i$, shown in Figure 3.23. The lattice vectors will never be parallel and can always be used to determine $\mathbf{F}$ and the Lagrange strain, $\mathbf{E}$, between two configurations.
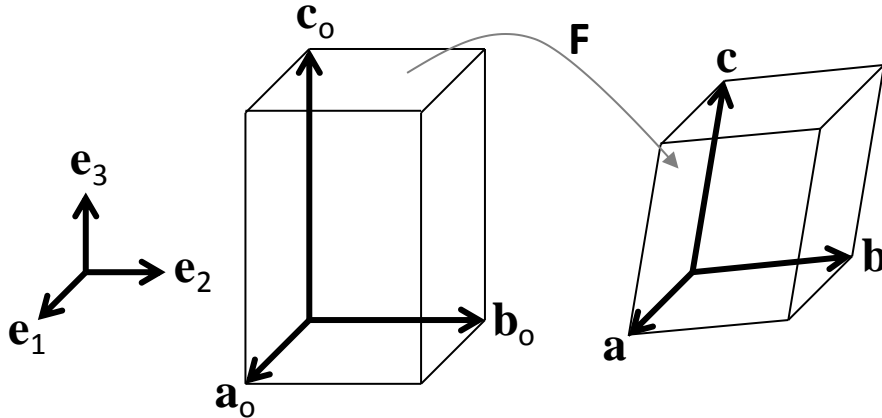
Figure 3.23: Mapping between initial ($\mathbf{a}_o$, $\mathbf{b}_o$, $\mathbf{c}_o$) and final ($\mathbf{a}$, $\mathbf{b}$, $\mathbf{c}$) state using the deformation gradient $\mathbf{F}$.

In this work, strain is imposed on the reference state by defining $\mathbf{F}$ and using it to map the atomic coordinates at $[\mathbf{h}_o]$ to $[\mathbf{h}]$ using equation (3.7). The atoms are mapped by the center of mass location of their RDX molecule. This strains the crystal without distorting the molecule. The Lagrange strain is symmetric and there are only 6 unique strain components. Each of the six unique strains, E_{ij}, are individually incremented up to

77

1% strain to determine the elastic constants. Each strain increment was equilibrated for 75ps. For these small strains the stress/strain response of the material is linear and the elastic constants for an orthotropic material in Voigt form is given by

$$\sigma = C : E$$

$$
\begin{Bmatrix} \sigma_{11} \\ \sigma_{22} \\ \sigma_{33} \\ \sigma_{23} \\ \sigma_{31} \\ \sigma_{12} \end{Bmatrix} =
\begin{bmatrix}
C_{11} & C_{12} & C_{13} & 0 & 0 & 0 \\
C_{21} & C_{22} & C_{23} & 0 & 0 & 0 \\
C_{31} & C_{32} & C_{33} & 0 & 0 & 0 \\
0 & 0 & 0 & C_{44} & 0 & 0 \\
0 & 0 & 0 & 0 & C_{55} & 0 \\
0 & 0 & 0 & 0 & 0 & C_{66}
\end{bmatrix}
\begin{Bmatrix} E_{11} \\ E_{22} \\ E_{33} \\ 2E_{23} \\ 2E_{31} \\ 2E_{12} \end{Bmatrix}
\tag{3.10}
$$

Voigt form uses major and minor symmetry of the stress and strain tensors to write the fourth order tensor, C, as a 6×6 matrix. Each volumetric strain component, E_{ii}, results in a triaxial state of stress, σ_{jj}, due to Poisson's effect and is used to determine the volumetric components of C. Each shear strain results in a single linearly proportional shear stress, giving the shear components of C. The elastic constants are given in terms of common orthotropic engineering constants by inverting C to give the compliance tensor as

$$
S = C^{-1} =
\begin{bmatrix}
1/E_1 & -v_{21}/E_2 & -v_{31}/E_3 & 0 & 0 & 0 \\
-v_{12}/E_1 & 1/E_2 & -v_{32}/E_3 & 0 & 0 & 0 \\
-v_{13}/E_1 & -v_{23}/E_2 & 1/E_3 & 0 & 0 & 0 \\
0 & 0 & 0 & 1/G_{23} & 0 & 0 \\
0 & 0 & 0 & 0 & 1/G_{31} & 0 \\
0 & 0 & 0 & 0 & 0 & 1/G_{12}
\end{bmatrix}
\tag{3.11}
$$

where E_i is the orthotropic Young's modulus, v_{ij} is the orthotropic Poisson's ratio and G_{ij} is the orthotropic shear modulus. Values for C_{ij}, E_i, v_{ij}, and G_{ij} are given in Table 3.6 and Table 3.7. The uniform strain expression for the bulk modulus, B_v, given by

$$
B_V = \frac{1}{9} \sum_{i,j}^{3} C_{ij}
\tag{3.12}
$$

and shear modulus, G_v, given by

$$G_V = \frac{1}{15}(C_{11} + C_{22} + C_{33}) - \frac{1}{15}(C_{23} + C_{31} + C_{12}) + \frac{1}{5}(C_{44} + C_{55} + C_{66}) \qquad (3.13)$$

are also given in Table 3.7.

Table 3.6: Orthotropic elastic constants (GPa)

	NVT	Sewell[a]	Haycraft[b]	Schwarz[c]	NVT γRDX (P=5.2GPa)
C_{11}	25.0	26.9	36.7	25.6	80.3
C_{22}	23.8	24.1	25.7	21.3	67.0
C_{33}	23.4	17.7	21.6	19.0	57.9
C_{44}	3.1	8.4	12.0	5.4	11.9
C_{55}	5.2	5.3	2.7	4.3	16.3
C_{66}	7.7	7.6	7.7	7.3	13.4
C_{23}	8.8	6.3	9.2	6.4	43.9
C_{31}	7.6	5.7	1.7	5.7	37.0
C_{12}	10.6	6.3	1.4	8.7	37.8

[a]Sewell et al. Ref. (40), [b]Haycraft et al. Ref. (33), [c]Schwarz et al. Ref. (31)

Table 3.7: Orthotropic engineering elastic constants (GPa)

	NVT	Sewell[a]	Haycraft[b]	Schwarz[c]
E_1	19.6	24.20	36.52	25.60
E_2	17.8	21.10	21.77	21.30
E_3	19.5	15.40	18.33	19.00
G_{23}	3.1	8.40	11.99	5.38
G_{31}	5.2	5.30	2.72	4.27
G_{12}	7.7	7.60	7.68	7.27
ν_{21}	0.34	0.17	0.02	0.34
ν_{12}	0.38	0.20	0.03	0.41
ν_{31}	0.18	0.16	0.03	0.12
ν_{13}	0.18	0.25	0.06	0.16
ν_{32}	0.29	0.22	0.36	0.30
ν_{23}	0.26	0.30	0.41	0.34
B_V	14.0	11.7	12.1	11.9
G_V	6.2	7.6	9.3	6.4

[a]Sewell et al. Ref. (40), [b]Haycraft et al. Ref. (33), [c]Schwarz et al. Ref. (31)

The uniaxial strain simulations are continued beyond the linear elastic limit by increasing F_{ii}=0.1 to 0.9 in increments of 0.1. For an orthorhombic material like αRDX, the [$\mathbf{h}_o$] matrix is diagonal and $F_{aa}=a/a_o$, $F_{bb}=b/b_o$ and $F_{cc}=c/c_o$. The stress components

that develop along each crystal axis ($\sigma_{a,b,c}$ along **a,b,c**-axis, respectively) are the principal stresses and are shown in Figure 3.24 for each F_{ii}. The maximum shear stress, shown by the dashed line, is equal to the minimum (σ_{min}) minus the maximum (σ_{max}) principal stresses. The maximum shear stress is an indicator of plastic material response when its magnitude exceeds the known yield strength of the material and acts on a plane oriented by 45 degrees to the directions of σ_{max} and σ_{min}.

The stress/strain curves are nonlinear at these strain levels and the slope becomes steeper with increasing uniaxial compression. There are kinks in the stress/strain curves for compression of the **b-** and **c-** axes indicating a phase change. Isotropic compression of αRDX in Section 3.2.1 was unable to trigger the transition to γRDX. However, the uniaxial strain simulations produce a triaxial state of stress that is able to trigger the phase change. As will be shown later, compression of the **c**-axis results in the γRDX phase and compression of the **b**-axis results in a phase similar to that observed by Cawkwell et al. (38). Compression of the **a**-axis does not result in a phase transition.
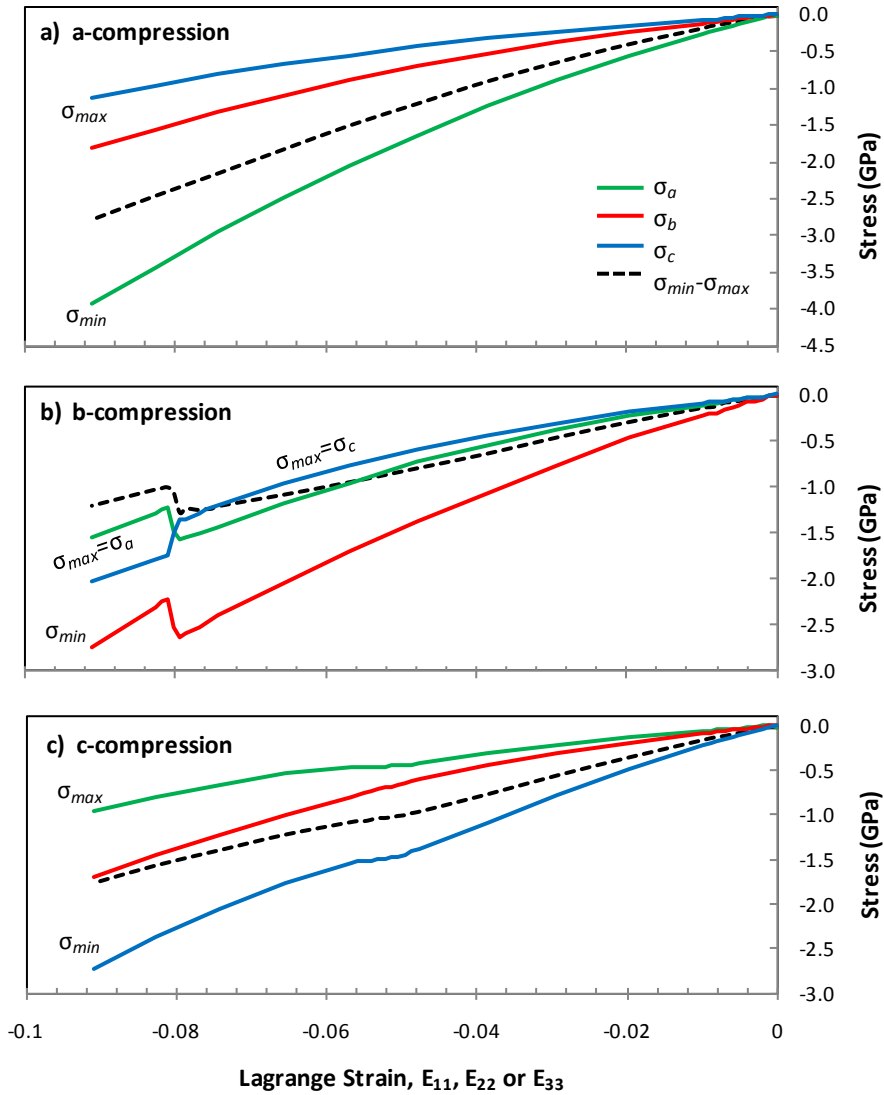
Figure 3.24: Stress versus Lagrange strain for uniaxial compression along the (a) **a**-axis, (b) **b**-axis and (c) **c**-axis. Principal stress components are labeled by crystal axis (e.g. σ_a is the principal stress oriented along the **a**-axis of α-RDX). Maximum shear stress (σ_{min} - σ_{max}) is shown by the dashed line.

For **b**-compression the principal stresses change abruptly across the transition with σ_c (blue line) decreasing and both σ_a (green line) and σ_b (red line) increasing. This abrupt change leads to the maximum principal stress in αRDX to be oriented along the **c**-axis ($\sigma_{max} = \sigma_c$) and after the transition it is oriented along the **a**-axis ($\sigma_{max} = \sigma_a$). The change in crystal phase leads to a reorientation of σ_{max} and in effect a reorientation of the

plane of maximum shear stress. Thus new slip systems may become active resulting in plastic slip on new planes that block the αRDX slip planes. Similar effects were observed in the simulated plastic response of αRDX under oriented shock loading (38) (56).

The RDF and wag angle distributions presented for the pressurization of αRDX in Figure 3.19 are shown in Figure 3.25 thru Figure 3.27 for the uniaxial deformation simulations. The RDFs are calculated from the molecule COM. The blue (αRDX) and red (γRDX) RDFs from simulation (solid line) and experimental data (dashed line) from Figure 3.6 are also shown. The black RDFs are labeled by the deformation gradient increment.

Figure 3.25 presents uniaxial compression of the **a**-lattice by F_{aa}. The peak locations of the RDF will shift as the molecules are uniaxially compressed. The single RDF peak between 8-10Å separates into two peaks with increasing **a**-compression and better matches the two peaks observed in the experimental αRDX data shown by the blue dashed lines. In the simulations of αRDX at P=0GPa presented in Section 3.1, the **a**-lattice was over predicted by 2%, the largest of all the lattice directions. When F_{aa}=0.98 the **a**-lattice length is within 0.1% of experiment and two distinct peaks develop in the RDF. A similar shift is seen in the other F_{ii} but at higher compressions. Overall, the shifts in RDF peaks are gradual and there is not a phase transition. The wag angle distributions in Figure 3.25c-e also do not show a large change that would indicate a conformation change. The compressed unit cell is shown in Figure 3.25b and is over laid on the αRDX unit cell shown in gray. The only difference between two structures is a

slight compression of the molecules along the **a**-axis as was observed in simulations by Cawkwell et al. (55) and Bedrov et al. (58).
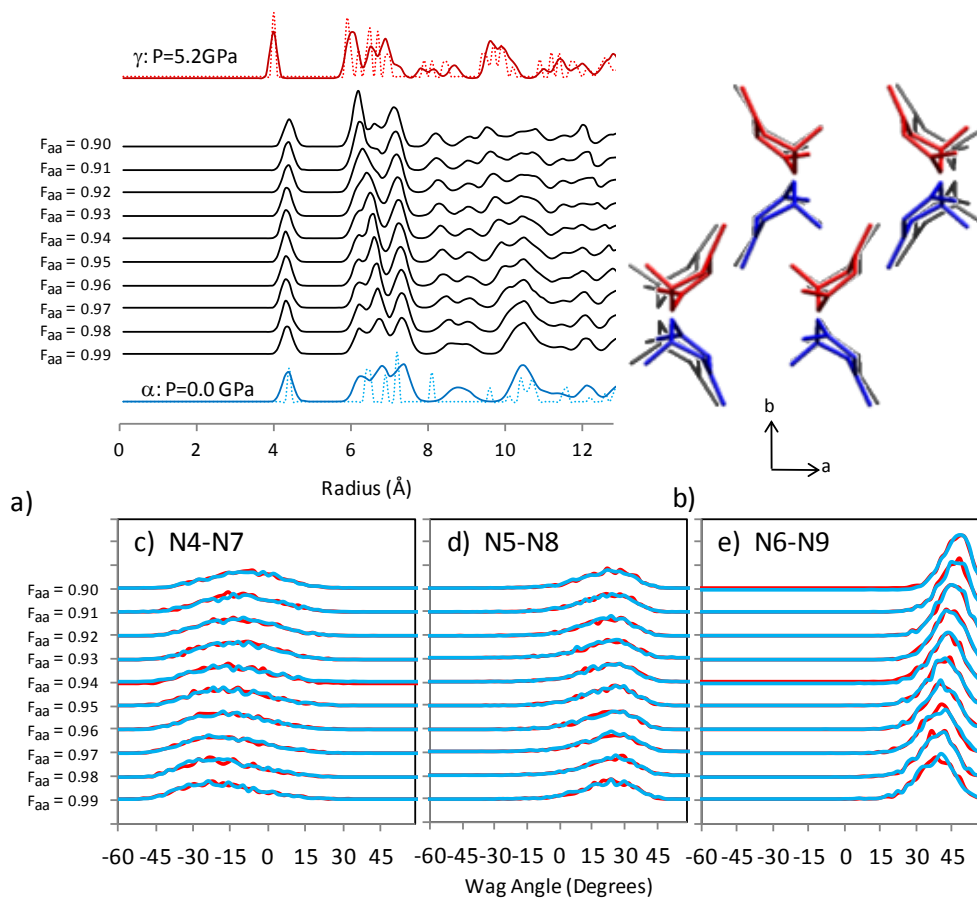
Figure 3.25: (a) Molecular center of mass RDF for uniaxial compression of the **a**-axis shown by black lines over a range of F_{aa} compared to γRDX at P=5.2GPa (red) and αRDX at P=0GPa (blue) shown in Figure 3.6. (b) Unit cell after compression overlaid on gray αRDX unit cell at P=0. (c)-(e) Nitro wag angle distributions as a function of mean strain with line color corresponding to red and blue molecules in (b).

Figure 3.26 presents uniaxial compression of the **b**-lattice by F_{bb}. The first peak in RDF curve shows a large shift at F_{bb}=0.92 indicating a phase change. This phase change resulted in the kink in the stress/strain data in Figure 3.24b. The RDF peak shift is a result of the two central red and blue molecules in the unit cell shown in Figure 3.26b moving closer together. The N5-N8 wag angle in Figure 3.26d shows a large shift from

axial to equatorial. This phase change results in a conformation change of all molecules from *AAE* to *AEE*. This same molecule conformation change has been noted in several other simulations of αRDX using the SB potential for tension (72) and compression (38) simulations.
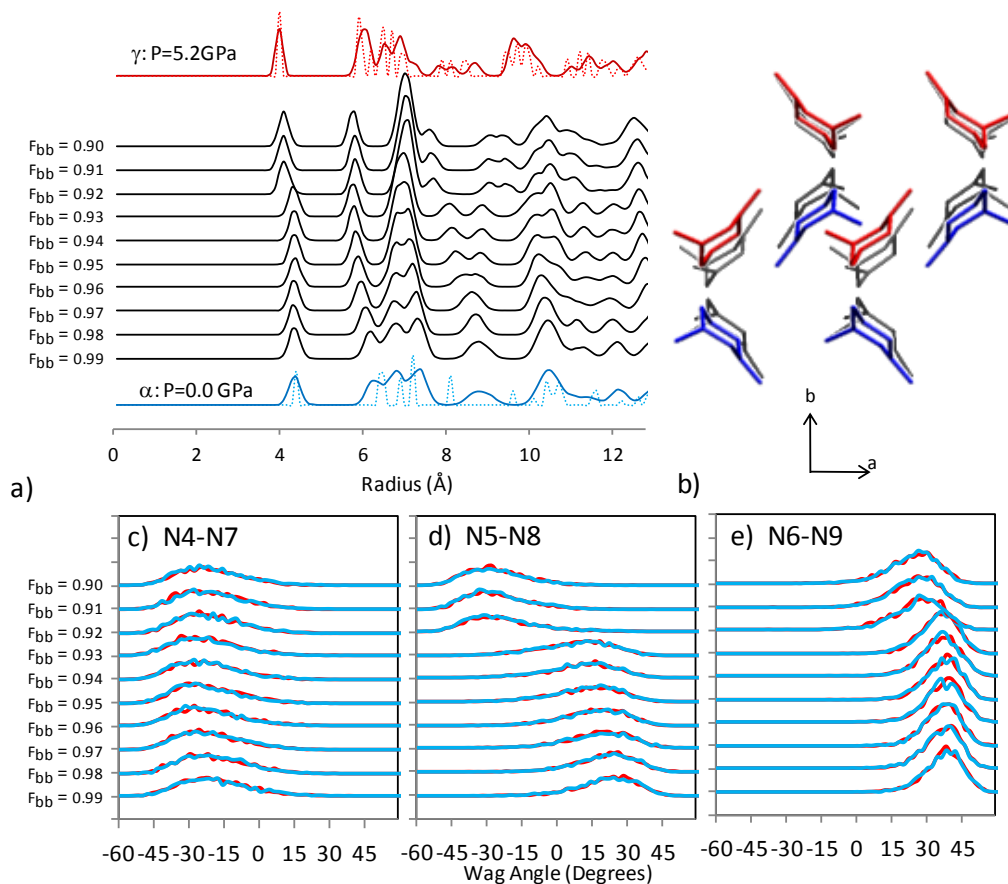
Figure 3.26: (a) RDF for uniaxial compression of the **b**-axis shown by black lines over a range of F_{bb} compared to γRDX at P=5.2GPa (red) and αRDX at *P*=0GPa (blue) shown in Figure 3.6. (b) Wireframe depiction of the symmetry equivalent molecules in the strained unit cell; hydrogen and oxygen atoms are not shown for clarity. This depiction is superimposed on a gray image of the αRDX unit cell at *P*=0. (c)-(e) Nitro wag angle distributions as a function of mean strain with line color corresponding to red and blue molecules in (b).

Figure 3.27 shows data for compression along the c-axis. The wag angle distributions in Figure 3.27c-e indicate the α to γRDX phase transition based on the development of a bimodal distribution of *AAE* and *AAI* molecules at F_{cc}=0.93. It is

difficult to discern the peaks in the RDF that are associated with the phase transition from those associated with the uniaxial strain. Figure 3.27b shows unit cell where the red *AAI* molecules have rotated, which is consistent with the γRDX structure. Overall, the visual inspection of the unit cell and the wag angle distributions indicate that this is equivalent to the experimental γRDX crystal. Bedrov et al. (58) were also able to trigger a similar γRDX transition of αRDX using uniaxial stress.
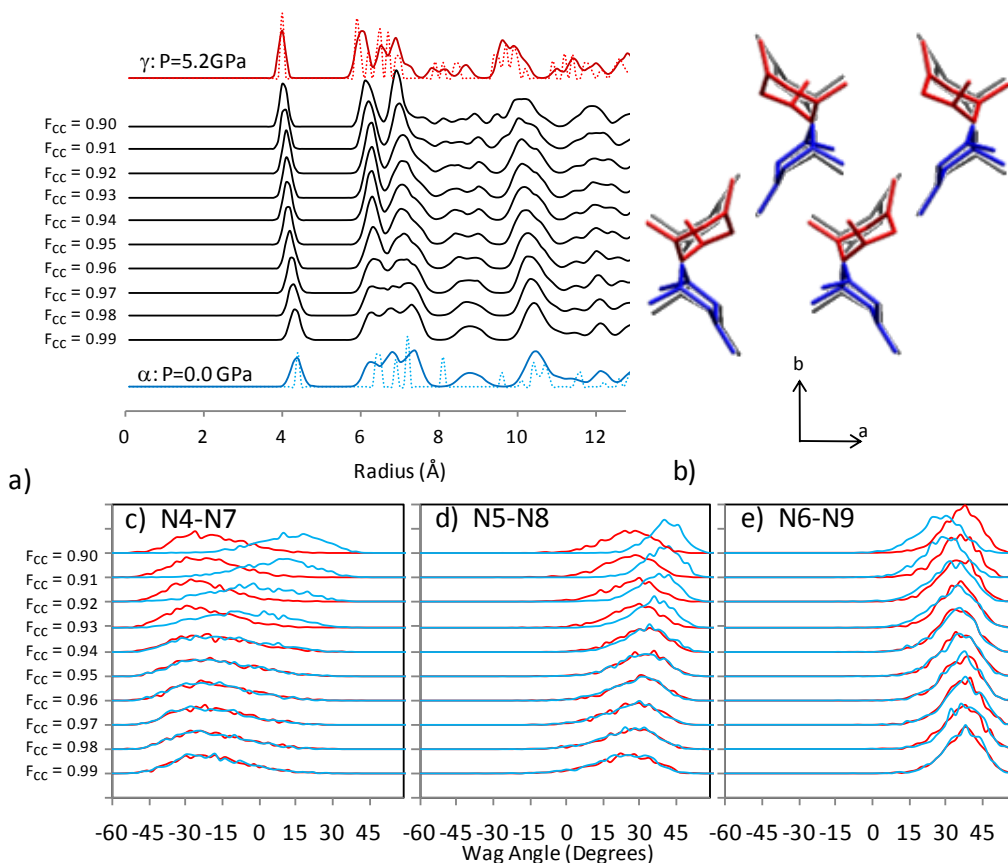
Figure 3.27: (a) RDF for uniaxial compression of the **c**-axis shown by black lines over a range of F_{cc} compared to γRDX at P=5.2GPa (red) and αRDX at *P*=0GPa (blue) shown in Figure 3.6. (b) Wireframe depiction of the symmetry equivalent molecules in the strained unit cell; hydrogen and oxygen atoms are not shown for clarity. This depiction is superimposed on a gray image of the αRDX unit cell at *P*=0. (c)-(e) Nitro Wag angle distributions as a function of mean strain with line color corresponding to red and blue molecules in (b).
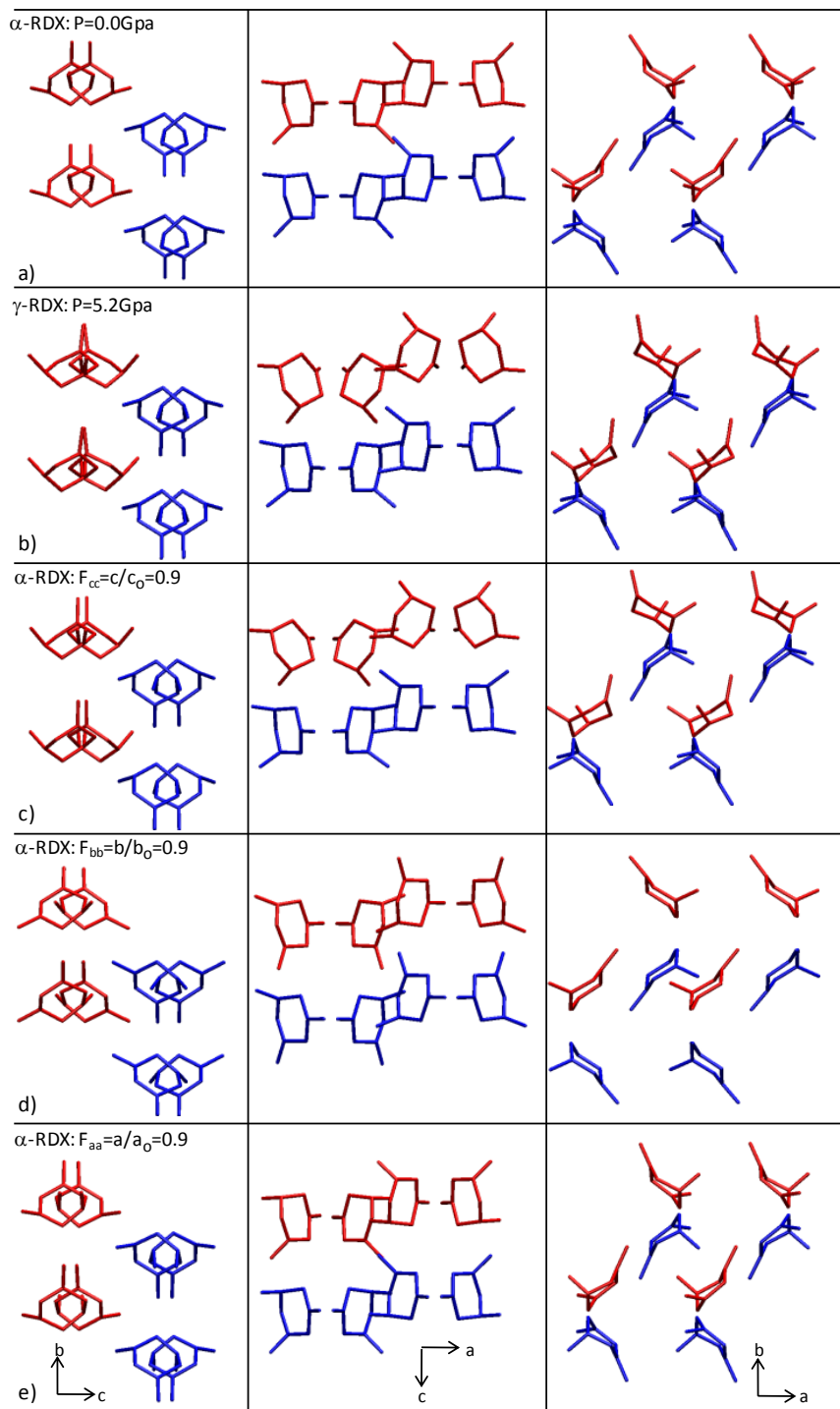
Figure 3.28: Wire frame molecule projections of each unit cell. a) αRDX at P=0GPa. b) γRDX at P=5.2GPa c) αRDX for F_{cc}=0.9 resulting in γRDX. d) αRDX for F_{bb}=0.9 resulting phase change. E) αRDX for F_{aa}=0.9. Molecules that are red are *AAI* in γRDX. Molecules that remain *AAE* are indicated in blue.

Figure 3.28 shows the entire collection of strained and pressurized unit cells projected onto each crystal axis. The αRDX unit cell is shown in Figure 3.28a and matches the structure shown for F_{aa}=0.9 in Figure 3.28. The γRDX unit cell is shown in Figure 3.28b and matches the structure for F_{cc}=0.9 in Figure 3.28c. The transition caused by F_{bb}=0.9 resulted in a phase transition that does not match the other structures presented. The *AEE* molecule conformation of the F_{bb}=0.9 structure also does not match any other known phase of RDX such as βRDX (26) or εRDX (30), which have molecules in the *AAA* conformation.

The change in enthalpy, ΔH, as a function of volumetric Lagrange Strain, E_V from equation (3.1) is presented in Figure 3.29. The enthalpy gives a measure of the system potenial energy plus the work put into the system due to the deformation. For a crystalline material at room temperature, the Gibb's energy is approximately equal to the enthalpy. It is difficult to determine the energetically favored crystal structure from ΔH since the state of deformation between simulations is very different. However, the simulations resulting in γRDX are the lowest energy structures as function of E_V. The potential energy change presented in Figure 3.29a is an order of magnitude smaller than the enthalpy rise meaning the largest contribution to increasing enthalpy is *PV* work. The abrupt change in ΔH for the *NST* simulation is due to the abrupt volume change shown in Figure 3.17 and the abrupt change in ΔH for *NVT* **b**-compression is due to an abrupt change in stresses, shown in Figure 3.24b.
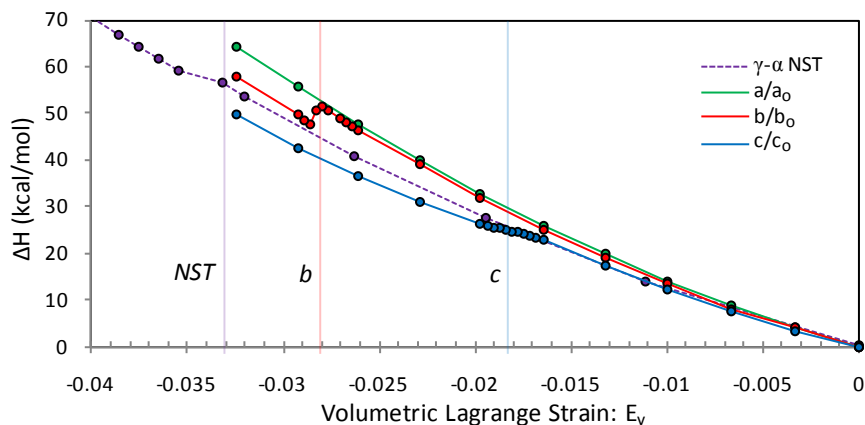
Figure 3.29: Change in enthalpy for each compression direction and γRDX *NST* depressurization. Zero mean strain signifies the αRDX reference configuration at ambient conditions.

The effect of uniaxial compression on the molecule conformation and packing are reflected by changes in the individual components of the SB potential given by equation (2.1). These energy changes are presented in Figure 3.30. The largest differences in loading direction are shown in the angle and dihedral energies in Figure 3.30c and d. Compression of the **b**-axis deforms the molecules in a way that causes the dihedral and angle energy to move in the opposite direction of the other simulations. Loading the molecules this way resulted in a phase change with an *AEE* molecule conformation shown in Figure 3.26. Compression of the **c**-axis increases the loading rate of the dihedral and angle bonds, which may have helped trigger the γRDX phase change.
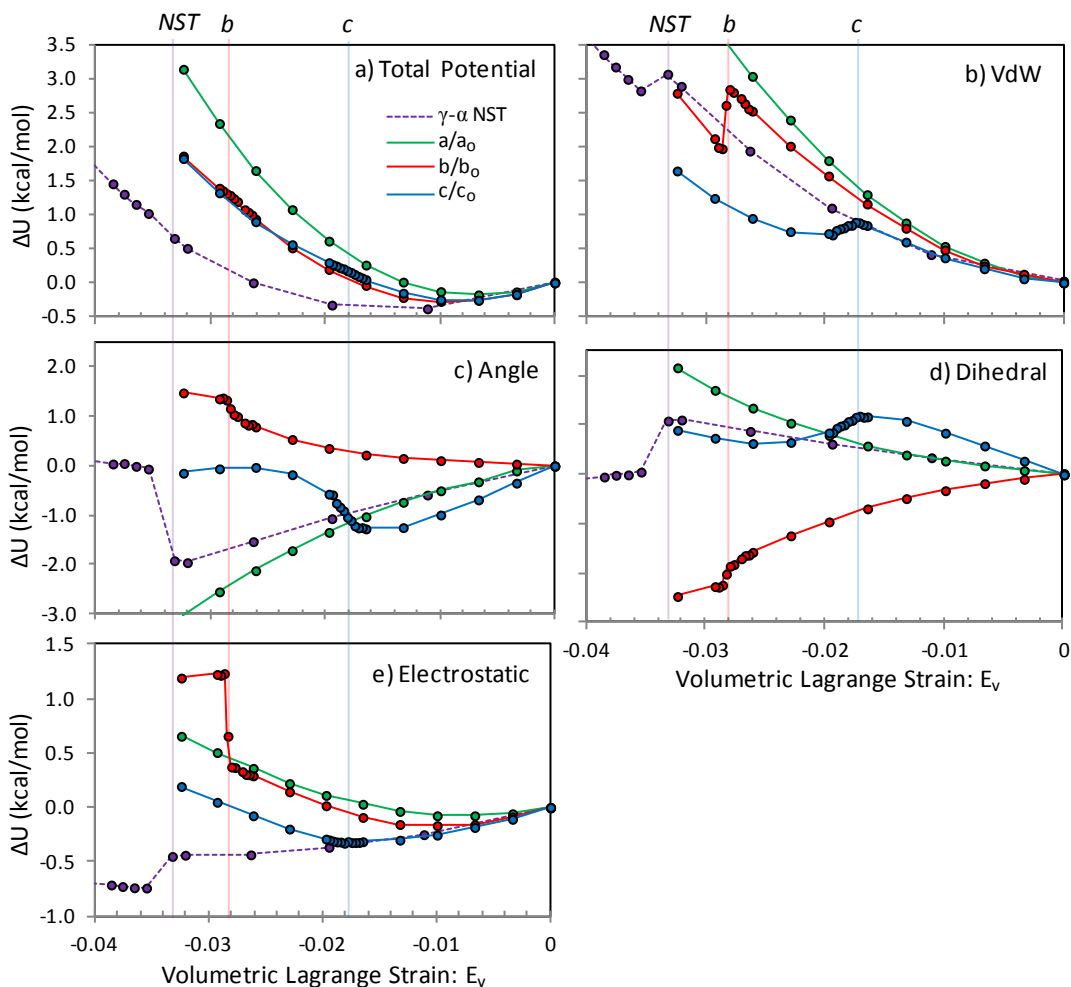
Figure 3.30: Change in (a) total potential energy, (b) van der Waals energy, (c) angle energy, (d) dihedral energy, and (e) electrostatic energy for each compression direction and γRDX *NST* depressurization. Zero mean strain signifies the αRDX reference configuration at ambient conditions.

Simulations of solid-solid phase transitions of the energetic molecular crystal hexahydro-1,3,5-trinitro-s-triazine (RDX) using the SB potential through a series of uniaxial strain thermalizations were shown to depend on crystal orientation. We showed that while uniaxial deformation leads to the α to γRDX transition, hydrostatic compression alone does not. However, hydrostatic depressurization from the γRDX phase reveals that the SB potential is capable of supporting the γRDX structure at high pressure and yields the γ to αRDX transition near 2.1 GPa.

Imposed uniaxial deformation of αRDX showed that the ability of the crystal to undergo phase transitions depends on the crystal axis being loaded. Compressive deformation along the **c**-axis reproduced the γRDX configuration for σ_c=-1.5GPa. Compression along the **b**-axis did not result in the γRDX structure but instead led to a structure similar to that identified in simulations by Cawkwell et al. (38) and Ramos et al. (56) as a stacking fault. Deforming along the different crystal axes had markedly different effects on the bonded SB potential terms where loading on the **b**-axis decreased the dihedral energy but it was increased for loading along the **c**-axis. The transitions were also shown to be more sensitive to the crystal orientation as opposed to the magnitude of the largest principal or shear stress.

3.2.3 Temperature Dependent αRDX Properties

Materials deform when subject to changes in temperature. For nitramine crystals and other materials held together mainly by van der Waals forces, this deformation is caused by the anharmonic shape of the interaction energy between the molecules. The equilibrium spacing of molecules relative to one another for a harmonic material will not change as the temperature is raised and the thermal expansion will be zero, as is the case for temperatures near absolute zero where the potential energy surface is approximately harmonic. As the temperature or kinetic energy is raised, the molecular spacing reaches points on the potential energy curve that are anharmonic and the equilibrium spacing between molecules changes. Van der Waals forces between molecules are anisotropic and dependent on the orientation of molecules, resulting in anisotropic thermal expansion. The relation between temperature change and thermal expansion is given in

general by the Coefficients of Thermal Expansion (CTE). Accurately predicting the CTE validates the functional forms of the van der Waals potential energy.

In this work, the CTE is found by calculating the thermal strains between molecular dynamics simulations at different temperatures at the same pressure. The strains, **E**, are calculated from equation (3.9) where the lattice vectors at the reference temperature are [**h**$_o$] and the deformed lattice vectors at the new temperature are [**h**]. The αRDX lattice is orthorhombic and remains orthorhombic during thermal expansion. This results in **E** being diagonal and given by

$$\begin{Bmatrix} E_a \\ E_b \\ E_c \end{Bmatrix} = \frac{1}{2} \begin{Bmatrix} (a/a_o)^2 - 1 \\ (b/b_o)^2 - 1 \\ (c/c_o)^2 - 1 \end{Bmatrix} \tag{3.14}$$

Like the bulk modulus presented in Section 3.2.1, the CTE, $\beta(T_o)$, is also a thermodynamic material property that relates two thermodynamic states, volume or strain, **E**, and temperature, and is given by (76)

$$\boldsymbol{\beta}(T_o) = \left(\frac{\partial \mathbf{E}(T_o)}{\partial T} \right)_\sigma \tag{3.15}$$

The relationship between strain and temperature is assumed to be linear for the range temperatures in this study and equation (3.15) can be solved by

$$\mathbf{E}(T_o + \Delta T) = \boldsymbol{\beta}(T_o)\Delta T \tag{3.16}$$

The CTE, $\beta(T_o)$, are found by dividing the thermal strain by $\Delta T = T - T_o$.

Molecular dynamics simulations are used to obtain the thermalized αRDX configurations at each temperature. The molecular dynamic simulations were done using the DL-POLY program (50). As before, the simulation cell is made up of 2×3×3 αRDX unit cells (144 molecules, 3024 atoms) with atomic positions given by Choi and Prince

(25). Parallelepiped periodic boundary conditions are used allowing for nonorthogonal lattice vectors of different lengths. An *NST* ensemble is used with temperature and pressure coupling time constants equal to 1.0 ps, along with the SB flexible molecule potential given in equation (2.1) (17). The real space cut-off for nonbonded potential parameters is 10Å and the Ewald sum relative error precision is set to 0.3e-6. The integration timestep is 1.0 fs.

After each temperature increment the system is warmed up for 20 ps using temperature scaling every 5 steps. After warm up the simulation is equilibrated for 80 ps where the temperature and pressure are controlled by the *NST* ensembles and all data presented below is collected from this portion of the simulation. All simulations are run at *P*=0GPa with the temperature held constant during the equilibration portion of the simulation. The temperature is incremented from 250 to 350 K.

Average lattice vector lengths as a function of simulation temperature are shown in Figure 3.31. This figure shows the lattice length to behave almost linearly with temperature for the temperature range of 250K to 350K. The largest crystal dimension along the **a**-direction increases by 0.04Å while the **b**- and **c**-dimensions increase by almost 0.08Å.
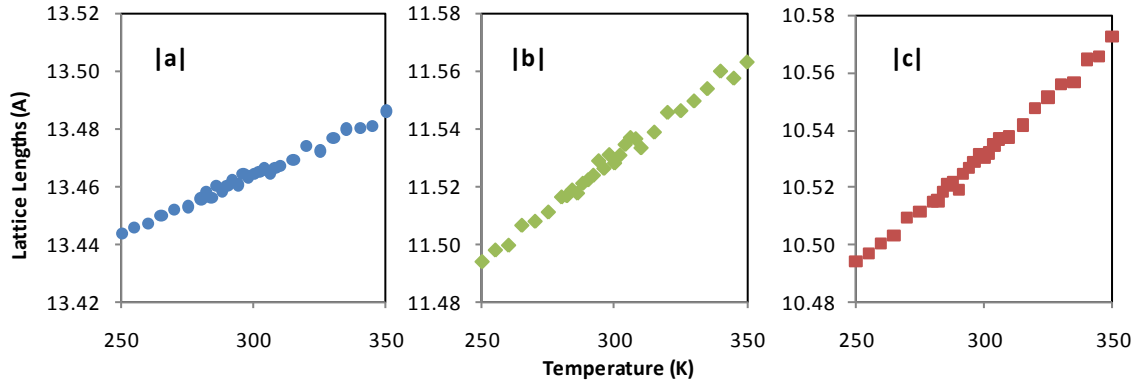
Figure 3.31: Lattice vector lengths as a function of temperature from MD simulations in this work.

The thermalized average lattice vectors are used in equations (3.14) to find the thermal strains. All thermal strain calculations are made relative to the same reference configuration, $[\mathbf{h}_o]$, at temperature $T_o = 250K$. Orthotropic thermal strains from equation (3.14) are shown by the data points in Figure 3.32.

$e_c = 71.9\Delta T$
$R^2 = 0.9923$

$e_b = 61.6\Delta T$
$R^2 = 0.9891$

$e_a = 30.3\Delta T$
$R^2 = 0.9880$
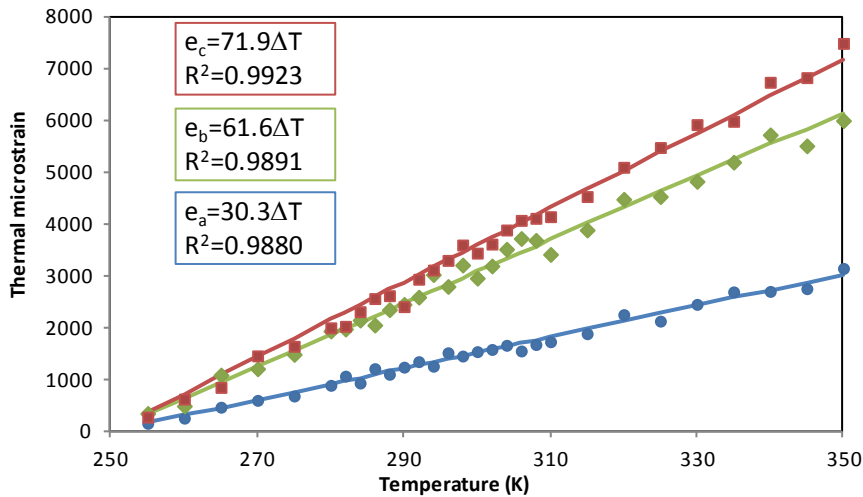
Figure 3.32: Orthotropic thermal strain data points (circles) and linear fit (line) as a function of temperature from $T_o = 250K$.

The thermal strain versus temperature data in Figure 3.32 is linear and the solid lines are linear curve fits to the data. Zero strain occurs at the reference state, $T_o = 250K$.

93

The equations for the linear curve fits are given in the boxes in the upper left of Figure 3.32 where the constant of proportionality provides the CTE.

Table 3.8 compares the CTE's calculated in this work to the CTE's from experiments and simulations conducted by others. Cady (36) experimentally measured temperature dependent CTE's along the three crystal axes and the values obtained are also listed in Table 3.8 for T = 300K. Podeszwa, Rice and Szalewicz (SAPT) (44) and Sorescu, Rice and Thompson (SRT) (39) published lattice lengths for several temperatures using their rigid molecule potentials. The SAPT and SRT lattice lengths for the temperature range T = 250 – 325K were used in equation (3.14) to find the thermal strains with the reference configuration at T_o = 250K. These were then fit to a linear equation whose slope is the CTE reported in Table 3.8.

Table 3.8: Orthotropic CTE for αRDX.

		Coefficient of Thermal Expansion (1/K)x10[-6]					
	Exptl[a]	This Work		SAPT[b]		SRT[c]	
a	26.8	30.3	(13%)	31.6	(18%)	23.9	(-11%)
b	87.1	61.6	(-29%)	36.2	(-58%)	49.5	(-43%)
c	79.7	71.9	(-10%)	41.6	(-48%)	47.8	(-40%)
V	193.4	163.8	(-15%)	109.4	(-40%)	121.2	(-37%)

[a]Cady Ref. (36), Podesczwa, Rice, Szalewicz Ref. (44), [c]Sorescu, Rice, Thompson Ref (39)

3.2.5 Temperature and Pressure Dependent Properties

Conservation of mass, momentum and energy across a shock front is described by the Hugoniot equation, given by

$$0 = e - e_o - \frac{1}{2}(P - P_o)(v - v_o) \tag{3.17}$$

where e is the Hamiltonian energy (kinetic + potential) per unit mass, P is the pressure, v is the volume per unit mass, and subscript o denotes the state of the material downstream

of the shock wave. In this work, the unshocked state is taken from the results of the *NST* simulations for α-RDX at *P*=0 and *T*=300K. Equation (3.17) is used to interpolate isobaric *NST* simulations at three temperatures and a single pressure to find the Hugoniot Temperature and Volume, T_{HG} and V_{HG} respectively. This is similar to approach used by Erpenbeck (77). These simulations provide the *PVT* points given in Table 3.9 that make up the Hugoniot curve over the pressure range 0.25GPa-6GPa shown in Figure 3.33 by triangles. Each simulation was started from the *P*=0, *T*=300K αRDX structure given by Choi and Prince (25).

The circle data points correspond to uniaxial Hugoniot simulations of αRDX using the SB potential by Bedrov et al. (58). Instead of linearly interpolating to find the Hugoniot points from three separate simulations, Bedrov et al. changed the equations of motion to always enforce the Hugoniot condition given by equation (3.17). Their data points show a phase transition for (001) compression (**c**-axis) corresponding to the α to γRDX phase transition. They also show a high pressure transition for (100) compression (**a**-axis) that corresponds to amorphization of the crystal. The close up in Figure 3.33b shows the experimental data given by Hooks et al. for oriented shock simulations. The simulation data from this work provides a softer *PV* response resulting from an isotropic instead of uniaxial state of stress.

Table 3.9: Hugoniot curve data for αRDX.

P (GPa)	T_{HG} (K)	V_{HG} (Å^3)
0.10	301.38	1622.22
0.25	302.86	1605.52
0.50	305.18	1581.54
0.75	307.33	1560.21
1.00	309.40	1541.60
1.50	313.92	1509.86
2.00	318.33	1482.53
3.00	327.64	1434.96
4.00	338.68	1401.44
5.00	350.86	1370.09
6.00	363.86	1343.96
7.00	378.47	1320.97
8.00	394.00	1300.51
9.00	410.46	1282.10
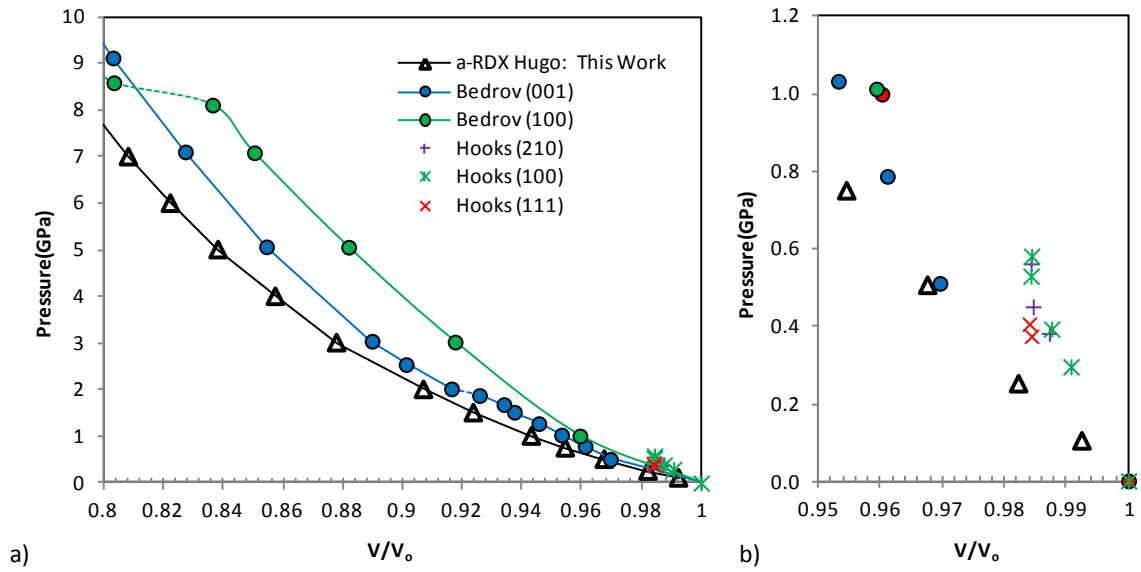
Figure 3.33: Hugoniot data from this work shown by triangles compared to result given in literature by Bedrov et al. (58) and Hooks et al. (37).

4. Interface and Surface Properties

αRDX crystals, like most other molecular crystals, show a brittle response to tensile loads. The fracture process in brittle materials was described by Griffith (89) as the energy required to extend a crack tip through the creation of two free surfaces. The competing mechanism is deformation through dislocation emission. The deformation mode with the lowest energy barrier will be energetically preferred. In this section the surface energy will be determined as the energy barrier to fracture and in Section 5 this will be compared to the energy barrier to dislocation nucleation.

Three methods for determining the surface energy and interfacial properties are presented in this section. The simplest is the attachment energy method, which is the energy released by attaching a single layer of molecules to the face of a crystal. The calculation procedure for the attachment energy provides a very simple method for determining the active interface of a crystal plane containing multiple interfaces. Multiple interfaces is a reference to a unit cell containing multiple unique interfaces with the same Miller indices (*hkl*). The second method calculates the free surface energy from a thick slab. The slab in these simulations is thick enough that the interfaces are isolated from one another providing a better estimate of the free surface energy. The final method simulates the decohesion of an interface as it is separated. This gives the same surface energy as the thick slab simulations but also provides information on the processes leading up to the creation of a free surface. All three of these methods are shown to predict the same interface for each plane. All of the simulations in this section use the LAMMPS molecular dynamics package (51) with the LAMMPS Smith and Bharadwaj (17) potential given in Appendix B.

97

4.1. Attachment Energy

The attachment energy provides a method of estimating the intermolecular bonding strength between layers of molecules (24). The attachment energy was first used in the Periodic Bond Chain (PBC) theory as the habit controlling factor in predictions of organic crystal growth (78) (79). In PBC theory the strong intermolecular forces connect the molecules together into chains. Several chains act together as a network to grow the crystal face in layers. The growth rate of the PBC network on a face is proportional to the strength of the intermolecular forces per molecule. The intermolecular bond energies can be calculated by comparing the energy per molecule of a perfect crystal (Figure 4.1a) to the energy per molecule of a single layer (Figure 4.1b). The difference in these two energies is the energy a system is reduced by when the layer is added to the bulk material. This energy difference is equal to twice the attachment energy given by

$$2E_{att} = U_{bulk} - U_{layer} \tag{4.1}$$

where U_{bulk} is the energy of the minimized bulk crystal per molecule in Figure 4.1a and U_{layer} is the energy per molecule of the layer in Figure 4.1b (80). The energy of the layer is found using a simulation cell with 3D periodic boundary conditions and a large vacuum region (100Å) separating the layers. The layer uses the atomic configuration of the minimized bulk crystal and is not further relaxed in the layer configuration. The growth layer thickness is given by d_{hkl}, the interplanar distance between adjacent planes with Miller indices (hkl) that have been corrected by the extinction conditions of the space group (81). For an orthorhombic crystal, the interplanar distance is given by (82)

$$d_{hkl} = \left(\frac{h^2}{|\mathbf{a}|^2} + \frac{k^2}{|\mathbf{b}|^2} + \frac{l^2}{|\mathbf{c}|^2} \right)^{-1/2} \tag{4.2}$$

where (**a**,**b**,**c**) are the lattice vectors. In the case of the Pbca space group, the extinction conditions of the glide planes reduce the interplanar distance of the (100), (010), and (001) planes to half a unit cell (82). Table 4.1 gives the interplanar spacings for the layers studied in this work. The fastest growing crystal faces will have the highest attachment energies. The weakest bonded layers where cleavage and slip will most likely occur have the lowest attachment energies, which will also make these the slowest growing habits.
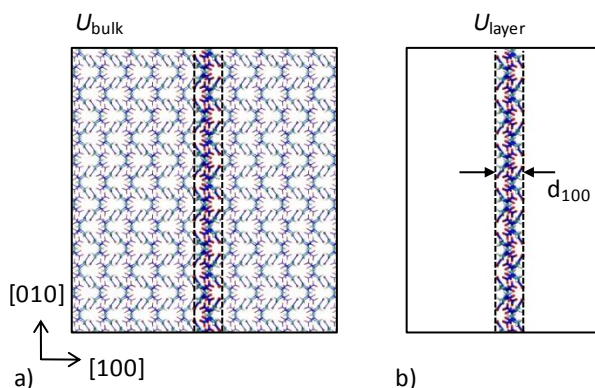
Figure 4.1: Addition of a layer to the (100) crystal face. a) Initial system containing bulk material with energy U_{bulk} and layer with energy U_{layer}. b) Attached layer to bulk lowers system energy by $2E_{att}$.

Figure 4.2a shows the αRDX lattice with spheres representing each molecule's center of mass (COM). The layers shown in Figure 4.1b and c are given by all of the COM's that fall within one interplanar spacing, d_{100}, of two (100) planes. As the planes are shifted in the [100] direction, two different layers are found, labeled b1 and b2 in Figure 4.2b and c. The b1 layer shown in Figure 4.2b contains the molecules along the face of the unit cell shown by the black box in Figure 4.2a (25). The b2 layer contains

molecules in the interior of the unit cell. The b1 and b2 layers for all of the planes are shown in Figure 4.3 thru Figure 4.7. The b1 layer is shown in blue and the b2 layer is shown in red. The attachment energy per molecule for each of the b1 and b2 layers and the interplanar spacing d_{hkl}, are given in Table 4.1.
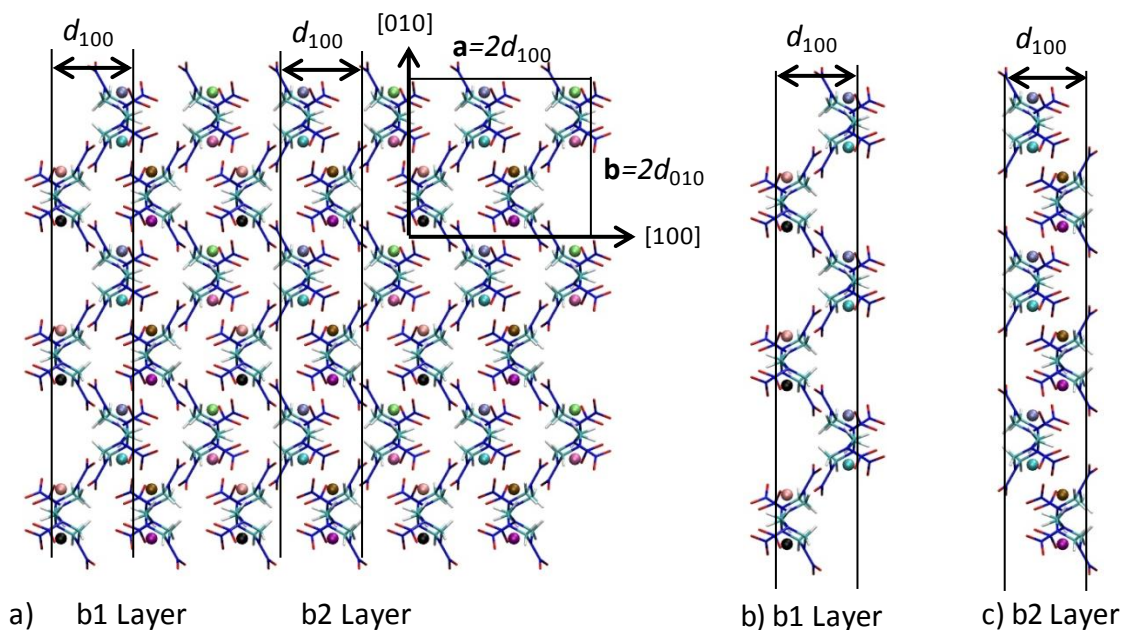
Figure 4.2: a) 3×3 αRDX molecules projected onto the (001) plane. The RDX molecule's centers of mass are represented by spheres. Planes separated by the interplanar spacing, d_{100}, shown by the black lines are used to determine the b) b1 layer and c) b2 layer.
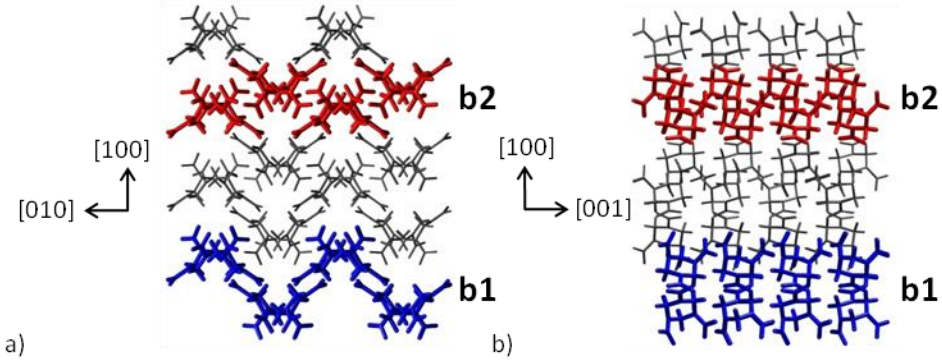
Figure 4.3: (100) attachment energy layers projected onto the a) (001) plane and b) (010) plane of a 2×2×2 αRDX supercell. Type b1 in blue is along the unit cell and b2 in red is by shifted ¼[100]. Interface between the blue and grey layers is the type b1 slip plane and the interface between red and grey layers is type b2 slip plane. Type b2 layer is lower in E_{att} given in Table 4.1.
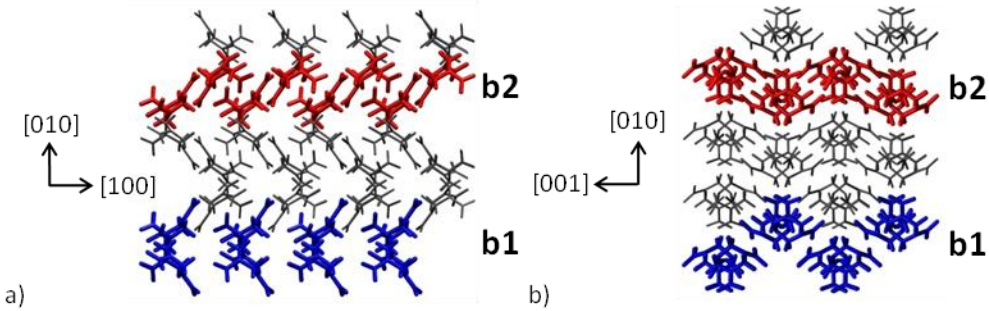
Figure 4.4: (010) attachment energy layers projected onto the a) (001) plane and b) (100) plane of a 2×2×2 αRDX supercell. Type b1 in blue is along the unit cell and b2 in red is by shifted ¼[010]. Interface between the blue and grey layers is the type b1 slip plane and the interface between red and grey layers is type b2 slip plane. Type b2 layer is lower in E_{att} given in Table 4.1.
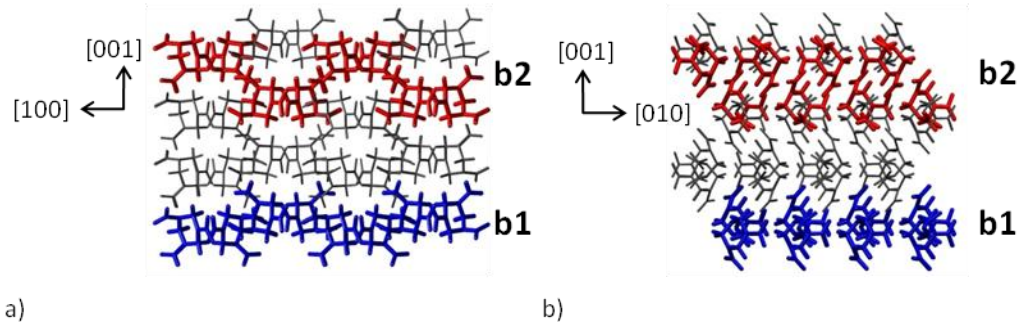
Figure 4.5: (001) attachment energy layers projected onto the a) (010) plane and b) (100) plane of a 2×2×2 αRDX unit cell. Type b1 in blue is along the unit cell and b2 in red is by shifted ¼[100]. Interface between the blue and grey layers is the type b1 slip plane and the interface between red and grey layers is type b2 slip plane. Type b1 layer is lower in E_{att} given in Table 4.1.
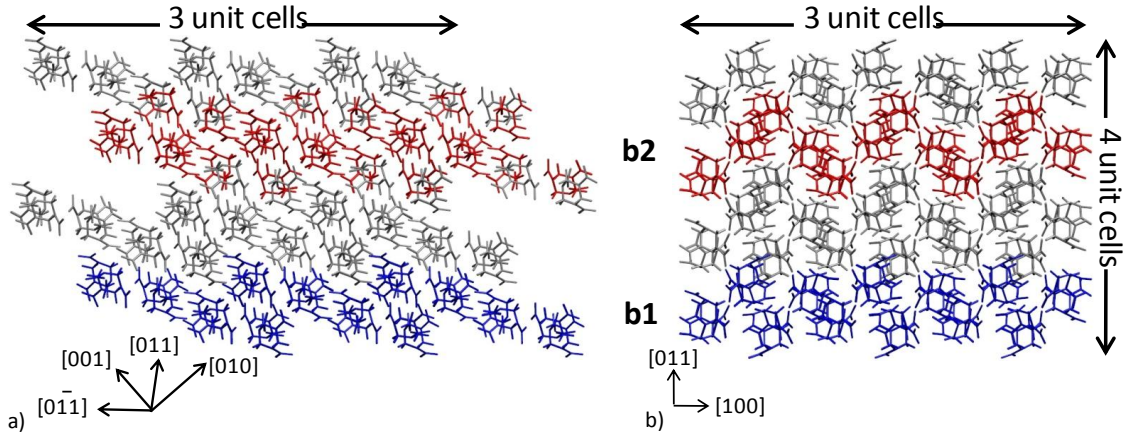
Figure 4.6: (011) attachment energy layers projected onto the a) (100) plane and b) (01̄1) plane of a 4×3×3 αRDX unit cell. Type b1 in blue is along the unit cell and b2 in red is by shifted ¼[100]. Interface between the blue and grey layers is the type b1 slip plane and the interface between red and grey layers is type b2 slip plane. Type b1 layer is lower in E_{att} given in Table 4.1.
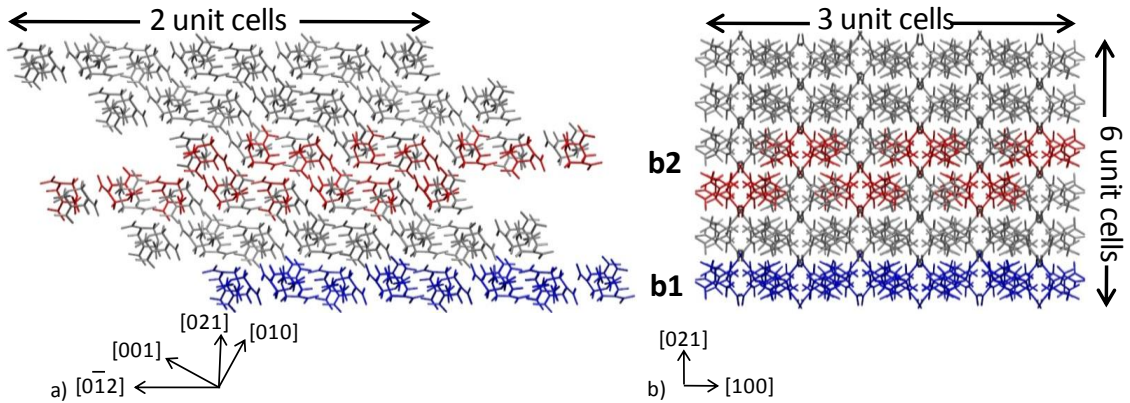
Figure 4.7: (021) attachment energy layers projected onto the a) (100) plane and b) (01̄2) plane of a 6×2×3 αRDX unit cell. Type b1 in blue is along the unit cell and b2 in red is by shifted ¼[100]. Interface between the blue and grey layers is the type b1 slip plane and the interface between red and grey layers is type b2 slip plane. Type b1 layer is lower in E_{att} given in Table 4.1.

The surface energy, γ_{att}, can be calculated from E_{att} by converting it to energy per unit area of the layer surface given by

$$2\gamma_{att} = \frac{1}{V} Z E_{att} d_{hkl} \tag{4.3}$$

where V is the volume of a unit cell layer and Z is the nuumber of molecules per unit cell layer (78). If E_{att} is approximately equal for all planes, then the surface energy is proportional to d_{hkl} and a smaller interplanar spacing results in a smaller surface energy (78). Values for $2\gamma_{att}$, V, and Z are also given in Table 4.1. Equation 4.3 only provides an approximate surface energy.

Table 4.1: Attachment energy for each layer. Lowest energy layer shown in bold letters.

Plane	d_{hkl} (Å)	Z(#)	V (Å^3)	E_{att} (kcal/mol/molc)	$2\gamma_{att}$ (mJ/m^2)
(100)	6.689	4	783.7	b1: 28.7 **b2: 24.7**	b1: 682 **b2: 585**
(010)	5.670	4	783.9	b1: 29.5 **b2: 19.2**	b1: 593 **b2: 385**
(001)	5.179	4	783.5	**b1: 24.4** b2: 25.4	**b1: 448** b2: 466
(011)	7.639	8	1566.2	**b1: 19.2** b2: 20.4	**b1: 520** b2: 554
(021)	4.971	8	1567.5	**b1: 24.1** b2: 30.4	**b1: 425** b2: 537

The layer with the lowest attachment energy, either b1 or b2, is shown in bold in Table 4.1. The lowest energy layer is the more stable layer and the layer more likely to control crystal growth (79). The lowest energy layer can also be picked out visually in Figure 4.3 thru Figure 4.7 as the layer with the higher in-plane molecular density. The attachment energy is related to the strength of bonding between layers and low attachment energy indicates a weakly bonded interface (24). These weakly bonded interfaces coincide with the experimental cleavage and slip planes in some molecular crystals (24) (5). This has been observed experimentally (24). However, the attachment energy was found to be only ~50% accurate in determining slip and cleavage planes in layered molecular crystals where the slip/cleavage planes could be determined by visual inspection (5).

From Table 4.1, E_{att} predicts the (010) and (011) to be active planes. Both planes contain experimental slip systems (6) (14) and (010) is also a cleavage plane (7). The surface energy, $2\gamma_{att}$, does not follow the same trends as E_{att} because the interplanar spacing and surfaces area are different for each plane. The surface energy predicts (010), (001), and (021) to be the active planes. The (021) plane is a slip plane (6) (14) and (001) is a cleavage plane (7). The surface energy given by the attachment energy is an approximation due to the simulation set-up. However, in Table 4.4 it is shown to compare well with other more computationally intensive methods of determining the surface energy.

The attachment energy provides a simple method to determine weakly bonded layers in a crystal. These layers provide planes where inelastic deformation is likely. The attachment energy cannot differentiate slip and cleavage planes and because of this it also cannot provide any details about the slip system. It has also been shown to be inaccurate, especially in crystals with corrugated layers like αRDX. Other computational procedures such as those that provide the generalized stacking fault energy can differentiate slip from cleavage planes, determine slip directions, and determine the slip limiting interactions. However, the generalized stacking fault calculations are computationally expensive and require more time to setup.

For the above reasons, the attachment energy is only used to determine which of the layers, either b1 or b2, to determine the generalized stacking fault energy for. The attachment energy is ideally suited for this purpose for several reasons. First, built into the calculation is the interplanar spacing corrected by the extinction conditions. This reduces the number of unique layers on the (100), (010), and (001) planes from four to

two. Of the two remaining unique layers, the layer with the lower energy is the more stable of the two layers and the active layer. As will be shown later, this method accurately determines the planes with the lowest surface energy, decohesion separation energy, and unstable stacking fault energies.

4.2 Surface Energy

The attachment energy presented in Section 4.1 was the difference in energy between the bulk crystal and a single layer of molecules. The layer had two free surfaces and was thin enough that the molecules on each surface are affected by both free surfaces. The surface energy was then calculated in equation (4.3) by assuming all of the molecules in the layer contributed equally to the surface energy. A better approximation of the surface energy is calculated here by isolating the surfaces from one another by increasing the layer thickness. The surface energy is then calculated by comparing the energy of the system containing a thick slab with two free surfaces to the energy of the bulk crystal. The energy difference is then divided by the area of the free surface, removing of assumption that all molecules contribute equally to the surface energy.

The thick slab simulation cell is created from a minimized supercell of αRDX with a vacuum layer added between the two layers within the supercell. The layers are the b1 or b2 layers presented in Section 4.1. The simulations cell is 3D periodic and adding the vacuum layer separates the bulk supercell into periodic slabs. A vacuum layer equal to 100Å is used to isolate the periodic images. This creates the simulation cell shown in Figure 4.8 where the vacuum layer has been placed between b2(100) layers in the αRDX supercell creating two b2(100) surfaces. This system has two free surfaces

and the energy difference per surface area, A, between this slab, U_{slab}, and the bulk

crystal, U_{bulk}, gives the free surface energy as

$$2\gamma_{slab}=(U_{\text{bulk}}-U_{\text{slab}})/A \tag{4.4}$$
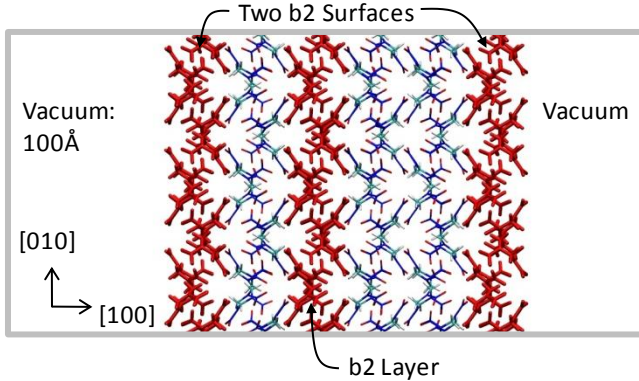
Figure 4.8: 3D periodic thick slab simulation cell used to determine the surface energy of the b2(100) surface.

We define two slab energies (U_{slab}) – one corresponding to an unrelaxed rigid slab

and the second corresponding to a rigid slab with a finite layer of flexible molecules on

the surface allowed to relax. The rigid slab energy is determined from molecular statics.

The flexible slab energy is calculated by replacing a layer of molecules d_{hkl} in thickness

on the free surfaces of the slab with flexible molecules and quenching them. The rigid

slab separating the flexible layers maintains the crystal order of the bulk and seperates the

elastic effects of the free surfaces from one another. The flexible molecules are quenched

by using molecular dynamics with a damping coefficient of 20 kcal/mole-fs. The

molecule motion is relaxed to T=~0K over 10ps. The interplanar spacing, d_{hkl}, used in

the attachment energy calculations in Section 4.1 are used here and values for d_{hkl} are

given in Table 4.2.

Rigid and flexible surface energies are presented in Table 4.2 along with the slab thickness. The rigid free surface energy compares well with the other methods of determining the attachment surface energy given in Table 4.4. The flexible layer is shown to lower the energy considerably by allowing surface reconstruction of the free surfaces. The limited thickness of the flexible layers makes the flexible free surface energy an over prediction of the actual value.

Table 4.2: Slab thickness (Å), flexible layer thickness d_{hkl} (Å) and Rigid and Flexible free surface energies (mJ/m^2). Lowest energy layer for each plane is shown in bold letters.

Plane	Slab Thickness: Unit Cells : (Å)	d_{hkl} (Å)	Rigid $2\gamma_{slab}$	Flexible $2\gamma_{slab}$
(100) b1	3 : (40.14)	6.689	684	597
(100) b2			**591**	**555**
(010) b1	3 : (33.99)	5.670	598	532
(010) b2			**384**	**367**
(001) b1	3 : (31.10)	5.179	**450**	**408**
(001) b2			494	479
(011) b1	6 : (45.84)	7.639	**509**	**465**
(011) b2			557	521
(021) b1	9 : (44.68)	4.971	**429**	**404**
(021) b2			609	559

4.3 Decohesion Separation Energy

The surface energy can also be determined by separating a large slab of material across an interface. A free surface is created when separation between the two interfaces is large enough that they no longer interact. The process of pulling material apart across the interface or decohesion provides details about the material response during failure. On a large scale, the process of separating the interface to create a free surface results in three material responses for a brittle material. For small displacements the material responds elastically as the lattice stretches to accommodate the separation. As the interfaces are further separated, microcracks or voids begin to form in the material reducing the load baring capacity of the interface. Continued separation of the interface

causes the microcracks or voids to coalesce into macrocracks with traction free interfaces at which point the material can no longer carry a tensile load. The localized effect of material softening and failure is captured by a decohesion constitutive model where the reduction in surface traction is given as a function of the interfacial displacement discontinuity (83). The initiation of decohesion occurs at a specific stress state. The stress state can be determined by a stress based decohesion criterion based on a measure of the surface traction on the failing surface. These measures take on familiar forms such as Von Mises (maximum shear stress), Rankine (maximum principal stress), Tresca or other forms fit to experimental data (83).

The decohesion plane being cleaved is described by an orthornormal coordinate system ($\mathbf{n,t,q}$), where $\mathbf{n}$ is normal to the cleavage plane and $\mathbf{q}$ and $\mathbf{t}$ lie on the cleavage plane. For these simulations the $\mathbf{qt}$ displacement of the lattice is held fixed and the lattice is separated by $\Delta_r\mathbf{n}$. The applied lattice separation results in an interfacial displacement discontinuity, $\delta\mathbf{n}$. Miller indices provide the directions of ($\mathbf{n,t,q}$) when possible. The vector given by the Miller indices [hkl] is normal to the plane (hkl) in reciprocal lattice space and is generally not normal to the (hkl) plane in real space except for cubic lattices. For an orthorhombic lattice like αRDX, the vector given by Miller indices [hkl] is only normal to the (hkl) plane in real space for the (100), (010) and (001) planes. The [0$\bar{1}$1] and [0$\bar{1}$2] vectors are skewed relative to the (011) and (021) planes, respectively.
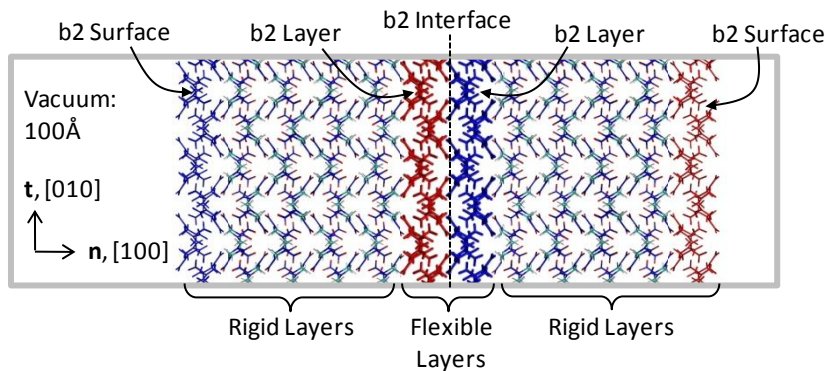
Figure 4.9: Decohesion simulation cell for the b2(100) interface shown between the red and blue b2 layers. The decohesion supercells are twice as thick as the free surface supercells used in Section 4.2.

The simulation technique used to model decohesion will be described for the b2(100) interface shown in Figure 4.9. The b2 interface is shown between the red and blue b2 layers. The decohesion simulation involves separating the single slab into two separate slabs. This requires the αRDX supercell shown in Figure 4.9 to be twice as large as the slab shown in Figure 4.8 used to determine the surface energy in Section 4.2. The simulation cell is 3D periodic and a 100Å vacuum is used to separate periodic images in the [100] or **n**-direction. The system initially contains two rigid free surfaces due to the vacuum layer and after decohesion it will contain four free surfaces.

The decohesion process for the b2(100) interface is shown in Figure 4.10. Figure 4.10 only shows the four layers surrounding the b2 interface. Decohesion is modeled by separating the supercell across the b2 interface in a series of 0.2Å increments up to 10Å. This creates a series of rigid lattice configurations separated by Δ_r. Each Δ_r configuration is restarted with a layer of flexible molecules at the b2 interface, shown by the red and blue b2 layers in Figure 4.9 and Figure 4.10. The thickness of the flexible layer, h_f, is equal to the interplanar spacing, d_{hkl}, presented in Section 4.1 in Figure 4.9 and Figure

4.10. The supercell now contains a sandwich structure of rigid layers surrounding layers of flexible molecules on the interface. The rigid layers are held fixed while the flexible molecules are quenched using molecular dynamics with a damping coefficient of 20 kcal/mole-fs. The flexible molecule motion is relaxed to $T=\sim0K$ over 10ps. This provides two different system energies – the first being the rigid U_{deco} at the start of the simulation and the other being the flexible U_{deco} of the final quenched structure. The energy of the separated system, U_{deco}, is compared to the initial energy of the intact slab, U_{slab}, to give the decohesion energy as

$$\gamma_d(\Delta_r)=(U_{deco}(\Delta_r)-U_{slab})/A \tag{4.5}$$

where A is the area of the decohesion surface and γ_d and U_{deco} are given as a function of the rigid lattice separation distance, Δ_r (84). In Figure 4.10b, small Δ_r results in an elastic response where the flexible layer of molecules across the interface recombine and the interface closes, $\delta=0$. In Figure 4.10d, $\Delta_r=10\text{Å}$ and the interface is completely separated and two free surfaces are created. The energy of the two free surfaces given by $\gamma_d(10\text{Å})$ is given in Table 4.3 for the rigid and flexible simulations. The decohesion surface energies are in good agreement with the other methods presented in Table 4.4. They all identify the same b1 or b2 layer for each plane.
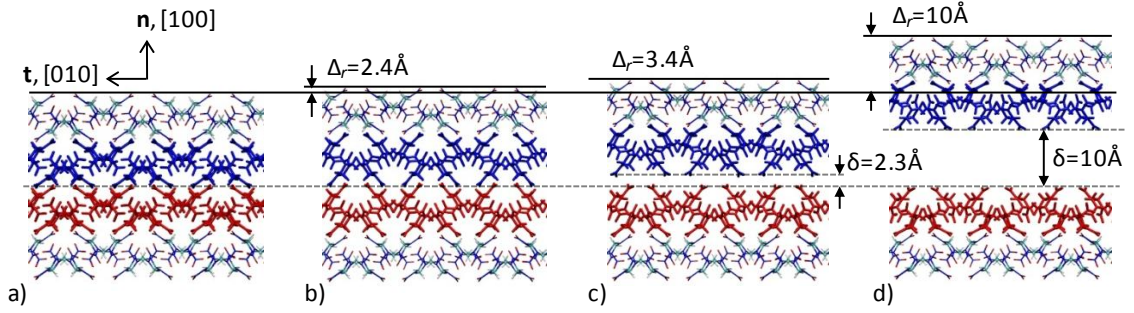
Figure 4.10: Decohesion of the b2(100) interface. A) Reference configuration where the red and blue b2 layers shown in blue and red are flexible molecules. b) Separation of the rigid lattices by $\Delta_r=2.4$Å, the point where the maximum stress is reached and decohesion begins. C) Material failure where $\Delta_r=3.4$Å and the interfacial opening $\delta=2.3$Å. d) Creation of two free surfaces for $\Delta_r=\delta=10$Å.

Table 4.3: Decohesion simulation parameters and results. Decohesion slab thickness (Å), flexible layer thickness $h_f=d_{hkl}$ (Å) and Rigid and Flexible free surface energies (mJ/m^2). Lowest energy layer for each plane shown in bold letters.

Slip Plane	Slab Thickness: Unit Cells : (Å)	$h_f=d_{hkl}$ (Å)	Rigid $2\gamma_d$	Flexible $2\gamma_d$
(100) b1	6 : (80.28)	6.689	690	602
(100) b2			**589**	**536**
(010) b1	6 : (67.98)	5.670	605	512
(010) b2			**391**	**364**
(001) b1	6 : (62.20)	5.179	**458**	**402**
(001) b2			526	501
(011) b1	12 : (91.68)	7.639	**505**	**463**
(011) b2			541	506
(021) b1	18 : (89.36)	4.971	**428**	**404**
(021) b2			607	559

Table 4.4: Free surface energy in mJ/m^2 calculated from the attachment energy, slab free surface energy, and decohesion free surface energy. Lowest energy layer for each plane shown in bold letters.

Slip Plane	Rigid Lattice			Flexible layer	
	$2\gamma_{att}$	$2\gamma_{slab}$	γ_d	$2\gamma_{slab}$	γ_d
(100) b1	682	684	690	597	602
(100) b2	**585**	**591**	**589**	**555**	**536**
(010) b1	593	598	605	532	512
(010) b2	**385**	**384**	**391**	**367**	**364**
(001) b1	**448**	**450**	**458**	**408**	**402**
(001) b2	466	494	526	479	501
(011) b1	**520**	**509**	**505**	**465**	**463**
(011) b2	554	557	541	521	506
(021) b1	**425**	**429**	**428**	**404**	**404**
(021) b2	537	609	607	559	559

Two flexible layer thicknesses were used in the decohesion simulations, $h_f = d_{hkl}$ and $h_f = 2d_{hkl}$. The flexible decohesion energies given by Equation (4.5) for both h_f's are plotted in Figure 4.11a as a function of Δ_r. The free surface energy labeled to the right of Figure 4.11a is nearly the same for both h_f. The $h_f = 2d_{hkl}$ model allows a thicker layer of flexible molecules to relax through surface reconstruction and elastic relaxation. However, the increased mobility for $h_f = 2d_{hkl}$ only slightly lowers the free surface energy.

The largest difference between h_f's in Figure 4.11a occurs for $\Delta_r = 0$ to 4Å where the interfaces are still interacting. In this region, the flexible molecule layers are being deformed in response to the separation, Δ_r. In this region, the flexible layers are strained and $\Delta_r \neq \delta$. This is shown in Figure 4.9b where interface has not separated, $\delta = 0$ and Figure 4.9c where surfaces have separated but are still interacting. The interatomic forces resulting from the deformation can be averaged over the volume of the flexible layers to give the virial stress tensor given by (85),

$$\sigma_{ij} = -\frac{1}{V_{flex}} \sum_k^N r_i^k f_j^k \tag{4.6}$$

where N is the number of atoms in the flexible layers, r_i^k is the i position of atom k, f_j^k is the total force in the j direction on atom k due to its interactions with all of the atoms in the entire system and V_{flex} is the volume of the region containing flexible molecules. The volume, V_{flex}, does not include the interfacial separation, δ, but does include the change in the flexible layer thickness due to elastic strain. The shear components of the stress tensor are nearly zero, $\sigma_{i \neq j} \approx 0$. This makes the surface traction, $\boldsymbol{\tau} = \sigma_{ii}\mathbf{n}$, equal to the normal stress, $\tau_n = \sigma_{nn}$. The surface traction calculated from the virial stress is shown in Figure 4.11b for both h_f.
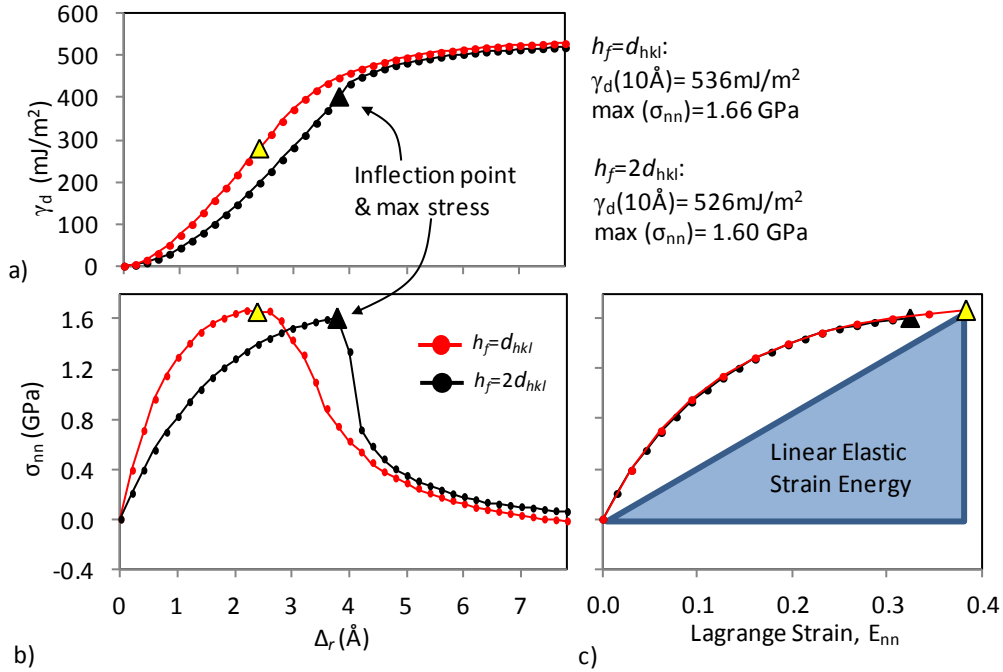
Figure 4.11: Surface energy and surface traction for the b2(100) layer for $h_f=d_{hkl}$ (red line) and $h_f=2d_{hkl}$ (black line). a) Change in decohesion energy, γ_d, versus Δ_r. where legend gives surface energy, $\gamma_d(10\text{Å})$, for each surface. b) Surface traction versus Δ_r. c) Surface traction plotted versus Lagrange strain, E_{nn}, up to the maximum stress. The shaded region is the linear elastic strain energy for the stress/strain state of the yellow triangle. Legend gives the surface energy and maximum normal traction.

In Figure 4.11a, the $\gamma_d(\Delta_r)$ curve changes from concave up to concave down at the point marked by the triangles corresponding to the maximum surface traction in Figure 4.11b. The concave up portion of the curve is the elastic portion where the interface closes and increasing deformation leads to an increase in surface traction. At the critical point, the maximum traction is reached and the surface traction begins decreasing with increased separation, Δ_r. The critical point is where decohesion initiates and the interface starts to separate, $\delta>0$. The critical point atomic configuration for the b2(100) interface is shown in Figure 4.10b. For large interfacial separations, the surface energy converges to a constant value equal to the energy for two free surfaces and the surface traction goes to zero.

In Figure 4.11a and b, $h_f=2d_{hkl}$ is able to respond elastically for larger Δ_r. Both h_f's result in almost the same maximum interfacial traction, $\max(\sigma_{nn}) \approx 1.6\text{GPa}$. Figure 4.11c shows the surface traction versus the Lagrange strain, E_{nn}, up to the point of decohesion. All of the strain in Figure 4.11c is elastic and decohesion has not initiated, $\delta=0$. The elastic strain at the point of decohesion is greater than 30% and for this reason the Lagrange finite strain measure is used instead of the infinitesimal strain.
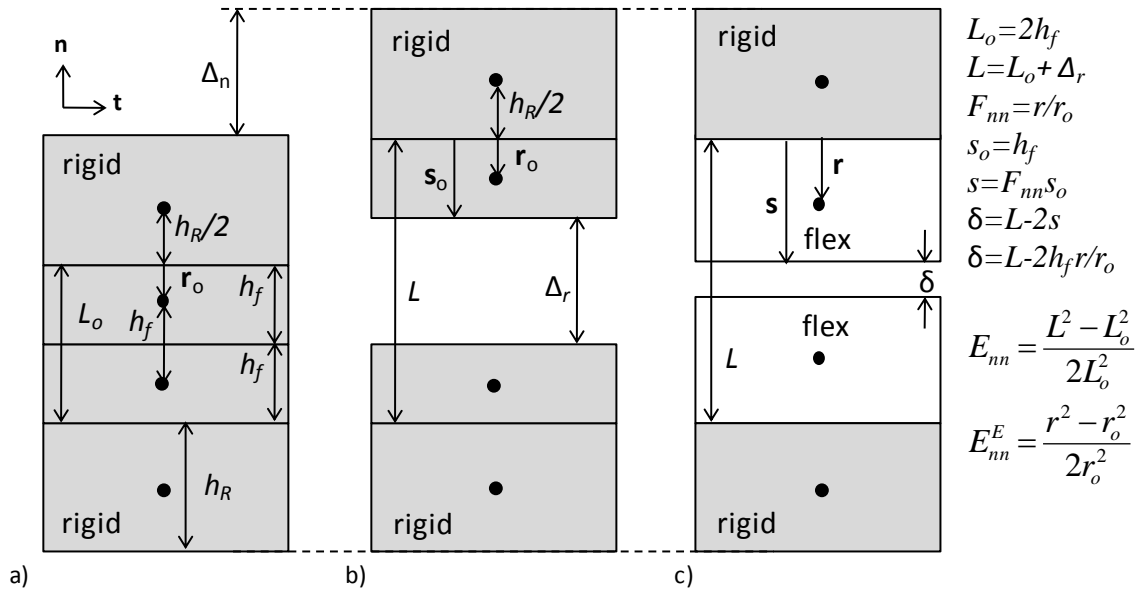
Figure 4.12: a) Initial decohesion supercell containing several rigid layers. The central rigid layers each of thickness h_f will be converted to flexible molecules. The layers sandwiching these of thickness h_R will remain rigid. The center of mass (COM) for each layer is shown by a black dot. b) Rigid decohesion configuration where halves have been separated by Δ_r. The total strain across the central layers is calculated from L. c) The central layers of thickness h_f are replaced with flexible molecules that relax and allow the interface to close to δ. The total strain remains unchanged but the strain in the flexible layers is calculated from the COMs of the rigid and flexible layer, $\mathbf{r}$. The flexible layer strain is then used to calculate δ.

The process for calculating the Lagrange strains and interfacial displacement, δ, from the center of mass location for each layer of thickness, d_{hkl}, is outlined in Figure 4.12. The reference configuration is shown in Figure 4.12a. The layers that will be

converted to flexible molecules have thickness h_f and the thickness of the central region containing two layers sandwiching the interface is $L_o=2h_f$. Their COM is located by r_o from the interface between the rigid and flexible layers. The rigid layer has thickness h_R and because it remains rigid through all of the simulations it does not change. In Figure 4.12b, the interface has been separated by Δ_r and the total thickness of the central region containing the two layers sandwiching the interface and the opening is given by $L=L_o+\Delta_r$. All of the other values remain the same. The total Lagrange strain plotted in Figure 4.11c for this configuration is given by

$$E_{nn} = \frac{L^2 - L_o^2}{2L_o^2} \tag{4.7}$$

The flexible decohesion configuration is shown in Figure 4.12c where the layers thickness h_f are replaced with flexible molecules and relax. The rigid lattices continue to be separated by Δ_r and the central region thickness is still L. The location of the flexible layer COM moves to r and is known. The interface moves from $\mathbf{s}_o=h_f\mathbf{n}$ to $\mathbf{s}$ and is unknown. The deformation gradient of the elastic layer is calculated from the rigid COM at r_o and the flexible COM at r and is given by

$$\mathbf{F} = \begin{bmatrix} 1 & 0 & 0 \\ 0 & 1 & 0 \\ 0 & 0 & r/r_o \end{bmatrix} \tag{4.8}$$

The deformation gradient is used to map the $\mathbf{n}$-components of the vector $\mathbf{s}_o$ to $\mathbf{s}$ giving

$$s=h_f r/r_o \tag{4.9}$$

The interfacial opening is then given by

$$\delta=L-2s=L-2h_f\, r/r_o \tag{4.10}$$

The normal tractions are plotted versus interfacial opening, δ, in Figure 4.13. The surface traction increases nearly vertically up to the maximum stress marked by the triangles where decohesion occurs and δ>0. During decohesion the surface tractions are decreased to zero as δ becomes large. The elastic response for $h_f=d_{hkl}$ shows δ<0, which means *s* in equation (4.9) is being over predicted. The elastic deformation is over predicted because it is not constant through the thickness of the flexible layers. The side of the flexible layer interfacing with the rigid lattice responds differently than the side interfacing with the decohesion interface. This difference in deformation of the flexible molecules is apparent in Figure 4.10b-c. The deformation gradient in equation (4.8) uses the COM location relative to the rigid interface, which builds in the assumption that all of the material responds in the same way as flexible/rigid interface material. A similar problem is encountered for $h_f=2d_{hkl}$ only now the elastic response predicts δ>0 prior to decohesion.
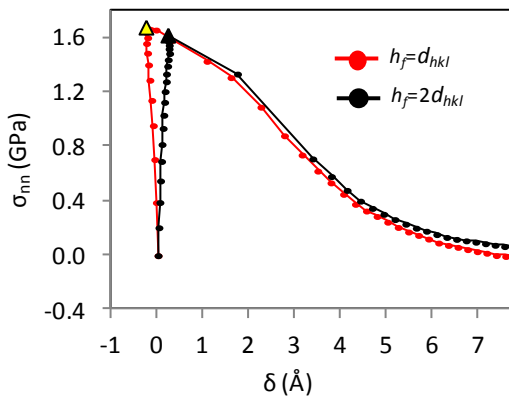
Figure 4.13: The b2(100) surface traction plotted versus interfacial opening, δ, for the two layer thicknesses, $h_f=d_{hkl}$ in red and $h_f=2d_{hkl}$ in black.

The Lagrange strain of the elastic layer using the deformatation gradient from equation (4.8) is given by

$$\mathbf{E}^E = \tfrac{1}{2}[\mathbf{F}^T\mathbf{F} - \mathbf{I}]$$

$$E_{nn}^E = \frac{r^2 - r_o^2}{2r_o^2} \qquad (4.11)$$

where only the normal component of the strain, $E^E{}_{nn}$, is nonzero. The elastic energy stored in the flexible layers due $E^E{}_{nn}$ is equal to the area under stress/strain curve in Figure 4.11c. This can be approximated by assuming a linear stress/strain relationship giving the elastic strain energy as

$$U_{elast} = \frac{1}{2} E_{ij}^E \sigma_{ij} = \frac{1}{2} E_{nn}^E \sigma_{nn} \qquad (4.12)$$

where σ_{nn} is given by the virial stress from equation (4.6). The filled in triangle in Figure 4.11c represents the linear elastic energy for the maximum stress/strain point indicated by the yellow triangle. It is clear that for large deformations the stress/strain relationship is nonlinear and that a linear elastic energy is going to under predict the actual elastic energy in the material. A more appropriate relationship would be a hypoelastic stress/strain relationship (75). A hypoelastic model could be developed by assuming a functional form for the strain energy density that matches the decohesion energy shown in Figure 4.11a up to the inflection point (marked by a triangle). Then the stress/strain relationship would be given by the derivative of the strain energy density with respect to the strain component. However, most hypoelastic models describe a nonlinear relationship resulting from large shear components of the strain tensor.

The deformation in this work is driven by uniaxial strain that is forced to take place between a few layers of molecules. This provides insight on the deformation processes taking place on the interface but does not physically describe the actual deformation process. Therefore, the nonlinear hypoelastic stress/strain relationship

developed from this data would probably not be applicable to any physical type of loading. For these reasons a simple linear elastic model is used here with the understanding that it may under predict the full elastic stress/strain behavior but still provide an estimate on the partition of energy between elastic and decohesion.

The linear elastic strain energy is shown in blue in Figure 4.14 for both layer thicknesses and the total energy, γ_d, is plotted in red. The elastic energy per unit area of decohesion area is found by multiplying U_{elast} by the thickness of the deformed flexible layers, $2s$, given in equation (4.9). The data shown in blue is the difference between γ_d and $2sU_{elast}$ and is the energy associated with the separating interface given by

$$U_{sep} = \gamma_d - 2sU_{elast} \tag{4.13}$$

Initially the energy increases elastically with $U_{sep} \approx 0$ up to the maximum stress where decohesion occurs. During decohesion $U_{sep} > 0$ and U_{elast} decreases to zero. The separation energy starts increasing prior to decohesion, $\delta \approx 0$, due to the elastic energy being under predicted. Using $h_f = d_{hkl}$ in Figure 4.14a provides more data points for the decohesion portion of the simulation. The decrease in surface traction with respect to interfacial displacement is given by the slope of U_{sep} or fitting a functional form directly to the data in Figure 4.13.
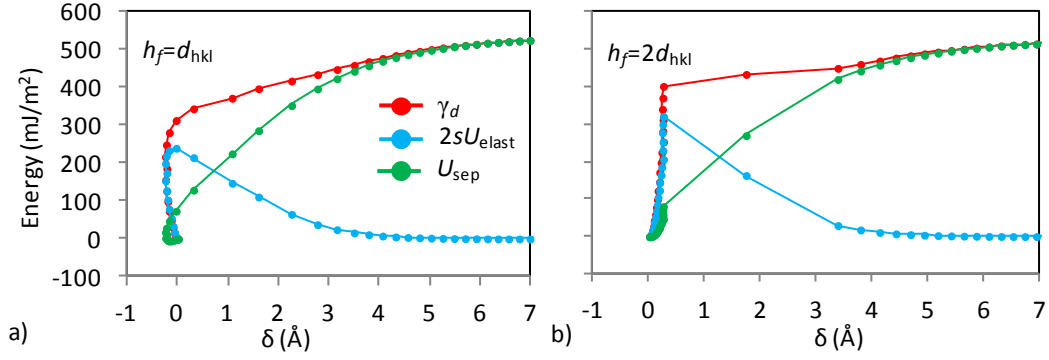
Figure 4.14: Decohesion energy (γ_d), elastic energy ($2sU_{elast}$), and separation energy, (E_{sep}) versus δ for a) $h_f=d_{hkl}$ and b) $h_f=2d_{hkl}$.

The decohesion energy curves for each plane and each interface, b1 and b2, are given in Figure 4.15 and Figure 4.16. The flexible layer thickness, h_f, was shown to not significantly affect the elastic stress/strain response, decohesion energy or final free surface energy for the b2(100) interface. Using $h_f=d_{hkl}$ provided more data points for the decohesion process and will be used for the remaining decohesion simulations. The interface with the lower surface energy when $\Delta_r=10$Å is shown in red and the high energy surface in gray. The low energy in red is the likely active plane for cleavage. The virial stresses given by equation (4.6) for the low energy interface are shown in the bottom plots in Figure 4.15 and Figure 4.16. The normal traction is given by the green line and labeled by σ_{nn}. The other volumetric components of the stress tensor shown in purple and blue are due to Poisson's effect that results from uniaxial strain.
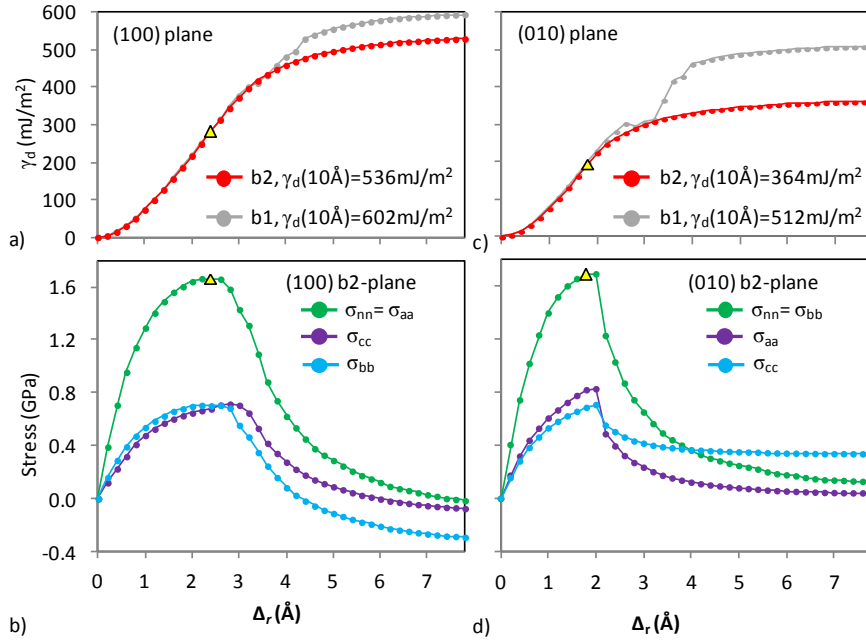
Figure 4.15: Decohesion simulation results for the (100) and and (010) planes. (a) & (c) Change in decohesion energy, γ_d, versus Δ_r for the b1 and b2 planes. (b) & (d) Virial stresses of the b2-interfaces. The yellow triangle indicates the maximum stress near the inflection point on the energy curve.
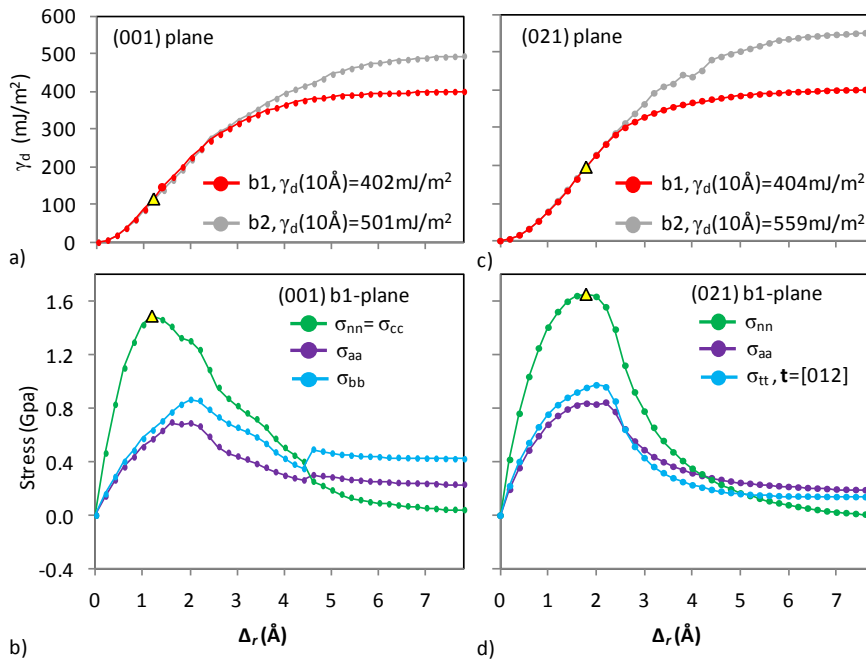
Figure 4.16: Decohesion simulation results for the (001) and (021) planes. (a) & (c) Change in decohesion energy, γ_d, versus Δ_r for the b1 and b2 planes. (b) & (d) Virial stresses of the b1-interfaces. The yellow triangle indicates the maximum stress near the inflection point on the energy curve.

The b1 and b2 interfaces in the energy plots in Figure 4.15 and Figure 4.16 all show a similar elastic response up to the inflection point, Δ_{crit}. Values for Δ_{crit}, the surface traction at Δ_{crit}, and strain at Δ_{crit} are tabulated for all of the planes in Table 4.5. During decohesion, $\Delta_r > \Delta_{crit}$, the interfaces respond differently. In Section 4.1, the interfaces, either b1 or b2, with the lower attachment and surface energies were those with the least amount of molecule overlap across the interface between layers, shown in Figure 4.3 thru Figure 4.7. During decohesion the interfaces are separated and large amounts of molecule overlap across the interface will lead to a large interactions. These interactions usually increase the energy of the decohesion process. Highly overlapping interfaces also create free surfaces where a large portion of the molecules are exposed. This is far from the preferred bonding structure of the bulk crystal resulting in a higher surface energy.

Table 4.5: Decohesion initiation conditions. Critical separation (Δ_{crit}), critical strain from equation (4.7), and maximum surface traction (σ_{nn}).

Decohesion Plane	Δ_{crit} (Å)	E_{nn} (Δ_{crit})	max σ_{nn} (GPa)
b2 (100)	2.4	0.20	1.66
b2 (010)	1.8	0.17	1.69
b1 (001)	1.2	0.12	1.49
b1 (011)	2.4	0.17	1.59
b1 (021)	1.8	0.20	1.66

Decohesion of the (011) plane shown in Figure 4.17 occurs differently than those shown in Figure 4.15 and Figure 4.16. In Figure 4.17a, elastic loading ($\Delta_r < \Delta_{crit}$) of the b2 interface (gray) leads to a slower increase in decohesion energy, γ_d, than the b1 interface (red). The normal surface traction, σ_{nn}, is approximately equal to the slope of the decohesion energy in Figure 4.17a. The slope of the b2 interface energy is smaller than the b1 interface. This makes the normal traction at the point of decohesion, Δ_{crit}, lower

on the b2 interface. The surface tractions of the b1 (red) and b2 (gray) interfaces are shown in Figure 4.17c and at $\Delta_r=\Delta_{crit}$ the b2 surface traction is lower. However, the final decohesion energy in Figure 4.17a for the b1 interface is lower and the energetically favorable free surface.

In Figure 4.6b, the b1(011) interface is shown by the blue/grey molecule interface. The blue and grey molecules are locked together by their nitro groups and the initial elastic stretching is opposed by dihedral and angle bonds of the interlocked nitro groups. For complete cleavage of the b1 interface, the conformation of the nitro groups must change to allow the molecules to move past one another resulting in a conformation change of the molecule. The b2 interface shown between the red and grey molecules in Figure 4.6b is only held together by nonbonded interactions. Once the interfaces begin decohesion ($\Delta_r>\Delta_{crit}$) the b1 interface becomes lower in energy than the b2 interface and results in a lower free surface energy.

The decohesion simulations are constrained to force the interfaces to separate normal to the cleavage plane. This forced the molecule conformation change of the b1 interface. However, a lower energy separation path exists if the interface is allowed to shift in-plane as it is separated, shown by the green line in Figure 4.17c. For this new deformation path, the surface traction of the b1 interface increases at the same rate as the b2 interface and undergoes decohesion at a much lower surface traction.

The reduction in surface traction versus interfacial separation is shown in Figure 4.18 for each of the low energy interfaces. All of the surfaces show a similar reduction in surface traction with interfacial opening, δ. Decohesion is also initiated at similar levels of maximum surface traction, $\sigma_{nn}\approx1.5$-1.7GPa, given in Table 4.5.
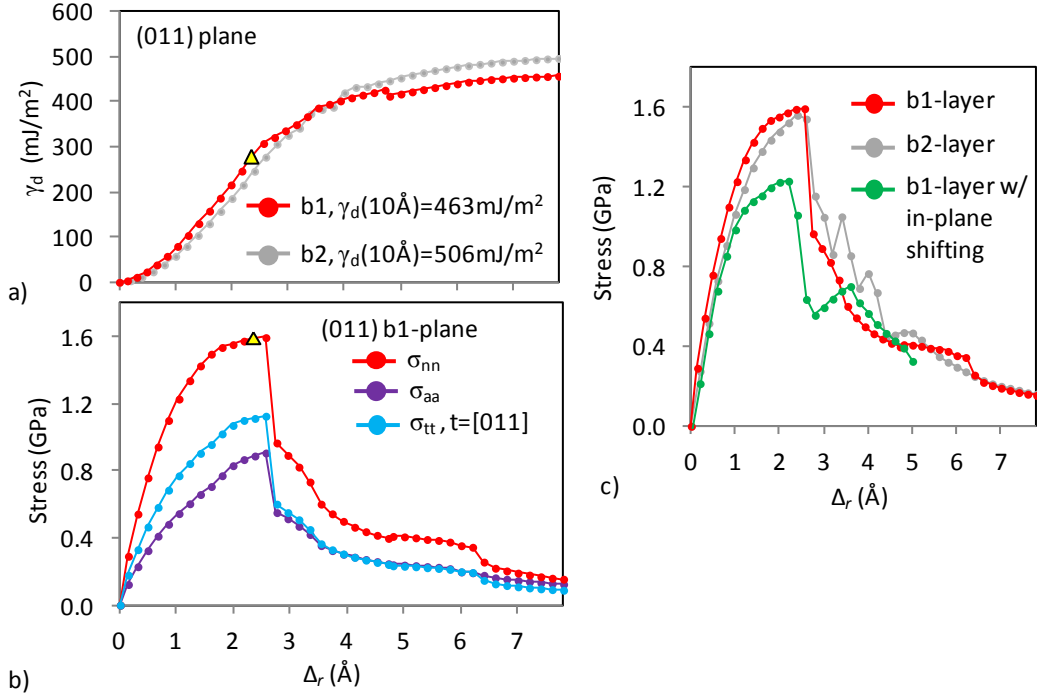
Figure 4.17: Decohesion simulation results for the (011) plane. a) Change in decohesion energy, γ_d, versus Δ_r for the b1 and b2 planes. b) Virial stress of the b1-interface. The yellow triangle indicates the maximum stress near the inflection point on the energy curve. c) Comparison of the normal stresses for the b1 interface (red), b2 interface (gray) and the b1 interface with in-plane shifting of the interfaces as they are separated (green).
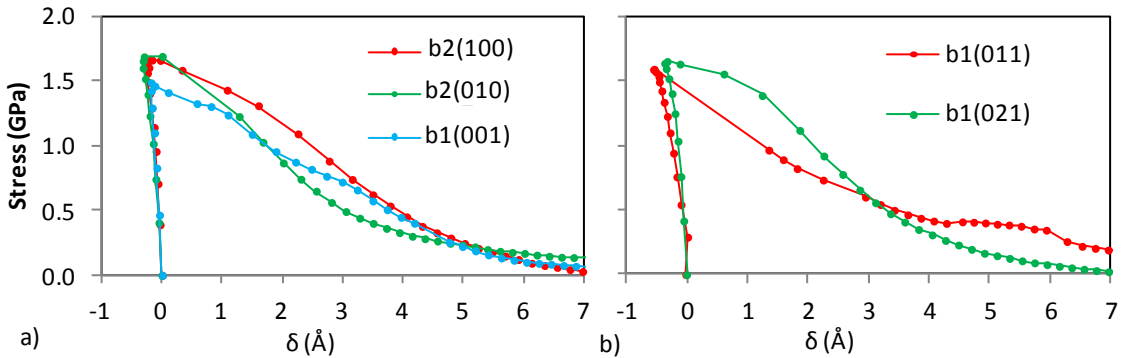
Figure 4.18: Normal surface traction, $\tau_n = \sigma_{nn}$, versus δ for the low energy interface for the a) (100), (010), (001) planes and b) (011) and (021) planes.

The first extension data point in the stress/strain curves in Figure 4.15 thru Figure 4.17 is used to determine the volumetric linear elastic constants presented in Table 4.6. The calculation procedure follows that used in Section 3 for the uniaxial strain simulations. A single stress/strain point fit through the origin has not statistical

significance but after the first extension increment the strain has already reached $\sim 2\%$, which is right at the linear elastic limit. Using 3 or 4 extension increments will under predict the linear elastic constant. The stress tensor given here does not have minor symmetry because the off diagonal terms, C_{iijj} and C_{jjii}, are determined from separate simulation and are not equal $e.g.$ C_{aabb} is from decohesion in the **a**-direction and C_{bbaa} is from decohesion in the **b**-direction. The elastic constants are presented for both the b1 and b2 slip planes. The actual elastic constants would be some combination of extension of both the b1 and b2 interfaces. The elastic constants use the orthonormal unit basis $\mathbf{e}_1=\mathbf{a}/|\mathbf{a}|$, $\mathbf{e}_2=\mathbf{b}/|\mathbf{b}|$, and $\mathbf{e}_3=\mathbf{c}/|\mathbf{c}|$ where **a**, **b**, and **c** are the unit cell lattice vectors. In Voigt index notation, 11=1=**a**, 22=2=**b**, 33=3=**c**, 23=4=**bc**, 31=5=**ca**, and 12=6=**ab**. This notation is only applicable here because αRDX lattice vectors are orthogonal.

The elastic constants from the decohesion simulations compare well with those presented in Section 3 for the uniaxial compression simulations done at T=300K (86) and experimental data (87). The elastic constants for the lower energy interface, either b1 or b2, are shown in bold and are all slightly larger than the high energy interface. This is surprising since a stiffer material would result in a larger surface traction for the same amount of extension, Δ_r. However, the stress/strain relationship is very nonlinear near Δ_{crit} and not related to the initial linear elastic coefficient.

Table 4.6: Volumetric elastic constants, C_{iijj}, in GPa for the b1 and b2 interfaces from this work compared to other simulations and experiment. Bold data indicates the elastic constants from the preferred b1 or b2 cleavage interface.

	$C_{11}=$ C_{aaaa}	$C_{22}=$ C_{bbbb}	$C_{33}=$ C_{cccc}	$C_{23}=$ C_{bbcc}	$C_{32}=$ C_{ccbb}	$C_{31}=$ C_{ccaa}	$C_{13}=$ C_{aacc}	$C_{12}=$ C_{aabb}	$C_{21}=$ C_{bbaa}
b1 layer	25.2	19.8	**24.1**	6.6	**8.3**	**7.4**	10.5	6.7	9.9
b2 layer	**26.1**	**23.0**	23.8	**8.8**	7.0	6.4	**10.7**	**8.0**	**9.9**
300K Sim[a]	25.0	23.8	23.4	8.8		7.6		10.6	
Experiment[b]	25.6	21.3	19.0	6.4		5.7		8.7	

[a]Munday (86) [b]Sun (87)

The SB potential energy from equation (2.1) is partitioned into the separate energy components and shown in Figure 4.19 for the b2(100), b2(010) and b1(001) interfaces. For all of the planes, the initial elastic separation results in a reduction of the nonbonded VDW energy shown by the green lines. The van der Waals energy reaches a minimum value near Δ_r=0.5Å. These initial deformation steps result in an increase in the electrostatic energy shown in purple. This response of the nonbonded energies indicates that the αRDX crystal is strongly bound together by electrostatic attraction and in the minimized bulk crystal the atoms are packed so closely together that they become exponentially repelled from one another according to the SB potential.

The vertical line labeled Δ_{crit} is the inflection point of the total energy in Figure 4.15 thru Figure 4.17. The material responds elastically for $\Delta_r<\Delta_{crit}$ and by decohesion when $\Delta_r>\Delta_{crit}$. Initially the molecules are intertwined to some extent across the decohesion interface as shown in Figure 4.10a. At the onset of decohesion, the interface becomes cleared of intertwined molecules as shown in Figure 4.10b. The b2(010) interface between the red and grey molecules in Figure 4.4 separates elastically with the change in dihedral and angle energies remaining near zero. Separation of the b1(001) interface shown in Figure 4.5 (blue/grey interface) results in the Axial nitro group across the interface to be pulled toward its equatorial position during elastic stretching. This

results in a large change in the dihedral and angle energy. Straining of bulk αRDX crystals in the [001] direction was shown by Mathew and Picu (72) to result in a conformation change from *AAE* to *AEE* of 15% of the molecules. They found the defects to be spatially correlated over 4 nearest neighbor molecule sites in MD simulations using the SB potential at room temperature.

At the onset of decohesion the interface is cleared of intertwined molecules and any change in conformational energies is due to the relaxation of the molecules as they become exposed to a free surface. The large amount of energy imparted to changing the molecule conformation for [001] elastic loading is undone during decohesion as the molecules relax. The changes in conformational energies for the other interfaces during decohesion is much smaller. Most of the interactions holding the interfaces together during decohesion come from the nonbonded energy components. If the electrostatic energy continues increasing, this indicates the surfaces are strongly held together by the oriented electrostatic interactions, as is the case for the (100) interface. A flat electrostatic energy during decohesion indicates an interface held together by van der Waals energy, as is the case for the (010) and (001) plane. The jumps in electrostatic energy for the (001) plane are caused by the conformation change of the molecule.
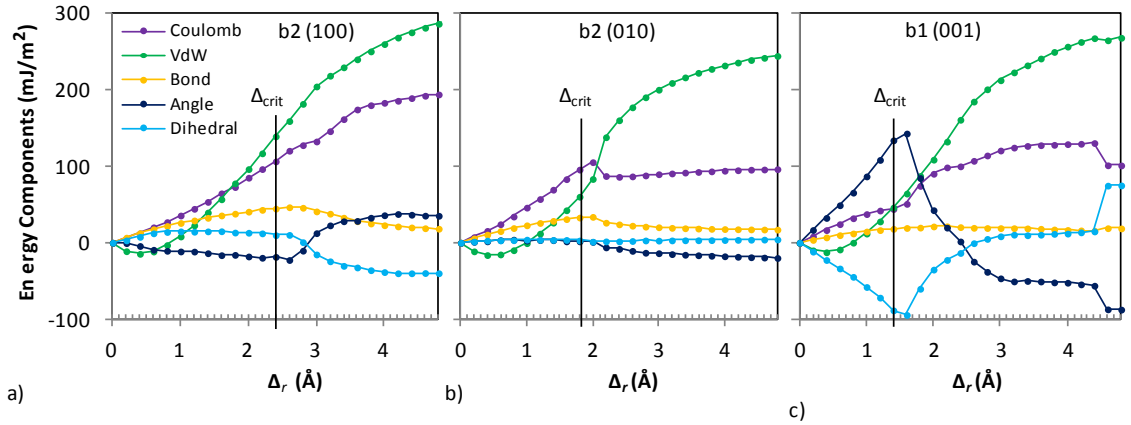
Figure 4.19: Change in energy components of the SB potential (see legend) versus Δ_r for the labeled interface and plane shown on the plot. Vertical black line corresponds to Δ_{crit}.

The simulations and analysis presented in this section provide an initial attempt at studying the decohesion process of several crystal planes in αRDX. The simulations were shown to reproduce the free surface energy and elastic constants. The maximum surface tractions at the onset of decohesion were given in Table 4.5. The reduction in surface traction during decohesion was presented in Figure 4.18. These simulations provide the decohesion response due to a tensile uniaxial strain load and would be suitable for use in a Rankine or maximum principal stress decohesion criterion. Other simulations involving shear and biaxial compression would be needed to develop a decohesion criterion suitable to modeling the failure process under a general state of deformation.

5. Generalized Stacking Faults

A "generalized" stacking fault (GSF) is created by slicing a perfect crystal lattice across a plane, displacing the two halves relative to one another by the stacking fault vector $\mathbf{f}$ and reconnecting the halves (16). The reconnected lattice has a surplus energy per unit area, $\Psi(\mathbf{f})$, due to the lattice disregistry, where $\mathbf{f}$ spans the area of a unit cell on the slip plane interface. The stacking fault is "generalized" because $\mathbf{f}$ points to a "general" location anywhere on the face of the unit cell. The GSF energy surface is a collection of all $\Psi(\mathbf{f})$ for $\mathbf{f}$ spanning the unit cell surface. A stacking fault created this way is independent of its deformation history. It is important to note that the process of offsetting the lattice by $\mathbf{f}$ to create a stacking fault is not a dynamical process where the molecules are sequentially sheared over one another. The stacking fault structures and their energy do not describe an actual deformation event; instead they provide parameters for a model of the actual deformation event.

Plasticity in metals occurs through the emission of dislocations. Several dislocation properties are determined from the GSF energy surface for metallic and atomic crystals. The unstable stacking fault energy, γ_{usf}, which are saddle points on the GSF energy surface, provide the energy barriers to dislocation motion. Local minima on the GSF energy surface provide the location and energy, γ_{sf}, of stable stacking faults. Full dislocations can dissociate into a partial dislocation at a stable stacking fault. A low ratio of γ_{sf}/γ_{usf} indicates a large energy barrier to the mobility of partial dislocations (88). The unstable stacking fault energy, γ_{usf}, and free surface energies, γ_s, calculated in Section 4 can be used to evaluate the brittle versus ductile response of slip planes. A

plane is expected to be brittle when the barrier to emit a dislocation, γ_{usf}, is larger than the energy required to create two free surface through Griffith cleavage, $2\gamma_s$ (18) (89). Otherwise it is energetically favorable to emit a dislocation. The gradient of the GSF energy surface gives the restoring stress in the Peirls Nabarro dislocation model, the dislocation core width and dislocation density (90).

Large deformations in molecular crystals may result in solid-solid phase transitions (Section 3), fracture and decohesion (Section 4) and slip deformation, the topic of the current section. Activation of slip systems is generally the preferred deformation mechanism in molecular crystals because the long range order of the crystal and its associated properties are maintained. The availability of several slip systems allows the molecular crystal to accommodate a general state of strain without fracturing. Slip, as opposed to cleavage or the formation of an amorphous phase, increases the tabletability of pharmaceutical molecular crystals (4) (8). Crystal engineering methods such as cocrystallization have been developed to exploit this mechanism by increasing the amount of slip in pharmaceutical crystals such as caffeine and paracetamol (8) (9).

In energetic molecular crystals such as αRDX (10) and PETN (11), initiation mechanisms are believed to be sensitive to shock loads that lead to shear deformations that cannot be easily accommodated by slip. A possible mechanism is blockage of certain slip systems by the large molecules on slip planes causing plane-on-plane slip motion to be hindered by steric interactions (11). The steric hindrance initiation model, in particular, presumes that when a large shear stress is directed along a sterically hindered plane, the crystal is unable to accommodate the strain through slip and therefore results in severe intramolecular deformations and bond rupture leading to initiation (11)

(12). Other proposed initiation-related events involving slip mechanisms include blocked dislocation motion leading to the pile-up and avalanche of dislocations accompanying a localized increase in temperature (13). The induction time to decomposition in αRDX has also been correlated to the alignment of known slip planes to the direction of shock load (10).

The actual mode of slip deformation is unknown in molecular crystals. Investigations through nanoindentation have indicated slip traces and pile-up features that suggest inelastic deformation mechanisms that are more complicated but build upon the ideas of dislocation motion on a single slip system (14) (91). Thus, a more thorough understanding of slip systems is needed and molecular simulations may provide an enabling capability. To this end, the generalized stacking fault concept, which has been successful in determining slip properties in atomic crystals, will be used to study slip motion in the molecular crystal αRDX.

The complexity of the molecular crystal structure – due to having several entire molecules instead of atoms at each lattice site – will require a significant modification to the normal procedures used to evaluate the GSF energy. In metallic crystals like copper, the slip plane is smooth and the atomic potential is does not include long ranged electrostatic interactions. The energy of a stacking fault in copper can be minimized by allowing the atoms to relax normal to the slip plane which does not affect the lattice disregistry. This procedure will not work for a molecular crystal. First, the slip plane is not smooth because the molecules overlap across the slip plane. The rough surface requires the slip plane to separate in order to produce a stacking fault. Secondly, the SB potential (17) given in equation (2.1) involves long range electrostatic interactions

requiring a 3D periodic simulation. Finally, relaxation of the stacking fault will involve molecule conformation and orientation changes requiring in-plane atomic motion.

In this work the GSF energy surfaces are determined for αRDX. Among the planes considered are experimentally observed slip and cleavage planes. Rigid stacking faults are produced by first specifying a stacking fault vector, **f,** and then allowing the two rigid halves to separate by Δ_r normal to the slip plane to relax the stacking fault under zero pressure. A flexible stacking fault is created from the rigid stacking fault by replacing the region surrounding the slip plane with flexible molecules. The flexible molecules and the separation of the rigid lattices are then relaxed. The atomic displacements of the flexible molecules are used to determine the shear strain and the interfacial displacement discontinuity at the stacking fault interface. This approach enables the GSF energy to be partitioned into two contributions. The first is the elastic energy due to shearing of the lattice containing flexible molecules. The second is due to lattice disregistry and molecule conformation changes providing an interfacial GSF energy.

Details of the simulation procedures for determining the GSF energy using the rigid and flexible forms of the stacking faults are presented in Section 5.1. The preprocessing steps and simulation cells for each slip system in αRDX are presented in Section 5.2. Simulation results are presented in Section 5.3 and are used to differentiate slip systems from cleavage planes using Rice's dislocation nucleation criterion (18). Validation of the GSF energy calculations are given in Section 5.4.

5.1 Generalized Stacking Fault Calculation

In the stacking fault descriptions that follow, the stacking fault is described by two measures of deformation. The first measure describes the rigid lattice deformation described by the stacking fault vector, $\mathbf{f}$, and any increase in the lattice length normal to the slip plane, Δ. The second measure describes the interfacial displacement discontinuity on the slip plane described by interfacial discontinuity vector, $\mathbf{u}$, and the interfacial opening, δ. The deformation measures are described by an orthonormal coordinate system $(\mathbf{n},\mathbf{q},\mathbf{t})$, where $\mathbf{n}$ is normal to the slip plane and $\mathbf{q}$ and $\mathbf{t}$ lie in the slip plane. The rigid lattice deformation vector is then given by $\Delta\mathbf{n}+f_q\mathbf{q}+f_t\mathbf{t}$ and the interfacial displacement is $\delta\mathbf{n}+u_q\mathbf{q}+u_t\mathbf{t}$.

The steps used to create the rigid and flexible stacking faults in αRDX are shown in Figure 5.1. Figure 5.1 shows a two unit cell thick slice of the actual 12 unit cell thick simulation cell (See Table 5.1). The first step shown in Figure 5.1a is the selection of the slip plane, either b1 or b2, based on the attachment or free surface energies given in Section 4. For the (010) plane shown in Figure 5.1a, the b2 surface has a lower surface energy in Table 4.4 and is used to create the corrugated slip plane interface separating the top (red) and bottom (blue) halves of the lattice.
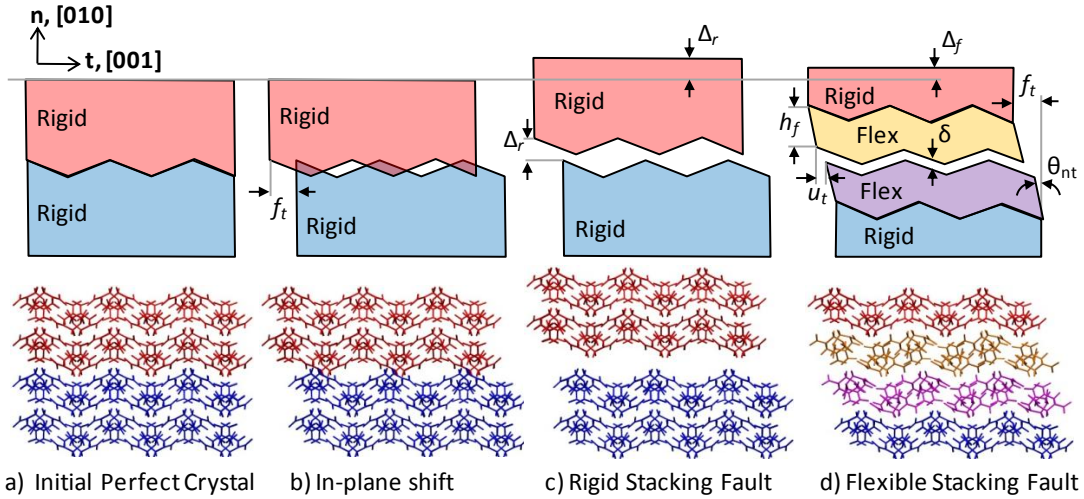
Figure 5.1: Process of creating an αRDX stacking fault. a) Initial perfect lattice of the (010) b2 stacking fault structure with the αRDX atomic lattice shown on the bottom and an outline shown on top. The red material is above the slip plane and the blue material is below the slip plane. This picture represents only a two unit cell thick slice of the actual 12 unit cell thick supercell. b) The red material is shifted by f_t relative to the blue material. c) The rigid stacking fault structure is created by shifting the red material by Δ_r to reduce the energy caused by the overlapping material across the interface. d) The flexible stacking fault structure is created by replacing a layer of molecules h_f thick above and below the slip plane with flexible molecules, shown in orange and purple. The flexible layers shear out of plane by θ_{nt}, the interfacial discontinuity changes to $\boldsymbol{u}=u_t\boldsymbol{t}+u_q\boldsymbol{q}$ and the interface closes to δ_n.

Figure 5.1b shows the creation of the stacking fault by shifting the two halves by the stacking fault vector, $\mathbf{f}=f_q\mathbf{q}+f_t\mathbf{t}$. This shift causes some of the molecules across the corrugated interface to overlap and experience unnaturally large repulsive forces between the two halves. To reduce the repulsive forces, the top and bottom halves of the lattice are treated as two separate rigid bodies and the top half is allowed to move in the **n**-direction with the bottom-half held fixed. This creates the fault structure shown in Figure 5.1c where the interface has opened by Δ_r and the lattice has increased in length by Δ_r. The surplus energy due to the lattice disregistry created by $\mathbf{f}$ is given by the stacking fault energy as

$$\Psi(\mathbf{f})=(U(\mathbf{f})-U(\mathbf{0}))/A \tag{5.1}$$

where U is the potential energy determined from the SB potential and A is the cross sectional area of the slip plane (16). There is no limit on Δ_r and the slip planes may in fact come apart creating two free surfaces. In that limit, $\Psi(\mathbf{f}) = 2\gamma_s$.

The energy of a rigid stacking fault can be greatly reduced by allowing molecule conformation and orientation changes. These molecule degrees of freedom can be manually adjusted to known conformers and configurations as was done by Ramdas et al. (92) to lower the stacking fault energy of anthracene. For more complex systems, molecular dynamics can be used to equilibrate and relax the molecules on the stacking fault using thermal energy as was done by Cawkwell et al. (38) for αRDX. This approach sandwiched a layer of flexible molecules between two fixed lattices. The fixed rigid lattices maintain the stacking fault vector, $\mathbf{f}$, between the rigid lattices, while the flexible layers shear, reducing the lattice disregistry across the interface. The fixed rigid layers also do not open to allow the large molecules to move over one another. This leads to large confinement tractions on the interface.

Like Cawkwell et al. (38) we create flexible stacking faults by sandwiching a flexible molecule layer between two rigid lattices as shown in Figure 5.1d. However, we allow the stacking fault interface to open in two ways. First, we create the flexible stacking fault from the rigid stacking fault structure that already contained interfacial separation. Second, the rigid lattice sandwiching the flexible molecules is allowed to move normal to the slip plane during quenching of the flexible layers. This reduces the normal tractions on the slip plane interface and removes their effect on the flexible stacking fault structure.

The flexible stacking fault is created from the rigid stacking fault by replacing a layer of rigid molecules of thickness h_f above and below the slip plane with flexible molecules, shown by the layers of orange and purple molecules. In Figure 5.1d, h_f is equal to half a unit cell, $|\mathbf{b}|/2$. The flexible stacking fault is relaxed using damped molecular dynamics of the flexible molecule layers in conjunction with damped rigid body dynamics of the top rigid lattice. The relaxed flexible molecules cause the lattice to shear changing the interfacial displacement discontinuity from $\mathbf{f}$ to $\mathbf{u}=u_q\mathbf{q}+u_t\mathbf{t}$ and the interfacial opening from Δ_r to δ. The stacking fault vector, $\mathbf{f}$, of the rigid lattices remains unchanged for the rigid and flexible stacking faults.

Using this approach, the surplus energy of the rigid stacking fault is used to drive the relaxation of the flexible molecules instead of thermal energy as was used by Cawkwell et al (38). Equation (5.1) is used to give the energy of the rigid lattice stacking fault, $\Psi_R(\mathbf{f})$, and the GSF energy of the system containing flexible molecules, $\Psi_F(\mathbf{f})$. The flexible stacking fault energy, $\Psi_F(\mathbf{f})$, includes atomic relaxation in the plane of the stacking fault resulting in energy due to elastic shear and lattice mismatch. The shear also causes the interface to shift resulting in $\mathbf{f}\neq\mathbf{u}$. To account for this we use the interfacial stacking fault energy defined by

$$\Phi(\mathbf{u})=\Psi_F(\mathbf{f})-2h_fE(\mathbf{f}) \tag{5.2}$$

where $E(\mathbf{f})$ is the elastic strain energy density due to the elastic shearing of the flexible layers. The interfacial stacking fault energy, $\Phi(\mathbf{u})$, is the energy associated with the displacement discontinuity across the slip plane, $\mathbf{u}$, and the molecule conformation and orientation changes. This energy is related to the interfacial traction by $\boldsymbol{\tau}(\mathbf{u})=\nabla\Phi(\mathbf{u})$ (18).

For a linear stress/strain relationship, the strain energy density, $E(\mathbf{f})$, is

$$E(\mathbf{f})=\frac{1}{2}\sigma_{ij}e_{ij} \tag{5.3}$$

where σ_{ij} is the virial stress tensor and e_{ij} is the strain tensor. The virial stress tensor is given by the virial theorem at zero temperature (85)

$$\sigma_{ij} = -\frac{1}{V_{flex}}\sum_{k}^{N} r_i^k f_j^k \tag{5.4}$$

where N is the number of atoms in the flexible layers, r_i^k is the i coordinate of atom k, f_j^k is the total force in the j direction on atom k due to its interactions with all of the atoms in the entire system and V_{flex} is volume of the region containing flexible molecules. The volume, V_{flex}, is assumed to remain constant during the flexible molecule relaxation. This assumption is valid if only shear strains occur in the flexible layers and the shear strain does not cause a change in volume.

The strain is calculated from the change in atomic displacements between the rigid and flexible models. The strain is calculated for the top and bottom flexible layers separately and does not include the interfacial displacement discontinuity, $\mathbf{u}$ and δ. The strain components $e_{tt}=e_{qq}=e_{qt}=0$ due to the simulation cell being fixed in the $\mathbf{qt}$-plane. With the $\mathbf{qt}$-displacement components held fixed, the deformation gradient, F, can be found from the change in the location of the flexible layer COMs relative to the rigid lattice. The deformation gradient can then be used to map any vector from the rigid stacking fault where all of the atomic positions are known to the flexible stacking fault structure where only the layer COMs are known.

The layer COM positions are shown in Figure 5.2. The COMs of the rigid layers are indicated by the black filled circles at the positions $\mathbf{r}^{Rtop}$ and $\mathbf{r}^{Rbot}$ and are always

located by $h_R/2$ from the rigid/flexible layer interface. The COMs of the flexible layers are shown by the hollow circles at $\mathbf{r}^{Ftop}$ and $\mathbf{r}^{Fbot}$ and only in the rigid stacking fault structure in Figure 5.2a are they located by $h_f/2$ from the rigid/flexible layer interface. In the flexible stacking fault, the flexible layer thickness changes and is no longer equal to h_f. The rigid stacking fault vector, $\mathbf{f}$, given by the $\mathbf{qt}$-components of the rigid layer COMs is

$$\mathbf{f(q,t)}=\mathbf{r}^{Rbot}\mathbf{(q,t)}\text{-}\mathbf{r}^{Rtop}\mathbf{(q,t)} \tag{5.5}$$

The stacking fault vector $\mathbf{f}$ is prescribed and always known. $\mathbf{f}$ describes the relative shift in the $\mathbf{qt}$-plane of the rigid lattice and does not change when the flexible layer is relaxed making it the same in Figure 5.2a and b. In the rigid stacking fault, the interfacial displacement discontinuity is equal to the stacking fault vector, $\mathbf{f}=\mathbf{u}$. The change in length of the rigid stacking fault supercell in Figure 5.2a is given by the $\mathbf{n}$-component of the rigid layer COMs by

$$\Delta_r\mathbf{n}=r_o^{Rbot}\mathbf{n}\text{-}r_o^{Rtop}\mathbf{n}\text{-}(h_R\text{-}2h_f)\mathbf{n} \tag{5.6}$$

where h_f and h_R are the flexible and rigid layer thicknesses and are known. The change in length of the rigid stacking fault supercell, Δ_r, in Figure 5.2a is also equal to the interfacial opening. Δ_r is a variable and must be determined from the rigid COMs. It is also allowed to change between the rigid and flexible stacking faults.

Figure 5.2b shows the flexible stacking fault where the flexible layers are sheared, $\mathbf{u}\neq\mathbf{f}$. The flexible layer COMs have now shifted relative to the rigid/flexible interface by

$$\mathbf{r}^{top}=\mathbf{r}^{Ftop}\text{-}(\mathbf{r}^{Rtop}+\tfrac{1}{2}h_R\mathbf{n})$$

$$\mathbf{r}^{bot}=\mathbf{r}^{Fbot}\text{-}(\mathbf{r}^{Rbot}\text{-}\tfrac{1}{2}h_R\mathbf{n}) \tag{5.7}$$

These COMs are used to find a deformation gradient that can be used to map vectors from the rigid to flexible stacking fault structure. Similar to what was previously done for the lattice vectors; the deformation gradient is defined using three linearly independent vectors $\mathbf{e}_q$, $\mathbf{e}_t$, and $\mathbf{r}$. The components, $\mathbf{e}_i$, are components of the orthornormal basis of unit vectors used to describe the slip plane and do not change because the $\mathbf{qt}$ components of the simulation cell are held fixed for the rigid and flexible stacking faults. The vector $\mathbf{r}=r_q\mathbf{e}_q+r_t\mathbf{e}_t+r_n\mathbf{e}_n$ is given by $\mathbf{r}^{top}$ and $\mathbf{r}^{bot}$ and is known. In the rigid stacking fault $|\mathbf{r}_o|=h_f/2$ and is normal to the slip plane. These three vectors are placed into the columns of the 3×3 matrices, $[\mathbf{h}_o]$ and $[\mathbf{h}]$, where $[\mathbf{h}_o]$ are rigid stacking fault vectors and $[\mathbf{h}]$ are the flexible stacking fault vectors with components

$$[\mathbf{h}_o] = [\mathbf{e}_q \quad \mathbf{e}_t \quad \mathbf{r}_o] = \begin{bmatrix} 1 & 0 & 0 \\ 0 & 1 & 0 \\ 0 & 0 & h_f/2 \end{bmatrix} \tag{5.8}$$

$$[\mathbf{h}] = [\mathbf{e}_q \quad \mathbf{e}_t \quad \mathbf{r}] = \begin{bmatrix} 1 & 0 & r_q \\ 0 & 1 & r_t \\ 0 & 0 & r_n \end{bmatrix} \tag{5.9}$$

The deformation gradient is then given by

$$\mathbf{F} = [\mathbf{h}][\mathbf{h}_o]^{-1} = \begin{bmatrix} 1 & 0 & 2r_q/h_f \\ 0 & 1 & 2r_t/h_f \\ 0 & 0 & 2r_n/h_f \end{bmatrix} \tag{5.10}$$

where a separate $\mathbf{F}^{top}$ and $\mathbf{F}^{bot}$ are found for the top and bottom flexible layers, respectively. $\mathbf{F}^{top}$ and $\mathbf{F}^{bot}$ provide a mapping for vectors in the flexible layer from the rigid ($\mathbf{s}_o$) to flexible ($\mathbf{s}$) stacking fault structure using

$$\mathbf{F} \cdot \mathbf{s}_o = \mathbf{s} \tag{5.11}$$

In Figure 5.2, $\mathbf{s}$ and $\mathbf{s}_o$ give the position of the slip plane interface relative to the rigid/flexible interface. The difference between $\mathbf{s}^{bot}$ and $\mathbf{s}^{top}$ gives the interfacial

138

displacement discontinuity $\mathbf{u(q,t)}$ and $\delta\mathbf{n}$. For this case, $\mathbf{s}_o = h_f\mathbf{n}$ and equation (5.11) is used to map this into the flexible stacking fault configuration as $\mathbf{s}$. The interfacial displacement discontinuity is then given by

$$\mathbf{u(q,t)} + \delta\mathbf{n} = \mathbf{s}^{bot} \text{-} \mathbf{s}^{top} = \mathbf{F}^{bot} \cdot \mathbf{s}_o^{bot} - \mathbf{F}^{top} \cdot \mathbf{s}_o^{top} \tag{5.12}$$

$$\mathbf{u(q,t)} = 2\left(r_q^{bot} - r_q^{top}\right)\mathbf{q} + 2\left(r_t^{bot} - r_t^{top}\right)\mathbf{t} \tag{5.12a}$$

$$\delta\mathbf{n} = 2\left(r_n^{bot} - r_n^{top}\right)\mathbf{n} \tag{5.12b}$$

The overall length of the lattice of the flexible stacking fault becomes

$$\Delta_f\mathbf{n} = r^{Rbot}\mathbf{n} \text{-} r^{Rtop}\mathbf{n} \text{-} (h_R\text{-}2h_f)\mathbf{n} \tag{5.13}$$

and is different from the interfacial opening ($\Delta_f \neq \delta$) if the thickness of the flexible layer, h_f, changes between the rigid and flexible stacking faults.

The Lagrange strain in each flexible layer is given by

$$\mathbf{E} = \tfrac{1}{2}[\mathbf{F}^T\mathbf{F}\text{-}\mathbf{I}] = \begin{bmatrix} 0 & 0 & r_q/h_f \\ 0 & 0 & r_t/h_f \\ r_q/h_f & r_t/h_f & 2\left(r_q^2 + r_t^2 + r_n^2\right)/h_f^2 \end{bmatrix} \tag{5.14}$$

and the infinitesimal strain tensor given by geometrical considerations such as the skewing of the lattice by θ and the change in the lattice length is given as

$$\mathbf{e} = \begin{bmatrix} 0 & 0 & \theta_{nq}/2 \\ 0 & 0 & \theta_{nt}/2 \\ \theta_{nq}/2 & \theta_{nq}/2 & \left(2r_q - h_f\right)/h_f \end{bmatrix} = \begin{bmatrix} 0 & 0 & r_q/h_f \\ 0 & 0 & r_t/h_f \\ r_q/h_f & r_t/h_f & \left(2r_q - h_f\right)/h_f \end{bmatrix} \tag{5.15}$$

where the small angle approximation is used, $\tan\theta_{nq,t} \approx r_{q,t}/h_f$. The Lagrange and infinitesimal strain only differ in the normal strain component (*nn*), which is usually small in these simulations. The average of the strain for the top and bottom flexible layers is used to calculate the strain energy in equation (5.3). The interfacial displacement vector found from the averaged strains and stacking fault vector is

139

$$\mathbf{u}(\mathbf{q},\mathbf{t}) = \mathbf{f} + 4h_f\left(e_{nt}^{avg}\right)\mathbf{t} + 4h_f\left(e_{nq}^{avg}\right)\mathbf{q} \tag{5.16}$$

where Lagrangian and infinitesimal strains give the same result.
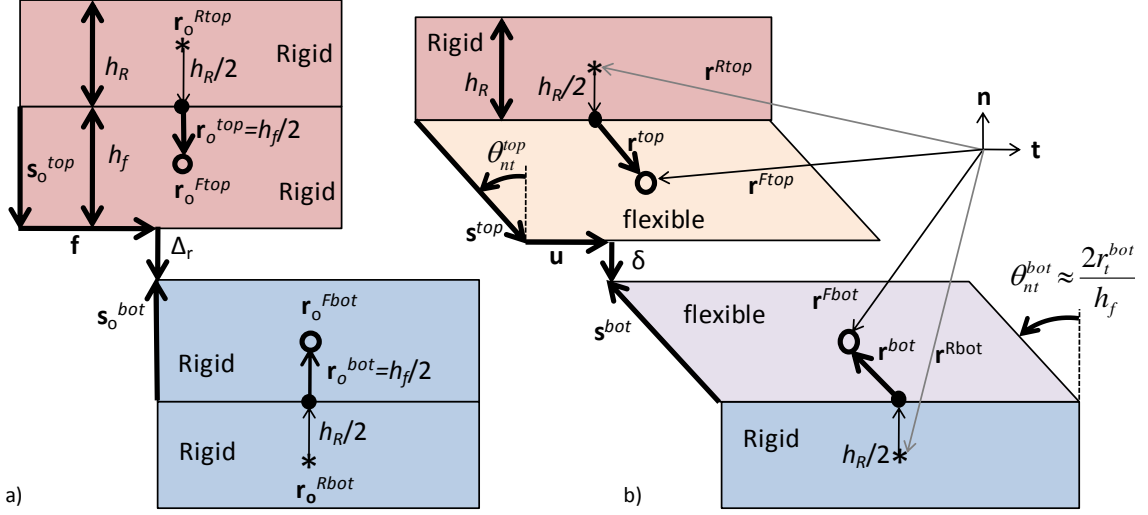
Figure 5.2: Centers Of Mass (COMs) shown by circles used to calculate the interfacial displacement discontinuity, $\mathbf{u}$ and δ, and the shear strain. The asterisk is the COM of the rigid layer sandwiching the flexible layers with COM shown by the black circle. The flexible/rigid interface is marked by the black dot and is always located by $\pm h_R/2\mathbf{n}$ from the rigid COM. a) Rigid stacking fault where $\mathbf{u}=\mathbf{f}$. b) Flexible stacking fault where the rigid central layers (orange and purple) are replaced with flexible molecules that shear, $\mathbf{u}\neq\mathbf{f}$. The vectors from the $\mathbf{nt}$ reference coordinates indicate the known COM positions used to calculate $\mathbf{u}$, δ, and the angle θ.

5.2 Generalized Stacking Fault Simulation Set up

The simulation set up for the stacking faults in αRDX and reasoning behind it are described in this section. The αRDX supercell used in the stacking fault simulations is created by replicating the minimized αRDX unit cell given in Appendix C. The Ewald sum is used to calculate the long range electrostatic forces present in the Smith and Bhardwaj potential (17). The Ewald sum requires the simulation cell to be 3D periodic and results in the simulation cell shown in Figure 5.1 to become an infinite array of slabs as shown in Figure 5.3a. The periodic boundary conditions in the red $\mathbf{qt}$-slip plane allow the shifted material used to create the stacking fault to move out one boundary and back

in the opposite boundary of the fixed simulation cell. This is shown in Figure 5.3b where the stacking fault causes the blue material to leave the simulation cell and the purple material to enter it. The stacking fault is repeated in all of the periodic images in the **qt**-plane creating a stacking fault with an infinite slip plane area. This removes the dependency of the **qt**-dimension of the simulation cell on the stacking fault energy per unit area of slip plane. The **qt**-dimensions of the simulation cell must still be at least twice as large as the 15Å real space cut-off used to calculate nonbonded forces. The area of the stacking fault in the **qt**-plane is held constant by fixing the **qt**-lattice vectors of the simulation cell. The number of unit cells replicated in the **qt**-plane, z_q and z_t, and the resulting slip plane dimensions are given in Table 5.1.
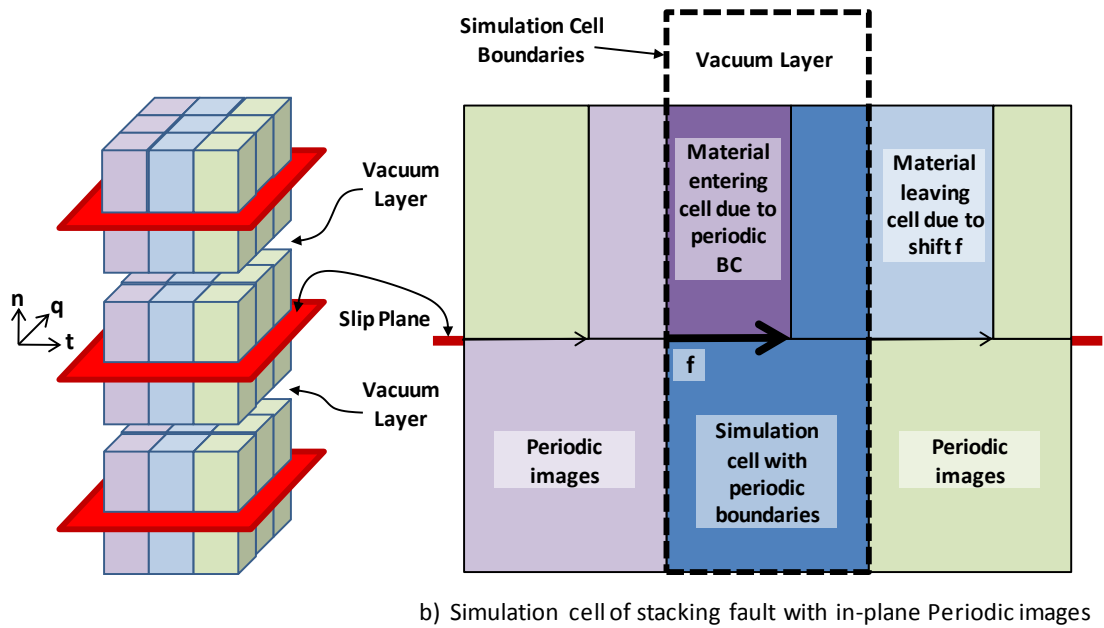
Figure 5.3: a) 3×3×3 replication of the simulation cell containing the initial supercell. The red plane is the slip plane and the supercells are separated in the n-direction by the vacuum layer. b) 2D projection of a stacking fault where the stacking fault vector **f** causes the blue material to leave the simulation cell (black dashed lines) and the purple material to enter the simulation cell. This creates an infinite plane of stacking faults.

A stacking fault is created within the supercell by shifting the upper and lower halves of the lattice relative to one another as shown in Figure 5.1c. This would cause a second stacking fault to be created between the periodic replicas of the supercell in **n**-direction and will be described in Section 5.4.1. The second stacking fault is unwanted and the effects of it are removed from the simulation cell by adding a vacuum layer to the top of the supercell. The periodic images in the **n**-direction are now separated by a vacuum layer as shown in Figure 5.3a. With the introduction of the vacuum layer, a free surface is created on the top and bottom of the supercell. The stacking fault is isolated from the free surfaces by increasing the number of unit cells, z_n, to give a thickness in the **n**-direction >90Å. The super cell and vacuum layer dimensions are labeled in Figure 5.4 with values given in Table 5.1. Figure 5.4a shows the simulation cell used when [hkl] is normal to the (hkl) plane, $\phi=90^o$. For (011) and (021), periodicity of the slab in the **qt**-direction requires the out-of-plane simulation cell vector [001] to be skewed by $\phi{\neq}90^o$ relative to the **qt**-plane.
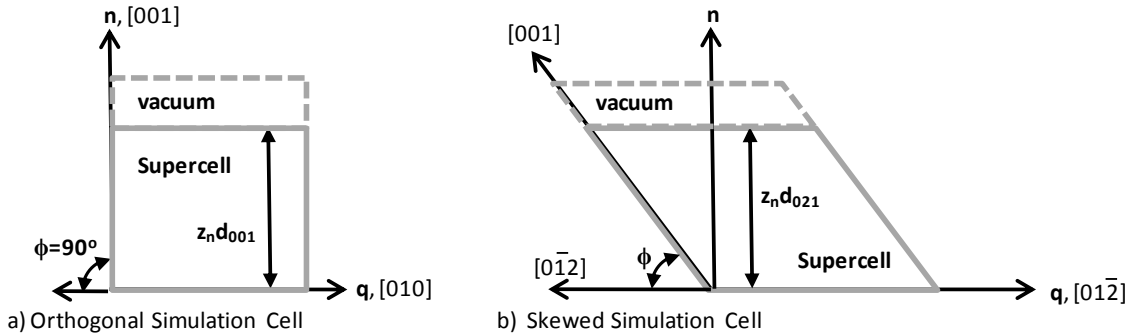
Figure 5.4: Simulation cell setup for the a) orthogonal simulation cell and b) skewed simulation cell used for the (011) and (021) stacking faults.

142

Table 5.1: Stacking fault simulation cell setup and dimensions showed in Figure 5.4. ϕ is always the angle between **q** and the [001] direction and is only relevant for the skewed simulation cells.

Slip Plane	Layer	d_{hkl} (Å)	Unit Cells $(z_n \times z_t \times z_q)$	**n** (Å)	**t** (Å)	**q** (Å)	ϕ (deg.)	Vac. (Å)
(100)	b2	6.689	12×3×3	160.553 [100]	31.031 [001]	34.722 [010]	90	30
(010)	b2	5.670	12×3×3	135.963 [010]	40.098 [100]	31.024 [001]	90	30
(001)	b1	5.179	12×3×3	124.286 [001]	40.049 [100]	34.002 [010]	90	30
(011)	b1	7.639	18×3×3	137.508	40.078 [100]	46.040 [1$\bar{1}$0]	47.6	40
(021)	b1	4.971	18×3×2	89.368	40.101 [100]	47.242 [0$\bar{1}$2]	28.7	40

5.3 Results and Discussion

5.3.1 (010)[100] Generalized Stacking Fault Energy

The concepts for determining the stacking fault energy were presented in Section 5.1 for systems containing flexible molecules that undergo shear deformation. The (010)[001] stacking faults shown in Figure 5.1 were used to present this concept because the flexible stacking faults undergo an observable amount of shear distortion. The shear was shown to be caused by the corrugated structure of the interface. In this section the results for the much more energetically favorable (010)[100] stacking faults are presented. These stacking fault are on the same b2(010) interface but are shifted along the grooves of the corrugated interface as shown in Figure 5.5. The stacking fault vector for these stacking faults is $\mathbf{f}=f_{100}\mathbf{[100]}/|\mathbf{a}|$.

Figure 5.5b shows the (001) plane of the αRDX crystal where the interface between the red and blue molecules is the slip plane. This is a 90° rotation about the [010] axis of the corrugated crystal lattice shown in Figure 5.1. Even though the molecules are shifted along the corrugated interface, the rigid stacking faults still separate

as shown in Figure 5.5c where f_{100}=0.5. The flexible stacking fault for f_{100}=0.5 is shown in Figure 5.5d where the flexible layers are colored orange and purple. The thickness of the flexible layers is h_f=|**b**|/2. The interface of the flexible stacking fault closes without shearing the lattice.
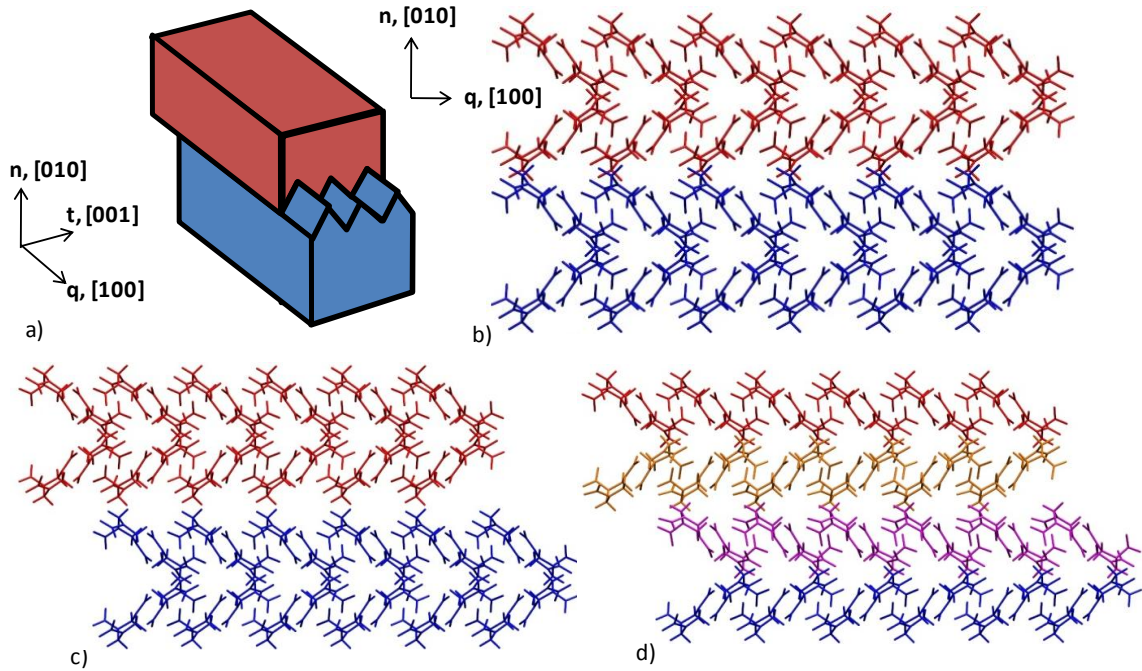
Figure 5.5: a) Geometric representation of a (010)[100] stacking fault created along the grooves of corrugated b2 slip plane. b) (001) view of the initial slip plane of the perfect crystal where the red molecules are above the slip plane and blue are below. c) Rigid and d) flexible stacking fault for f_{100}=0.5.

This set of stacking faults describing the b2(010)[100] slip system were created by increasing f_{100} from 0 to 1 in increments of 0.01. This created 100 rigid stacking fault structures. The energy of each rigid stacking fault is minimized by allow the interface to open. The rigid stacking fault energy, $\Psi_R(f_{100})$, given by equation 5.1 is shown by the black circles in Figure 5.6b and the corresponding interfacial opening, Δ_r, is shown in Figure 5.6a. The rigid $\Psi_R(f_{100})$ energy can be due only to electrostatic and dispersion/repulsion interactions between the two crystal halves. The rigid interface will

open until the repulsive interactions are balanced out by the attractive interactions. No limit is placed on Δ_r and the repulsive forces can cause the interface to completely separate creating two free surfaces. The maximum opening of $\Delta_r=1.5$Å occurs at $f_{100}=0.5$. This is also the location of the rigid unstable stacking fault energy, $\Psi_R(f_{100}=0.5)=\gamma_{usf}=247$mJ/m^2. Table 5.2 gives the rigid free surface energy for the b2(010) interface as $2\gamma_s=391$mJ/m^2. Since $\Psi_R(f_{100}) < 2\gamma_s$ the interface does not separate. The rigid stacking fault for $f_{100}=0.5$ is shown in Figure 5.5c. The alignment of the red and blue molecules across the interface in Figure 5.5c appears to be the same as that in Figure 5.5b but their orientation are slightly different leading to repulsive interactions that push the interface apart.
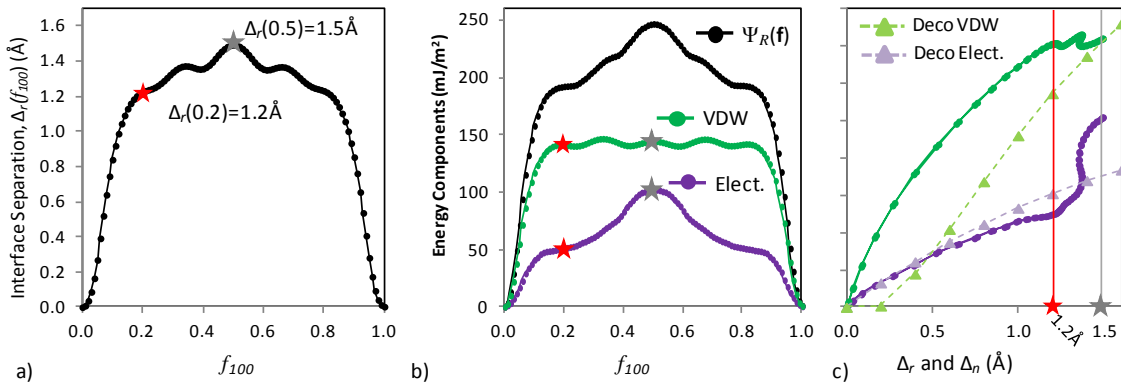
Figure 5.6: a) Interfacial displacement, Δ_r, for the (010)[100] rigid stacking fault. b) Rigid GSF energy, $\Psi_R(f_{100})$, and nonbonded SB energy components for the (010)[100] rigid stacking faults. c) Energy components plotted as a function of interfacial seperation. The circles and solid lines are the rigid stacking stacking fault data from a) and b). The triangles and dashed lines are from the rigid decohesion seperation simulations from Section 4.3 as a function the interfacial seperation, Δ_r. Stars in a) and b) indicate equivalent energy versus opening data shown by the stars and lines in c).

The repulsive interactions can be due to the Pauli exclusion principal keeping two atoms from occupying the same space as was the case for the (010)[001] stacking fault shown in Figure 5.1b. In the SB potential this leads to an exponential increase in energy.

The repulsive interactions can also be caused by electrostatic interactions between like charged atoms. In αRDX these can become strongly repulsive in the rigid stacking faults as several H..H and O..O atoms become aligned across the interface. Electrostatic interactions are long ranged where the energy dies off with separation distance as r^{-1}. These two repulsive interactions are balanced out by electrostatic attraction of oppositely charged atoms and London dispersion forces. London dispersion describes the interaction between two atoms that adjust their electron clouds in response to one another, inducing a weak attractive dipole like interaction with energy proportional to separation distance as r^{-6}. The van der Waals energy is the combination of Pauli exclusion and London dispersion energies.

The total energy shown by the black data points in Figure 5.6b is the sum of the VDW (green) and electrostatic (purple) energies. The VDW energy will increase when atoms get to close (Pauli Exclusion) or when atoms move apart, reducing the attractive dispersion energy. The electrostatic energy will also increase as oppositely charged atoms are separated or when like charged atoms get too close. Ideally, the change in VDW or electrostatic energy would follow the decohesion separation energy given in Section 4.3. The electrostatic and VDW energy from the rigid stacking fault simulations are plotted as circles in Figure 5.6c versus the interfacial opening, Δ_r, from Figure 5.6a. Also shown in Figure 5.6c by the triangle data points is the decohesion separation energy components for the (010)b2 interface from Section 4.3. Deviations between VDW energies in green indicate molecules coming into repulsive contact with one another. Deviations in electrostatic energies in purple indicate a change in the types of atom interacting across the interface.

Even though the (010)[100] rigid stacking faults do not require molecules to shift over one another, the interface still opens significantly to reduce nonbonded interactions. At the first red star in Figure 5.6a located at f_{100}=0.2, the interface opens to Δ_r=1.2Å and the nonbonded energies increase by VDW=141mJ/m^2 and Electrostatic=51mJ/m^2. Up to this point in Figure 5.6c, the Electrostatic energy for the decohesion and stacking fault simulations are similar. However, the difference in VDW energy (dashed line) of the stacking fault is much larger, indicating molecules coming into close contact across the slip plane and repelling one another.

At f_{100}=0.5 marked by the gray star in Figure 5.6a, the interface has opened to Δ_r=1.5Å and the change in VDW=144mJ/m^2 and Electrostatic=102mJ/m^2. The decohesion separation energy for Δ_r=1.5Å is VDW=144mJ/m^2 and Electrostatic=71mJ/m^2. In this case, the VDW energy is the same but the stacking fault electrostatic energy is 31mJ/m^2 larger. The differences in electrostatic energy in Figure 5.6c indicate an unfavorable change in the charge of atoms aligned across the stacking fault interface.

The alignment of like partial charges across the interface of rigid stacking faults makes the rigid Ψ_R-energy surface in Figure 5.6c an over estimate of the GSF energy. The rigid stacking faults are computationally efficient to make but the rigid GSF energy is of limited use. In this work, the rigid stacking faults are only used to provide an initial atomic configuration for the flexible stacking faults to begin from.

Figure 5.5d shows the the flexible stacking fault where a layer of molecules h_f=|$\mathbf{b}$|/2 have been replaced with flexible molecules and quenched. The addition of flexible molecules lowers the $\Psi(f_{100})$ energy for every stacking fault structure, shown by

comparing the red data points in Figure 5.7a to the black data points in Figure 5.6b. The GSF energy given by $\Psi(f_{100})$ describes the surplus energy of the system due to the displacement of the rigid portion of the lattice by $\mathbf{f}$. In the rigid stacking fault structures, $\mathbf{f}$ was equal to the interfacial dispacement vector $\mathbf{u}$. However, in the flexible stacking fault, $\mathbf{f}$ and $\mathbf{u}$ are usually not equal due to shearing of the flexible lattice and $\Psi_F(f_{100})$ describes both elastic shear energy and the energy due to the lattice disregistry.

The elastic energy shown by the green data points is calcualted from the shear stress and strain shown in Figure 5.7b. The elastic energy in Figure 5.7a coincides with $\Psi_F(f_{100})$ for $f_{100}<0.1$ and $f_{100}>0.9$. In this region the GSF energy predicted by $\Psi_F(f_{100})$ is due only to elastic shearing of the flexible layer and is not a result of lattice disregistry. For this reason, the interfacial GSF energy, $\Phi(\mathbf{u})$, was introduced in equation (5.2) to describe only the energy associated with the lattice disregistry caused by the interfacial displacement vector, $\mathbf{u}$. The $\Phi(\mathbf{u})$ energy was given as the difference between $\Psi_F(\mathbf{f})$ and $2h_f E(\mathbf{f})$. The intefacial displacement vector, u_{100}, is calculated from the shear strain in Figure 5.7a using equation (5.12). For $f_{100}<0.1$ and $f_{100}>0.9$ the interfacial displacement vector is equal to zero, $u_{100}=0$, indicating no lattice disregistry. For no lattice disregistry, $\Phi(u_{100})=0$, and the increase in system energy due to $\mathbf{f}$ is stored as elastic shear strain energy, $\Psi_F(f_{100})= 2h_f E(f_{100})$ as previously stated. This all indicates that $\Psi_F(f_{100})$ can be partioned into $E(f_{100})$ and $\Phi(u_{100})$ and the method of determining the shear strain and $\mathbf{u}$ is accurate.

For $f_{100}<0.2$, the strain is negative and u_{100} moves toward the origin, $u_{100}<f_{100}$. For $f_{100}>0.8$ the strain is positive and u_{100} moves toward the unfaulted structure at one, $u_{100}>f_{100}$. The strain energy drops off to nearly zero in the unstable stacking fault regions

labeled by γ_{usf}. At these points, the lack of strain energy makes $\Psi_F(f_{100})$ and $\Phi(u_{100})$ equal. The shear strain is nearly zero at these points as well making $f_{100}=u_{100}$. The strain energy and strain are also zero at the stable stacking fault at $f_{100}=0.5$ resulting in $f_{100}=u_{100}$ and $\Psi_F(f_{100}=0.5)=\Phi(u_{100}=0.5)$.

In Figure 5.7a there are two $\Phi(u_{100}=0)>0mJ/m^2$ data points that are associated with a slight conformation change of the molecules under large amounts of shear. This shows that $\Phi(\mathbf{u})$ may sometimes not only be due to lattice disregistry but to any change in the crystal not associated with elastic shearing.
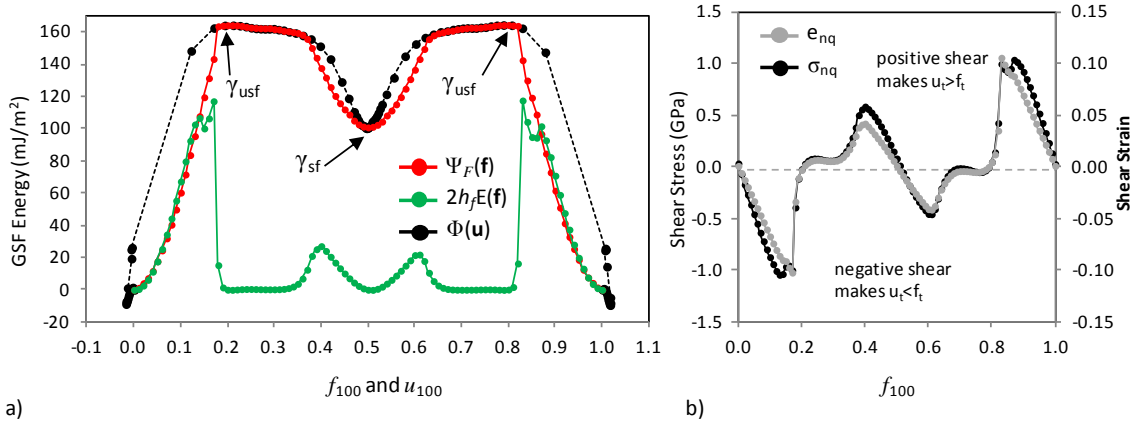
Figure 5.7: a) (010)[100] flexible $\Psi_F(\mathbf{f})$, $\Phi(\mathbf{u})$ and Elastic strain energy with unstable and stable stacking fault energies labeled. b) Out-of-plane shear stress (black line, left axis) and strain (gray line, right axis) used to calculate the elastic strain energy.

Figure 5.8a shows the interfacial separation, δ, and change in supercell length, Δ_f, for the f_{100} flexible stacking faults. For $f_{100}<0.1$, the supercell height increases by Δ_f while the interface remains closed, $\delta=0$. This suggests a coupling between shear and extensional deformation of the flexible molecules. This coupling is partially due to the Lagrange strain, E_{nn}, in equation (5.14) containing second order components of shear displacement. At the largest shear deformations near $f_{100}=0.2$ this accounts for only 3%

of E_{nn}. The length change could also result from coupling of the shear and volumetric components of the elastic tensor. For small deformations the elastic tensor was shown to be orthotropic in Section 3. However, large deformations may result in molecule orientation and conformation changes that could couple shear/extensional deformation. This shear/extensional coupling causes $\delta < \Delta_f$ at the stable and unstable stacking faults.

The flexible stacking fault electrostatic, VDW, and bonded energies are shown in Figure 5.8b. It is assumed that the energy components can also be partitioned into elastic shear energy and inelastic stacking fault energy. The stacking fault portion of the of the energy component plotted in Figure 5.8b is found by removing the elastic portion by

$$VDW(\mathbf{u}) = VDW(\mathbf{f}) - VDW(\mathbf{f})\frac{E(\mathbf{f})}{\Psi(\mathbf{f})} \qquad (5.17)$$

The bonded energy includes the energy from dihedral, angle, improper and bonds that are now allowed to change with addition of flexible molecules. A change in the bonded energy indicates a change in the molecules conformation. At the unstable stacking fault near $f_{100}=0.2$, the addition of flexible molecules reduces the VDW energy while the electrostatic and bonded energy remain nearly unchanged when compared to the rigid stacking fault energies in Figure 5.6b. At the flexible stable stacking fault structure, $f_{100}=0.5$, the electrostatic energy drops to zero. This brings the interface closer together, $\delta=0.24$, resulting in a decrease in VDW energy. The interface reconstruction that reduces the electrostatic energy also causes a change in the molecule conformation reflected by an increase in bonded energy. The directionally oriented electrostatic interactions are able to push or pull on particular atoms in the molecule to reduce the electrostatic energy. These directionally oriented forces heavily influence the surface reconstruction of the flexible molecules. Figure 5.5d shows the atomic configuration of the flexible stable

stacking fault. The energy was reduced through a slight orientation change of the RDX molecules and the conformation change is not noticeable.
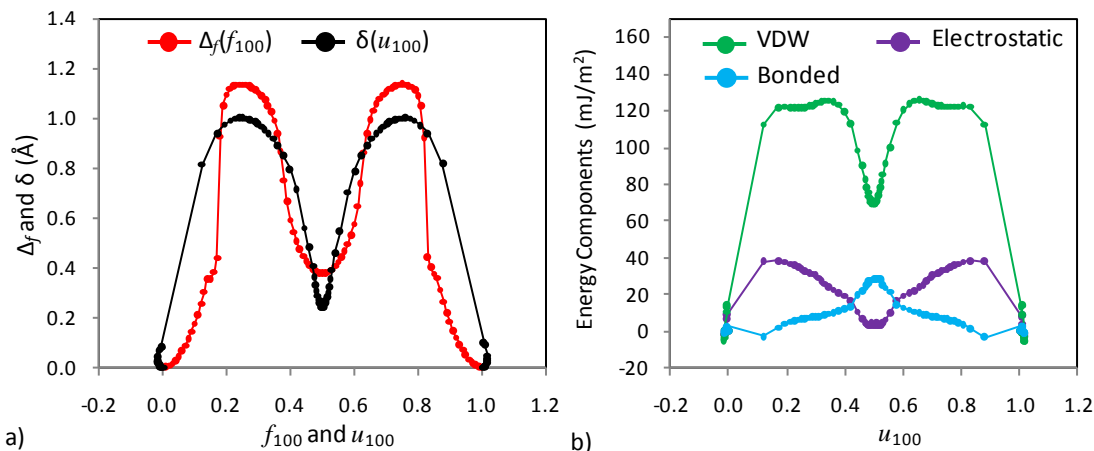
Figure 5.8: a) Change in flexible lattice height, Δ_f, and intefacial opening, δ. b) Flexible stacking fault VDW, Electrostatic and bonded energy components.

Figure 5.9a shows the relaxation paths that the flexible stacking faults take as they are quenched from the rigid stacking fault structure. The open circles are the black data points from Figure 5.6b for the rigid Ψ_R-surface and the filled in circles are the black data points from Figure 5.7a for the flexible Φ-surface. Each line indicates the path taken as the flexible molecules relax from the rigid to flexible configurations. The path start and end points are emphasized by the larger symbols. Every rigid to flexible stacking fault relaxation path is shown in Figure 5b by different colored lines for f_{100}=0 to 0.5.
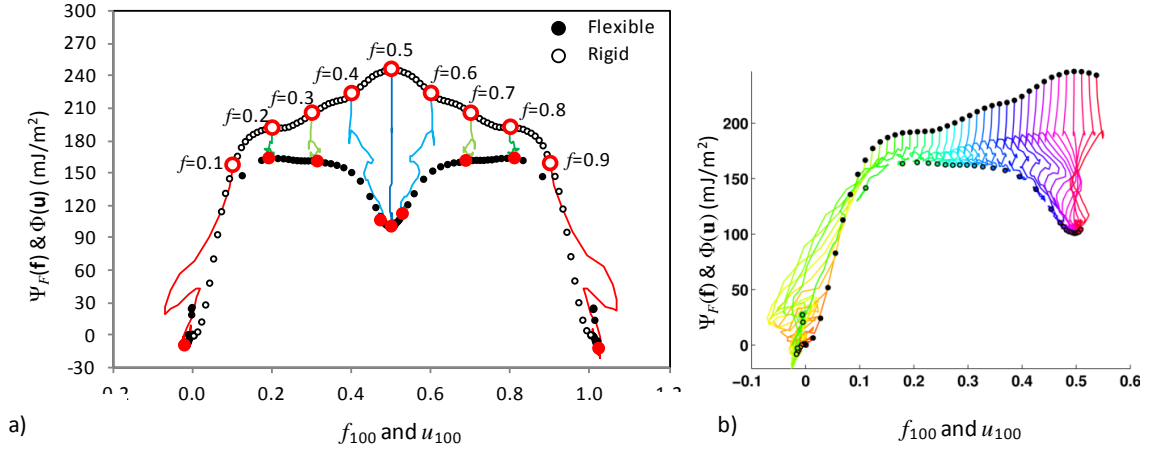
Figure 5.9: Rigid $\Psi_R(\mathbf{f})$ and flexible $\Phi(\mathbf{u})$ energy surfaces where lines indicate the relaxation path of the rigid to flexible stacking fault. Open symbols denote the initial rigid configurations and the closed symbols indicate the subsequently relaxed flexible configurations. a) Relaxation paths for select rigid to flexible stacking fault structures are shown by the lines connecting the larger symbols given at f_{100} increments of 0.1. b) Colored lines show relaxation paths for every rigid to flexible stacking fault for $f_{100}=0$ to 0.5.

For $f_{100}<0.1$ and $f_{100}>0.9$, the flexible model is incapable of accommodating the partial slip configuration. The system unslips completely and the energy is stored purely as elastic strain energy, $\Phi(u_{100}=0)=0$. For $f_{100}=0.2$ and 0.8, the initial rigid fault configurations relax to the flexible unstable stacking fault configurations. The energy relaxes nearly vertically with $f_{100}=u_{100}$ and the flexible stacking fault energies are equal, $\Psi_F(f_{100})=\Phi(u_{100})=\gamma_{usf}$ as previously shown in Figure 5.7a.

When $f_{100}=0.3$ and 0.7, the energies are in the unstable stacking fault region, namely the energy profile of $\Phi(u_{100})$ is near a local maximum or a saddle point on the $\Phi(\mathbf{u})$-surface. The relaxation paths of the flexible stacking faults in this region land in a local minimum during the quenching process. Some type of flexible molecule change occurs that allows the molecule to escape the local minimum and settle to the final flexible stacking fault energy. Every relaxation path in Figure 5.9b for $f_{100}>0.2$ is shown

to traverse through this same local minimum. This local minimum highlights a weakness in the simulation procedure. Here we rely on the surplus energy of the rigid stacking fault structure to be sufficient to overcome the energy barriers separating the rigid and flexible stacking faults. Without additional energy being input into the system, the flexible stacking faults could easily get stuck in local minimums. We also used viscous damping to quench the flexible stacking faults, which could further impede the flexible stacking fault from reaching the global minimum energy. For this reason, Cawkwel et al (38) added thermal energy to the system to provide sufficient energy to escape local minimums. However, the additional thermal energy will increase the mobility of the interface causing it to shear, similar to what occurs for f_{100}<0.1 and f_{100}>0.9. In this work, the surplus energy in the rigid stacking fault was found to be sufficient in minimizing each flexible stacking fault to the correct minimum energy configuration.

The same local minimums are encountered for the relaxation paths starting at f_{100}=0.4 and 0.6, which end up shearing toward the stable stacking fault configuration at u_{100}=0.5. The highest energy rigid stacking fault for the (010)[100] slip system occurs at f_{100}=0.5 indicating that the slip plane interface created from the perfect αRDX lattice does not favor the stable stacking fault. However, the flexible molecules cause a reconstruction of the interface that favors a stable stacking fault structure at f_{100}=0.5. The interface reconstruction does not cause the interface to shift and the relaxation path from f_{100}=0.5 is vertical resulting in u_{100}=0.5. Again, this results in the flexible stacking fault energies being equal, $\Psi_F(f_{100}=0.5)=\Phi(u_{100}=0.5)$.

Figure 5b shows all of the relaxation paths for all of the f_{100} rigid to flexible stacking fault simulations. Several of the final flexible stacking faults shear to create the

unfaulted crystal or the stable stacking fault, u_{100}=0,0.5, or 1. This reduces the number

$\Phi(u_{100})$ data points in unstable regions. These data points can be filled in by using the

lowest lying data points from the relaxation curves shown by the colored lines in Figure

5.9b. The curve traced out by the relaxation paths can be approximated by a composite

of the rigid and flexible stacking fault energies. This approach could be used to extract

the Φ-surface from simulations where thermal energy is used to facilitate the

equilibration of the stacking fault structure but also results in large amounts of shear.

5.3.2 (010) Generalized Stacking Fault Surface

The entire b2(010) GSF energy will be presented in this section by allowing **f** to

span the entire surface of the unit cell, $\mathbf{f}=f_{100}[100]/|\mathbf{a}|+f_{001}[001]/|\mathbf{c}|$. In this section 900 **f**-

vectors are used to create a regularized 30×30 grid of stacking faults that span the surface

of the b2(010) slip plane. The rigid $\Psi_R(\mathbf{f})$-surface is shown in Figure 5.10a and the

resulting interfacial opening, Δ_r, is given in b. The $\mathbf{f}=f_{100}[100]/|\mathbf{b}|$ trace along the x-axis

of Figure 3.3.1 were presented in Figure 5.6. As expected, the f_{001} stacking faults shown

in Figure 5.1 where the corrugated interfaces move over one another results in the highest

rigid $\Psi_R(\mathbf{f})$-energy and the largest amount of interfacial opening. The rigid free surface

energy given in Table 5.2 is $2\gamma_s$=384mJ/m^2 and is very close to $\Psi_R(f_{001}=0.5)$=383mJ/m^2.

With $\Psi_R(f_{001}=0.5)\approx 2\gamma_s$ the Rice criterion (18) would predict brittle behavior for the

(010)[001]. At f_{001}=0.5, the interface only separates by $\Delta_r\approx$4Å, which is not far enough to

create two free surfaces as shown in Figure 4.15 for the (010) decohesion separation

simulation.
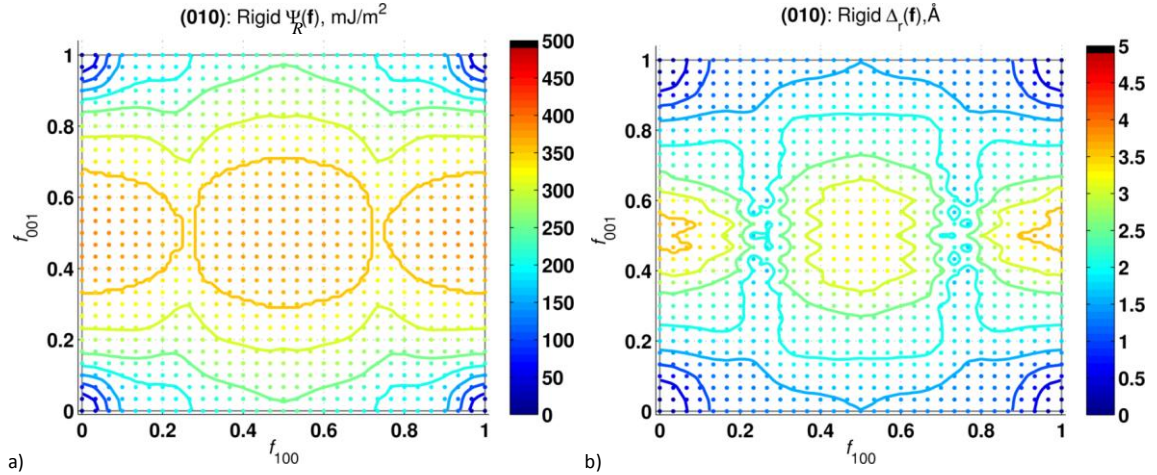
Figure 5.10: a) Rigid $\Psi_R(\mathbf{f})$ stacking fault energy surfaces for the b2(010) slip plane. b) Interfacial seperation, Δ_r, for the rigid stackign fautl structures.

A flexible molecule layer of thickness $h_f=|\mathbf{b}|/2$ is added to each rigid stacking and quenched. This produces the flexible stacking faults shown in Figure 5.1d for $\mathbf{f}=f_{001}[001]$ and Figure 5.5d for $\mathbf{f}=f_{100}[100]$. The flexible $\Psi_F(\mathbf{f})$ energy presented by the red data points in Figure 5.7a are presented for the entire (010) surface in Figure 5.11a. Again, the flexible layers lower the energy of every rigid stacking fault. The local minimum also appears at $f_{100}=0.5$ and is the only local minimum on the surface. Vectors are also shown representing the direction and relative magnitude of the (010) suraface tractions, $\boldsymbol{\tau}=\boldsymbol{\sigma}\cdot\mathbf{n}$, where $\boldsymbol{\tau}$ is surface traction, $\mathbf{n}=[010]/|\mathbf{b}|$, and $\boldsymbol{\sigma}$ is the 3×3 virial stress tensor given by equation (5.4).

The surface shear tractions for f_{100} were shown in Figure 5.7b and were multiplied with the shear strain of the flexible layer to to give the elastic strain energy shown by the green data in Figure 5.7a. The entire elastic strain energy surface is shown in Figure 5.11b. Figure 5.7b showed the stress and strain to have the same sign and to be linearly proportional to one another. This is also true in Figure 5.11b where the elastic strain energy is highest in regions that correspond to the largest magnitude shear tractions in

155

Figure 5.11a and is never negative. The traction vectors in Figure 5.11a indicate the approximate direction the interface displaces. The vectors approximately point in the direction of steepest decent on the $\Psi_F(\mathbf{f})$ surface and toward the corners where the perfect lattice is recreated or to the local stable stacking fault. The largest strain energy occurs for f_{100} and corresponds to the sheared flexible molecules shown in Figure 5.1d.
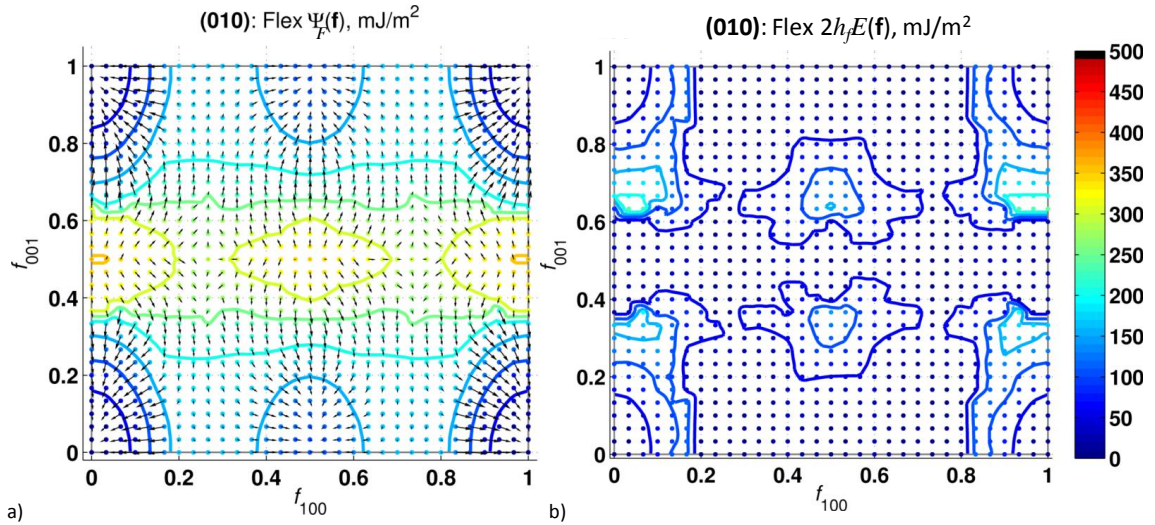
Figure 5.11: a) Flexible $\Psi_F(\mathbf{f})$ where vectors indicate the direction and relative magnitude of the shear components of the surface traction. b) Elastic strain energy of the flexible layer given by equation (5.3).

The GSF energy of interest in this work is the component that only includes the effects of the lattice disregistry. This was referred to as the interfacial stacking fault energy, $\Phi(\mathbf{u})$, given in equation (5.2) to be the difference between the flexible $\Psi_F(\mathbf{f})$ surface in Figure 5.11a and the elastic strain energy in Figure 5.11b. This was shown by the black data points in Figure 5.7a and is shown for the entire $\Phi(\mathbf{u})$ surface in Figure 5.12. The data points in Figure 5.12a correspond to the final flexible stacking fault energies. Most of the black $\Phi(u_{100})$ data points in Figure 5.7a displace toward the origin, which left large regions of the Φ-energy contour unknown. This is still the case for the

entire $\Phi(\mathbf{u})$ in Figure 5.12a where the highest density of data points are near the stable

stacking fault (u_{100}=0.5) or the sheared lattice configurations, (f_{100}, f_{001}=0, 1). There are

also some data points in unsteady regions where the shear traction vectors in Figure 5.11a

were negligible.

The rigid to flexible stacking fault relaxation histories for $\Phi(u_{100})$ were shown in

Figure 5.9 and the lowest lieing $\Phi(u_{100})$ energy from these paths provides an approximate

$\Phi(u_{100})$-curve. Figure 5.12b shows the lowest $\Phi(\mathbf{u})$ energy data for all of the relaxation

histories for the entire (010) surface. The relaxation history data fills in the missing data

points in Figure 5.12a and is used to create the contours. The white regions in Figure

5.12b are grid points where the relaxation history does not cross.
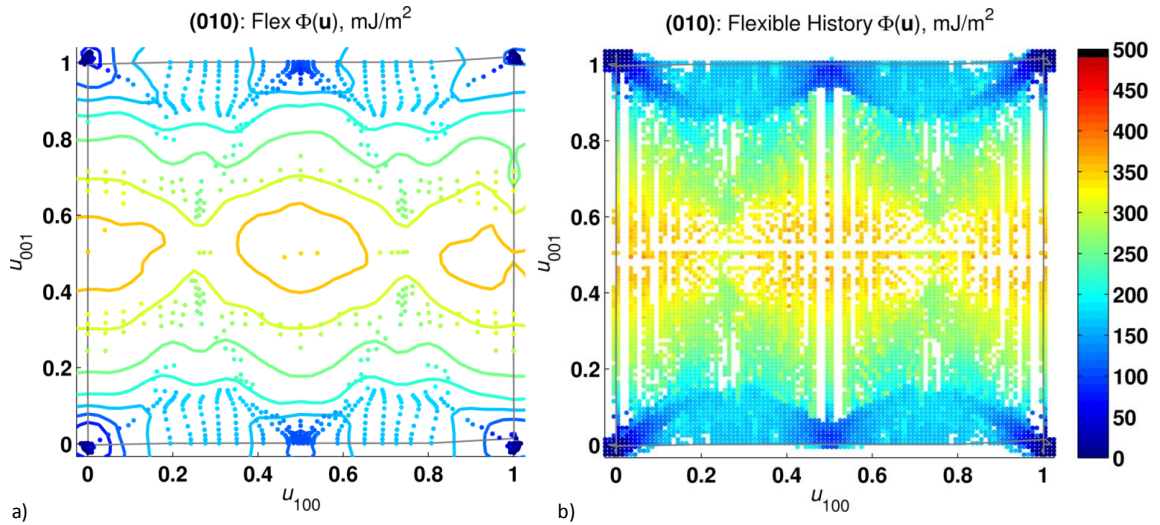
Figure 5.12: a) Quenched flexible $\Phi(\mathbf{u})$ energy surface. B) Flexible $\Phi(\mathbf{u})$ contours from all rigid to flexible stacking fault relaxation histories. This data is used to create the contours in (a).

The maximum $\Phi(\mathbf{u})$ energy occurs at u_{001}=0.5 and is γ_{usf}=351mJ/m^2 and the

energy of two free flexible b2(010) surfaces is γ_s=367mJ/m^2. This unstable stacking fault

energy is only slightly less than the energy needed to create two free surfaces. In this

case, slip on the (010)[001] slip system would probably result in fracture according to

Rice's dislocation nucleation criterion (18). However, Figure 5.12 shows the maximum energy encountered in the u_{001} direction can be slightly reduced to $2\gamma_{usf}\approx300\text{mJ/m}^2$ if the slip path shuffles around the global maximum on the saddle point at $(u_{100},u_{001})=(0.25,0.5)$. There also appears to be a lower energy slip path for the formation of the stable stacking fault shown by following the dark blue streaks in Figure 5.12b emanating from the origin. This streak curves around the $u_{100}=0.2$ unstable stacking fault to reach the stacking fault at $u_{100}=0.5$. These lower energy slip paths are possible if the molecules shear around the maximum energy barriers with **u** in a slightly different direction than **f**. Thermal energy may help activate this shuffle type motion. However in this work, the structures were quenched and the lattice usually shears in the direction of the largest gradient of elastic energy in Figure 5.11b.

The change in length of the flexible supercell, Δ_f, is shown in Figure 5.13a and the interfacial opening, δ, is shown in b. These were presented for f_{100} in Figure 5.8a. The change in length of Δ_f is a function of the stacking fault vector, **f**. The interfacial opening is given at the interfacial displacement vector, **u**. The δ(**u**) of the corresponding history Φ(**u**) data points shown in Figure 5.12b are used to determine the contour levels in Figure 5.13b. It is interesting that the shear/extensional coupling mentioned for f_{100} where $\Delta_f>\delta$ does not occur for f_{001}. This is evident from $\Delta_f(f_{001})\leq\delta(f_{001})$, indicating the flexible layer thickness does not expand as the flexible molecules are sheared.
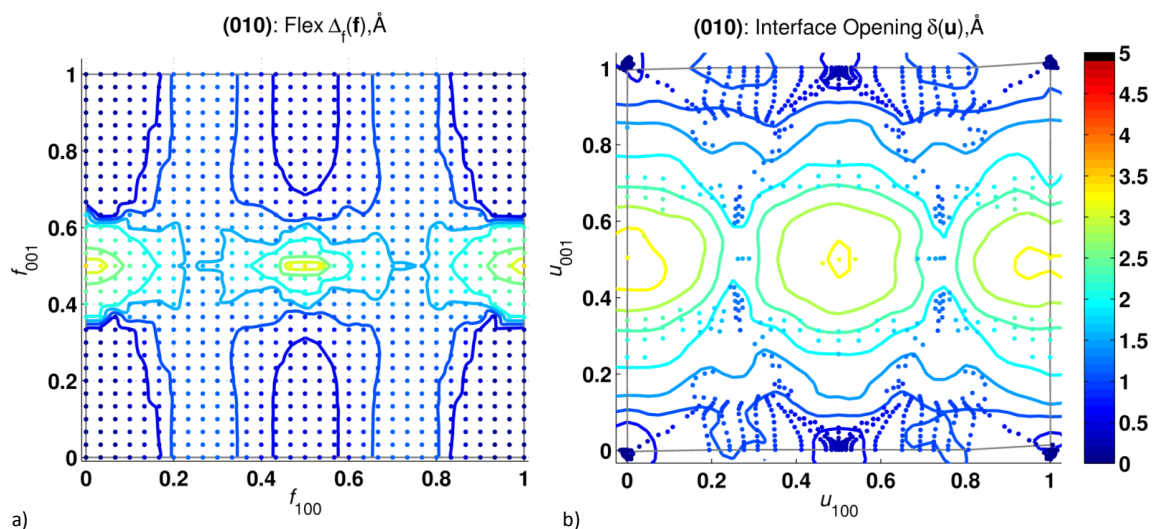
Figure 5.13: a) Change in the flexible supercell height, Δ_f, as a function of **f**. b) Intefacial opening, δ, as function of interfacial displacement, **u**.

The method for determining the various GSF energies was shown to work well in Section 5.3.1 for a series of stacking faults on a low energy (010)[100] slip system. The same methods are shown in this section to work well for all of the (010) stacking faults. The methods were able to model the stable stacking fault structure on the (010)[100] slip system. The stable stacking fault was stabilized through molecule orientation and conformation changes. The elastic shear energy was also accurately predicted for the (010)[001] stacking faults, which are shown in Figure 5.1d to undergo extensive shear and interfacial opening. The $\Phi(\mathbf{u})$ surface is useful because it is able to show all local minimums on the surface that indicate stable stacking faults. It also shows saddle points and maximum energies that are barriers to any type of slip motion on the plane. The surfaces can also indicate lower energy slip paths that maybe thermally activated.

5.3.3 Other αRDX Generalized Stacking Fault Surfaces Surface

The interfacial flexible $\Phi(\mathbf{u})$ energy for all of the slip plane systems described in Table 5.2 are presented in Figure 5.14. The interface with the lower surface energy in

Table 4.4, either b1 or b2, was used as the slip plane interface. The $\Phi(\mathbf{u})$ surfaces were created from a 30×30 grid of stacking fault vectors as was done for the b2(010) plane presented in Section 5.3.2. Figure 5.15 shows the $\Phi(\mathbf{u})$ relaxation history data points used to construct the contours in Figure 5.14. The color limit on the plots for $\Phi(\mathbf{u})$ is 500mJ/m^2 and data points above this are shown in black.

The gray line connects all of the $\Phi(\mathbf{u})$ data points along the edges of the 30×30 grid. On the $\Psi(\mathbf{f})$ surface, plotted with $\mathbf{f}$ on the xy-axis, the grey line traces out a square box surrounding the regularized 30×30 grid of $\mathbf{f}$ points. The $\Phi(\mathbf{u})$ surface is plotted with $\mathbf{u}$ on the xy-axis in Figure 5.14 and the grey square is deformed as the interface shifts due to shearing of the flexible layers. The maximum energy barriers along the grey lines are given in Table 5.2 for rigid stacking faults and in Table 5.3 for the flexible stacking faults shown in Figure 5.14. The trace of the $\Phi(\mathbf{u})$-surface along the grey lines describe the slip systems with the shortest Burgers vectors and are presented in Figure 5.16.

The b2(100) plane shown in Figure 5.14a shows the highest $\Phi(\mathbf{u})$ energy barriers to dislocation motion and no local energy minima. This plane also has the highest surface energy in Table 4.4, $2\gamma_s$=555mJ/m^2, making inelastic deformation on it unlikely (24). The b1(001), b1(011), and b1(021) planes all have local minimums $\Phi(\mathbf{u})$ for stacking faults created with f_{100}=0.5 as was the case for the b2(010) plane. The b1(001), b1(021) planes also show local minimums in the interior of the $\Phi(\mathbf{u})$-surface.
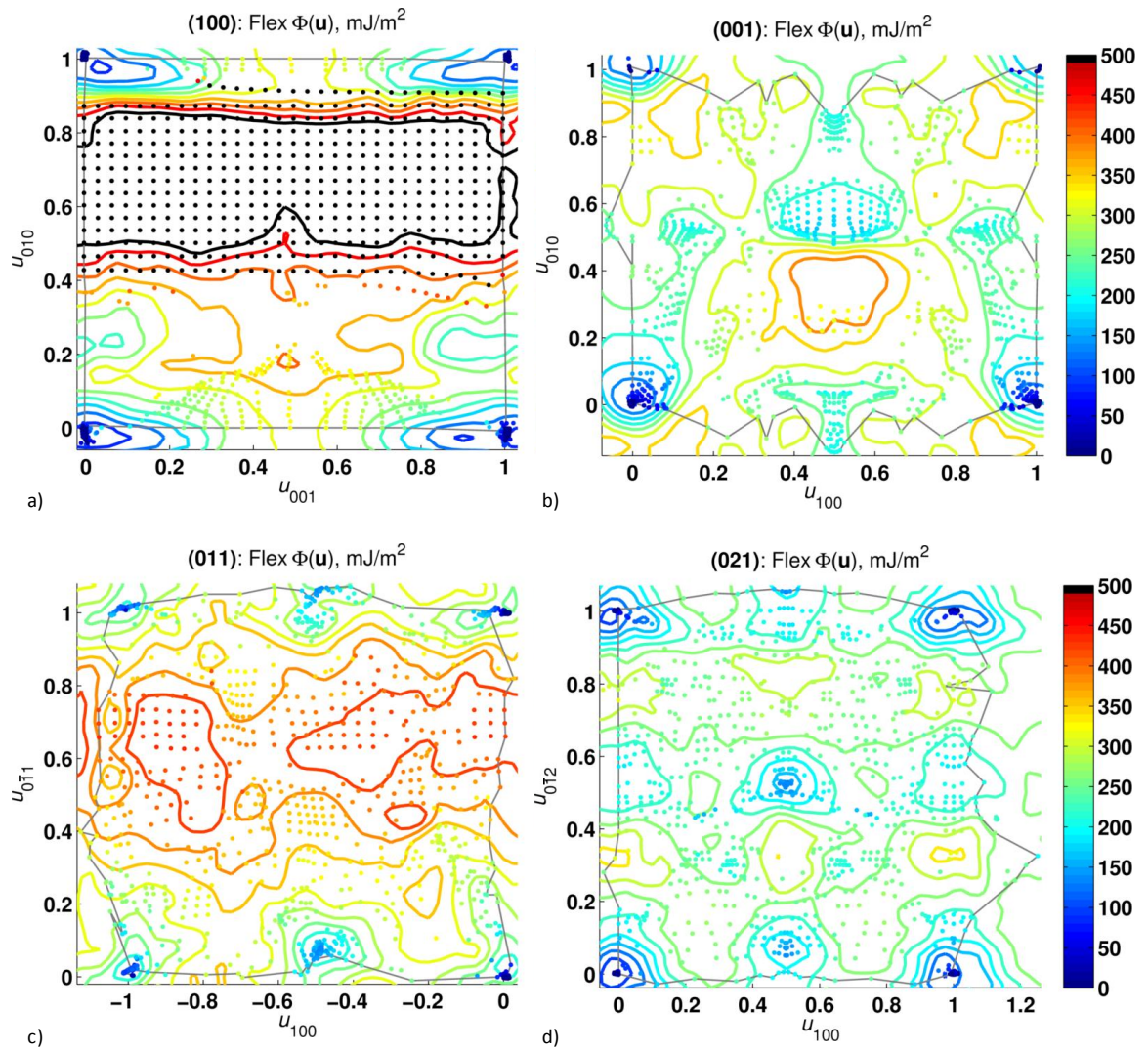
Figure 5.14: Flexible $\Phi(\mathbf{u})$-surfaces for the a) b2(100), b) b1(001), c) b1(011) and d) (021) planes as described in Table 5.1.

161
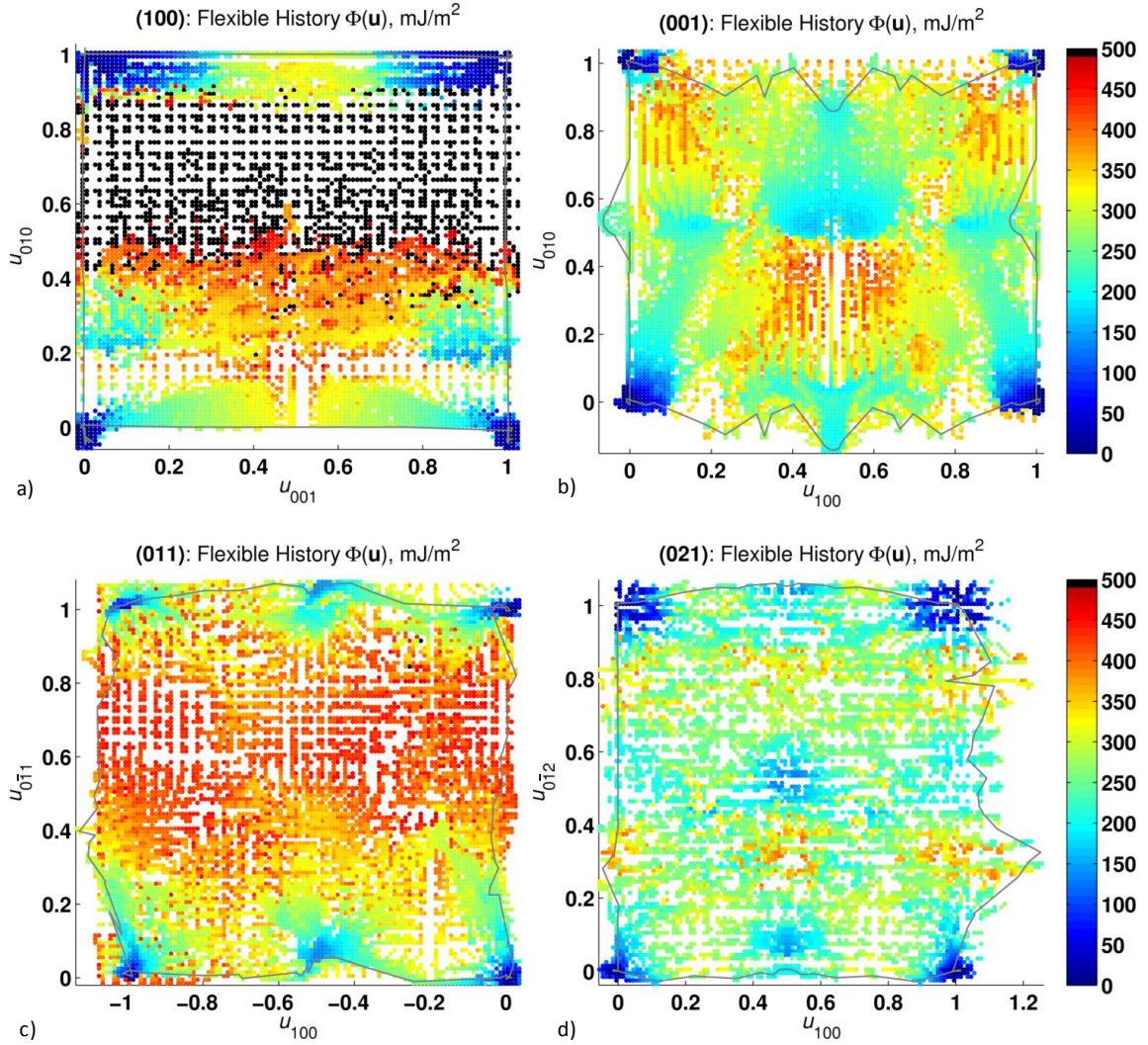
Figure 5.15: Flexible history $\Phi(\mathbf{u})$-surfaces for the a) b2(100), b) b1(001), c) b1(011) and d) (021) planes used to construct the contours in Figure 5.14.

In Figure 5.14b, the interior b1(001) local minimum is the lowest energy stable stacking fault structure for this plane. The local minimum energy at u_{100}=0.5 for the b1(001)[100] stacking faults is actually a saddle point. This results in the gray line skewing toward the actual local minimum at (u_{100}, u_{010})=(0.5,0.6). In Figure 5.15b, the $\Phi(\mathbf{u})$ history data indicates that partial dislocations would first travel in the [010] direction and then in the [100] direction to the interior local stable stacking fault.

The b1(021) plane also shows an interior local energy minimum in Figure 5.14d at (u_{100}, $u_{0\bar{1}2}$)=(0.5,0.5). The initial interface of the (021)[$0\bar{1}$ 2] slip system is shown in Figure 5.16a where the colored molecules represent the flexible layers and the black molecules represent a single (021) unit cell as described in Appendix C. The stacking fault shown in (b) is created by shifting the pair of molecules circled in red to the location of the molecules circled in blue. The two pairs of circled molecules are very similar and the stacking fault interface they create by switching position is very similar to the perfect crystal. This results in the entire series of stacking faults with $\mathbf{u}=u_{100}[100]+0.5[0\bar{1}$ 2] being similar in energy to the $\mathbf{u}=u_{100}[100]$ series of stacking faults. The history data for the (021) surface in Figure 5.15 is more sparse than the other surfaces because the [$0\bar{1}$ 2] unit cell length is 23.621Å, almost twice as long as the other unit cell dimensions. A dislocation on this slip system would have a very large energy associated with it due to the large Burgers vector. Even the partial dislocation would have a Burgers vector equal to the length of the **c**-lattice length.
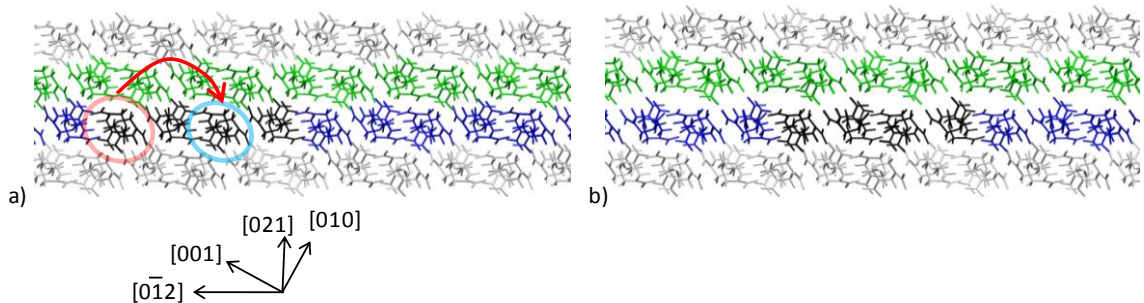
Figure 5.16: a) (021)[$0\bar{1}$ 2] slip plane and b) stacking fault for $u_{0\bar{1}2}$=-0.54. Molecules use the same coloring scheme as Figure 5.18. Only the flexible layer of molecules are colored, the white molecules are part of the rigid lattice. The black molecules show a single (021) unit cell on the slip plane with dimensions given in Appendix A3. The stacking fault in (b) is created by displacing the pair of black molecules circled in red to the location of the molecules circled in blue. This creates a stacking fault interface in (b) with a similar structure to the perfect crystal in (a).

The $\Phi(\mathbf{u})$ energy trace along the $\mathbf{u}$ path shown by the grey lines on the $\Phi(\mathbf{u})$-surfaces in Figure 5.12 and Figure 5.14 are plotted in Figure 5.17. One hundred stacking faults were used to determine the $\Phi(\mathbf{u})$ energy traces shown in Figure 5.17. Figure 5.17a contains the slip systems with a u_{100} slip direction. These slip systems all have stable stacking faults and the lowest unstable stacking fault energies. Figure 5.17b presents the other GSF energy contours mentioned in literature (10) (38) (6) (14). Figure 5.17c completes the series by presenting the other slip system GSF traces not mentioned in literature. Table 5.3 summarizes the flexible stacking fault data presented in the Figure 5.17.

The slip systems with a [100] slip direction are shown in Figure 5.18a where [100] slip is in the direction toward the reader. Rigid/flexible composite $\Phi(\mathbf{u})$-curves for the slip systems with u_{100} are shown together in Figure 5.17a and have the lowest energy barriers to slip. These slip systems all produce a stable stacking fault at $u_{100}=0.5$. The jaggedness of the $\Phi(\mathbf{u})$-curves is caused by several local minima being encountered during the quenching process as was shown for the (010)[100] curve in Figure 5.9. Since no energy is put into the systems, the quenching process may freeze some flexible stacking faults into these local minima. The (010), (001) and (021) $\Phi(\mathbf{u})$-curves are nearly symmetric.
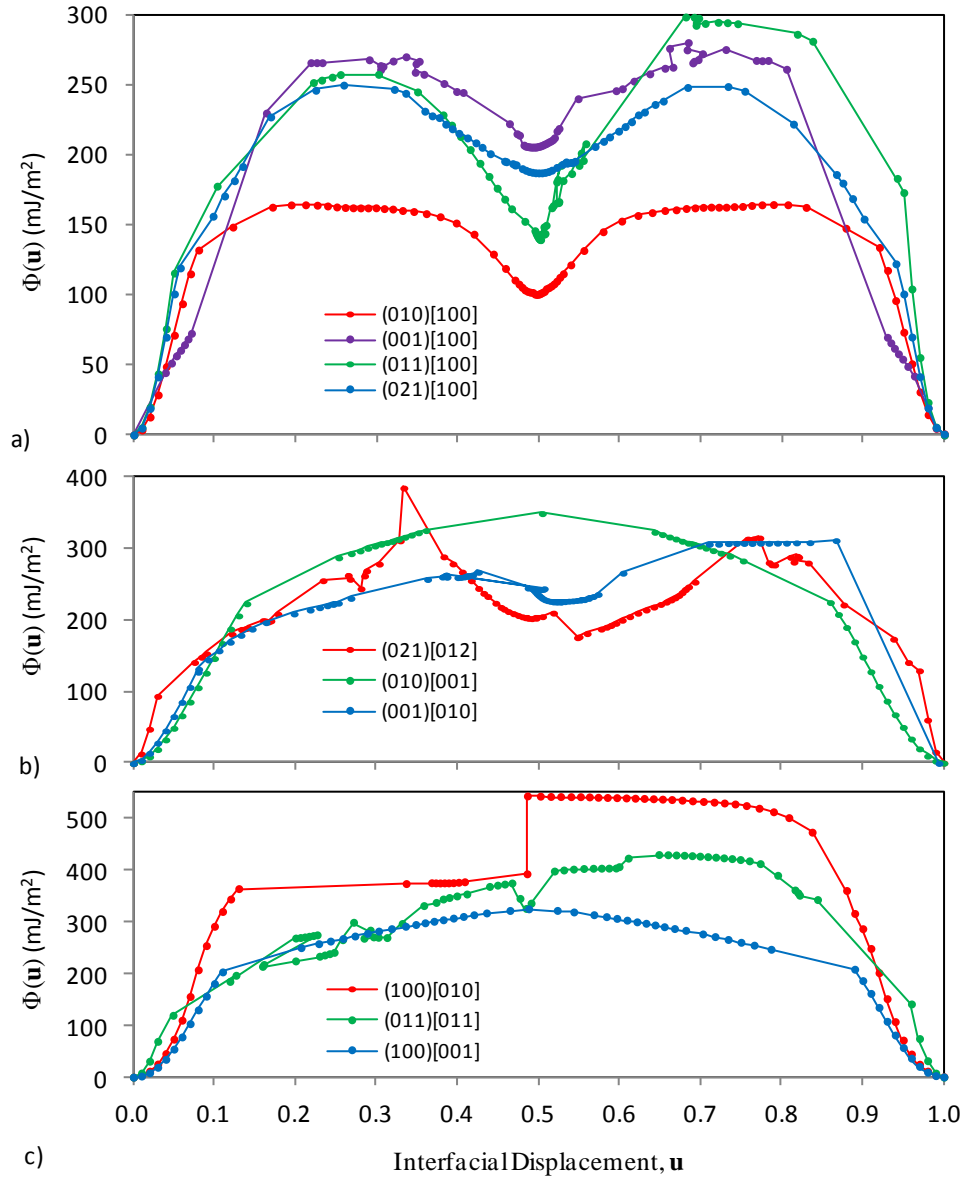
Figure 5.17: Composite rigid/flexible $\Phi(\mathbf{u})$ energy traces along grey lines from Figure 5.12 and Figure 5.14. a) Slip systems in the u_{100} direction with the lowest γ_{usf} and stable stacking faults. b) Slip systems from literature where $(021)[01\,2]$ is an experimental slip system (14), $(010)[001]$ is also an experimental slip system (14) correlated to reduced sensitivity to shock loading (10), and $(001)[010]$ is related to partial dislocations in MD simulations (38). c) Other slip systems completing the set for the presented $\Phi(\mathbf{u})$-surfaces.

The (010)[100] slip system has the lowest energy barrier to slip and the lowest stacking fault energy for all slip systems in the crystal. In Figure 5.18, the (010) slip plane is between the red and blue molecules. There is a large spacing between the red

and blue molecules along the extent of the (010) plane and the molecules can easily slip in the [100] direction. The (001)[100] slip system has the largest energy barrier to slip in Figure 5.17a. This slip plane is between the grey and purple molecules in Figure 5.18 and is sterically hindered to [100] slip by the nitro groups circled in red. Slip on this system causes the flexible molecules to change conformation by moving their nitro groups away from the slip planes to reduce the O..O electrostatic repulsion of the nitro groups. Two sets of these nitro groups are encountered per unit cell for this slip system (indicated by the two circled sets between the green and grey molecules). Slip on the (011)[100] and (021)[100] systems occurs on planes containing a composite of the unhindered (010)[100] system and sterically hindered (001)[100] system. The energy barrier to slip for the (001)[100], (011)[100], and (021)[100] systems is in the range γ_{usf}=250-260mJ/m^2 indicating that the steric nitro group of the (001)[100] system limits slip on the (011)[100] and (021)[100] systems. The (011)[100] system is sterically hindered by two sets of nitro groups per unit cell and is slightly higher in γ_{usf} than the (021)[100] system, which is only sterically hindered by one set.
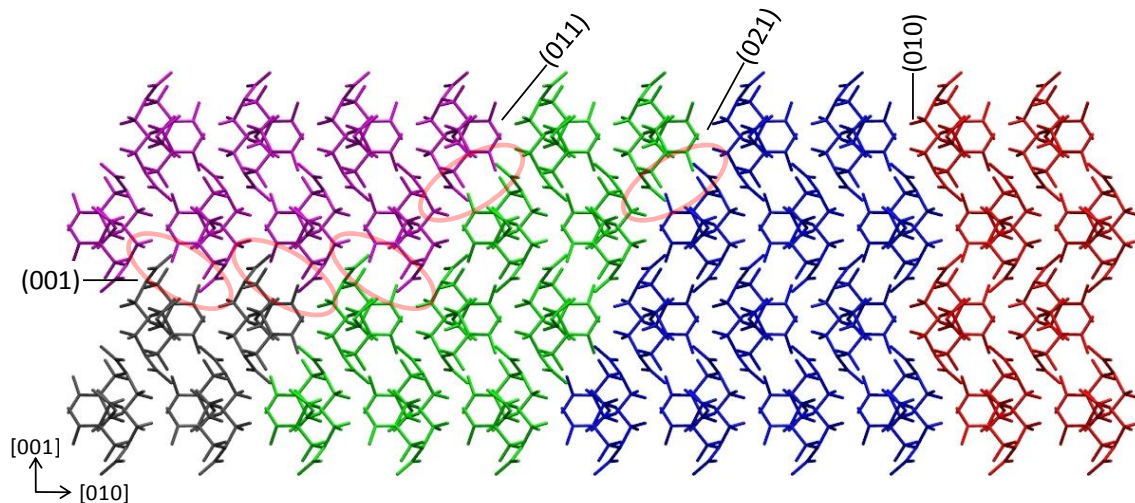
Figure 5.18: (100) projection of αRDX lattice with molecules colored to differentiate the slip systems with [100] slip direction. Division between grey and purple molecules is the (001) plane, between purple/grey and the green molecules is the (011) plane, between green and blue is the (021) plane, and between blue and red is the (010) plane. The red circles indicate the steric nitro group that inhibit slip on the (001), (011), and (021) planes.

Figure 5.19 shows a projection of the flexible molecule layer for each of the [100] slip systems shown in Figure 5.18. The same coloring scheme is used in both figures. The initial perfect crystal slip plane is shown in the left column of Figure 5.19 and the stacking fault structure for $u_{100}=0.5$ is shown on the right column. For u_{100} there are two main types of stacking faults. The first type occurs for the (021)[100] and (010)[100] in Figure 5.19 b and c, where the stacking fault structure recreates an interface close to the perfect crystal structure. This can be observed by the circle regions in Figure 5.19b and c, which are nearly the same between the stacking fault and initial structure. The second type causes all of the molecules on the interface to take on a similar interfacial configuration. For the (011)[100] stacking fault in Figure 5.19a the perfect crystal contains interlocked molecule groups across the interface circled in red. In the stacking fault structure, all of the molecules take on a similar stacking fault structure circled in

167

blue. This is also true in Figure 5.19d for the (001)[100] slip system where the interlocking nitro groups (red circles) flatten out in the stacking fault structure (blue circles). Figure 5.14 shows the (001)[100] stable stacking fault shown in Figure 5.19d to be at a saddle point energy and the interface slips considerably in the u_{010} direction.
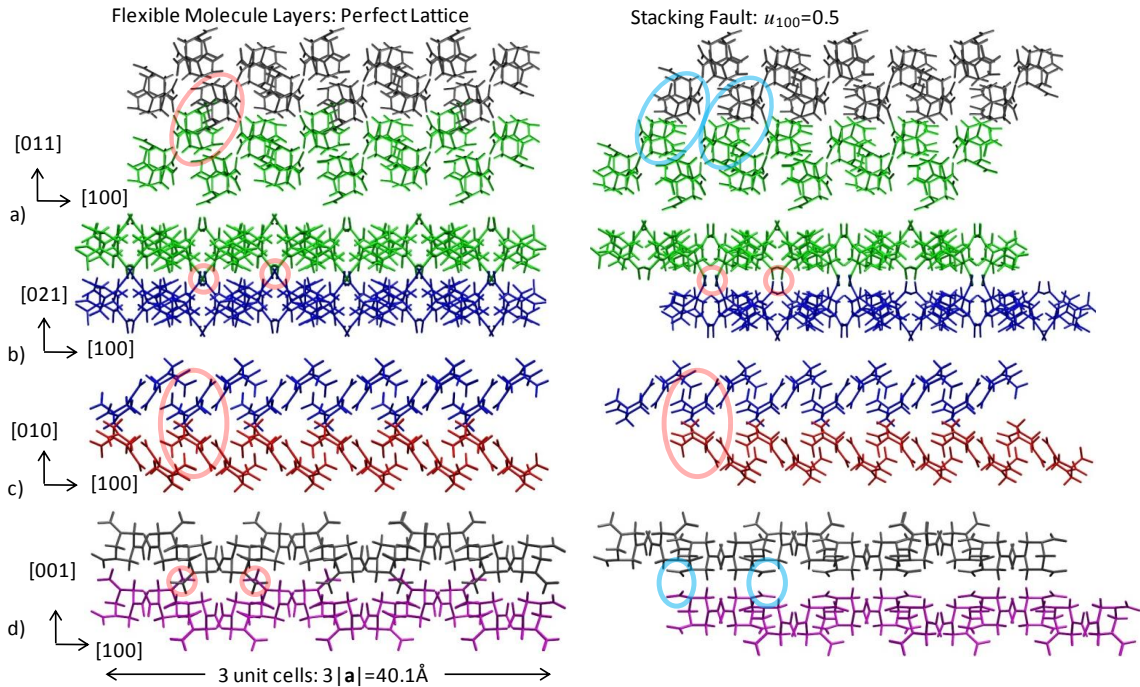
Figure 5.19: Projections of the flexible molecule layers of the stacking fault simulation cells where the left column contains the initial perfect lattice and the right column contains the stacking fault structures at $u_{100} \approx 0.5$. Each lattice is 3 unit cells wide in the [100] direction. The coloring scheme from Figure 5.18 is used here. The circles indicate important features between the perfect crystal and stacking fault. The slip systems are a) (011)[100], b) (021)[100], c) (010)[100], and d) (001)[100].

The (011)[100] $\Phi(\mathbf{u})$ curve in Figure 5.17a is asymmetric with γ_{usf}=255 mJ/m^2 at u_{100}=0.25 and γ_{usf}=295 mJ/m^2 at u_{100}=0.75. This is due to the interlocked green and grey molecules in Figure 5.19a. As the grey molecules are shifted in the [100] direction, in Figure 5.19a, they easily slip over the first group of green molecules and create the stacking fault. As they continue moving in the [100] direction they encounter the group of green molecules that they are initially interlocked within the perfect crystal. The grey

molecules must shift over this set of green molecules, which is responsible for the increase in energy at u_{100}=0.75. It would be difficult for an actual dislocation to move in the opposite direction, [0$\bar{1}$ 1], because the interlocked molecules would move through one another instead of sliding over one another. These interlocked molecules were also shown in the decohesion separation simulations in Section 4.3 to hold the interface together.

Ramos et al. (14) observed deviations in slip traces of the (010), (011), and (021) slip planes, which they attributed to cross slip if these planes all share a common slip direction. This work supports this notion of cross slip. First, the (001), (010), (011), and (021) planes all share the [001] slip direction making cross slip possible. Second, all of these slip systems produce stable stacking faults. Stable stacking faults are associated with partial dislocations, which are an essential element of cross slip (93). Third, the barrier to slip (γ_{usf}) on several of these systems is nearly equal and caused by the same nonbonded nitro group interaction. Alternatively, the slip trace deviation could be a result of alternately activated (010) and (100) slip planes, which would appear as slip on the (011), (021) or even higher aspect ratio planes.

The likelihood of forming partial dislocations is determined by the ratio of the stable to unstable stacking fault energy in Table 5.3. For γ_{sf}/γ_{usf} near unity a full dislocations will be nucleated. For intermediate to low ratios, partial dislocations will be produced (1). The ratios given for αRDX in Table 5.3 for (011)[100] are in the same range of nickel, which was shown in MD simulations to nucleate partial dislocations that were able to extend across 20nm grains without nucleating a trailing partial (1).

The asymmetric (011)[100] and (001)[010] $\Phi(\mathbf{u})$ curves in Figure 5.17 also increase the likelihood of partial dislocations under monotonic loading. A dislocation moving on these slip systems encounters two energy barriers. The first energy barrier is γ_{usf} listed in Table 5.3 and is lower than the second energy barrier. This asymmetry in energy barriers makes it easy to emit a partial dislocation but difficult for the partial dislocation to traverse the second barrier to create the full dislocation. In this case, it is energetically favorable to accommodate inelastic deformation on these slip planes by emitting a series of partial dislocation on parallel slip planes. The low γ_{sf}/γ_{usf} ratio in Table 5.3 makes it easy for these systems to unslip back to the perfect crystal upon unloading. This would make these partial dislocations difficult to observe in experiments at low pressures.

The atomic configurations for the series of stacking faults created for the asymmetric (001)[010] $\Phi(\mathbf{u})$ curve are presented clockwise in Figure 5.20. This slip system is orthogonal to the (001)[100] slip system shown in Figure 5.19d and the molecules in Figure 5.20 use the same coloring scheme. The first energy barrier configuration at $u_{010}=0.25$ is shown in Figure 5.20b. In this configuration the molecules start changing their conformations by moving their nitro groups that intersect the slip

plane. This allows them to move over the first molecule pair on the interface to create the stable stacking fault in (c) at u_{010}=0.56. In the stable stacking fault the molecules on the slip plane change from the *AAE* to *AEE* conformation. The highest energy stacking fault is shown in (d) for u_{010}=0.75 where the *AEE* interfacial molecules must slip over one another. This slip system and stable stacking fault are likely related to the slip direction that produces the stable stacking fault at (u_{100},u_{010})=(0.5,0.6) on the $\Phi(\mathbf{u})$-surface in Figure 5.14b.

A thermalized flexible $\Psi_F(\mathbf{f})$-curve was determined for this system by Cawkwell et al (38) for f_{010}=0 to 0.2[010] at zero pressure and under an applied normal traction, τ_n=1GPa. Normal traction was shown to produce a local energy minimum at f_{010}=0.16 that they did not observe at zero pressure. They found this stable stacking fault to be related to loops of partial dislocations observed in MD simulations of shock compression (38). The asymmetry of the (001)[001] $\Phi(\mathbf{u})$ curve shown in Figure 5.17b would also favor the pileups of partial dislocations. The dislocation pileups in their work were characterized by a change in molecule conformation from *AAE* to *AEE*. Our simulations also show this same *AAE* to *AEE* conformation change at the stable stacking fault in Figure 5.20c for f_{010}=0.56.

In the oriented shock simulations by Cawkwell et al. (38), the loops of partial dislocations resulted in a change in molecular packing from 14 nearest neighbors to alternating planes of 13 and 15 nearest neighbors. In Figure 5.20a, the (001)[010] slip system is dependent on the slip direction as was the case for the (011)[100] slip system. The molecules on the slip plane interface will easily slip over one another in the [010] direction but will become entangled in the [01̄0] direction. However, the (001) slip

plane offset by ½[001] has the opposite properties and will easily slip in the [01̄0] direction. This feature could explain the alternating planes of stacking faults with 13 or 15 nearest neighbors by Cawkwell et al. (38).
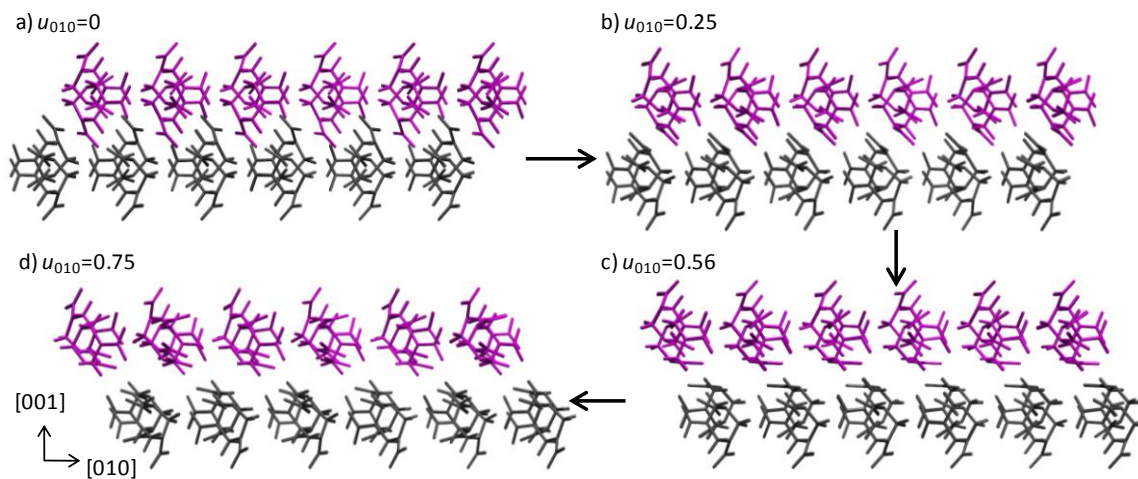
Figure 5.20: Series of stacking faults on the (001)[010] slip system using the same molecule coloring scheme from Figure 5.19. Only the flexible molecule layers are shown. The series of stacking faults move clockwise where a) is the initial perfect crystal, b) first lower energy unstable stacking fault, c) stable stacking fault configuration, and d) high energy unstable stacking fault structure.

Rice's criterion [20] is applied to the data in Table 5.2 and Table 5.3 by comparing $2\gamma_s$ to γ_{usf} to determine if the response of this slip system is likely to be brittle or ductile. For the brittle to ductile ratio, $\alpha = \gamma_{usf}/2\gamma_s$, given in Table 5.3, Rice's criterion predicts ductile for $\alpha < 1$ and brittle for $\alpha > 1$. In this work the stacking faults were allowed to open unconstrained across the slip plane. This limits $\gamma_{usf} \leq 2\gamma_s$ or $\alpha \leq 1$, which severely limits the applicability of Rice's criterion to this work. However, the ratio α does provide a method of qualitatively ranking the different slip systems for the likelihood of slip or cleavage.

Table 5.2: Rigid free surface energy (mJ/m^2) from Table 4.2, unstable stacking fault energy (mJ/m^2) and associated stacking fault vector, and brittle to ductile ratio, α=γ_{usf}/2γ_s.

Slip System	2γ_s	γ_{us}	$\mathbf{f}_{us}$	α
b2(100)[010]	591	609	0.42	1.0
b2 (100)[001]		359	0.5	0.6
b2 (010)[100]	384	247	0.5	0.7
b2 (010)[001]		383	0.5	1.0
b1(001)[100]	450	430	0.12	1.0
b1 (001)[010]		445	0.9	1.0
b1 (011)[100]	509	397	0.35	0.8
b1 (011)[0$\bar{1}$ 1]		497	0.5	0.9
b1 (021)[100]	429	365	0.3	0.9
b1 (021)[0$\bar{1}$ 2]		416	0.17	1.0

Table 5.3: Flexible lattice free surface energy (mJ/m^2) from Table 4.2, unstable/stable stacking fault energy (mJ/m^2) and associated stacking fault vector (**f**), brittle to ductile ratio (α=γ_{usf}/2γ_s), ratio of stable to unstable stacking fault energies, and interpretation of slip plane from literature. For asymmetric Φ(**u**) traces, the lower energy γ_{usf} is given.

Slip System Interface (plane)[direction]	2γ_s	γ_{usf}	$\mathbf{f}_{usf}$	α	γ_{sf}	$\mathbf{f}_{sf}$	γ_{sf}/γ_{usf}	Experiment
	555	542	0.5	1.0	--	--	--	Cleavage[a]
b2(100)[001]		325	0.5	0.6	--	--	--	Cleavage[a]
b2(010)[100]	367	164	0.2	0.4	101	0.5	0.6	Slip[b]
b2(010)[001]		351	0.5	1.0	--	--	--	Slip[a, c], Cross Slip[b], Insensitive[d]
b1(001)[100]	408	260	0.25	0.6	206	0.5	0.8	Cleavage[a]
b1(001)[010]		260	0.4	0.7	230	0.5	0.9	Cleavage[a], Partial Dislocation[e]
b1(011)[100]	465	255	0.25	0.6	140	0.5	0.5	Slip[b, c]
b1(011)[0$\bar{1}$ 1]		430	0.7	0.9	--	--	--	--
b1(021)[100]	404	250	0.25	0.6	187	0.5	0.8	Slip[b, c]
b1(021)[0$\bar{1}$ 2]		291	0.2	0.7	177	0.45	0.6	Slip[b, c]

[a]Reference (7), [b]Reference (14), [c]Reference (6), [d]Reference (10), [e]Reference (38)

In the last column of Table 5.3, experimental observations are noted for each of the slip systems. There is strong agreement between $\alpha=2\gamma_s/\gamma_{usf}$ from the present calculations and most of the experimental data. There is disagreement for the b2(100)[001] system, which is predicted to be ductile but is an experimental cleavage plane. The high surface energy for the (100) plane causes $\alpha<1$ but this also makes it the most unlikely system to undergo any kind of deformation according to attachment energy ranking (24).

The stacking fault simulations estimate (010)[001] to be brittle, $\alpha=1$, which disagrees with experiments that showed this to be a slip (6) or cross slip (14) system. Dang et al (10) observed a reduced sensitivity to initiation for shock directions with a [001] component. They proposed these shock directions would activate slip on the experimentally observed (010)[001] system. The $\Phi(\mathbf{u})$-curve for the (100)[001] system is shown in Figure 3.4.4b. There are no local energy minimums on this slip system and it would emit full dislocations. However, the (010) surface energy is low resulting in $\alpha\sim1$ in Table 5.3. The (100)[001] system shown in Figure 5.17c can also resolve slip in the [001] direction and the high surface energy makes $\alpha=0.6$. This system also does not have a local energy minimum and would emit full dislocations. Both slip systems are sterically hindered, the (010)[001] system shown in Figure 5.1b by nonbonded H..H interactions and the (100)[001] system by nitro groups.

5.4 Validation

5.4.1 (010)[100] Stable Stacking Fault Bulk Properties

In this section we determine the fully relaxed αRDX stacking fault energy for the stable stacking fault created on the b2(010)[100] slip system by shifting the lattices by ½[100] relative to one another. This stacking fault occurs at the local energy minimum in Figure 5.7 and is the stable stacking fault configuration shown in Figure 5.19c in Section 5.3.1.

The experimental unit cell given by Choi and Prince (25) is used to create this stable stacking fault structure. The origin of the unit cell is shifted by ¼[010] to create a unit cell with faces given by the low energy b2 interface shown in Figure 4.4. A 3×3 layer of b2 unit cells are created on the (010) plane. Two types of stacking faults are created in this work. The first type shown in Figure 5.21a is called the orthogonal stacking fault and is created with orthogonal simulation cell vectors. The orthogonal SF is created by stacking $2n$ layers of unit cells in the [010] direction and then shifting the top n layers by the stacking fault vector, $\mathbf{f}$=½$\mathbf{a}$[100]. The simulation cell now contains two stacking faults as shown in Figure 5.21a where one is within the simulation cell and another stacking fault is created between the periodic images. The interface between the stacking faults must be opened to accommodate the rigid stacking fault structure, which was shown to open by Δ_r=1.4 Å in Figure 5.6. This is accomplished by separating the top n layers by Δ_r=1.25Å from the bottom n layers and then increasing the simulation cell vector in the $\mathbf{b}$-direction by $2\Delta_r$=2.5Å.

The second type of stacking fault shown in Figure 5.21b-d is call the skewed stacking fault, created from skewed simulation cell vectors. It is created by replicating

the 3×3 layers n times in the [010] where n is the number of layers between stacking faults. The simulation cell lattice vector initially in the [010] direction is skewed along the stacking fault vector, $\mathbf{f}=\frac{1}{2}a$[100] and the length of the simulation vector is increased the **b**-direction by $\Delta_r=1.25$Å. This creates a single stacking fault between the periodic images in the [010] direction.

The stacking faults in Figure 5.21a and b both create stacking faults separated by $n=1$ layer and are energetically equivalent. The orthogonal SF shown in Figure 5.21a required the simulation cell to be twice as large as the skewed SF in Figure 5.21b. For $n=3$ to 14, the skewed SF is used to create stacking faults. The orthogonal SF must be used for $n=1$ or 2 because the simulation must be at least twice as large as the real space cut-off used to calculate the nonbonded interactions, which was $r_{cut}=15$Å.
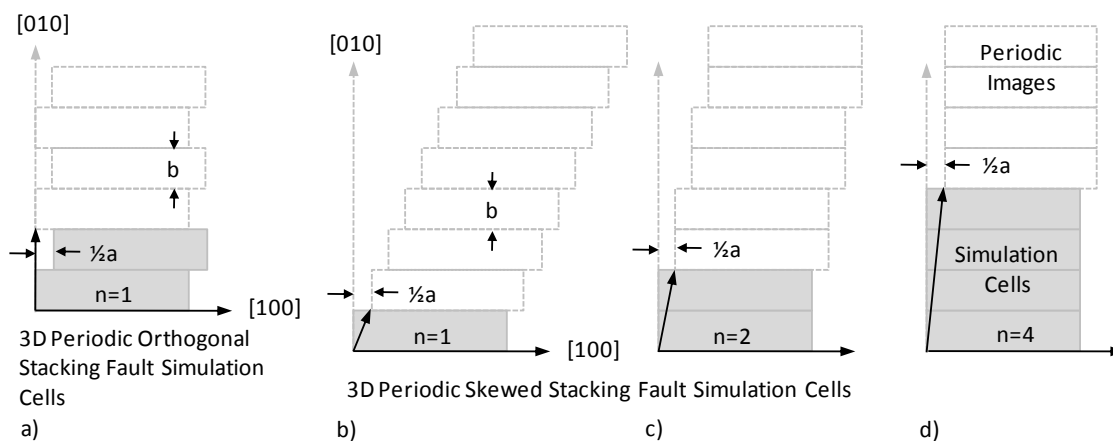
Figure 5.21: Stacking fault simulation cells where simulated material is shown in gray and periodic images are shown by the dashed lines. The black arrows are the simulation cell vector. a) Orthogonal stacking fault created with orthogonal simulation cell vectors. A stacking fault is created within the simulation cell and on the periodic boundary. b) Skewed stacking fault created by skewing the simulation cell vectors to create a single stacking fault between periodic images.

In these simulations, all of the molecules within the simulation cell are modeled as fully flexible molecules. These stacking fault structures are minimized using an

isenthalpic ensemble at P=0GPa and a Langevin thermostat. No constraints are placed on the isenthalpic ensemble and lattice vectors and their angles relative to one another are able to change during quenching. The structure is initially equilibrated at T=300K for 0.1ps with 0.1fs integration steps to allow the flexible molecules on the stacking fault interface to relax and assume the stable stacking fault structure. The structure is then quenched from T=300K to 0K over 10ps with a 1fs integration timestep. The quenched structure is then equilibrated at T=20K for 10ps and then quenched again from T=20K to 0K over 10 ps. The final equilibration and quenching step is an attempt to bring the structure closer to the minimized configuration. The quenched stacking fault structure is then recursively minimized with atomic and volume relaxations.

Results from the stable stacking fault simulations are shown in Figure 5.22 where the x-axis is n, the number of unit cells between stacking faults. The black line is for the orthogonal SF's in Figure 5.21a, which contain multiple stacking faults within the simulation cell. The red line is for skewed SF's shown in Figure 5.21b, which uses a skewed simulation cell to create a stacking fault between the periodic images. Both types of stacking faults were created for n=3 and 4 and the energy and geometry data in Figure 5.22 agree well for both methods.

Figure 5.22a shows the change in energy per molecule caused by the stacking fault given by

$$\Delta U = U_{SF} - U_{bulk} Z_{SF}/Z_{bulk} \quad\quad\quad (5.18)$$

where U_{SF} is the energy of the system with the stacking fault, U_{bulk} is the energy of the perfect crystal, and Z_{SF} and Z_{bulk} are the number of molecules in the stacking fault and perfect crystal simulation cell, respectively. The amount of perfect crystal within the

simulation cell is increased by increasing the distance between stacking faults, which

lowers the energy per molecule of a single stacking fault.
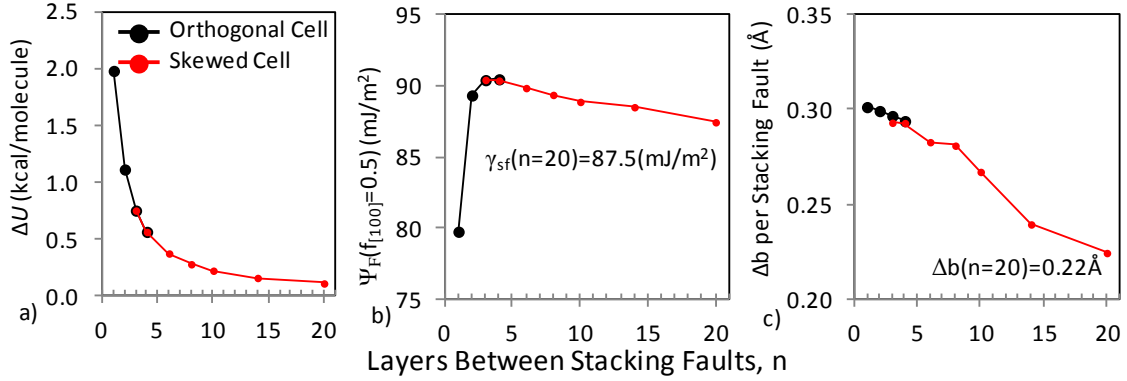
Figure 5.22: Stacking fault simulations where the black line is for orthongal SF simulation cells shown in Figure 5.21a and the red line is for the skewed SF simulations cells shown in Figure 5.21b-d. The x-axis is the number of layers between stacking faults. a) Change in energy due to the stacking fault per molecule and b) per unit area of stacking fault interface. c) Change in b-lattice length per stacking fault.

The stacking fault energy per unit area of stacking fault interface is shown in Figure 5.22b and is given by

$$\Psi=(U_{SF}-U_{bulk}Z_{SF}/Z_{bulk})/n_{SF}A \quad\quad\quad (5.19)$$

where A is the area of the (010) plane given by $3|\mathbf{b}|\times 3|\mathbf{c}|$ and n_{SF} is the number of stacking faults in the simulation cell. Equation (5.19) scales up the bulk energy, U_{bulk}, to the size of the stacking fault super cell. The skewed SF's have a single stacking fault (n_{SF}=1) and the orthogonal SF's have $n_{SF}\geq 2$.

Figure 5.22b shows the lowest stacking fault energy to occur for n=1, which was $\gamma_{sf}(n=1)$=79.7mJ/m^2, and not at the largest stacking fault separation distance of n=20. In This is an unexpected result and could be due to a number of different factors. Figure 5.22a, n=1 is by far the highest energy structure and n increasing n decreases the energy per molecule in the system. For n=1, the stacking faults are separated by $|\mathbf{b}|$=11.33Å,

178

which should be far enough to shield atomic interactions between stacking faults. This suggests that the decrease in SF energy for $n=1$ compared to $n=20$ is due to the strain field the stacking faults induce on one another. The maximum stacking fault energy occurs for $n=3$ or 4 and for $n>4$ the stacking fault energy decreases. At $n=20$, the stacking fault energy is $\gamma_{sf}(n=20)=87.5$ mJ/m^2 and may slightly decrease further for larger n.

The stable stacking fault causes the **b**-lattice vector to increase in length. Each stacking fault was initially separated by 1.25Å in the [010] direction. The flexible molecules next to the stacking fault change their conformation and orientation during quenching allowing them to reduce the interfacial energy and the separation. Figure 5.22c gives the increase in the **b** lattice length per stacking fault given by

$$\Delta_f=(L_{SF}-L_{bulk}Z_{SF}/Z_{bulk})/n_{SF} \tag{5.20}$$

where L_{SF} and L_{bulk} are the simulation cell length in the [010] direction for the stacking fault and bulk structure, respectively. The change in lattice length for each stacking fault decreases as n increases. Increasing the number of layers between stacking faults increases the amount of bulk crystal to absorb the change in lattice length. However, this difference is small where $\Delta_f(n=1)=0.30$Å and $\Delta_f(n=20)=0.22$Å. The lattice vectors are free to expand or contract due to the isenthalpic ensemble with a set point pressure of $P=0$GPa. The strain resulting from the lattice expansion is not accompanied by a change in stress and the stacking fault does not create any elastic energy in the system.

A second set of simulations are used to determine the interaction of two stacking faults separated by a variable number of layers. For these simulations a single stacking fault is created within the simulation cell and a second stacking fault is created on the

periodic boundary, as shown in Figure 5.23a. The first stacking fault is created a fixed distance of n_a=10 layers from the bottom of the simulation cell. This stacking fault is separated by n_b=1 to 10 layers from the top of the simulation cell where the second stacking fault is created. The previous set of stable stacking fault simulations show the stacking faults to be weakly interacting for n=10 in Figure 5.22b. The first stacking fault disregisters the lattice and the second stacking fault returns the lattice to the unfaulted structure. This creates a lattice containing a layer of faulted material n_b layers thick. The same equilibration, quenching, and minimization procedure used for the other stacking fault simulations are used again here.
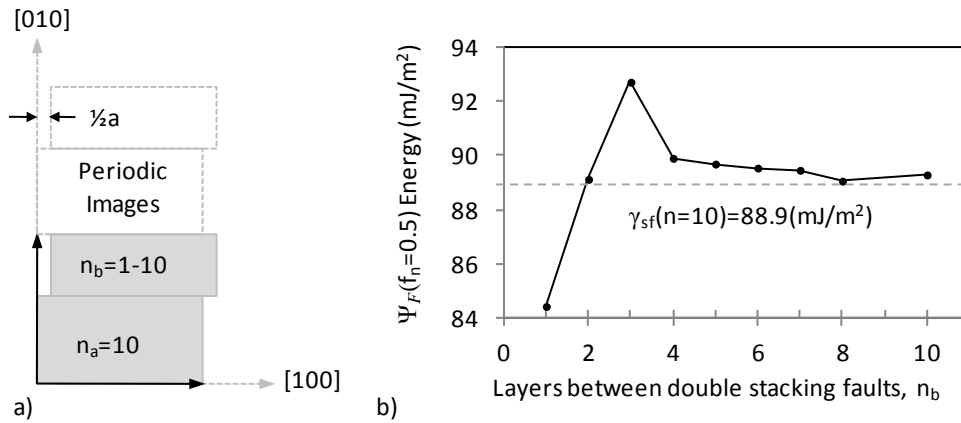
Figure 5.23: a) Double stacking fault simulation cell where layers between consecutive stacking faults is n_b=1-10 and fixed number of layers between stacking faults is 10. b) Stacking fault energy, which converges to the stacking fault energy for n=10 in Figure 5.22b, shown by the dashed line and labeled on the plot.

The stacking fault energy given by equation (5.19) with n_{SF}=2 is plotted in Figure 5.23b. The lowest energy stacking faults are again found for n_b=1. The maximum stacking fault energy occurs for n_b=3. For n_b>3 the stacking fault energy converges to $\gamma_{sf}(n$=10)=88.9mJ/m^2 from Figure 5.22b and shown by the dashed line on the chart. This set of simulations shows that two stacking faults next to one another (n_b=1) are lower in

energy than a single stacking fault in the bulk material where $\gamma_{sf}(n_b=1)=84.4\text{mJ/m}^2$ and $\gamma_{sf}(n=20)=87.5\text{mJ/m}^2$. This may indicate that a leading partial dislocation would be closely followed by a trailing partial.

5.4.2 αRDX Flexible Layer Thickness

Elastic shearing of the flexible molecule layer is an unwanted side effect of allowing the flexible molecules to change conformation and orientation to reduce the stacking fault energy. The flexible layer thickness, h_f, must be large enough to allow for molecule orientation and conformation changes but small enough to limit shear motion. To study the effect of h_f, three flexible models will be compared for the b2(010)[100] stacking faults: $h_f=|\mathbf{b}|/2$, $h_f=|\mathbf{b}|$, and $h_f=20|\mathbf{b}|$. The results from the model with $h_f=|\mathbf{b}|/2$ were presented in Section 5.3.1. The model with $h_f=20|\mathbf{b}|$ is the skewed stacking fault from Section 5.4.1 containing only flexible molecules and no vacuum layer or rigid molecule layers.

All three models stabilize the stable stacking fault configuration at $f_{100}=u_{100}=0.5$. The stable stacking fault energies for the systems were found to be $\gamma_{sf}=101$, 95, and 88 mJ/m^2, respectively. The interfacial opening at the stable stacking fault was δ=0.24, 0.23 and 0.22 Å, respectively. The $h_f=20/|\mathbf{b}|$ model is the least constrained and the most physically realistic model. The percent error between $h_f=20/|\mathbf{b}|$ and the other models for γ_{sf} is 14% for $h_f=|\mathbf{b}|/2$, which drops to 8% for $h_f=|\mathbf{b}|$. Increasing $\underline{h}_f$ also drops the error in interfacial displacement from 10% to 5%. This is the only structure the $h_f=20/|\mathbf{b}|$ model is able to stabilize. Due to the permitted flexibility of the $h_f=20/|\mathbf{b}|$ model, the fault will slip completely into the stable fault configuration or unslip completely into a sheared lattice configuration.

Both $h_f=|\mathbf{b}|/2$ and $|\mathbf{b}|$ start from the same rigid stacking fault structures but the change in the flexible layer thickness allows them to shear differently. The amount of shear stress and strain that develops in the flexible layers is shown in Figure 5.24a and b where the black data is for $h_f=|\mathbf{b}|/2$ and red data is $h_f=|\mathbf{b}|$. Even though the $h_f=|\mathbf{b}|$ layer is more mobile, it develops a lower amount of the shear stress and strain in the flexible layer. The total elastic strain energy in the flexible layers is shown in Figure 5.24c and is nearly equal for both layer thicknesses.
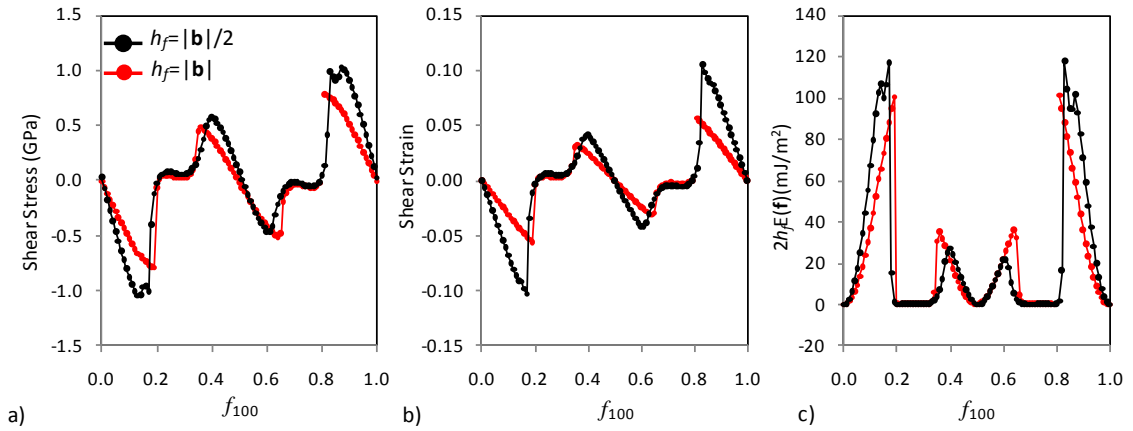
Figure 5.24: Comparison of a) shear stress, b) shear strain and c) total elastic strain energy in the flexible layers for $h_f=|\mathbf{b}|/2$ (black) and $h_f=|\mathbf{b}|$ (red).

The final flexible $\Phi(u_{100})$ energies are shown in Figure 5.25a. The curves are nearly identical for both layer thicknesses. The $h_f=|\mathbf{b}|$ model gives slightly less data points in unstable regions. Both models are in exact aggreement at the the unstable stacking faults, $f_{100}=0.2$ and 0.8, with unstable stacking fault energy, $\gamma_{usf}=164\text{mJ/m}^2$. The largest variation in $\Phi(u_{100})$ occurs near the stable stacking fault where the increased layer thickness of $h_f=|\mathbf{b}|$ allows the molecules to reach a lower energy closer to the actual value as previously discussed. The interfacial opening in Figure 5.25b shows similar

agreement between the two models. The maximum opening at the unstable stacking fault (f_{100}=0.2 or 0.8) for both models is 1Å.
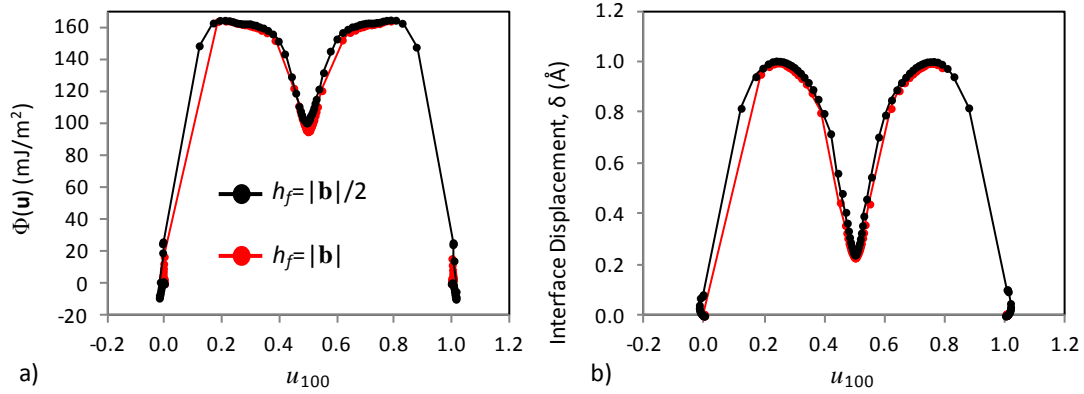
Figure 5.25: a) Flexible $\Phi(\mathbf{u})$ energy for h_f=|$\mathbf{b}$|/2 (black) and h_f=|$\mathbf{b}$| (red). Flexible intefacial opening, δ.

Both layer thicknesses are in good agreement for all of the f_{100} flexible stacking faults. The increased molecule mobility for the h_f=|$\mathbf{b}$| model allows it to reach a lower stable stacking fault energy that is in better agreement with the actual value given by h_f=20|$\mathbf{b}$|. However, both h_f=|$\mathbf{b}$| and h_f=|$\mathbf{b}$|/2 are in perfect agreement for the unstable stacking fault energy and interfacial opening. The additional degrees of freedom in the h_f=|$\mathbf{b}$| model makes it more computationally expensive and difficult to quench. Given the fact that the GSF energy is a theoretical construct useful for estimating properties of crystals, h_f=|$\mathbf{b}$|/2 was used to determine all of the GSF energies in Section 5.3 and is a limiting case that accounts for the molecular features while still permitting unstable stacking fault configurations.

The flexible layer thickness used here as |$\mathbf{b}$|/2 is the interplanar spacing, d_{hkl}, specified in the attachment energy calculations. This interplanar spacing was adjusted by the extinction conditions of the space group, reducing it from |$\mathbf{b}$| to |$\mathbf{b}$|/2. The space

group symmetry operators such as a glide plane, screw axis, and inversion center are necessary to create a translationally invariant unit cell but do not create a unique layer of molecules. Instead, layers in the unit cell are just a rotation or reflection of one another. In this work, using a flexible layer thickness of d_{hkl} includes all of the degrees of freedom of a unique layer of molecules. For the other slip plane, $h_f = d_{hkl}$, as specified in Table 5.1.

5.4.3 Validation of Interface Selection

In RDX and several other crystals, each crystal plane contains two unique interfaces, which we identify as b1 and b2. In Section 4.4, decohesion was shown to occur at a lower maximum stress on the interface with the lower attachment energy. Likewise, slip will occur on the interface with the lower unstable stacking fault energy determined from the GSF energy. The GSF energy calculation is computationally expensive and it is therefore preferred to reduce the number of planes it is determined for. The attachment energy is commonly used to identify weakly bonded layers in a crystal that are likely to undergo slip or cleavage (24) (5). In this work, the attachment energy is only used to rank the interfaces on each plane for slip or cleavage. This is opposed to using it to rank planes against one another, which was shown to be only ~50% accurate in identifying the experimental slip or cleavage planes (5).

In this section the GSF energy will be determined for both the b1 and b2 interfaces for the (010)[100], (010)[001], (011)[100], and (011)[0$\bar{1}$1] slip systems. The (010) and (011) planes are experimental slip planes. The GSF energy for the (010)[100] and (011)[100] experimental slip systems were also shown to have stable stacking fault structures in Section 5.3.3. It will be shown that for these slip systems the attachment energy identifies the correct slip plane interface.

The two different (010) slip plane interfaces are shown in Figure 4.4. The b1 interface between the blue and grey molecules contains the molecules on the face of the experimental unit cell (25). The b2 interface shown between the red and grey molecules was created in the interior of the unit cell. The b2 interface was shown in Table 4.1 to be lower in attachment energy by 10.3kcal/mol/molecule or 208 kJ/m^2. This is the largest difference in b1-b2 attachment energies for all the planes. It would be expected that such a large difference in attachment energies causes the GSF energy on these two interfaces to be very different.

In Figure 5.26, the $\Phi(\mathbf{u})$ energy for the (010) plane is shown for the b1 interface in red and the b2 interface in black. The b1 interface has a much higher GSF energy for both slip systems. In Figure 5.26a, the b1(010)[100] system also shows a stable stacking fault that is ~50mJ/m^2 higher than the b2 stable stacking fault. Most of the b1(010)[100] stacking faults shear back to u_{100}=0 or 1 or to the stable stacking fault. The b1(010)[001] stacking faults in Figure 5.26b are are very unphysical and result in a very high GSF energy. Only a portion of the $\Phi(\mathbf{u})$ energy is shown because for 0.1<u_{001}<0.9 the energy increases to >1000mJ/m^2. For these stacking faults it would be much more energetically favorable for the interface to create a free surface. However, the interaction forces did not result in a normal force large enough to separate the flexible stacking fault surfaces. This is one instance where the rigid stacking faults provide unreasonable starting configurations for the flexible stacking faults.
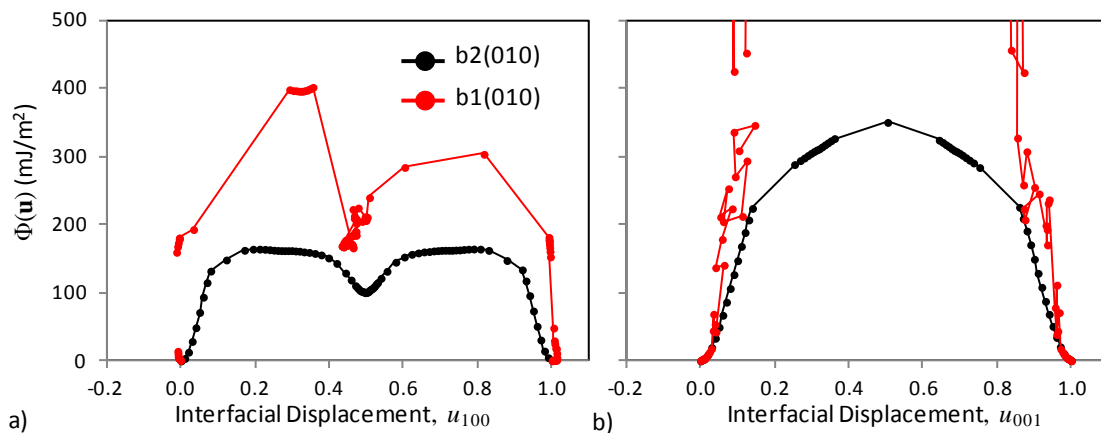
Figure 5.26: a) Flexible $\Phi(\mathbf{u})$ energy for the (010) interface where the b1 interface is shown in red and the b2 interface is shown in black. a) (010)[100] slip system b) (010)[001] slip system.

The (011) layers used to create the b1 and b2 slip plane interfaces are shown in Figure 4.6. The b1 slip plane is between the blue and grey molecules and has a lower attachment energy than the b2 layer shown between the red and grey molecules. The difference in the attachment energies (Table 4.1) for these two layers is only 1kcal/mol/molecule or 34 mJ/m2. This is the second smallest difference between attachment energies for the two b1 and b2 interfaces for a plane. The b2 interface was shown to undergo decohesion at a slightly smaller maximum stress in Figure 4.17 in Section 4.3. With the attachment and free surface energies being so close, the GSF energies should also be similar.

Figure 5.27 gives the $\Phi(\mathbf{u})$ energy for the (011) plane where the b1 interface is shown in black and the b2 interface in red. In Figure 5.27a for the (011)[100] slip system, the b1 interface is lower in energy. The b2 interface does not show a stable stacking fault and γ_{usf}=450mJ/m2; 150mJ/m^2 higher than the b1 interface. The free surface energies for the b1 and b2 interfaces given in Table 4.4 for $2\gamma_{slab}$ are 465 mJ/m^2 and 521mJ/m^2, respectively. The b2 surface γ_{usf} is high enough to create a free surface on the b1

186

interface but not the b2 interface. In Figure 5.27 for the (011)[0$\bar{1}$ 1] slip system, γ_{usf} for the b2 interface is 380mJ/m^2; 50 mJ/m^2 less than the b1 interface at 430 mJ/m^2. This is still a high γ_{usf} and the ratio $\gamma_{usf}/2\gamma_{slab}$=0.8 means this interface is still close to being brittle according the Rice criterion (18).
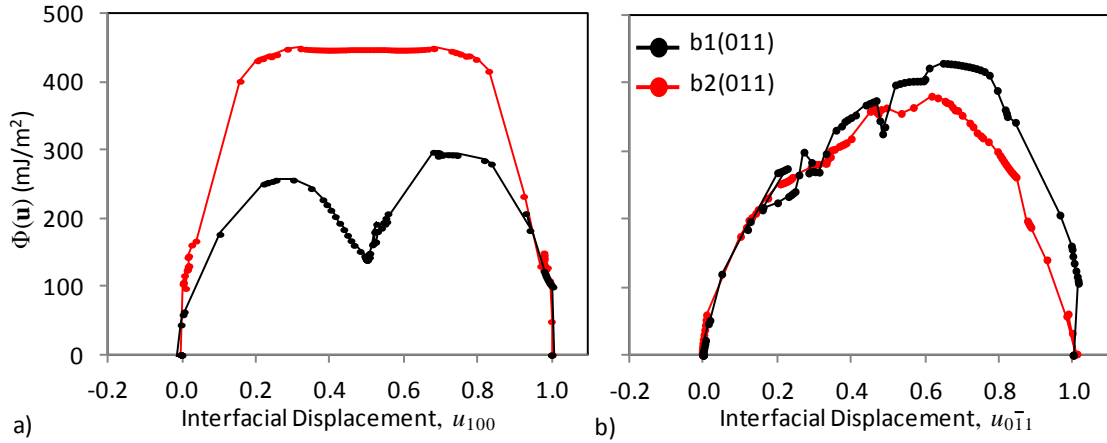
Figure 5.27: a) Flexible $\Phi(\mathbf{u})$ energy for the (011) interface where the b1 interface is shown in black and the b2 interface is shown in red. a) (011)[100] slip system b) (011)[0$\bar{1}$ 1] slip system.

Overall, the attachment energy works well in identifying the probable slip interface when multiple unique layers exist on a given plane. The attachment energy is easy to calculate and is implemented in several commercial molecular modeling suites like Accelrys Material Studio. Several of the flexible stacking fault simulations the b1(010) simulations failed due to high energy starting configurations. For the (011)[0$\bar{1}$ 1] sytem, the attachment energy predicted the wrong slip plane interface. However, the unstable stacking fault energy was still high and would probably result in cleavage.

5.4.4 Validation of Simulation Method: Nickel GSF

The interfacial GSF energy, $\Phi(\mathbf{u})$, given by equation (5.2) will be validated here for Nickel. Several studies in literature have determined the GSF energy of nickel and will be used to validate the interfacial GSF energy method against. Nickel crystallizes into an FCC lattice with 4 atoms per unit cell. The unit cell contains four Ni atoms with lattice constant a=3.52Å. On the {111} close packed planes in FCC crystals, the layer packing follows an ABCABCABC order shown in Figure 5.28b. An intrinsic stacking fault results when the blue plane is displaced relative to the red plane to create the stacking sequence AB**CBC**ABCABC. Local stacking faults occur on the {111}<112> family of slip systems and result in a local minimum of the GSF energy curve.

In this section the GSF energy surface will be determined for the (111) plane. The Ni unit cell is cubic and the lattice vector given by [hkl] is normal to the plane given by (hkl). The Ni lattice is oriented in the simulation cell as shown in Figure 5.28 where the ($\mathbf{n,q,t}$) orthonormal coordinate system describing the slip plane is $\mathbf{n}$=[111], $\mathbf{t}$=[2̄11] and $\mathbf{q}$=[011̄]. In Figure 5.28, $\mathbf{n}$ and $\mathbf{t}$ are shown by the axes where $\mathbf{n}$=[111] is up and $\mathbf{t}$=[2̄11] points left. Slip in the [2̄11] direction creates a stacking fault when $f_{211}=a\sqrt{6}$ as shown in Figure 5.28c. The Ni unit cell is replicated to give 15 complete lattices normal to the slip plane and a 3×3 unit cell slip plane in the [2̄11] and [011̄] directions. The simulation cell is 2D periodic in the plane of the slip system, and nonperiodic in the $\mathbf{n}$-direction.
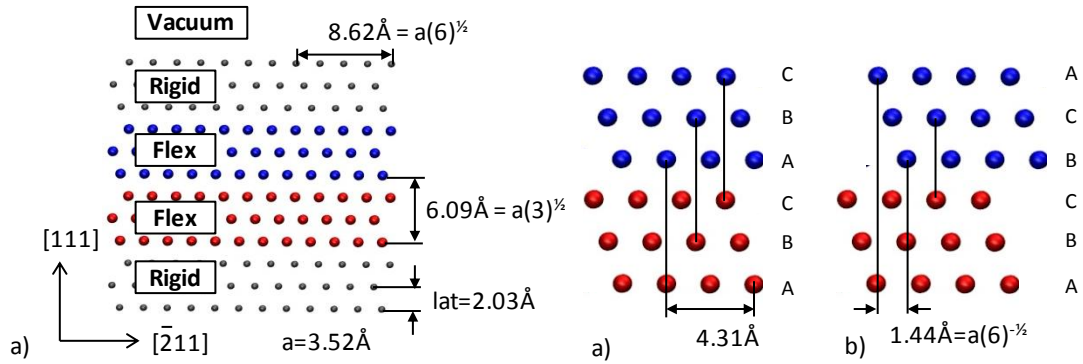
Figure 5.28: a) Nickel simulation cell used for (111) stacking fault simulations. Red and blue layers are treated as flexible atoms. The grey region represents the rigid Ni lattice. b) Cubic close packed layer sequence ABCABC. c) Intrinsic stacking fault with layer AB**CBC**A created by shifting the blue layers of atoms in the [02 1] direction.

The potential function describing the Ni atoms is given by the embedded atom model (EAM). EAM potentials describe atomic interactions based on the local atomic density and separation distance. The density dependence describes the electronic bonding of atoms and is determined by fitting the model to Density Functional Theory (DFT) simulations (50). The Ni potential used here was determined by Mishin and Farkas (MF) (94). The MF potential was used in large scale simulations of dislocation in nickel nanocrystals (1). It was also used to determine GSF energies in Nickel (95) and those results will be used to here as validation. The simple Ni crystal with the EAM potential has a much smoother potential energy surface than the SB potential applied to RDX and therefore will be much easier to minimize.

Five different GSF energies are determined and presented in Figure 5.29 for (111)[2 11] slip system. The GSF curves shown in Figure 5.29 are created from 100 stacking faults created for f_{211}=0 to 4.31Å. The GSF energy given by rigidly displacing the lattices relative to one another across the slip plane by **f** results in $\Psi_o(\mathbf{f})$ given by equation (5.1) and is shown in red. This is the unrelaxed and highest energy structure.

The energy of the atomic configuration given by $\Psi_o(\mathbf{f})$ is then minimized by allowing the atoms to move normal to the slip plane with the volume held fixed, giving the GSF energy $\Psi_{min}(\mathbf{f})$, shown in green. This is the lowest energy configuration. This same procedure is repeated with volume relaxation normal to the slip plane giving the GSF energy $\Psi_{min\Delta}(\mathbf{f})$, shown in blue. For some materials this has the lowest energy. These are the common procedures used to determine the GSF energy in literature (90) (95) (96) where in-plane atomic motion is not allowed. The stable and unstable stacking fault energies shown in Figure 5.29b are listed in Table 5.4 along with those given in literature (95).

The other two GSF energies given in Table 5.4 are those presented in Section 5.1. These are alternative methods of reducing the GSF energy given by $\Psi_o(\mathbf{f})$. The configuration given by $\Psi_o(\mathbf{f})$ is treated as two separate rigid bodies that separate across the interface by Δ_r, resulting in the rigid GSF energy $\Psi_R(\mathbf{f})$ shown in black. For Ni, this results in only a slight decrease in energy because the slip plane is unobstructed. The $\Psi_R(\mathbf{f})$ configuration is then restarted with a flexible layer of nickel atoms, shown by the red and blue layers in Figure 5.28, which are allowed to shear, resulting in the interfacial GSF energy, $\Phi(\mathbf{u})$ given by equation (5.2), and shown by the purple data points. The purple line is from the minimums of the $\Phi(\mathbf{u})$ relaxation histories shown in Figure 5.30 and Figure 5.32. Each red and blue flexible layer thickness is one unit cell in the [111]-direction, $h_f = a(3)^{\frac{1}{2}} = 6.09\text{Å}$.
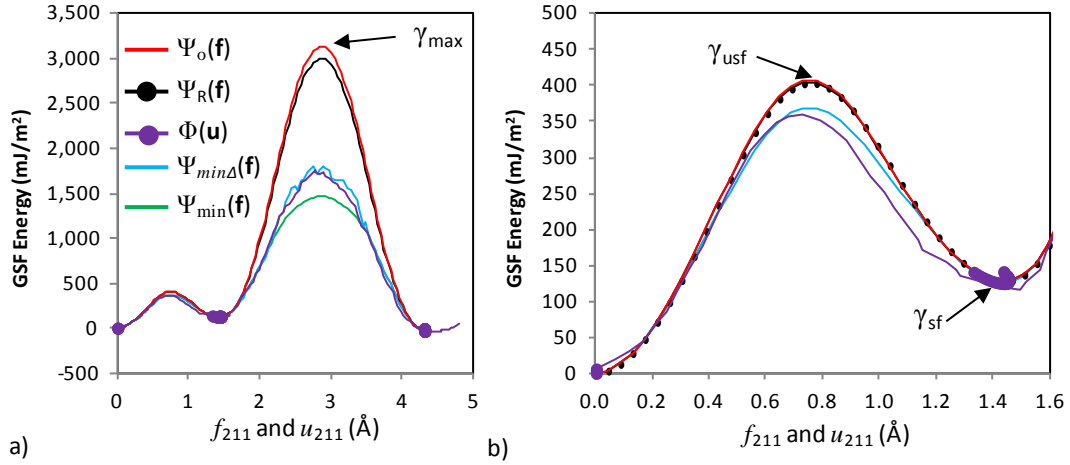
Figure 5.29: a) GSF energies of the entire (111)[02 1] stacking fault. b) GSF energies up to the stable stacking fault configuration.

Table 5.4: Comparison of stable, unstable, and maximum GSF energies.

	γ_{usf} (mJ/m^2)	γ_{sf} (mJ/m^2)	γ_{max} (mJ/m^2)
Gao[a] $\Psi_o(\mathbf{f})$	405	129	NA
$\Psi(\mathbf{f})$	405	129	3130
$\Psi_{min\Delta}(\mathbf{f})$	367	125	1805
$\Psi_{min}(\mathbf{f})$	368	125	1466
$\Psi_R(\mathbf{f})$	406	141	3135
$\Phi(\mathbf{u})$	360*	125	1750*

[a]Reference (95), *From $\Phi(\mathbf{u})$ relaxation history

The flexible layers allow the interface of the flexible stacking fault structures to shear all the way to the local minimums on the GSF energy curve. This is indicated by all of the purple dots in Figure 5.29 being bunched up near the origin, local minimum, or next equivalent lattice site at $u_{211}=4.31$Å. Figure 5.30 shows the region up to the stable stacking fault. The relaxation histories for two data points are shown by the colored lines in Figure 5.30a. The relaxation histories show the path the interface takes as the flexible atoms are quenched from the rigid stacking fault structure. The green line is for $f_{211}=0.73$Å, which shears back to the origin where the interface follows the green line as the energy is relaxed. The interface oscillates around the origin as the kinetic energy is quenched from the system. In this configuration the system only contains elastic shear

energy and no energy due to a mismatched lattice. The blue line is for f_{211}=0.91Å and the interface shears to the stable stacking fault structure, u_{211}=1.35Å. The kinetic energy allows this stacking fault interface to overshoot the minimum energy curve near the stable stacking fault. As the kinetic energy is quenched from the system the interface settles to the stable stacking fault structure. The interfacial GSF energy given by equation (5.2) uses the potential energy and is really only applicable in the absence of kinetic energy. The interfacial GSF energy becomes less accurate as the kinetic energy or temperature of the system increases, leading to the GSF energies that are less than the minimum energies. In the stable stacking fault configuration given by the blue line the system contains elastic shear energy and energy due to the stacking fault. All of the relaxation histories are shown in Figure 5.30b and the minimum energy from the relaxation histories are used to determine the $\Phi(\mathbf{u})$ relaxation history shown by the purple line in Figure 5.29.
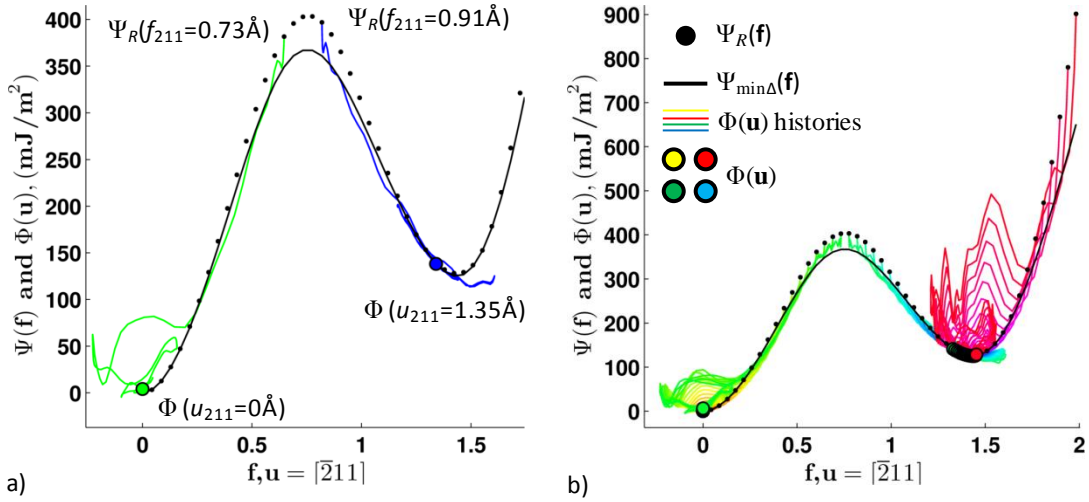
Figure 5.30: a) (111)[02 1] rigid $\Psi_R(\mathbf{f})$ energy shown by black dots relaxed to the flexible interfacial $\Phi(\mathbf{u})$ energy along the relaxation history paths. b) All of the relaxation histories. Error caused by kinetic energy causes some of the relaxation history data to fall below the $\Psi_{min\Delta}(\mathbf{f})$ curve, shown by the black line.

The amount of shear stress that develops in the flexible layers is shown in black in Figure 5.31a. The stress is calculated from the virial theorem given by equation (5.4). The shear strain in the flexible layer calculated from the COM motion using equation (5.15) is shown in green. The shear strain and stress are both linear functions of the stacking fault vector f_{211} indicating the material has a linear stress/strain relationship. The shear strain and stress are used to calculate the linear elastic strain energy using equation (5.3) and is shown in red in Figure 5.31.

The energy of the flexible stacking fault system containing elastic shear and lattice mismatch energy is $\Psi_F(\mathbf{f})$ and is shown in black in Figure 5.31b. The elastic strain energy and $\Psi_F(\mathbf{f})$ match almost exactly up to the unstable stacking fault energy and then again after the maximum stacking fault energy. These are the configurations where the flexible stacking fault interfaces shear back to the origin or to the next equivalent lattice site, shown by the purple data points. In the central stable stacking fault region, the $\Psi_F(\mathbf{f})$

energy is offset from the elastic energy by the stable stacking fault energy, γ_{sf}. In this region, all of the flexible stacking faults shear to the stable stacking fault structure also indicated by the purple data points. The interfacial $\Phi(\mathbf{u})$ energy accuratly represents the lattice mismatch energy and does not include any of the effects of lattice shear. The interfacail displacement, $\mathbf{u}$, is accurately determined from the flexible layer COM motion and the kinematic relationship given by $\mathbf{F}$ in equation (5.12a).
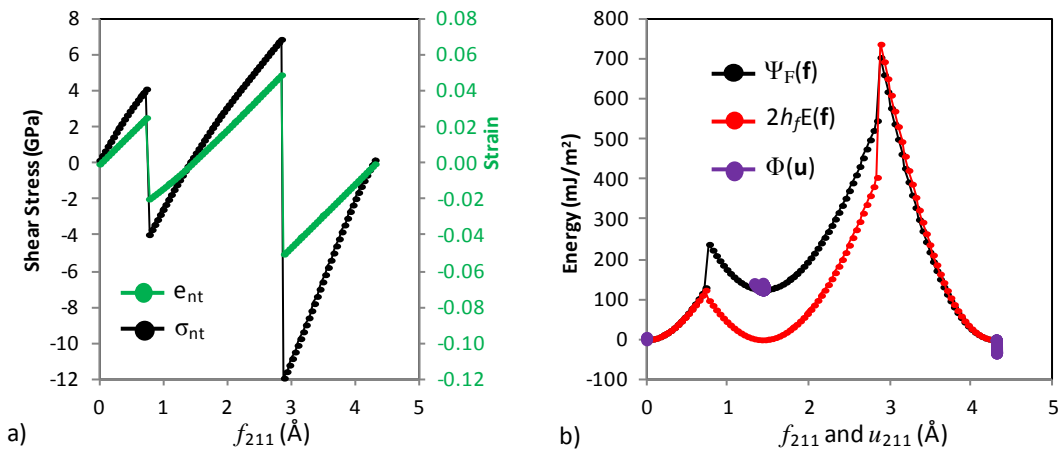
Figure 5.31: a) Shear stress and strain in for the (111)[02 1] flexible stacking fault structures calculated form the flexible layer COM positions. b) Flexible $\Psi_F(\mathbf{f})$ energy shown in black is equal to the elastic energy, $2h_fE(\mathbf{f})$ shown in red up to the stable stacking fault. $\Phi(\mathbf{u})$ energy shown in purple shears to the local minimum energies.

The entire interfacial GSF energy, $\Phi(\mathbf{u})$, must be determined from the relaxation history of $\Phi(\mathbf{u})$ since all of the quenched configurations are at local minimums. In Figure 5.32 all of the $\Phi(\mathbf{u})$ relaxation histories are shown in grey and the GSF energy given by $\Psi_o(\mathbf{f})$ is shown by the black dashed line. $\Psi_o(\mathbf{f})$ is the initial energy for all of the systems and the highest energy stacking faults. The volume relaxed GSF energy, $\Psi_{min\Delta}(\mathbf{f})$, is shown by the black line. The red line is the minimum $\Phi(\mathbf{u})$ energy from the relaxation histories. The blue line is a smoothed $\Phi(\mathbf{u})$ relaxation history and was plotted for $\Phi(\mathbf{u})$ in Figure 5.29. Gaussian smoothing is used to smear out the jagged data points by their five

nearest neighbors. The relaxation history data is a close approximation to the actual

minimized GSF energy given by $\Psi_{min\Delta}(\mathbf{f})$. Small errors in $\Phi(\mathbf{u})$ occur near the stable

stacking fault where the kinetic energy is not properly accounted for by equation (5.2).

Increasing the damping coefficient would slow down the rate of atomic relaxation giving

more accurate relaxation histories. For more complex potentials, this would cause the

lattice to possibly get stuck in local energy minimums but for the EAM potential this is

not an issue.
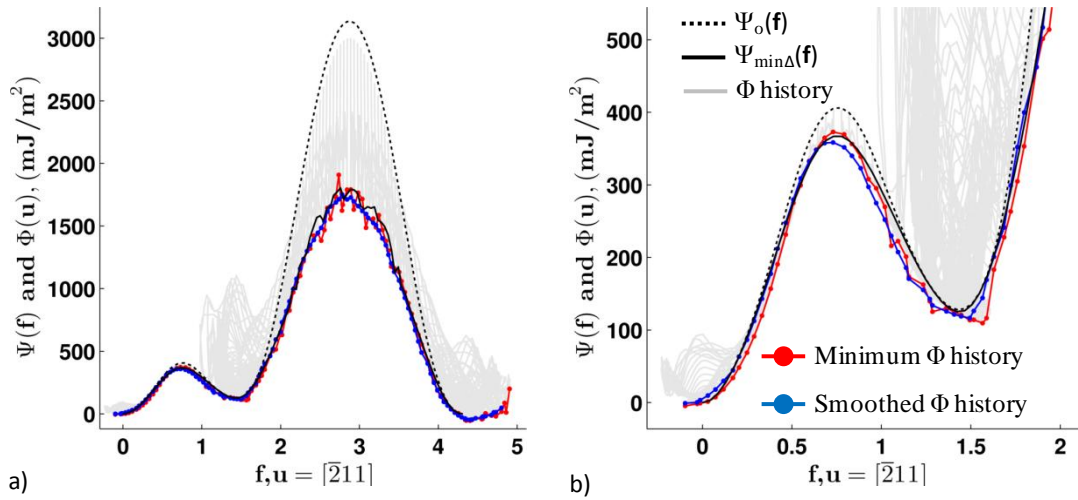
Figure 5.32: Flexible $\Phi(\mathbf{u})$ energy relaxation paths shown in gray. Blue and red lines trace out the minimum energies from the relaxation paths. The volume minimized GSF energy, $\Psi_{min\Delta}(\mathbf{f})$, shown in black matches the relaxation history in blue and red. a) Full (011)[02 1] curve. (b) (011)[02 1] curve up to stable stacking fault structures.

Very little energy is removed from the system by allowing the interface to rigidly

separate, shown by comparing $\Psi_o(\mathbf{f})$ and $\Psi_R(\mathbf{f})$ in Figure 5.29a. The largest difference

occurs near γ_{max}. The γ_{max} stacking fault represents an unphysical stacking fault where

two atoms come into very close contact across the slip plane. In reality, dislocations

move around the γ_{max} energy barrier to create full dislocations and this configuration is

not included in most studies (95) (1). However it provides the largest difference between

the different GSF energies and is considered here. The GSF energy given by $\Psi_o(\mathbf{f})$ does not allow any atomic relaxation. By allowing the lattices to rigidly separate across the slip plane, the GSF energy given by $\Psi_R(\mathbf{f})$ is slightly lower. The amount of lattice separation, Δ_r, and interfacial separation, δ are shown in Figure 5.33. The maximum rigid lattice separation at γ_{max} is Δ_r=0.007Å. The flexible lattice increases in length by Δ_f shown by the red data. The largest increase in Δ_f occurs for the stacking faults with the largest shear strains. The increase in lattice length for the volume minimized stacking faults given by $\Psi_{min\Delta}(\mathbf{f})$ are shown in blue and are much larger. All of the atoms in these stacking fault structures are minimized in the $\mathbf{n}$-direction allowing the entire lattice to strain normal to the stacking fault.

The interfacial opening, δ, is shown in Figure 5.33b. The interfacial opening of the volume minimized lattice, again shown in blue, is larger than its increase in lattice height. This indicates the volume minimized unit cell reduces the GSF energy by allowing the lattice to strain normal to the stacking fault. This mode of deformation is not allowed in our simulation method because of the use of rigid layers. The interfacial opening for the flexible lattice is shown by the purple data points and the relaxation history is shown by the purple line. The interfacial opening history is jagged but does not open further than the volume minimized stacking faults.
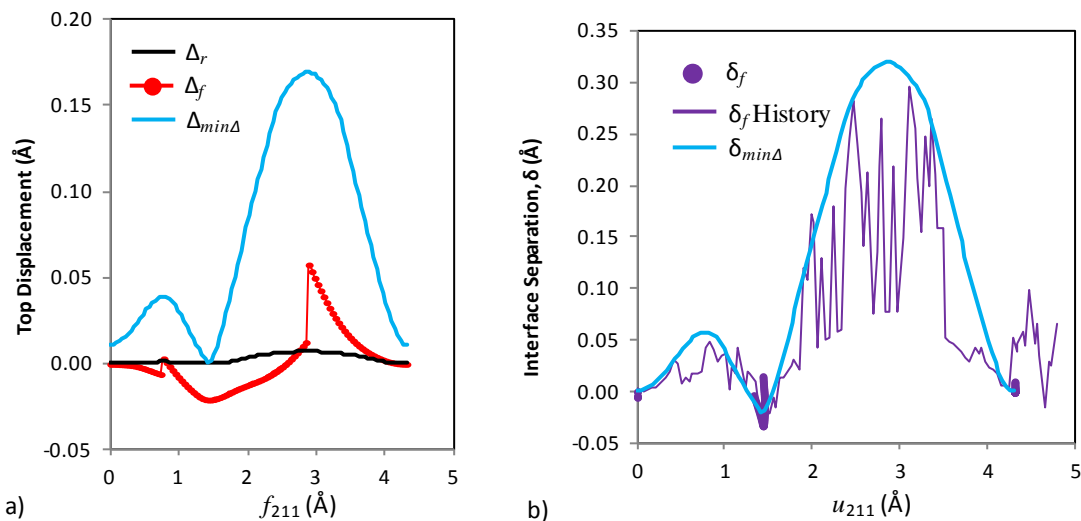
Figure 5.33: a) Change in lattice length of the rigid and flexible (011)[02 1] stacking fault structures (black and red) compared to the volume minimized lattice in blue. b) interfacial opening of the flexible lattice in purple where the purple lines are from the relaxation histories and the purple data points are the final quenched configurations. The intefacial opening of the volume minimized structure is shown in blue.

The entire Ni GSF energy surface for the (111) plane was then determined and is shown in Figure 5.34. A 40×40 grid of stacking faults were created in the first quadrant of the (111) plane with f_{011}=0 to 2.49Å and f_{211}=0 to 4.31Å. The first quadrant of the (111) plane in Ni can be translated in each direction to create the entire GSF energy surface. This was not the case for αRDX because each of the eight molecules in the space group had orientational degrees of freedom, unlike a single atom of Ni. The rigid GSF energy, $\Psi_R(\mathbf{f})$, is shown in Figure 5.34a. The energy contours are cut off at 500mJ/m^2 and regions of higher energy are shown in black. The [2 11] $\Psi_R(\mathbf{f})$ energy trace shown in Figure 5.29a is along the y-axis in Figure 5.34a. The regions labeled as "Bulk" point to locations where the GSF energy returns to zero. At these locations the stacking fault recreates the bulk perfect crystal structure. There are five "Bulk" locations in the quadrant of the $\Psi_R(\mathbf{f})$-surface; one in each corner and one in the interior. There are

also three stable stacking faults labeled by "γ_{sf}" and separating each stable stacking fault from the "Bulk" perfect crystal is the unstable stacking fault labeled by "γ_{usf}". The interior black regions are the maximum energy configurations and are labeled "γ_{max}". A dislocation on the (111) plane would move from a "Bulk" region along the colored contours over the unstable stacking fault labeled "γ_{usf}" and down to the local stable stacking fault, "γ_{sf}". To create a full dislocation and regain the bulk crystal structure interface, the partial dislocation at the stable stacking fault, "γ_{sf}", would continue moving along the colored contours over "γ_{usf}" and back to the "Bulk" configuration. This dislocation motion skips the high energy regions shown in black labeled "γ_{max}". This type of dislocation motion is described by the Shockley partial dislocation.
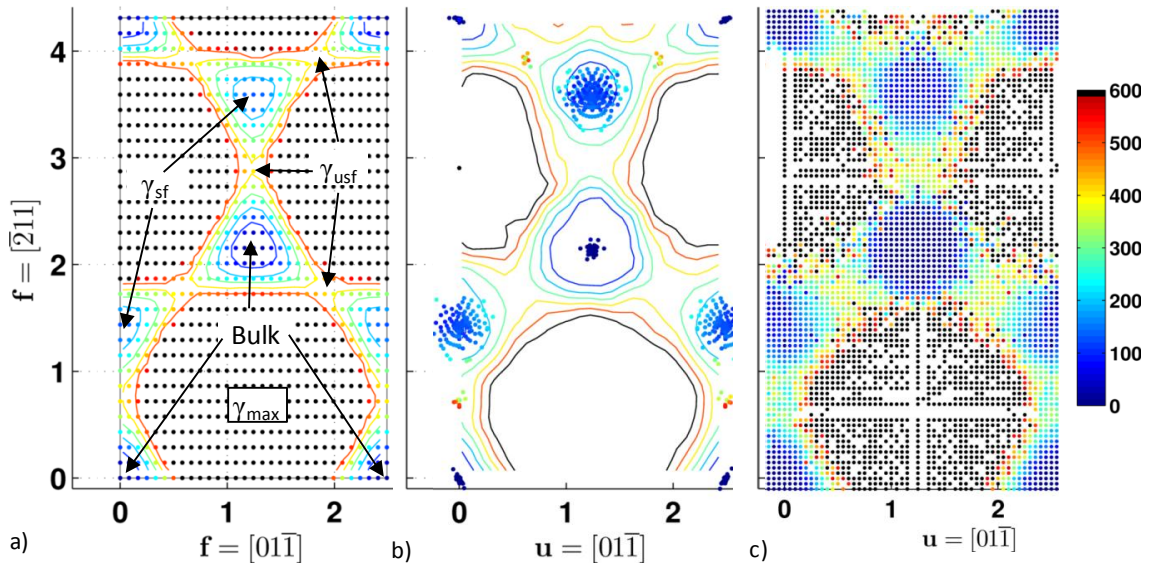
Figure 5.34: (111) GSF energy surfaces for a) rigid $\Psi_R(\mathbf{f})$ surface where each point is a rigid stackign fault configuration given by $\mathbf{f}$, b) flexible interfacial $\Phi(\mathbf{u})$ energy where the rigid stacking fault interfaces shear from $\mathbf{f}$ to $\mathbf{u}$ and c) $\Phi(\mathbf{u})$ energy relaxation histories. All GSF energies above 600mJ/m^2 are shown in black.

The interfacial GSF energy, $\Phi(\mathbf{u})$, is shown in Figure 5.34b. All of the data points at position $\mathbf{f}$ in Figure 5.34a shear to u in Figure 5.34b. All of the positions given by u

are local minimums. This amount of data is insufficient to determine the GSF energy surface. The GSF surface provides the energy barriers separating the stacking faults form the "bulk" configurations and the minimum energy path between the configurations.

The minimum energies from the interfacial $\Phi(\mathbf{u})$ energy histories are shown in Figure 5.34c. This data is used to create the contours in Figure 5.34b. The energy levels shown in color are for the stacking fault and unstable stacking fault regions shown in Figure 5.30. In this region the relaxed $\Phi(\mathbf{u})$ history curve should be only slightly lower in energy with a similar shape. The energy contours in Figure 5.34a and b have a similar energy range and give the same stable stacking fault energy. The unstable stacking fault energy from the $\Phi(\mathbf{u})$ energy history is below 400 mJ/m^2 (yellow contour level) and is slightly lower than that given by $\Psi_R(\mathbf{f})$. The energy difference between $\Phi(\mathbf{u})$ and $\Psi_R(\mathbf{f})$ is largest in the "γ_{max}" region and contours along "γ_{max}" will be much broader for the $\Phi(\mathbf{u})$ history data. The error caused by kinetic energy will also cause the $\Phi(\mathbf{u})$ contours to broaden near the local minimums.

The shape of the of the $\Phi(\mathbf{u})$ contours is affected by the initial grid of $\mathbf{f}$ vectors. The interface will shear to the closest local minimum causing the centrally located local minimums to contain more history data than those on the edges of Figure 5.34a. In Figure 5.34b and c, the $\Phi(\mathbf{u})$ data was only shown for the first quadrant of the GSF energy surface. However, the interface of the stacking faults shown in Figure 5.35a are able to shear in every direction, resulting in the $\Phi(\mathbf{u})$ history data shown in Figure 5.35b. Several of the final flexible $\Phi(\mathbf{u})$ data points shear to low energy configurations outside quadrant shown to scale in Figure 5.35a. Some data points shear to a stable stacking fault below $\Psi_R(\mathbf{f})$. Stacking faults starting in the "γ_{max}" regions have enough energy to shear long distances, shown by the $\Phi(\mathbf{u})$ history data to the left and right of the quadrant. These reach local energy minimums that are not related to the perfect crystal or stable

stacking fault.   In these cases, the high energy stacking faults probably result in an interfacial reconstruction of the flexible atoms.
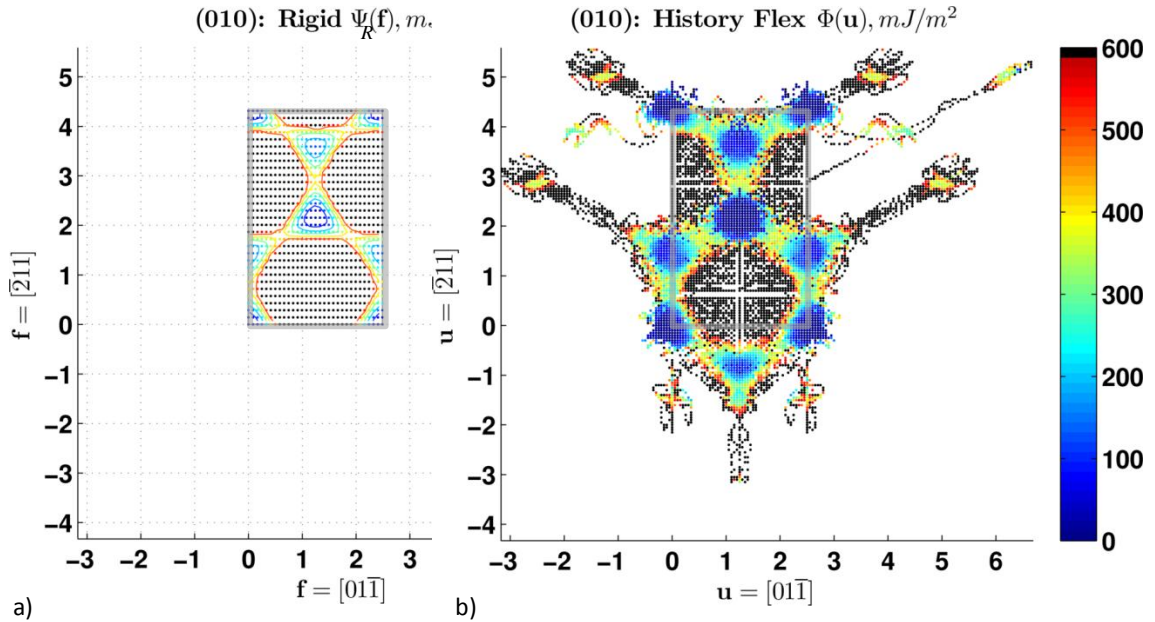
Figure 5.35: a) (111) rigid GSF energy, $\Psi_R(\mathbf{f})$, and b) all of the flexible intefacial $\Phi(\mathbf{u})$ relaxation history data. The grey line encompassing all $\mathbf{f}$ points in a) is shown in b) and several of the relaxation paths shear outside its borders.

The flexible stacking faults are shown to behave as a linear elastic material. The shear strain can be accurately predicted from the flexible layer COM motion. This in turn provides an accurate determination of the stacking fault inteface location and the linear elastic energy stored as shear strain. The $\Phi(\mathbf{u})$ histories are shown to provide a good approximation of the minimized GSF energies, $\Psi_{\min}(\mathbf{f})$ and $\Psi_{\min\Delta}(\mathbf{f})$. The stable and unstable stacking fault energies, γ_{sf} and γ_{usf}, are accurately predicted form the $\Phi(\mathbf{u})$ histories. Kinetic energy during the relaxation process causes the $\Phi(\mathbf{u})$ histories to slightly distort the energy contour levels. The contour shapes are also affected by the initial $\mathbf{f}$-vector grid. Overall the flexible stacking fault procedure is shown to reproduce the important features of the GSF energy curves for Nickel.

6. Conclusions

This chapter provides a summary of the intellectual contributions and the anticipated benefits to the research community and military from the advances reported as part of this dissertation.

6.1 Intellectual Contributions

This work contributes to the methods available for modeling molecular crystals. The most important contribution is the procedure used for determining the generalized stacking fault energy in molecular crystals. This involved the implementation of simulation procedures suitable to modeling the complex interface of a molecular crystal. A new procedure was then used to partition the system energy into an elastic and lattice disregistry component equivalent to the generalized stacking fault energy. The GSF energy surfaces determined for αRDX were then shown to reproduce experimentally observed slip features and also help explain the process of cross slip through the development of partial dislocations (14). Through the process of developing the new GSF method, the Smith and Bhardawaj potential (17) was shown to accurately reproduce RDX crystal structures and properties in Section 3 and the RDX cleavage and free surface energies in Section 4.

6.1.1 Validation of Smith and Bharadwaj Potential to RDX

The simulations and procedures in section 3 provide validation of the Smith and Bharadwaj (17) potential to RDX and the ability of the potential to model the various common phases of RDX, namely the ambient condition αRDX and high pressure γRDX phase. These simulations determined the bulk modulus and its derivative for use in the

3rd order BMEOS. The orthotropic elastic constants and coefficients of thermal expansion were also determined. These were all shown to be in good agreement with the available experimental data. This data can also be used as a bench mark for other models derived from the SB potential including coarse grained potentials.

It was also shown that while uniaxial deformation leads to the α to γRDX transition, hydrostatic compression alone does not. However, hydrostatic depressurization from the γRDX phase reveals that the SB potential is capable of supporting the γRDX structure at high pressure and yields the γ to αRDX transition near 2.1 GPa.

Imposed uniaxial deformation of αRDX showed that the ability of the crystal to undergo phase transitions depends on the crystal orientation. Compressive deformation along the **c**-axis reproduced the γRDX configuration for σ_c=-1.5GPa. Compression along the **b**-axis did not result in the γRDX structure but instead led to a structure similar to that identified in simulations by Cawkwell et al. (38) and Ramos et al. (56) as a stacking fault. Deforming along the different crystal axes had markedly different effects on the bonded SB potential terms where loading on the **b**-axis decreased the dihedral energy but it was increased for loading along the **c**-axis. The transitions were also shown to be more sensitive to the crystal orientation as opposed to the magnitude of the largest principal and shear stresses.

6.1.2 Attachment, Free Surface, and Decohesion Energy

The theoretical framework used for determining the attachment energy makes it well suited to this work. It uses common symmetry arguments to determine the unique planes on a crystal habit. It then provides a computationally efficient method for

determining the energetically favorable slip plane from the remaining unique planes on each crystal habit. This was shown to accurately predict the slip plane with the lower unstable stacking fault energy on each crystal face of αRDX. The attachment energy simulation procedure was slightly modified by increasing the layer thickness and was used to determine the free surface energy.

The molecular level decohesion process of several crystal planes in αRDX was also studied. The simulations were shown to reproduce the free surface energy and elastic constants. The maximum surface tractions and the reduction in surface traction during decohesion was presented. These simulations provide the decohesion response due to a tensile uniaxial strain load and would be suitable for use in a Rankine or maximum principal stress decohesion criterion (83). Other simulations involving shear and biaxial compression would still be needed to develop a decohesion criterion suitable to modeling the failure process under a general state of deformation.

6.1.3 Generalized Stacking Fault Energy

A large set of Generalized Stacking Fault (GSF) energies have been computed for a molecular crystal (αRDX) using molecular dynamics. A computational procedure was proposed that extends the approach traditionally applied to metals to account for the molecular degrees of freedom. Such a feature is important for materials whose steric interactions across crystal defects and molecular conformations can have significant effects on deformation mechanisms. The GSF energies provide estimates of the stable and unstable stacking fault energies which, together with the surface energy calculation, are then employed through Rice's dislocation nucleation criterion (18) to predict whether a given slip system is likely to respond to mode II loading in a brittle ($2\gamma_s < \gamma_{usf}$) or ductile

($2\gamma_s$>γ_{usf}) manner. Rice's criterion applied to the GSF and free surface energies calculated in this work agree well with the experimentally known slip systems.

For αRDX in particular, features in the GSF energies suggest exhibition of both brittle and ductile behavior depending on loading direction. Unstable stacking fault energies in the (010) plane can be as small as half that of any other plane. All slip systems with a [100] slip direction produced a stable stacking fault structure. The stable stacking fault of these slip systems could be related to the experimental observation of cross slip between these systems.

Although the present study has specifically considered an energetic compound, similarities can be seen that make the approach transferrable to similar classes of materials across broad ranges of applications.

6.2 Assumptions and Limitations

The use of simulations to model real materials will always involve simplifying assumptions to make the problem computationally feasible. All of the simulations produced in this work assume that the SB potential accurately describes the RDX molecule and crystal. This assumption limits the processes that can be modeled to nonreactive mechanisms that do not involve the breaking of bonds or chemical reactions. This also assumes that polarization of the RDX molecule is not affected by the state of deformation or molecular neighborhood of molecules.

The electrostatic interactions of the SB potential limit all models in this work to be 3D periodic for the calculation of the Ewald sum. This required the addition of vaccum layers to create 2D slabs of materials with the assumption that the vacuum layer is large enough to separate the slabs from one another. This also limits the processes that

can be modeled to those that can be represented periodically. For this reason, several simulations involved the properties of planes or interfaces of materials. The Ewald summation is also computationally expensive, limiting the size of the simulation cells to ~4000 atoms for dynamic simulations and ~20000 atoms in quenching simulations. The periodicity requirement and limited simulation cell size causes all of the results presented in this work to be for pristine RDX crystals free of defects.

Molecular dynamics limits the processes that can be modeled to those that occur within a few nanoseconds. The limited timespan and small simulation cell size are possible reasons the α→γRDX transition was not observed in Section 3.2.1. Other atomistic simulation protocols can be used to increase the simulation times.

These assumptions and limitations were known before the start of this work and drove the direction of the dissertation work. This included evaluating the application of the SB potential to RDX by showing that it stabilizes the α and γRDX polymorphs. These *NPT* simulations were limited to features involving only the stabilized phase and not the kinetics of the phase transition. Second, instead of attempting to directly model dislocations or fracture using large scale atomistic simulations, a multiscale modeling approach was used where molecular dynamics was only used to parameterize mesoscale deformation models.

6.3 Future Directions

The stacking fault procedure in this work will be useful in studying several other molecular crystal systems. It can also be extended to include the effects of temperature and strain on the slip systems.

6.3.1 Stacking faults in other Molecular crystals

The procedure for determining the stacking faults in αRDX could easily be used to study other molecular crystals. The unstable stacking energy and free surface energy could then be used to predict the active slip systems in those materials. Nanoindentation is now becoming a common method of studying molecular crystals and can be used to validate these models (38) (91). The stacking faults would provide the molecular barriers to slip motion and could be used in designing molecular crystals to attain particular slip properties.

6.3.2 Thermalized Stacking Faults

The flexible stacking faults in this work used to the energy of the initial rigid stacking fault as the driving force for their relaxation. This may have caused some of the stacking faults to relax into local minimum during quenching. This could be overcome by using thermal energy to relax the many degrees of freedom of the molecule as was done by Cawkwell et al. (38). This could also be used to study the change in the GSF energy with temperature. This could cause some inactive slip directions to become active as thermal energy helps the molecules to shuffle past one another. The procedure used to determine the interfacial displacement and stacking fault energy $\Phi(\mathbf{u})$ is ideally suited to this type of thermal analysis.

6.3.3 Uniaxially Compressed Stacking Faults

Cawkwell et al. (38) demonstrated the effect of uniaxial strain on the GSF energy of αRDX. They show the development of a local minimum on the GSF energy curve due to the uniaxial compression but they were not able to determine the entire GSF energy

surface. In this work, the entire GSF energy surface was determined and it is shown that there was already a local energy minimum on the GSF at zero pressure. However, it appears that uniaxial strain moves the location of the local minimum. It would therefore be interesting to determine the effect of uniaxial stress on the entire GSF energy surface to see if new local energy minimums appear or if they only move around on the surface. This would be easy to implement by applying a constant force to the floating rigid lattice.

Appendices

Appendix A: DLPOLY αRDX FIELD and CONFIG Files

A1: DLPOLY FIELD FILE (71)

This contains potential parameters from Table 2.2for the SB potential (17) from equation

(2.1). The bond numbering and connectivity is for the RDX molecule numbering scheme

presented above. This provides the same results as the LAMMPS implementation of the

SB potential given in Appendix B.

```
DL_POLY RDX molecule
UNITS kcal
MOLECULES 1
RDX
NUMMOLS 144
ATOMS 21
C        12.0110000  -0.5400
C        12.0110000  -0.5400
C        12.0110000  -0.5400
N        14.0072       0.056375
N        14.0072       0.056375
N        14.0072       0.056375
N        14.0072       0.860625
N        14.0072       0.860625
N        14.0072       0.860625
O        15.99943   -0.4585
O        15.99943   -0.4585
O        15.99943   -0.4585
O        15.99943   -0.4585
O        15.99943   -0.4585
O        15.99943   -0.4585
H        1.00800000   0.2700
H        1.00800000   0.2700
H        1.00800000   0.2700
H        1.00800000   0.2700
H        1.00800000   0.2700
H        1.00800000   0.2700
BONDS   21
harm  12  8  1990.1  1.23
... 1-2 bonds 1-21
harm  21  3  641.6  1.09
ANGLES  36
harm  12  8  13  125.00  120.92
```

```
... 1-3 bonded angles 1-36
harm  4   1   5   70.00   110.52
DIHEDRALS   72
cos 12   8   5   1   4.225   180.00   2.00   1.00   1.00
... 1-4 bonded dihedrals 1-66
cos  2   5   1   4   5.50   180.00   3.00
harm  4   3   1   7   8.00   0.00
... 1-4 bonded improper dihedral 67-72
harm  9   14   15   6   89.30   0.00
FINISH
VDW         10
C         C         buck 14976.0      .3236246      640.8
H         H         buck  2649.7      .2673797       27.4
C         H         buck  4320.0      .2928258      138.2
N         N         buck 60833.9      .2645503      500.0
O         O         buck 75844.8      .2461236      398.9
H         N         buck 12695.88     .2659574      116.96
H         O         buck 14175.97     .2563445      104.46
C         N         buck 30183.57     .2911208      566.03
C         O         buck 33702.4      .2796421      505.6
N         O         buck 67925.95     .2550370      446.6
CLOSE
```

A2: DLPOLY CONFIG File

This is the input file used in DLPOLY to define the atom types and their positions in a

DLPOLY input file. The field file defining the molecule connectivity uses this atom

configuration and number scheme.

```
Single RDX Molecule
        0            3
 26.36400000000000    0.00000000000000    0.00000000000000
  0.00000000000000   34.72200000000000    0.00000000000000
  0.00000000000000    0.00000000000000   32.12700000000000
   C            1          1
  2.42416980          4.14117720          4.71196000
   C            2          1
  0.66305460          2.82405600          3.63570550
   C            3          1
  1.96016340          4.41316620          2.31207310
   N            4          1
  2.32135020          5.04626400          3.56609700
   N            5          1
  1.15606140          3.46757040          4.85867330
   N            6          1
  0.70655520          3.72914280          2.49412610
   N            7          1
  2.97913200          6.22565460          3.58323140
   N            8          1
  0.20432100          4.07983500          5.66934460
   N            9          1
 -0.43896060          4.48492500          2.22533020
```

209

```
O              10          1
 2.99231400          6.86569680          2.55730920
 O              11          1
 3.49191180          6.58213380          4.64556420
 O              12          1
-0.91351260          3.63655080          5.63507580
 O              13          1
 0.59846280          4.94325540          6.41469100
 O              14          1
-1.47770220          4.09025160          2.68153360
 O              15          1
-0.31109520          5.42936340          1.48855100
 H              16          1
 3.16499820          3.40738560          4.52562340
 H              17          1
 2.65353660          4.70830320          5.61579960
 H              18          1
-0.34405020          2.45021580          3.79098600
 H              19          1
 1.33797300          1.99998720          3.41831280
 H              20          1
 2.70494640          3.66432840          2.05291530
 H              21          1
 1.89820800          5.12959680          1.51318170
```

Appendix B: LAMMPS αRDX FIELD and CONFIG File

B1: LAMMPS Potential File (51)

This is the LAMMPS implementation of the SB potential (17) given by equation (2.1) with parameters given in Table 2.2. This field file using the atomic numbering and connectivity given below in the LAMMPS atomic configuration file. This provides the same SB potential as that given in Appendix A for DLPOLY.

```
bond_style  harmonic  # quadratic
angle_style harmonic  # quadratic
dihedral_style    harmonic  # cosine series
improper_style    harmonic  # improper dihedral quadratic
pair_style  buck/coul/long 8
pair_modify       tail yes
kspace_style    ewald/n 1.0e-4   #only non-ortho ewald sum

#SB Pot 0.5K in Bedrov et al. (2001) J Comp Matl design paper
pair_coeff  1 1 14976.00  0.323625  640.80
pair_coeff  1 2 30183.57  0.291121  566.03
pair_coeff  1 3 30183.57  0.291121  566.03
pair_coeff  1 4 33702.40  0.279642  505.60
pair_coeff  1 5 4320.000  0.292826  138.2
pair_coeff  2 2 60833.90  0.264550  500.00
pair_coeff  2 3 60833.90  0.264550  500.00
pair_coeff  2 4 67925.95  0.255037  446.60
pair_coeff  2 5 12695.88  0.265957  116.96
pair_coeff  3 3 60833.90  0.264550  500.00
pair_coeff  3 4 67925.95  0.255037  446.60
pair_coeff  3 5 12695.88  0.265957  116.96
pair_coeff  4 4 75844.80  0.246124  398.90
pair_coeff  4 5 14175.97  0.256345  104.46
pair_coeff  5 5 2649.700  0.267380  27.400

bond_coeff  1  995.05  1.23
bond_coeff  2  495.85  1.36
bond_coeff  3  336.05  1.44
bond_coeff  4  320.80  1.09

angle_coeff 1  62.5  120.917
angle_coeff 2  62.5  107.453
angle_coeff 3  65.0  95.816
angle_coeff 4  35.0  105.596
angle_coeff 5  43.2  107.006
angle_coeff 6  38.5  108.507
angle_coeff 7  35.0  110.518

dihedral_coeff    1   4.225 -1 2
dihedral_coeff    2   0.395 -1 4
```

```
dihedral_coeff    3   0.002 -1 8
dihedral_coeff    4  -0.080 -1 3
dihedral_coeff    5   1.650 -1 1
dihedral_coeff    6  -0.805 -1 2
dihedral_coeff    7   0.055 -1 3

improper_coeff    1 4.000 0.0
improper_coeff    2 44.65 0.0

special_bonds     lj/coul 0.0 0.0 1.0   #allowing all topo 1-4 coul/lj
```

B2: LAMMPS Atomic Configuration and Connectivity File

This is the input file used in LAMMPS to define the atom types and their positions for a single RDX molecule. The bonds and their connectivity are also given and correspond to the above LAMMPS field file.

```
      21 atoms
      21 bonds
      36 angles
      66 dihedrals
       6  impropers

   5 atom types
   4 bond types
   7 angle types
   7 dihedral types
   2 improper types

   0.00000  13.18200  xlo xhi
   0.00000  11.57400  ylo yhi
   0.00000  10.70900  zlo zhi
   0.00000   0.00000   0.00000  xy xz yz

Masses
1 12.011000
2 14.007200
3 14.007200
4 15.999430
5 1.0080000

Atoms
1      1      1   -0.540000   2.42420000   4.14120000   4.71200000
2      1      1   -0.540000   0.66310000   2.82410000   3.63570000
3      1      1   -0.540000   1.96020000   4.41320000   2.31210000
4      1      2    0.056375   2.32140000   5.04630000   3.56610000
5      1      2    0.056375   1.15610000   3.46760000   4.85870000
6      1      2    0.056375   0.70660000   3.72910000   2.49410000
7      1      3    0.860625   2.97910000   6.22570000   3.58320000
8      1      3    0.860625   0.20430000   4.07980000   5.66930000
9      1      3    0.860625  -0.43900000   4.48490000   2.22530000
```

212

```
10      1      4   -0.458500    2.99230000    6.86570000    2.55730000
11      1      4   -0.458500    3.49190000    6.58210000    4.64560000
12      1      4   -0.458500   -0.91350000    3.63660000    5.63510000
13      1      4   -0.458500    0.59850000    4.94330000    6.41470000
14      1      4   -0.458500   -1.47770000    4.09030000    2.68150000
15      1      4   -0.458500   -0.31110000    5.42940000    1.48860000
16      1      5    0.270000    3.16500000    3.40740000    4.52560000
17      1      5    0.270000    2.65350000    4.70830000    5.61580000
18      1      5    0.270000   -0.34410000    2.45020000    3.79100000
19      1      5    0.270000    1.33800000    2.00000000    3.41830000
20      1      5    0.270000    2.70490000    3.66430000    2.05290000
21      1      5    0.270000    1.89820000    5.12960000    1.51320000
```

Bonds
```
      1    1      12       8
```
… 1-2 bonds 1 to 21
```
     21    4      21       3
```

Angles
```
      1    1      12       8      13
```
…1-3 bonded angles 1 to 36
```
     36    7       4       1       5
```

Dihedrals
```
      1    1      12       8       5       1
```
… 1-4 bonded dihedrals 1 to 66
```
     66    7       2       5       1       4
```

Impropers
```
      1    1       4       3       1       7
```
… 1-4 bonded improper dihedrals 1 to 6
```
      6    2       9      14      15       6
```

Appendix C: LAMMPS Quenching Procedure and Skewed Cells

This appendix describes the quenching procedure and the unit cells used in the simulations. These include the skewed unit cells used to create the (021) and (011) surfaces and stacking faults.

The experimental αRDX unit cell is replicated to create a 3×3×3 supercell and is minimized in LAMMPS (51). The experimental atomic coordinates are given at T=300K so the structure must first be quenched from T=300K to T≈0K. The quenching process must also allow the lattice vectors to contract with the crystal structure due to thermal expansion. This is accomplished in Lammps by using an isenthalpic ensemble (NPE) in conjunction with a Langevin thermostat to reduce the temperature down to ~0K over a 10 ps simulation. The isenthalpic ensemble used here allows the lengths of the lattice vectors to change while fixing their orientation relative to one another in order to maintain the orthorhombic space group. The Langevin thermostat implemented in Lammps applies a viscous like force to the atomic motion proportional to (m/$damp$) where m is the atomic mass and $damp$ is the damping parameter set to 100fs. The Langevin thermostat also applies a random force due to solvent atoms at temperature, T, proportional to $\sqrt{(K_b Tm)/(dt\ damp)}$ where K_b is Boltzman's constant, m is the atomic mass, dt=1fs and $damp$=100fs is the damping parameter. This damp parameter relaxes the temperature of the system to T in approximately the amount of time it is set to (100fs). The temperature is ramped down from T=300K to 0K over a 10ps simulation time. This approach should effectively quench the structure to T~0K and the random forces should help the structure escape local minima as it is cooled. The quenched structure is then recursively minimized at constant volume and then with lattice

relaxations. This process yields a minimized unit cell with orthogonal lattice vectors $13.366 \times 11.330 \times 10.342$ Å. This minimized unit cell is used to create the supercells for the simulations of the (100), (010) and (001) planes.

Simulations of the (011) and (021) planes are created by minimizing a skewed unit cell of the experimental structure. In Figure A1, a 4×5 supercell of αRDX is shown projected onto the (100) plane. The spheres represent the RDX molecules by their centers of mass (COM) location. The COMs use eight colors representing each of the eight molecules in the unit cell. Figure A1(a) shows the experimental αRDX unit cell given by Choi and Prince (25) where the black arrows are the lattice vectors, the gray lines are the edges of the unit cell and the eight molecules are those that make up the unit cell. The skewed (011) and (021) unit cells must contain each of the eight molecules of the unit cell in order for it to be a complete αRDX unit cell. The (011) unit cell used in this work is shown in Figure A1(b) created from the [0$\bar{1}$ 1], [001], [100], lattice vectors and the eight molecules shown. The blue arrows show the [0$\bar{1}$ 1] and [001] lattice vectors and the blue lines represent the edges of the unit cell. The (021) unit cell used in this work is shown in Figure A1(c) created from the [0$\bar{1}$ 2], [001], [100], lattice vectors and the same eight molecules used in the (011) unit cell. The red arrows show the [0$\bar{1}$ 2] and [001] lattice vectors and the red lines represent the edges of the unit cell.

The skewed (011) and (021) unit cells are quenched and minimized using same procedure as that used for the experimental unit cell. The constraint on the orthogonality of the lattice vectors is changed to enforce monoclinic lattice vectors. The [100] and [001] pair of lattice vectors and the [0$\bar{1}$ 1] or [0$\bar{1}$ 2] and [100] pair of lattice vectors are constrained to be orthogonal. The angle that [0$\bar{1}$ 1] or [0$\bar{1}$ 2] make with [001] is allowed

215

to change during the quenching and minimization. The (011) supercell was created from $3\times3\times6$ unit cells in the [100], [0$\bar{1}$1], and [001] directions, respectively. The minimized (011) unit cell dimensions are $13.36\times15.35\times10.35$ Å in the [100], [0$\bar{1}$1], and [001] directions, respectively, with an angle between [0$\bar{1}$1] and [001] equal to 47.6 degrees. The (021) supercell was created from $3\times2\times9$ unit cells in the [100], [0$\bar{1}$1], and [001] directions, respectively. The minimized (021) unit cell dimensions are $13.36\times23.60\times10.35$ Å in the [100], [0$\bar{1}$2], and [001] directions, respectively, with an angle between [0$\bar{1}$2] and [001] equal to 28.7 degrees. The xyz dimensions of the simulation cell must be twice as large as r_{cut}=15Å, the real space cutoff used to calculate nonbonded interactions. This requires more skewed unit cells than orthorhombic unit cells in the supercell.
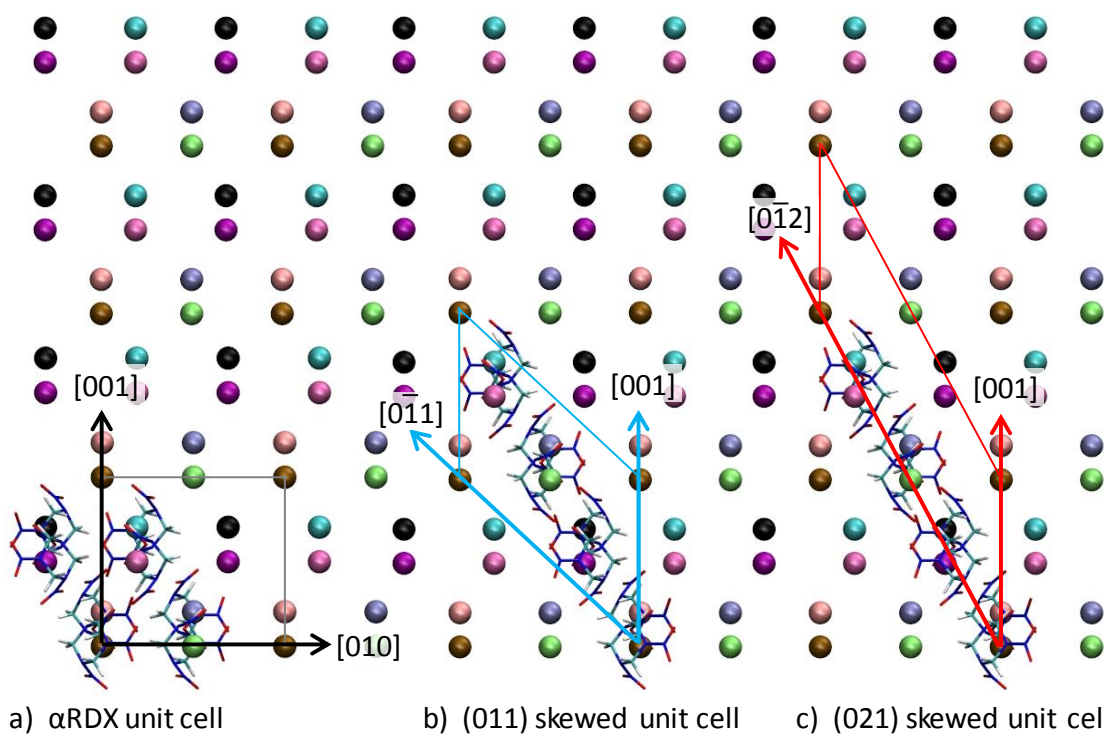
Figure A1. 4×5 αRDX unit cells projected onto the (100) plane with RDX molecules center's of mass represented by spheres. The COM's are shown in eight colors corresponding to the eight molecules making up a unit cell. (a) Experimental (25) αRDX unit cell from Figure 2b where arrows represent the lattice vectors, molecules represent the unit cell molecules and the gray lines represent the edges of the unit cell. (b) Monoclinic (011) αRDX unit cell shown in blue with the eight molecules making up the unit cell. (c) Monoclinic (021) αRDX unit cell shown in blue with the eight molecules making up the unit cell.

Bibliography

[1] Van Swygenhoven, H., Derlet, P. M., and Froseth, A. G. (2004). Stacking Faults Energies and Slip in Nanocrystalline Metals. Nature Materials, **3**, 399-403.

[2] Wildfong, P. L., Hancock, B. C., Moore, M. D., and Morrise, K. R. (2006). Towards an Understanding of the Structurally Based Potential for Mechanically Activated Disordering of Small Molecular Organic Crystals. Journal of Pharmaceutical Sciences, **95**, 2645-2656.

[3] Reddy, C. M., Kirchner, M. T., Gundakaram, R. C., Padmanabhan, K. A., and Desiraju, G. R. (2006). Isostructurality, Polymorphism and Mechanical Properties of Some Hexahalogenated Benzenes: The Nature of the Halogen...Halogen Interactions. Chemistry. A European Journal, **12**, 2222-2234.

[4] Reddy, C. M., Krishna, G. R., and Ghosh, S. (2010). Mechanical Properties of Molecular Crystals - Applications to Crystal Engineering. CrystEngComm, **12**, 2296-2314.

[5] Sun, C. C., and Kiang, Y. -H. (2008). On the Identification of Slip Planes in Organic Crystals Based on Attachment Energy Calculation. Journal of Pharmaceutical Sciences, **97**, 3456-3461.

[6] Gallagher, H. G., Halfpenny, P. J., Miller, J. C., Sherwood, J. N., and Tabor, D. (1992). Dislocation Slip Systems in Pentaerythritol Tetranitrate (PETN) and Cyclotrimethylene Trinitramine (RDX) [and Discussions]. Philosophical Transactions of the Royal Society A, **339**, 293-303.

[7] Connick, W., and May, F. G. (1969). Dislocation Etching of Cyclotrimethylene Trinitramine Crystals. Journal of Crystal Growth, **5**, 65.

[8] Karki, S., Friscic, T., Fabian, L., Laity, P. R., Day, G. M., and Jones, W. (2009). Improving Mechanical Properties of Crystalline Solids by Cocrystal Formation: New Compressible Forms of Paracetamol. Advanced Materials, **21**, 3905.

[9] Sun, C. C., and Hou, H. (2008). Improving Mechanical Properties of Caffeine and Methyl Gallate Crystals by Cocrystallization. Crystal Growth and Design, 8 (5), 1575-1579.

[10] Dang, N. C., Dreger, Z. A., Gupta, Y. M., and Hooks, D. E. (2010). Time-Resolved Spectroscopic Measurements of Shock-Wave Induced Decomposition in Cyclotrimehtylene Trinitramine (RDX): Anisotropic Response. Journal of Physical Chemistry A, **114**, 11560-11566.

[11] Dick, J. J., and Ritchie, J. P. (1994). Molecular Mechanics Modeling of Shear and the Crystal Orientation Dependence of the Elastic Precursor Shock Strength in Pentaerythritol Tetranitrate. Journal of Applied Physics, **76**, 2726-2737.

[12] Dick, J. J., Mulford, R. N., Spencer, W. J., Pettit, D. R., Garcia, E., and Shaw, D. C. (1991). Shock Response of Pentaerythritol Tetranitrate Single Crystals. Journal of Applied Physics, **70**, 3572.

[13] Armstrong, R. W. (2009). Dislocation Mechanics Aspects of Energetic Material composites. Reviews on Advanced Materials Science, **19**, 13-40.

[14] Ramos, K. J., Hooks, D. E., and Bahr, D. F. (2009). Direct observation of plasticity and quantitative hardness measurements in single crystal cyclotrimethylene trinitramine by nanoindentation. Philosophical Magazine, **89**, 2381-2402.

[15] Smith, G. D., and Bharadwaj, R. K. (1999). Quantum Chemistry Based Force Field for Simulations of HMX. Journal of Physical Chemistry B, **103**, 3570-3575.

[16] Rice, J. R. (1992). Dislocation nucleation from a cracktip: An analysis based on teh Peierls concept. Journal of the Mechanics and Physics of Solids, **40**, 239-271.

[17] Heggen, M., Houben, L., and Feuerbacher, M. (2010). Plastic-deformation mechanism in complex solids. Nature Materials, **9**, 332-336.

[18] Vitek, V. (1968). Intrinsic Stacking Faults in Body-centred Cubic Crystals. Philosophic Magazine, **18**, 773-786.

[19] Gibbs, T. R., and Popolato, A. (1981). LASL Explosive Property Data (Los Alamos Scientific Laboratory Series on Dynamic Material Properties) (Vol. 4). University of California Press.

[20] Dlott, D. D., and Fayer, M. D. (1990). Shocked molecular solids: Vibrational up pumping, defect hot spot formation, and the onset of chemistry. Journal of Chemical Physics, **92**, 3798-3812.

[21] Chakraborty, D., Muller, R. P., Dasgupta, S., and Goddard, I. W. (2000). The Mechanism for Unimolecular Decomposition of RDX (1,3,5-Trinitro-1,3,5-triazine), an ab Initio Study. The Journal of Physical Chemistry A, **104**, 2261-2272.

[22] Zhao, X., Hintsa, E. J., and Lee, Y. T. (1988). Infrared multiphoton dissociation of RDX in a molecular beam. The Journal of Chemical Physics, **88**, 801-810.

[23] Muthurajan, H., Sivabalan, R., Talawar, M. B., Anniyappan, M., and Venugopalan, S. (2006). Prediction of heat of formation and related parameters of high energy materials. Journal of Hazardous materials, **133**, 30-45.

[24] Roberts, R. J., Rowe, R. C., and York, P. (1994). The Relationship between indentation hardness of organic solids and thier molecuar structure. Journal of Materials Science, **29**, 2289-2296.

[25] Choi, C. S., and Prince, E. (1972). The Crystal Structure of Cyclotrimethylene-trinitramine. Acta Crystallographica, **B28**, 2857-2862.

[26] Millar, D. I., Oswald, I. D., Francis, D. J., Marshall, W. G., Pulham, C. R., and Cumming, A. S. (2009). The crystal structure of β-RDX - an elusive form of an explosive revealed. Chemical Communications, **5**, 562-564.

[27] Davidson, A. J., O., I. D., Francis, D. J., Lennie, A. R., Marshall, W. G., Millar, D. I., Pulham, C. R., Warren, J. E., and Cumming, A. S. . (2008). Explosives under pressure - the crystal structure of γ-RDX as determined by high-pressure X-ray and neutron diffraction. Crystal Engineering Communication, **10**, 162-165.

[28] Cockcroft, J. K. (1999). A Hypertext Book of Crystallographic Space Group. Retrieved 2010, from http://img.chem.ucl.ac.uk/sgp/mainmenu.htm

[29] Ciezak, J. A., and Jenkins, T. A. (2008). The Low-temperature high-pressure phase diagram of energetic materials: I. Hexahydro-1,3,5-Trinitro-s-Triazine. Propellants, Explosives, Pyrotechnics, **33**, 390-395.

[30] Millar, D. I., Oswald, I. D., Francis, D. J., Marshall, W. G., Pulham, C. H., and Cumming, A. S. (2010). Pressure-cooking of explosives—the crystal structure of ε-RDX as determined by X-ray and neutron diffraction. Chemical Communications, **46**, 5662-5664.

[31] Schwarz, R. B., Hooks, D. E., Dick, J. J., Archuleta, J. I., and Martinez, A. R. (2005). Resonant ultrasound spectroscopy measurement of the elastic constants of cyclotrimethylene trinitramine. Journal of Applied Physics, **98**, 1-3.

[32] Haussühl, S. (2001). Elastic and thermoelastic properties of selected organic crystals: acenaphthene, trans-azobenzene, benzophenone, tolane, trans-stilbene, dibenzyl, diphenyl sulfone, 2,2´-biphenol, urea, melamine, hexogen, succinimide, pentaerythritol, urotropine, malonic. Zeitschrift für Kristallographie, **216**, 339-353.

[33] Haycraft, J. J., Stevens, L. L., and Eckhardt, C. J. (2006). The elastic constants and related properties of the energetic material cyclotrimethylene trinitramine (RDX) determined by Brillouin scattering. The Journal of Chemical Physics, **124**, 1-11.

[34] Olinger, B., Roof, B., and Cady, H. (1978). The Linear and Volume Compression of β-HMX and RDX to 9 GPa (90KiloBar). Symposium International Sur Le comportement Des Milieux Denses Sous Hautes Pressions Dynamiques (pp. 1-7). Paris, France: Commissariat a l'Energie Atomique Centre d'Etudes de Vajours, Sevran, France.

[35] Yoo, C., Cynn, H., Howard, W. M., and Holmes, N. (1998). Equations of state of unreacted high explosives at high pressures. 11th International Detonation Symposium, (pp. 951-957). Snowmass Village, CO.

[36] Cady, H. H. (1972). Coefficient of Thermal Expansion of Pentaerythritol Tetranitrate and Hexahydro-1,3,5-trinitro-s-triazine (RDX). Journal of Chemical and Engineering Data, **17**, 369-371.

[37] Hooks, D. E., Ramos, K. J., and Martinez, A. R. (2006). Elastic-plastic shock wave profiles in oriented single crystals of cylotrimethylene trinitramine (RDX) at 2.25 GPa. Journal of Applied Physics, **100**, 1-7.

[38] Cawkwell, M. J., Ramos, K. J., Hooks, D. E., and Sewell, T. D. (2010). Homogeneous dislocation nucleation in cyclotrmethylene trinitramine under shock loading. Journal of Applied Physics, **107**, 1-11.

[39] Sorescu, D. C., Rice, B. M., and Thompson, D. L. (1997). Intermolecular Potential for the Hexahydro-1,3,5-trinitro-1,3,5-s-triazine Crystal (RDX): A Crystal Packing, Monte Carlo, and Molecular Dynamics Study. The Journal of Physical Chemistry B, **101**, 798-808.

[40] Sewell, T. D., and Bennett, C. M. (2000). Monte Carlo calculations of the elastic moduli and pressure-volume-temperature equation of state for hexahydro-1,3,5-trinitro-1,3,5-triazine. Journal of Applied Physics, **88**, 88-95.

[41] Parrinello, M., and Rahman, A. (1982). Strain fluctuations and elastic constants. Journal of Chemical Physics, **76**, 2662-2666.

[42] Sorescu, D. C., Rice, B. M., and Thompson, D. L. (1998). A Transferable Intermolecular Potential for Nitramine Crystals. The Journal of Physical Chemistry A, **102**, 8386-8392.

[43] Podeszwa, R., Bukowski, R., Rice, B. M., and Szalewicz, K. (2007). Potential energy surface for cyclotrimethylene trinitramine dimer from symmetry-adapted perturbation theory. Physical Chemistry Chemical Physics, **9**, 5561-5569.

[44] Podeszwa, R., Rice, B. M., and Szalewicz, K. (2009). Crystal structure prediction for cyclotrimethylene trinitramine (RDX) from first principles. Physical Chemistry Chemical Physics, **11**, 5512-5518.

[45] Todorov, I. T., and Smith, W. (2009). The DL_POLY_3 User Manual Version 3.10.0. Cheshire, UK: STFC Daresbury Laboratory.

[46] Smith, G. D., Bharadwaj, R. K., Bedrov, D., and Chakravarthy, A. (1999). Quantum-Chemistry-Based Force Field for Simulations of Dimethylnitramine. Journal of Physical Chemistry B, **103**, 705-713.

[47] Sorensen, R. A., Liau, W. B., Kesner, K., and Boyd, R. H. (1988). Prediction of polymer crystal structures and properties: polyethylene and poly(oxymethylene). Macromolecules, **21**, 200-208.

[48] Bedrov, D., Smith, G. D., and Sewell, T. D. (2000). Thermal conductivity of liquid octahydro-1,3,5,7-tetranitro-1,3,5,7-tetrazocine (HMX) from molecular dynamics simulations. Chemical Physics Letters, **324**, 64-68.

[49] Bedrov, D., Ayyagari, C., Smith, G. D., Sewell, T. D., Menikoff, R., and Zaug, J. M. (2001). Molecular dynamics simulations of HMX crystal polymorphs using a flexible molecule force field. Journal of Computer-Aided Materials Design, **8**, 77-85.

[50] Smith, W., Forester, T. R., and Todorov, I. T. (2009). The DLPOLY_2 User Manual Version 2.20. Cheshire, UK: STFC Daresbury Laboratory.

[51] Plimpton, S. (1995). Fast Parallel Algorithms for Short-Range Molecular Dynamics. Journal of Computation Physics, **117**, 1-19.

[52] Sewell, T. D., Menikoff, R., Bedrov, D., and Smith, G. D. (2003). A molecular dynamics simulation study of elastic properties of HMX. Journal of Chemical Physics, **119**, 7417-7426.

[53] Jaramillo, E., Sewell, T. D., and Strachan, A. (2007). Atomic-level view of inelastic deformation in a shock loaded molecular crystal. Physical Review B, **76**, 1-6.

[54] Zheng, L., and Thompson, D. L. (2006). Molecular dynamics simulations of melting of perfect crystalline hexahydro-1,3,5-trinitro-1,3,5-s-triazine. The Journal of Chemical Physics, **125**, 1-9.

[55] Cawkwell, M. J., Sewell, T. D., Zheng, L., and Thompson, D. L. (2008). Shock-induced shear bands in an energetic molecular crystal: Application of shock-front absorbing boundary conditions to molecular dynamics simulations. Physical Review B, **78**, 014107.

[56] Ramos, K. J., Hooks, D. E., Sewell, T. D., and Cawkwell, M. J. (2010). Anomalous hardening under shock compression in (021)-oriented cyclotrimethylene trinitramine single crystals. Journal of Applied Physics, **108**, 066105.

[57] Patterson, J. E., Dreger, Z. A., and Gupta, Y. M. (2007). Shock wave-induced Phase transition in RDX single Crystals. Journal of Physical Chemistry B, **111**, 10897-10904.

[58] Bedrov, D., Hooper, J. B., Smith, G. D., and Sewell, T. D. (2009). Shock-induced transformations in crystalline RDX: A uniaxial constant-stress Hugoniotstat molecular dynamics simulation study. The Journal of Chemical Physics, **131**, 1-12.

[59] Boyd, S., Gravelle, M., and Politzer, P. (2006). Nonreactive molecular dynamics force field for crystalline hexahydro-1,3,5-trinitro-1,3,5 triazine. The Journal of Chemical Physics, **124**, 1-10.

[60] Boyd, S., Murray, J. S., and Politzer, P. (2009). Molecular dynamics characterization of void defects in crystalline (1,3,5-trinitro-1,3,5-triazacyclohexane). The Journal of Chemical Physics, **131**, 1-7.

[61] Agrawal, P. M., Rice, B. M., Zheng, L., and Thompson, D. L. (2006). Molecular dynamics simulations of Hexahydro-1,3,5-trinitro-1,3,5-s-triazine (RDX) Using a combined Sorescu-Rice-Thompson AMBER Force Field. Journal of Physical Chemistry B, **110**, 26185-16188.

[62] Wang, J., Wolf, R. M., Caldwell, J. W., Kollman, P. A., and Case, D. A. (2004). Development and Testing of a General Amber Force Field. Journal of Computational Chemistry, 25 (9), 1157-1174.

[63] Lu, L., Wei, D., Chen, X., Ji, G., Wang, X., Chang, J., Zhang, Q., and Gong, Z. (2009). The pressure-inuced phase transition of the solid β-HMX. Molecular Physics, **107**, 2373-2385.

[64] Sun, H. (1998). COMPASS: An ab Initio Force-Field Optimized for Condensed-Phase Applications - Overview with Details on Alkane and Benzen Compounds. Journal of Physical Chemistry B, **102**, 7338-7364.

[65] Ye, S., Tonokura, K., and Koshi, M. (2002). Theoretical calculations of lattice properties of secondary explosives. Journal of the Japan Explosive Society, **63**, 104-115.

[66] Gale, J. D. (1997). GULP: Acomputer program for the symmetry-adapted simulation of solids. Journal of the Chemical Society, Faraday Transactions, **93**, 629-637.

[67] van Duin, A. C., Dasgupta, S., Lorant, F., and Goddard III, W. A. (2001). ReaxFF: A Reactive Force Field for Hydrocarbons. Physical Chemistry A, **105** (41), 9396-9409.

[68] Rahaman, O., van Dui, A. C., Bryantsev, V. S., Mueller, J. E., Solares, S. S., Goddard III, W. A., and Doren, D.J. (2010). Development of a ReaxFF Reactive Force Field for Aqueous Chloride and Copper Chloride. The Journal of Physical Chemistry A, 114 (10), 3556-3568.

[69] Strachan, A., van Duin, A. C., Chakraborty, D., Dasgupta, S., and Goddard III, W. A. (2003). Shock Waves in High-Energy Materials: The Initial Chemical Events in Nitramine RDX. Physical Review Letters, 91 (9), 1-4.

[70] Liu, L., Liu, Y., Zybin, S. V., Sun, H., and Goddard, I. W. (2011). ReaxFF-lg: Correction of the ReaxFF Reative Force Field for London Dispersion, with Applications to the Equations of STate for Energetic Materials. The Journal of Physical Chemistry A, 115 (40), 11016-11022.

[71] Smith, W., and Forester, T. R. (1996). DLPOLY 2.0: A general purpose parallel molecular dynamics simulation package. Journal of Molecular Graphics, 14 (3), 136-141.

[72] Mathew, N., and Picu, R. C. (2011). Molecular conformational stability in cyclotrimethylene trinitramine crystals. The Journal of Chemical Physics, 135, 024510.

[73] Wright, K., and Catlow, R. (1998). Microstopic Properties and Processes in Minerals (Vol. 543). II Giocco, Lucca, Italy: Kluwer Academic Publishers.

[74] Birch, F. (1947). Finite Elastic Strain of Cubic Crystals. Physical Review, 71 (11), 809-824.

[75] Bowers, A. F. (2009). Applied Mechanics of Solids. CRC Press.

[76] Wallace, D. C. (1998). Thermodynamics of Crystals. Dover Publications.

[77] Erpenbeck, J. J. (1992). Molecular dynamics of detonation. I. Equation of state and Hugoniot curve for a simple reactive fluid. Physical Review A, 46 (10), 6406-6416.

[78] Hartman, P., and Bennema, P. (1980). The Attachment Energy as a Habit Controlling Factor. Journal of Crystal Growth, 49, 145-156.

[79] Berkovitch-Yellin, Z. (1985). Toward an ab Initio Derivation of Crystal Morphology. Journal of the American Chemical Society, 107, 8239-8253.

[80] Docherty, R., Clydesdale, G., Roberts, K. J., and Bennema, P. (1991). Application of Bravais-Friedel-Donnay-Harker, attachment energy and Ising models to. Journal of Physics D: Applied Physics, 24 (89), 89-99.

[81] Donnay, J. D., and Harker, D. (1937). A New Law of Crystal Morphology Extending the Law of Bravais. Journal Mineralogical Society of America, 446-466.

[82] Graef, M. D., and McHenry, M. E. (2007). Structure of Materials: An Introduction to Crystallography, Diffraction and Symmetry. N.Y: Cambridge University Press.

[83] Schreyer, H. L. (2007). Modelling Surface Orientation and stress at failure of concrete and geological materials. International Journal for Numerical and Analytical Methods in Geomechanics, 31, 147-171.

[84] Rose, J. H., Ferrante, J., and Smith, J. R. (1981). Universal Binding Energy Curves for Metals and Bimetallic Interfaces. Physical Review Letters, 47 (9), 675-678.

[85] Allen, M. P., and Tildesley, D. J. (1987). Computer Simulation of Liquids. NY: Oxford University Press.

[86] Munday, L. B., Chung, P. W., Rice, B. M., and Solares, S. D. (2011). Simulations of High-Pressure Phases in RDX. The Journal of Physical Chemistry B, 115, 4378-4386.

[87] Sun, B., Winey, J. M., Hemml, N., Dreger, Z. A., Zimmerman, K. A., Gupta, Y. M., Torchinsky, D. H., and Nelson, K. A. (2008). Second-order elastic constants of pentaerythritol tetranitrate and cyclotrimethylene trinitramen using impulsive stimulated thermal scattering. Journal of Applied Physics, 104, 073517.

[88] Tadmor, E. B., and Hai, S. (2003). A Peierls Criterion fo rthe onset of deformation twinning at a crack tip. Journal of the Mechanics and Physics of Solids, 51, 765-793.

[89] Griffith, A. A. (1921). The phenomena of rupture and flow in solids. Philosophical Transactions of the Royal Society of London, A, 221, 163-198.

[90] Lu, G., Kioussis, N., Bulatov, V. V., and Kaxiras, E. (2000). Generalized-Stacking-Fault Energy Surface and Dislocation Properties of Aluminum. Physical Review B, 62 (5), 3099-3108.

[91] Jing, Y., Zhang, Y., Blendell, J., Koslowski, M., and Carvajal, M. T. (2011). A nano-indentation method to study slip planes in molecular crystals in a systematic manner. Crystal Growth and Design, "Just Accepted".

[92] Ramdas, S., Thomas, J. M., and Goringe, M. J. (1977). Computational Approach to the study of Extended Defects in Molecular Crystals. Journal of the Chemical Society. Faraday Transactions, 73, 551.

[93] Puschl, W. (2002). Models for dislocation cross-slip in close-packed crystal structures: a critical review. Progress in Materials Science, 47, 415-461.

[94] Mishin, Y., Farkas, D., Mehl, M. J., and Papaconstantapoulos, D. A. (1999). Interatomic Potentials for monoatomic metals from experimental data and ab initio calculations. Physical Review B, 59, 3393-3407.

[95] Zimmerman, J. A., Gao, H., and Abraham, F. F. (2000). Generalized Stacking Fault Energies for embedded atom FCC metals. Modelling and Simulation in Materials Science and Engineering, 8, 103-115.

[96] Duesberry, M. S., and Vitek, V. (1998). Plastic anisotropy in b.c.c transition metals. Acta Materialia, 46 (2), 1481-1492.

[97] Kuklja, M. M., Stefanovich, E. V., and Kunz, A. B. (2000). An excitonic mechanism of detonation initiation in explosives. Journal of Chemical Physics, 112 (7), 3417-3423.